

# **EPI at 7T : Functional Imaging and Off-Resonance Correction Techniques**

by

Jack Harmer, MSc. MPhys. Dip. IPEM

Thesis submitted to  
The University of Nottingham  
for the degree of  
Doctor of Philosophy

School of Physics and Astronomy

July 2013

# Contents

<b>1</b>	<b>Introduction</b>	<b>1</b>
1.1	Thesis Outline . . . . .	2
<b>2</b>	<b>NMR Theory</b>	<b>4</b>
2.1	First Principles . . . . .	4
2.1.1	Nuclear Spin . . . . .	5
2.1.2	Precession . . . . .	6
2.1.3	Spin Ensembles and the Spin Density Operator . . . . .	7
2.1.4	Radio Frequency Pulse . . . . .	10
2.2	Relaxation . . . . .	13
2.2.1	$T_1$ (Spin-Lattice) Relaxation . . . . .	14
2.2.2	$T_2$ (Spin-Spin) Relaxation . . . . .	14
2.3	The Bloch Equations . . . . .	15
2.4	The NMR signal . . . . .	17
2.4.1	Free Induction Decay . . . . .	17
2.4.2	The Spin Echo . . . . .	17
2.4.3	The Gradient Echo . . . . .	19
2.5	From Echoes to Images . . . . .	20
2.5.1	Quadrature Detection . . . . .	20
2.5.2	Fourier Transformations . . . . .	23
2.5.3	$k$ - space . . . . .	26
2.5.4	Slice Selection . . . . .	30

2.5.5	Image Contrast . . . . .	31
2.5.6	Signal to Noise Ratio . . . . .	35
2.5.7	Relaxation Constant Parameter Mapping . . . . .	40
<b>3</b>	<b>BOLD Contrast: Imaging The Brain</b>	<b>43</b>
3.1	Susceptibility Effects . . . . .	44
3.2	Spatial Resolution . . . . .	46
3.3	Field Strength . . . . .	47
3.4	Water Diffusion . . . . .	48
3.5	SE Bold . . . . .	49
3.6	BOLD contrast in fMRI . . . . .	52
<b>4</b>	<b>Spatial location and strength of BOLD activation in high spatial resolution fMRI of the motor cortex: a comparison of SE and GE fMRI at 7 T</b>	<b>56</b>
4.1	The Motor Cortex . . . . .	56
4.2	Introduction . . . . .	59
4.3	Methods . . . . .	61
4.3.1	Data Acquisition . . . . .	61
4.3.2	Data Analysis . . . . .	62
4.4	Results . . . . .	75
4.5	Discussion . . . . .	81
4.6	Conclusion . . . . .	86
<b>5</b>	<b>Off-Resonance Field Effects: EPI Artefact Correction</b>	<b>88</b>
5.1	Theory . . . . .	88
5.1.1	Off-Resonance Effects in Conventional imaging Sequences	90
5.1.2	Off-Resonant Field Effects in EPI . . . . .	92
5.1.3	Phase Information . . . . .	100
5.1.4	Image Artefact Correction Strategies . . . . .	101

5.1.5	Dynamic Correction . . . . .	104
5.2	Introduction . . . . .	111
5.3	Application: Dynamic $\Delta B_0$ measurement during Hyperoxia . .	113
5.3.1	Introduction . . . . .	113
5.3.2	Method . . . . .	113
5.3.3	Results . . . . .	115
5.3.4	Discussion . . . . .	122
5.3.5	Conclusion . . . . .	127
5.4	Development of a Dual GE / SE EPI sequence . . . . .	129
5.4.1	Introduction . . . . .	129
5.4.2	Method . . . . .	129
5.5	Application : Dynamic Off-Resonance Correction of Simulta- neously Acquired GE and SE EPI data measured using a dual GE/SE EPI sequence . . . . .	139
5.5.1	Introduction . . . . .	139
5.5.2	Method . . . . .	140
5.5.3	Results . . . . .	144
5.5.4	Discussion . . . . .	145
5.6	Conclusion . . . . .	148
<b>6</b>	<b>Dual GE/SE EPI : Resting State Functional Magnetic Reso- nance Imaging</b>	<b>149</b>
6.1	Background . . . . .	149
6.1.1	Resting State Network Detection . . . . .	152
6.2	Introduction . . . . .	153
6.3	Methods . . . . .	154
6.3.1	Data acquisition . . . . .	154
6.3.2	Filtering . . . . .	155
6.3.3	$T_2/ T_2^*/ T_1$ maps . . . . .	157
6.3.4	Masks . . . . .	158

6.3.5	Resting state GE/SE signal fluctuations . . . . .	160
6.4	Results . . . . .	163
6.5	Discussion . . . . .	173
6.6	Conclusion . . . . .	178
<b>7</b>	<b>Conclusion</b>	<b>180</b>
	<b>Bibliography</b>	<b>183</b>

# Abstract

The work presented in this thesis describes the development and implementation of a number of ideas and methods that allow fMRI to be carried out using echo-planar imaging at ultra high field strength, despite the significant problems associated with this.

In the first study, EPI is used to probe how the gradient echo (GE) and spin echo (SE) BOLD responses relate to the underlying neurological processes, whilst the brain is in both its active and resting states. These finding show that SE BOLD contrast is harder to detect but less localised to areas around large draining veins than GE BOLD contrast and thus potentially more localised to sites that represent true functional areas of activation.

The second study describes how dynamic  $\Delta B_0$  mapping can be performed during fMRI experiments with a hyperoxic challenge, in order to assess the magnitude and extent of  $\Delta B_0$  effects that arise due to susceptibility differences between air and tissue. Developing on this, this work describes the steps involved in the design and implementation of a dual echo GE/SE EPI sequence and how it can be used to enable off-resonance effects, such as image distortion and signal concentration/dilution, to be corrected on a dynamic basis for simultaneously acquired, GE and SE data.

The final study demonstrates how such a sequence can be used to detect resting state networks. Showing that the correspondingly low temporal separation of the GE and SE data allows GE and SE BOLD contrast mechanisms to be compared in a number of novel ways in different resting state networks.

# Acknowledgements

I would like to take this opportunity to thank all those who helped me during my PhD. First and foremost I would like to thank both my supervisors, Richard Bowtell and Susan Francis, for their guidance and inspiration throughout my time in Nottingham. Their novel ideas and foresight are what made this work possible. I would also like to thank Rosa Sanchez, who in all but name acted as my third supervisor during the first few years, Denis Schluppeck, for helpful discussions regarding fMRI concepts and processing techniques and Ian Driver, for acquiring the respiract data for the dynamic field mapping project.

My time in Nottingham wouldn't have been the same without the welcome distractions of colleagues and friends at the MR centre. I have especially fond/foggy memories of after-work meetings at the Johnson Arms, and corresponding, ale fuelled, intellectual/unintellectual conversations that were had there. Not to mention, camping, mountain biking trips and intradepartmental football-style matches.

I would also like to thank my Dad and close friend Chris for their part in numerous conversations that helped spark my interest in science at an early age, all of my family, for their unending support and encouragement throughout my education and Maria, whose wonderful cooking spilled light onto gloomy write-up days. I would also like to thank Lisa for encouraging me to apply for a PhD and Mark Horsfield for recommending Nottingham.

# Chapter 1

## Introduction

The drive to increase signal to noise ratio (SNR), and hence diagnostic quality of MR images, has led to the development of MR systems that operate at increasingly high field strengths. In theory, the additional SNR can be utilised in a number of ways, such as for improving image resolution and acquisition speed or for viewing contrast mechanisms that are otherwise hard to detect. However, this is not plain sailing, because realising these gains in practice, when using these systems, is often quite challenging since there are also a number of problems that either arise, or increase in severity, when imaging at increasingly high field strengths.

A significant proportion of recent MR publications describe how MRI can be used to probe the functional nature of the human brain, by taking advantage of a contrast mechanism known as blood oxygenation level dependent contrast (BOLD). BOLD contrast based techniques are especially promising at high field strengths due to the increase in BOLD contrast with field strength. This increased BOLD sensitivity allows functional MRI (fMRI) to be carried out using spin echo based acquisition sequences, where activation related signal changes are, in theory, more spatially localised to the underlying neurological activation.

To date, the majority of fMRI is carried out using Echo Planar Imaging

(EPI) readout modules (originally developed here in Nottingham (Mansfield 1977)) that allow rapid signal sampling whilst acquiring images at relatively high spatial resolution. However, EPI acquisitions are highly susceptible to off-resonant field effects, that are exacerbated at higher field strengths, that can cause severe geometric distortions, signal modulation and in extreme cases complete signal dephasing.

The work in this thesis aims to look at how the increase in BOLD contrast at ultra high field strength, can be used to carry out robust functional imaging using both gradient echo (GE) and spin echo (SE) EPI. The goal is to use this to probe the underlying contrast mechanisms that are responsible for the BOLD response and, more specifically, to show how these differ for GE and SE acquisitions. This work also aims to alleviate some of the problems associated with using EPI at ultra high field strength by correcting for off-resonance field effects on a dynamic basis, whilst minimising any changes to the nature of the functional image acquisition.

## 1.1 Thesis Outline

In **Chapter 2** the fundamental principles that allow the technique of magnetic resonance imaging to exist and hence be used as a clinical tool are described. A basic quantum mechanical description is given that explains the nature of the underlying physical processes that occur when a nucleus is placed in an external magnetic field. This description is then expanded to explain how such a spin state system can be manipulated so that it produces a detectable radio frequency signal, when irradiated with electromagnetic pulses, and how this signal can be manipulated so as to produce images.

In **Chapter 3** the theory behind blood oxygenation level dependant contrast is presented. This work describes some potentially fundamental limitations to the spatial resolution in fMRI and explains how the level of BOLD

contrast that is attainable is influenced by factors such as magnetic field strength and water diffusion. This chapter also describes how the BOLD contrast mechanism changes when imaging is carried out using GE and SE based acquisition schemes.

**Chapter 4** describes the first major study in this thesis and presents work that was carried out to compare the spatial location and strength of BOLD activation in the motor cortex, from data acquired using SE and GE EPI sequences, in order to scrutinise the theoretical descriptions of the different contrast mechanisms. Specifically this study assesses the relative location of the GE and SE activation to the underlying vascular network.

**Chapter 5**, the second major study, describes a technique that can be used to measure  $\Delta B_0$  on a dynamic basis during a functional experiment. The work demonstrates how it is possible to carry out dynamic  $\Delta B_0$  mapping to monitor field variations during a functional hyperoxia experiment without having to change the acquisition parameters. A further method is presented that enables dynamic off resonance correction to be carried out on SE EPI data, circumventing the problem associated with using SE sequences to measure  $\Delta B_0$ . A final technique is then described that allows for the almost simultaneous collection of both GE and SE EPI data and that also enables dynamic distortion correction to be carried out on both data sets. This is demonstrated in a preliminary study in which dynamic distortion correction is carried out on SE and GE EPI data acquired during an auditory and motor fMRI experiment.

In **Chapter 6**, the final study in this thesis, a dual GE/SE EPI sequence is used to probe the nature of the resting state BOLD response with the aim of identifying and comparing functional connectivity maps from SE- and GE-BOLD data. Further, a novel technique is described for measuring  $\delta R_2^*/\delta R_2$  using non task-related resting state data.

# Chapter 2

## NMR Theory

### 2.1 First Principles

This chapter describes some of the fundamental principles that allow the technique of magnetic resonance imaging to exist. The first section starts by explaining why arguably the most important and immediately apparent feature of an MR scanner, its large static magnetic field, is a fundamental necessity for MRI. To do this, a basic quantum mechanical description is given that explains the nature of the underlying physical processes that occur when a nucleus is placed in an external magnetic field, namely the splitting of spin state energy levels, and how the strength of the static magnetic field directly affects the degree of splitting and consequently the available signal strength. This description is then expanded to explain how such a spin state system can be manipulated so that it produces a detectable radio frequency signal when irradiated with electromagnetic pulses, and also how the evolution over time of such a system can be understood using relatively straightforward quantum mechanics. The steps required to predict what effect this has on a macroscopic scale are then described along with a description of the empirically derived relaxation factors that make the theory agree with experimental evidence. The sections after this explain how the emitted signal can be manipulated

to produce images, introducing methods and concepts such as quadrature detection, the Fourier Transform and reciprocal space ( $k$ -space). The main factors that affect the contrast and signal to noise ratio of the resulting images are also described.

### 2.1.1 Nuclear Spin

Protons have a fundamental quantum mechanical property known as spin, which is analogous to the spin of a rotating ball, although strictly speaking spin angular momentum is an intrinsic property of the particle with no real classical meaning. A proton is a spin-1/2 particle. This means that it has a spin quantum number  $m_s = \frac{1}{2}$ , due to its quantum mechanical nature, and it exists in a superposition of two states  $|\alpha\rangle$  and  $|\beta\rangle$ :

$$|\psi\rangle = c_\alpha|\alpha\rangle + c_\beta|\beta\rangle \quad (2.1)$$

Where  $c_\alpha$  and  $c_\beta$  are the superposition coefficients and must be normalised such that  $|c_\alpha|^2 + |c_\beta|^2 = 1$ . In the presence of an external magnetic field in the  $z$ -direction the two spin states of the  $z$ -component of spin angular momentum ( $I_z$ ),  $|\alpha\rangle$  and  $|\beta\rangle$ , have well defined energy levels. The energy difference between the states is given by:

$$\Delta E = \hbar\omega \quad (2.2)$$

This process is known as Zeeman splitting (Figure 2.1). The term  $\omega$  is the Larmor frequency, more commonly written as  $\omega_0$  and is equal to :

$$\omega_0 = \gamma B_0, \quad (2.3)$$

where  $\gamma$  is the gyromagnetic ratio and  $B_0$  is the magnetic field strength.

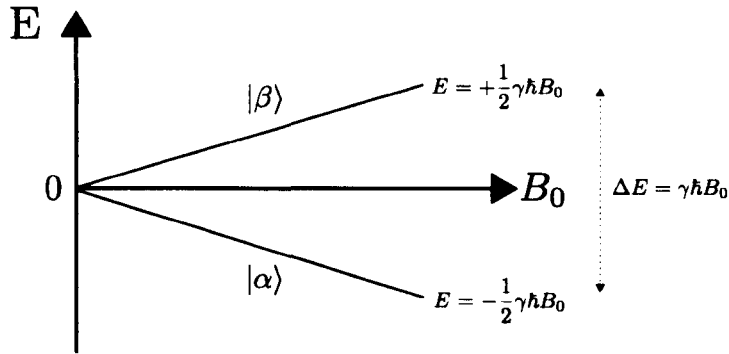


Figure 2.1: Zeeman splitting: The presence of an external magnetic field causes the two spin states to have different energy levels

### 2.1.2 Precession

The spin state  $|\psi\rangle$  described in Equation 2.1 also evolves over time. Such temporal variancy is described by the time-dependent Schrödinger equation:

$$\frac{d}{dt}|\psi\rangle(t) = -i\hat{H}|\psi\rangle(t). \quad (2.4)$$

where the Hamiltonian operator is given by:

$$\hat{H} = \omega_0 \hat{I}_z. \quad (2.5)$$

Thus the spin state at a time point  $t_1$  is related to the spin state at a time point  $t_0$  (with a temporal separation of  $\tau$ ) by the following relation:

$$|\phi\rangle(t_1) = e^{-i\omega_0\tau\hat{I}_z}|\phi\rangle(t_0). \quad (2.6)$$

The exponential term is simply a rotation operator ( $R_z$ ) that acts about the z-axis. Thus after a time period  $\tau$  the spin will have rotated around the z-axis by an angle  $\omega_0\tau$ .

### 2.1.3 Spin Ensembles and the Spin Density Operator

A typical macroscopic sample is made up of a huge number of spins  $>> 10^{20}$  with each spin in either the spin state  $|\alpha\rangle$ ,  $|\beta\rangle$  or in a superposition of the two. As a result the net magnetisation vector will be a function of the net state of all of these spins. Thus at first sight it seems impossible, in a practical sense, to predict the theoretical result of an observation on a macroscopic system as it requires the calculation of an inordinate number of spin states. However, it turns out that the vast majority of these spins have little if any affect on other spins in the sample and so, to a high degree of accuracy, the system can be considered to consist of only independent spins. This saving grace enables a quantum mechanical operator known as the spin density operator  $\hat{\rho}$ , based on the quantum mechanical expectation value, to be used to predict the result of an observation on a macroscopic scale, where

$$\hat{\rho} = \overline{|\phi\rangle\langle\phi|} = \begin{pmatrix} \overline{c_\alpha c_\alpha^*} & \overline{c_\alpha c_\beta^*} \\ \overline{c_\beta c_\alpha^*} & \overline{c_\beta c_\beta^*} \end{pmatrix} = \begin{pmatrix} \rho_\alpha & \rho_- \\ \rho_+ & \rho_\beta \end{pmatrix}. \quad (2.7)$$

Here the density matrix terms give values for the average contribution of each spin in the sample and represent the populations and coherences of the various spin states. The diagonal elements give the population of the  $|\alpha\rangle$  and  $|\beta\rangle$  states and the off-diagonal elements describe the coherences between these two states. The average value contributed by each spin for an observation of  $Q$  is then given by:

$$\langle Q \rangle = \text{Tr} \left\{ \hat{\rho} \hat{Q} \right\}, \quad (2.8)$$

with an accuracy of  $N^{-1/2}$ , where  $N$  is the number of spins. Thus in the example where  $N = 10^{20}$  the error is of the order of 1 in  $10^{10}!$ . Hence the density operator provides a method for determining the average result of an

observation independent of the number of spins in the sample.

As the coefficients of the spin states are normalised for each individual spin, it stands to reason that the spin population terms in the density matrix are also normalised such that  $\overline{c_\alpha c_\alpha^*} + \overline{c_\beta c_\beta^*} = 1$ . Only the difference between these populations is of interest. When the population of the lower energy state  $|\alpha\rangle$  is higher than that of the  $|\beta\rangle$  state there is a net polarization of spins in the direction of the  $B_0$  field. When the population of the higher energy state  $|\beta\rangle$  is greater, there is a net spin polarization in the opposite direction to the  $B_0$  field (Figure 2.2). For coherences to exist there must be a superposition

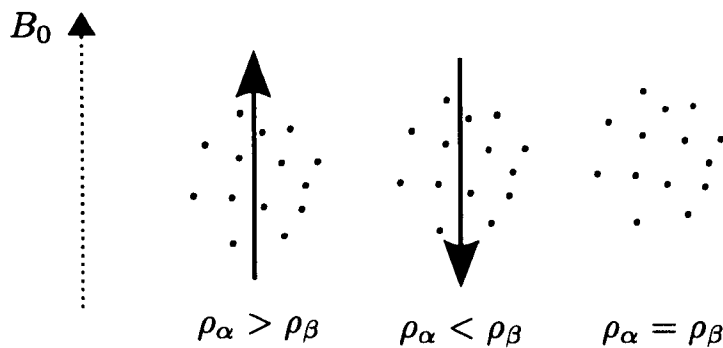


Figure 2.2: Population States: A net spin polarization (solid arrow) is produced when the population of the  $|\alpha\rangle$  and  $|\beta\rangle$  states are not equal

of spin states present and the spins must be in phase in the transverse plane. The phase of the complex coherences  $\phi_-$  represents the orientation of the net spin polarization where  $\phi_-$  is the angle of the net polarization vector from the +ve x-axis (Figure 2.3). If we know the state of the spin ensemble at some time point then the Schrödinger equation provides a method to determine its state at a later time point. A good technique to determine the starting state of a system is to consider what happens when it is in thermal equilibrium with its surrounding environment. Given the very large number of spins in a typical sample this kind of statistical analysis provides a very accurate result.

There are two points to consider when a spin system is at thermal equilibrium, firstly there is no coherence between spin states and secondly the spin

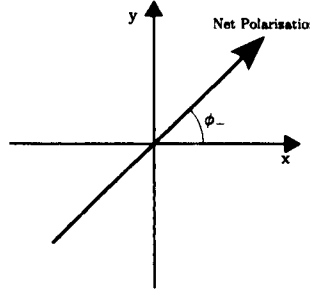


Figure 2.3: Coherence States: The net spin polarization is at angle  $\phi_-$  to the x-axis

state populations are described by a Boltzmann distribution. The population of the spin state  $|\alpha\rangle$  is then given by:

$$\rho_{\alpha}^{eq} = \frac{e^{-E_{\alpha}/k_b T}}{e^{-E_{\alpha}/k_b T} + e^{-E_{\beta}/k_b T}}. \quad (2.9)$$

A first order approximation of this can be calculated by expanding the exponentials into a power series and using only the first term of the series. This gives:

$$\rho_{\alpha}^{eq} = \frac{1}{2} + \frac{1}{4} \frac{\hbar \gamma B_0}{k_b T} \quad (2.10)$$

$$\rho_{\beta}^{eq} = \frac{1}{2} - \frac{1}{4} \frac{\hbar \gamma B_0}{k_b T}, \quad (2.11)$$

$$(2.12)$$

such that in matrix form we have:

$$\rho^{eq} = \begin{pmatrix} \frac{1}{2} + \frac{1}{4} \frac{\hbar \gamma B_0}{k_b T} & 0 \\ 0 & \frac{1}{2} - \frac{1}{4} \frac{\hbar \gamma B_0}{k_b T} \end{pmatrix}. \quad (2.13)$$

Using this expression it can be calculated that the difference between the spin population states, which will later be shown to relate to the amount of signal that can be detected in an MRI experiment, depends fundamentally on the strength of the external magnetic field (at 7T this is of the order of  $1 \times 10^5$ ).

In MRI we are more concerned with the macroscopic effects from spin ensembles and the spin density operator is typically represented by a magnetisation vector,  $\mathbf{M}$ . Where the  $M_z$  component is related to the population difference between the spin states and the  $M_{xy}$  component is related to the quantum coherences.

### 2.1.4 Radio Frequency Pulse

If an MR sample is irradiated with a radio-frequency (RF) electromagnetic pulse. The spins in the sample will experience a very weak oscillating magnetic field. If the frequency of the RF pulse is matched to the resonance frequency of the spins this will have a large effect on the nature of the spin states due to a property known as resonance. Simply put, because the magnetic field from the RF pulse then oscillates at the same frequency as that at which the spins are precessing, the overall effect of the pulse is amplified significantly (in analogy to pushing a child on a swing). When considering the nature of these effects it is much simpler to consider the problem in a frame rotating at the same frequency as the RF pulse ( $\omega_{ref}$ ). In this rotating frame the time-dependent spin Hamiltonian then becomes:

$$\hat{H} = \Omega_0 \hat{I}_z, \quad (2.14)$$

where

$$\Omega_0 = \omega_0 - \omega_{ref} \quad (2.15)$$

and is known as the resonance offset frequency. During the application of a RF pulse this becomes:

$$H = \Omega_0 \hat{I}_z + \omega_{nut} \left( \hat{I}_x \cos(\phi_p) + \hat{I}_y \sin(\phi_p) \right). \quad (2.16)$$

where  $\omega_{nut}$  is the nutation frequency and is effectively a measure of the strength of magnetic field component of the RF field and  $\phi_p$  is the phase of the RF pulse. Thus for an exactly on resonance pulse with phase,  $\phi_p = 0$  the Hamiltonian becomes:

$$H = \omega_{nut} \left( \hat{I}_x \cos(\phi_p) \right). \quad (2.17)$$

Then by applying the Schrödinger equation it can be seen that the spin state after application of an RF pulse is simply related to state before it by the following:

$$|\psi\rangle_1 = \hat{R}_{\phi_p}(\beta_p) |\psi\rangle_0, \quad (2.18)$$

where  $\beta_p$  is known as the flip angle of the pulse and is given by  $\beta_p = \omega_{nut}\tau_p$  and  $\hat{R}_{\phi_p}$  is simply a rotation operator:

$$\hat{R}_{\phi_p}(\beta_p) = \begin{pmatrix} \cos(\frac{1}{2}\beta_p) & -i\sin(\frac{1}{2}\beta_p e^{-i\phi_p}) \\ -i\sin(\frac{1}{2}\beta_p e^{+i\phi_p}) & \cos(\frac{1}{2}\beta_p) \end{pmatrix} \quad (2.19)$$

This quantum mechanical description then makes it fairly trivial to determine what effect different pulses have on a spin state.

### 90° RF pulse

In the case of a  $\beta_p = \pi/2$  pulse, otherwise known as a 90° pulse, with a phase of 0, the following effects are observed on a spin in state  $|\alpha\rangle$ :

$$\hat{R}_0|\alpha\rangle = \frac{1}{\sqrt{2}} \begin{pmatrix} 1 & -i \\ -i & 1 \end{pmatrix} \begin{pmatrix} 1 \\ 0 \end{pmatrix} = \frac{1}{\sqrt{2}} \begin{pmatrix} 1 \\ -i \end{pmatrix} = e^{-i\pi/4} \frac{1}{2} \begin{pmatrix} 1+i \\ 1-i \end{pmatrix} = e^{-i\pi/4} | -y \rangle \quad (2.20)$$

Thus the  $90^\circ$  RF pulse converts the  $|\alpha\rangle$  state into the  $|-\gamma\rangle$  state (a superposition of the  $|\alpha\rangle$  and  $|\beta\rangle$  state), with an additional phase factor. Hence the spin polarization is rotated into the transverse plane. In a similar manner it can be shown that a  $\pi$  pulse ( $180^\circ$ ) transforms a spin in state  $|\alpha\rangle$  into state  $|\beta\rangle$  with an additional  $-i$  phase factor, i.e. the spin polarization is flipped.

To expand this to a macroscopic description we need to consider what happens to the density matrix. If we again consider what happens to the spin state after an RF pulse, as described in Equation 2.18, then we find that the density matrix after the RF pulse is given by:

$$\hat{\rho}_1 = \overline{|\phi\rangle_1\langle\phi|_1} = \overline{\hat{R}_{\phi_p}(\beta_p)|\phi\rangle_0\langle\phi|_0\hat{R}_{\phi_p}(-\beta_p)} \quad (2.21)$$

$$\hat{\rho}_1 = \hat{R}_{\phi_p}(\beta_p)\hat{\rho}_0\hat{R}_{\phi_p}(-\beta_p) \quad (2.22)$$

For a starting state of thermal equilibrium  $\hat{\rho}_0 = \frac{1}{2}\hat{I} + \frac{1}{4}\frac{\hbar\gamma B_0}{k_b T}\hat{I}_z$  and a flip angle of  $90^\circ$  we get the following:

$$\hat{\rho}_0 = \frac{1}{2}\hat{I} + \frac{1}{4}\frac{\hbar\gamma B_0}{k_b T}\hat{I}_z \quad (2.23)$$

$$\hat{R}_{\phi_p}(\beta_p)\hat{I}_z\hat{R}_{\phi_p}(-\beta_p) = -\hat{I}_y \quad (2.24)$$

$$\hat{\rho}_1 = \frac{1}{2}\hat{I} - \frac{1}{4}\frac{\hbar\gamma B_0}{k_b T}\hat{I}_y \quad (2.25)$$

and in terms of the density matrix:

$$\rho_0 = \begin{pmatrix} \frac{1}{2} + \frac{1}{4}\frac{\hbar\gamma B_0}{k_b T} & 0 \\ 0 & \frac{1}{2} - \frac{1}{4}\frac{\hbar\gamma B_0}{k_b T} \end{pmatrix} \quad (2.26)$$

$$\rho_1 = \begin{pmatrix} \frac{1}{2} & -\frac{1}{4i} \frac{\hbar\gamma B_0}{k_b T} \\ +\frac{1}{4i} \frac{\hbar\gamma B_0}{k_b T} & \frac{1}{2} \end{pmatrix} \quad (2.27)$$

Thus the 90° RF pulse makes the populations of the two state equal and introduces coherences, shifting the net magnetisation vector  $\mathbf{M}$  into the transverse plane along the  $-y$  axis. In a similar manner it can be shown that a 180° pulse inverts the spin populations without adding coherences.

## 2.2 Relaxation

In the previous section a mathematical description was given to show how rotation operators about  $z$  leave the populations of the  $|\alpha\rangle$  and  $|\beta\rangle$  states unchanged and simply add a phase term to the coherence:

$$\rho_{\alpha,1} = \rho_{\alpha,0} \quad (2.28)$$

$$\rho_{\beta,1} = \rho_{\beta,0} \quad (2.29)$$

$$\rho_{-,1} = e^{i\Omega_0\tau} \rho_{-,0} \quad (2.30)$$

From this it would appear that the spin magnetisation vectors precess around the  $z$ -axis indefinitely. Indeed the induced current from this rotating magnetisation can be detected by placing tuned coils around the sample. However experiments show that the amplitude of the measured signal decreases over time. It turns out that to model the detected signal accurately, two empirically determined decay constants,  $T_1$  and  $T_2$ , are needed, where  $T_1$  gives a measure of the return to equilibrium as a result of spin-lattice effects and  $T_2$  due to spin-spin effects.

### 2.2.1 $T_1$ (Spin-Lattice) Relaxation

The energy gained by a system due to the application of an RF pulse is eventually lost to the surrounding lattice by a process known as  $T_1$  relaxation. This causes the population of the spin states to return to the thermal equilibrium condition. The probability of an interaction occurring that causes spins to lose energy to the surrounding lattice, depends on the frequency of the vibrational, translational and rotational motion of magnetic entities within the sample. If these occur at the Larmor frequency, stimulated emission takes place and energy is lost. If the sample contains a very large number of magnetic entities moving at frequency  $\omega_0$ , energy will be lost rapidly and the  $T_1$  time will be short. To take account of this the spin populations can be modelled in the following way:

$$\rho_{\alpha,1} = (\rho_{\alpha,0} - \rho_{\alpha}^{eq})e^{-\frac{t}{T_1}} + \rho_{\alpha}^{eq} \quad (2.31)$$

$$\rho_{\beta,1} = (\rho_{\beta,0} - \rho_{\beta}^{eq})e^{-\frac{t}{T_1}} + \rho_{\beta}^{eq} \quad (2.32)$$

### 2.2.2 $T_2$ (Spin-Spin) Relaxation

The phase coherence generated as a result of nuclear magnetic resonance during an RF excitation pulse is also lost, due to local variations in the magnetic field strength. This is due to the presence of small magnetic fields generated by other nuclei ( $T_2$  decay) and magnetic field inhomogeneities ( $T_2'$  decay). The combination of this dephasing  $T_2^*$  is described by the following

$$\frac{1}{T_2^*} = \frac{1}{T_2} + \frac{1}{T_2'} \quad (2.33)$$

For example, liquids, like water, have a long  $T_2$  because the molecules are free to move around rapidly and so any fluctuations in the local magnetic field strength, imparted by the presence of other molecules, are rapid. In comparison the molecules in rigid structures generally have a short  $T_2$  because

the interactions between spins occur for a longer period of time and have a greater effect. In terms of the spin density operator, this effect can be modelled by adding a decay term to the coherence states:

$$\rho_{-,1} = e^{i(\Omega_0 - \frac{1}{T_2})\tau} \rho_{-,0} \quad (2.34)$$

## 2.3 The Bloch Equations

When imaging macroscopic samples it is often preferable to describe NMR using classical physics. This is reasonable, as the time dependence of the expectation value in quantum mechanics follows the classical case almost exactly when a large number of spins are considered (Bloch 1946). Thus the net torque,  $\bar{T}$ , acting on the spins within a unit volume due to the net angular momentum vector of the spins within the volume (the spin isochromat),  $\bar{S}$ , will follow the following classical description very accurately:

$$\bar{T} = \frac{d\bar{S}}{dt} = \bar{M} \times \bar{B}, \quad (2.35)$$

where  $\bar{M}$  is the magnetic moment per unit volume (magnetisation). Then using:

$$\bar{M} = \gamma \bar{S} \quad (2.36)$$

the following expression can be derived:

$$\frac{d\bar{M}}{dt} = \gamma [\bar{M} \times \bar{B}] \quad (2.37)$$

This is the general form of the Bloch equation that does not take into account relaxation effects. If we add the empirically determined relaxation terms  $T_1$

and  $T_2$  and set

$$\bar{B} = \begin{pmatrix} B_x \\ B_y \\ B_z \end{pmatrix} = \begin{pmatrix} B_1 \cos(\omega t) \\ B_1 \sin(\omega t) \\ B_0 \end{pmatrix} \quad (2.38)$$

we get the full Bloch equations:

$$\frac{dM_x}{dt} = \gamma(M_y B_0 + M_z B_1 \sin(\omega t)) - \frac{M_x}{T_2} \quad (2.39)$$

$$\frac{dM_y}{dt} = \gamma(M_z B_1 \cos(\omega t) - M_x B_0) - \frac{M_y}{T_2} \quad (2.40)$$

$$\frac{dM_z}{dt} = \gamma(M_x B_1 \sin(\omega t) + M_y B_1 \cos(\omega t)) - \frac{M_z - M_0}{T_1}, \quad (2.41)$$

in the presence of an RF field. This can then be solved using a number of limiting conditions, such as the fact that  $B_1 = 0$  just after the application of a  $90^\circ$  RF pulse, and that if the pulse is applied in the x-direction then  $M_x = M_z = 0$  and  $M_y = M_0$ . This gives:

$$M_x(t) = M_0 \sin(\omega_0 t) e^{\frac{-t}{T_2}} \quad (2.42)$$

$$M_y(t) = M_0 \cos(\omega_0 t) e^{\frac{-t}{T_2}} \quad (2.43)$$

$$M_z(t) = M_0 \left[ 1 - e^{\frac{-t}{T_1}} \right]. \quad (2.44)$$

Using complex notation this gives

$$M_{xy}(t) = M_0 e^{i\omega_0 t} e^{\frac{-t}{T_2}} \quad (2.45)$$

$$M_z(t) = M_0 \left[ 1 - e^{\frac{-t}{T_1}} \right]. \quad (2.46)$$

where  $M_{xy} = M_x + iM_y$ .

## 2.4 The NMR signal

### 2.4.1 Free Induction Decay

After RF excitation the rotating transverse component of the net magnetisation vector will induce an oscillating voltage in any tuned coils that are placed near to the sample (Faraday's Law), whose amplitude decays due to  $T_2^*$  effects (Figure 2.4). It is the detection of this induced voltage that is the fundamental goal of any NMR experiment, because contained within the signal is information about the spins within the sample. Further, various techniques can be used to increase the amount of useful information contained within the signal, the most common being methods that allow spatial localisation of the different components of the signal, using methods such as frequency and phase encoding (see Sections 2.5.3 and 2.5.4).

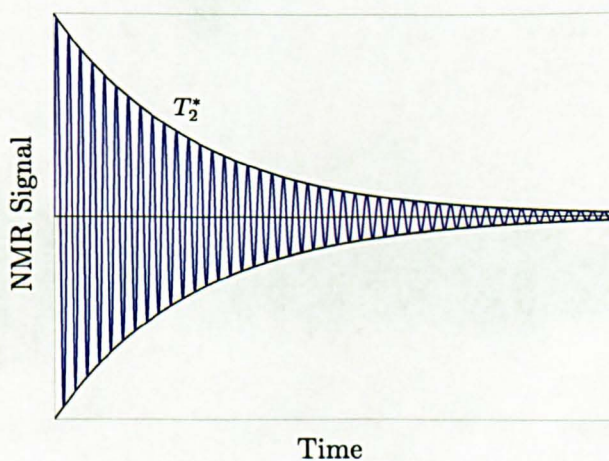


Figure 2.4: Free Induction Decay.

### 2.4.2 The Spin Echo

To remove the dephasing effects due to magnetic field inhomogeneities, i.e.  $T_2'$  in Equation 2.33, it is also possible to measure the induced voltage after a combination of pulses has been applied in a pre-determined sequence, known

as a spin echo (SE) pulse sequence (Figure 2.5). In such a sequence, an initial  $90^\circ$  RF pulse excites the nuclei within the sample, converting longitudinal magnetisation into in-phase coherent transverse magnetisation, which then induces a signal within the RF receiver coils. The transverse magnetisation loses phase coherence due to  $T_2^*$  decay, reducing the signal intensity. However, a second  $180^\circ$  RF pulse is then applied, which effectively flips the spins about their axes in the transverse plane, and rephasing occurs (Figure 2.6). This reverses the dephasing effect of magnetic field inhomogeneities because the phase accumulated by the transverse magnetisation due to magnetic field inhomogeneities is reversed after application of the  $180^\circ$  RF pulse (assuming the magnetic field inhomogeneities are time invariant).

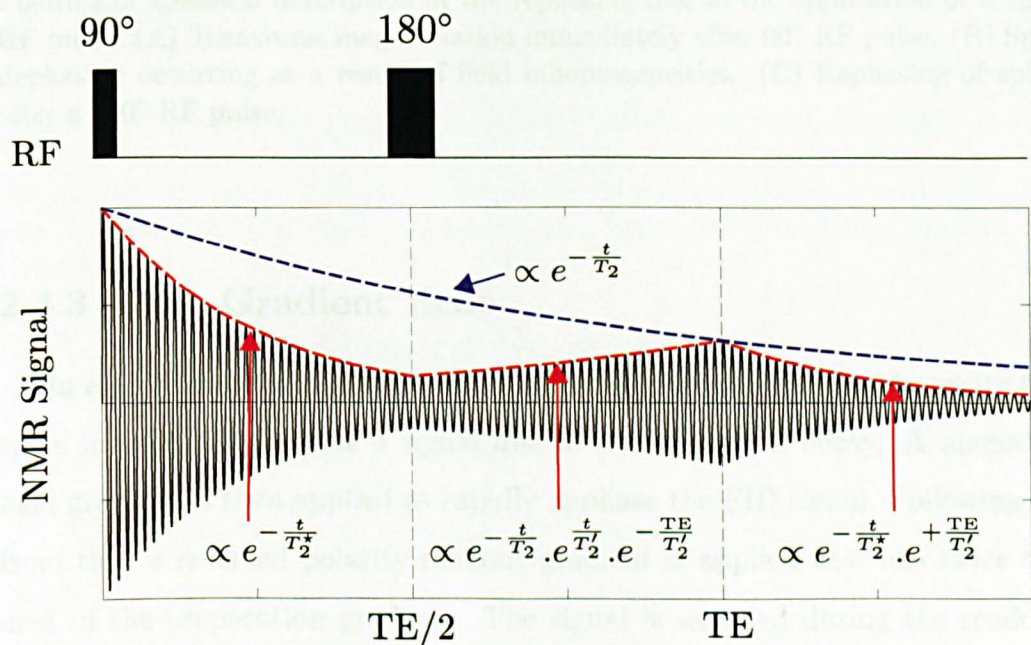


Figure 2.5: A simulated SE pulse sequence. The red line shows the decay due to both  $T_2$  and  $T_2^*$  effects whereas the blue line describes decay due to  $T_2$  and incorporates the rephasing effects of the  $180^\circ$  RF pulse. In a SE pulse sequence, the red line intercepts the blue line at time TE.

Thus after a time  $TE/2$ , the phase of the nuclei will change by an amount identical (ideally) to that experienced in the time period between the initial  $90^\circ$  RF pulse and the subsequent  $180^\circ$  RF pulse, producing a signal known

as a spin echo at time TE; this phenomenon was accidentally discovered by the US physicist Erwin L. Hahn and described in his seminal paper (Hahn 1950). However, the dephasing effects due to spin-spin interactions ( $T_2$ ) are essentially random and so are not rephased; because of this, the spin-echo has a signal amplitude that decays with the time constant,  $T_2$ .

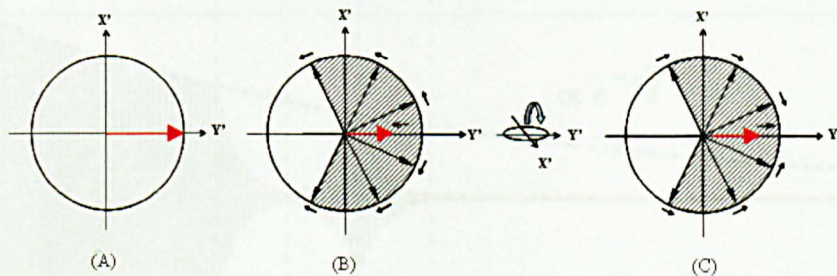


Figure 2.6: Classical description of the rephasing due to the application of a  $180^\circ$  RF pulse. (A) Transverse magnetisation immediately after  $90^\circ$  RF pulse. (B) Spin dephasing occurring as a result of field inhomogeneities. (C) Rephasing of spins after a  $180^\circ$  RF pulse.

### 2.4.3 The Gradient Echo

In a gradient echo pulse sequence, an initial RF pulse is used to excite the spins in order to generate a signal due to free induction decay. A magnetic field gradient is then applied to rapidly dephase the FID signal. Following on from this, a reversed polarity readout gradient is applied that has twice the area of the preparation gradient. The signal is sampled during the readout gradient. At the point half way through the readout gradient the dephasing effects of the preparation gradient are cancelled out leading to a gradient echo. Reversing the gradient in this way does not remove the dephasing effect of any magnetic field inhomogeneities in the same way as the SE sequence. Instead the gradient echo (GE) that is produced has a signal intensity that is dependent on  $T_2^*$  not  $T_2$  (Figure 2.7).

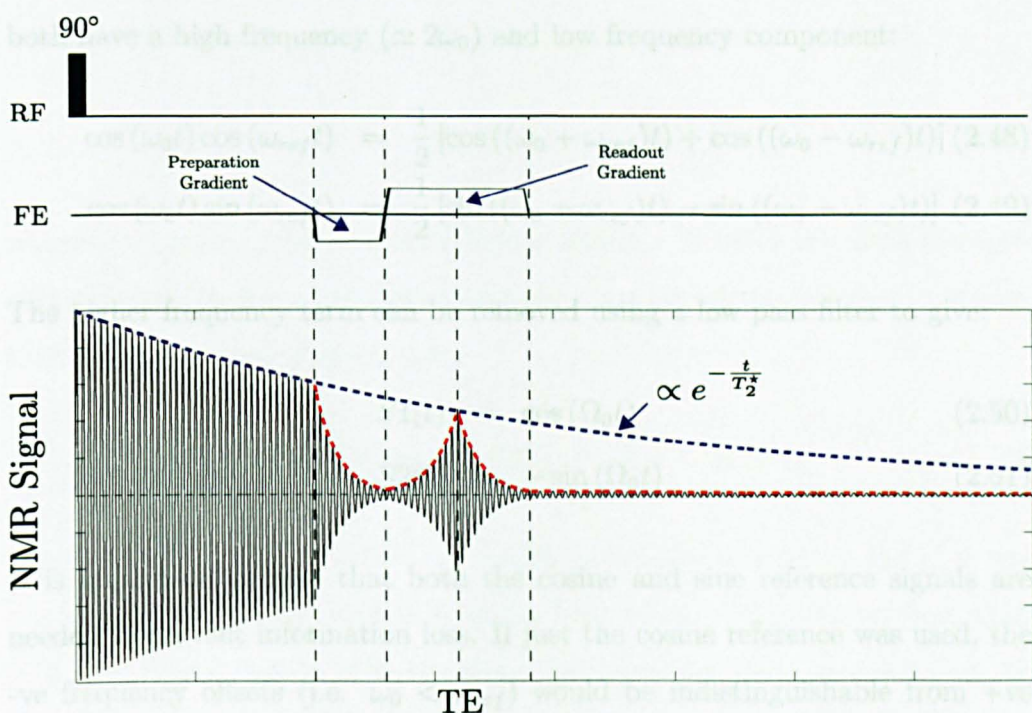


Figure 2.7: A simulated GE pulse sequence. The red line shows the decay due to both  $T_2^*$  effects and the imaging gradients, whereas the blue line describes decay due to only  $T_2^*$ . The preparation gradient dephases the initial signal, this is then followed by a reversed polarity readout gradient with twice the area of the preparation gradient.

## 2.5 From Echoes to Images

### 2.5.1 Quadrature Detection

The signal from the MR scanner is independently mixed with cosine and sine reference signals (at frequency  $\omega_{ref}$ ) to generate two signals that oscillate with a much lower frequency ( $\Omega_0$ ) than the original signal:

$$\Omega_0 = \omega_0 - \omega_{ref}, \quad (2.47)$$

where  $\omega_{ref}$  is set to a frequency which is very close to the expected Larmor frequency for the field strength in question. The two signals that are produced

both have a high frequency ( $\simeq 2\omega_0$ ) and low frequency component:

$$\cos(\omega_0 t) \cos(\omega_{ref} t) = \frac{1}{2} [\cos((\omega_0 + \omega_{ref})t) + \cos((\omega_0 - \omega_{ref})t)] \quad (2.48)$$

$$\cos(\omega_0 t) \sin(\omega_{ref} t) = \frac{1}{2} [\sin((\omega_0 + \omega_{ref})t) - \sin((\omega_0 - \omega_{ref})t)] \quad (2.49)$$

The higher frequency term can be removed using a low pass filter to give:

$$S1(t) = \cos(\Omega_0 t) \quad (2.50)$$

$$S2(t) = -\sin(\Omega_0 t) \quad (2.51)$$

It is important to note that both the cosine and sine reference signals are needed to prevent information loss. If just the cosine reference was used, the -ve frequency offsets (i.e.  $\omega_0 < \omega_{ref}$ ) would be indistinguishable from +ve offsets ( $\omega_0 > \omega_{ref}$ ). For simplicity, the two terms that are generated can be considered as the real and imaginary parts of a complex signal:

$$S(t) = S1(t) + iS2(t) \quad (2.52)$$

This complex signal retains all the original information and distinguishes between positive and negative values of  $\Omega_0$ . This is a very convenient way of describing the signal because it allows it to be modelled as an exponential. If this technique was not used the FID would be described by:

$$S(t) = \cos(\omega_0 t) e^{-\lambda t} \quad (2.53)$$

Where,  $\lambda = \frac{1}{T_2^*} = \frac{1}{T_2} + \frac{1}{T_2'}$ . However when using the complex signal notation along with Euler's relation, the FID can be described as :

$$S(t) = e^{(-i\Omega_0 t)} e^{-t/T_2^*}, \quad (2.54)$$

where,  $e^{ix} = \cos(x) + i\sin(x)$ .  $\Omega_0$  then depends on:

$$\Omega_0 = \gamma B(r), \quad (2.55)$$

where  $B(r)$  is the total magnetic field strength. In MRI this field strength varies due to  $B_0$  inhomogeneities and the strength of the imaging gradients that have been applied, such that:

$$B(r) = \Delta B_0(r) + G_x x + G_y y + G_z z, \quad (2.56)$$

where,  $G_x x$ ,  $G_y y$  and  $G_z z$  are the magnetic fields imparted by the x, y and z gradients respectively and  $\Delta B_0$  is the field offset. Following on from this, it is easy to see that in MRI the signal produced by spins precessing in the transverse plane, after RF excitation at a position  $\mathbf{r}$ , can be described by the following Equation :

$$S(r, t) = \rho(r) e^{i\phi(t)} e^{-t/T_2^*}, \quad (2.57)$$

where,  $\rho(r)$  is the spin density and  $\phi(t)$  is the phase at time, t, which can be written as:

$$\phi(t) = 2\pi\gamma \left[ \int_0^t G_x(t)x dt + \int_0^t G_y(t)y dt + \int_0^t G_z(t)z dt + \int_0^t \Delta B_0(r) dt \right]. \quad (2.58)$$

The phase of the signal does not depend on the static magnetic field strength but on  $\Delta B_0$ , i.e the field offset, and the gradient history.

The gradient dependent components of the phase (Equation 2.58) are used to encode the signal in k-space (see Section 2.5.2), as a result the pixel by pixel phase in the phase image, created from the complex data after Fourier

transformation of the signal, is described by the following formula:

$$\phi_{image}(x, y) = \arctan \frac{\Im(S(x, y))}{\Re(S(x, y))} \quad (2.59)$$

Where  $S$  is the complex signal from the MR scanner. Ideally, this phase is not dependent on the gradients that were applied during imaging (assuming perfect echo centring in k-space).

### 2.5.2 Fourier Transformations

The 18th century French mathematician Jean Baptiste Joseph Fourier developed a mathematical technique known as a Fourier Transformation (FT) that can be used to determine the spectral composition of a signal. The transformation along with its inverse are described by the following relations:

$$S(\Omega) = \int_0^\infty s(t)e^{-i\Omega.t} dt \quad (2.60)$$

$$s(t) = \int_0^\infty S(\Omega)e^{i\Omega.t} d\Omega \quad (2.61)$$

An NMR signal which is made up of a number of components ( $l$ ) with different frequencies,  $\Omega_l$ , and decay constants,  $\lambda_l$ , can be described by the following:

$$s(t) = \sum_l a_l e^{(i\Omega_l - \lambda_l)t} dt, \quad (2.62)$$

where  $a_l$  represents the amplitude of each signal component  $l$ . The Fourier transform of this gives:

$$s(\Omega) = \sum_l a_l \int_0^\infty e^{-(i(\Omega - \Omega_l) + \lambda_l)t} dt. \quad (2.63)$$

After evaluating the integral this leads to:

$$s(\Omega) = \sum_l a_l \left[ \frac{1}{\lambda_l + i(\Omega - \Omega_l)} \right], \quad (2.64)$$

where the term in brackets is a complex Lorentzian function. Thus, Fourier transformation of the NMR signal produces a frequency domain signal that is a superposition of Lorentzian spectral components. This can be seen in Figure 2.8 where a simulated signal is shown broken down into its three constituent components along with the Lorentzian of each. It can be seen that the Fourier transform of the signal (using a discrete Fast Fourier Transform algorithm (FFT)) produces a result that is almost identical to the sum of the Lorentzian components. In magnetic resonance imaging the frequency in the signal is used

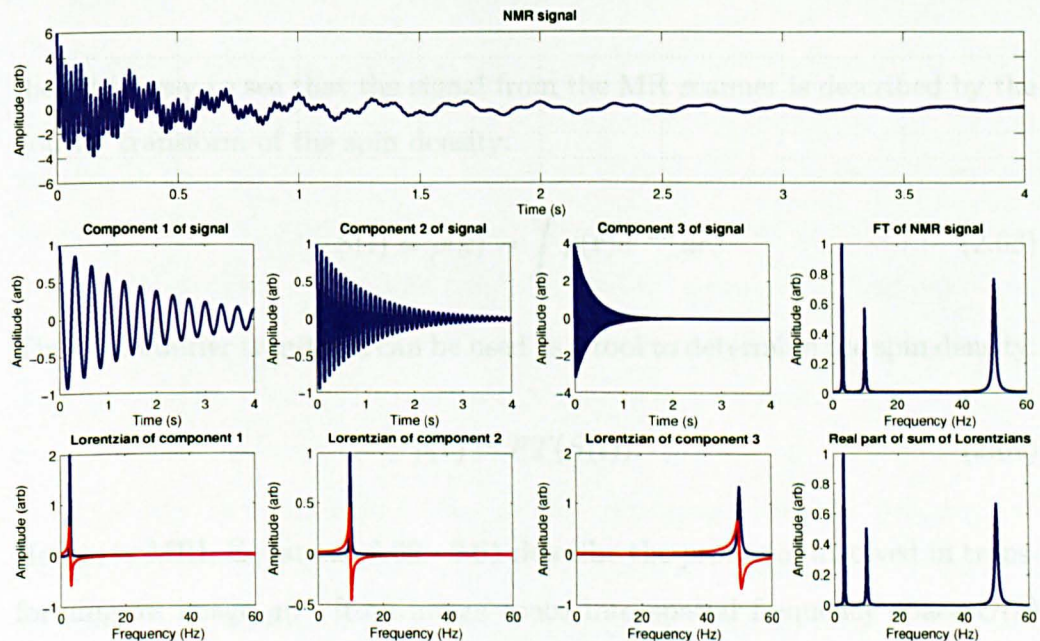


Figure 2.8: Top: Simulated NMR time series containing three different component signals. Middle (left to right) Three individual components that make up the signal and the Fourier Transform of the signal. Bottom: Lorentzians of each of the signal components and the real part of the sum of the three.

to encode its spatial location and the  $a_l$  term in Equation 2.62 is governed by the proton density of the sample being scanned. This can be seen by changing

Equation 2.57 to describe the total detected signal whilst ignoring decay and off-resonance effects, so that:

$$S(t) = \int \rho(\mathbf{r}) e^{i\gamma\mathbf{r} \cdot \int_0^t \mathbf{G}(t') dt'} d\mathbf{r}, \quad (2.65)$$

where  $\rho(\mathbf{r})$  is the spin density at position vector  $\mathbf{r}$  and  $\mathbf{G}(t')$  is the gradient at time  $t'$ , such that in the 2D case

$$\mathbf{G}(t') = G_x(t)\mathbf{i} + G_y(t)\mathbf{j}. \quad (2.66)$$

If the following substitution is made:

$$k(t) = \gamma \int_0^t \mathbf{G}(t') dt', \quad (2.67)$$

then it is easy to see that the signal from the MR scanner is described by the Fourier transform of the spin density:

$$S(t) = \rho(k) = \int \rho(\mathbf{r}) e^{i \mathbf{k} \cdot \mathbf{r}} d\mathbf{r}. \quad (2.68)$$

Thus the Fourier transform can be used as a tool to determine the spin density:

$$\rho(\mathbf{r}) = FT(S(t)). \quad (2.69)$$

Hence, in MRI, Equations 2.60 - 2.61 describe the processes involved in transforming an image  $g(r)$  from image space into spatial frequency space  $G(k)$  along with its inverse.

It is also simple to see from Equation 2.67 that if no imaging gradients are applied during sampling, i.e.  $k(t) = 0$ , the signal only provides information regarding the number of spins that are present not their positions:

$$S(t) = \int \rho(\mathbf{r}) d\mathbf{r}. \quad (2.70)$$

In reality the signal is only sampled for a limited period of time and at discrete intervals, thus a discretised version of the Fourier transform has to be used (DFT).

### 2.5.3 k - space

To generate useful diagnostic information from the NMR signal it is usually necessary to localise the signal in at least two dimensions. This can be accomplished by employing frequency and phase encoding gradients, as eluded to in the previous section, to modify the frequency and phase of the signal in a manner that depends upon spatial location.

#### Frequency Encoding

Frequency encoding gradients can be used to spatially encode the NMR signal in one dimension. To achieve this, a linear magnetic field gradient is applied, in the required encoding direction, during the acquisition of the free induction decay or spin echo signal. The magnetic field gradients are created using gradient coils. The resulting spatial variation in magnetic field strength causes the spin isochromats to precess at different frequencies depending on their position in the sample. Fourier transformation of this signal then provides the amplitude of each frequency component. Since each frequency component has a direct one to one correspondence with position, 1D spatial localisation is achieved (Figure 2.9). There are a number of factors that can alter the effectiveness of this process by disrupting the correspondence of frequency with position, such as the presence of unwanted local magnetic field inhomogeneities.

#### Phase Encoding

Unfortunately, frequency encoding can not be used to encode the second spatial dimension, as the signal associated with any given frequency band

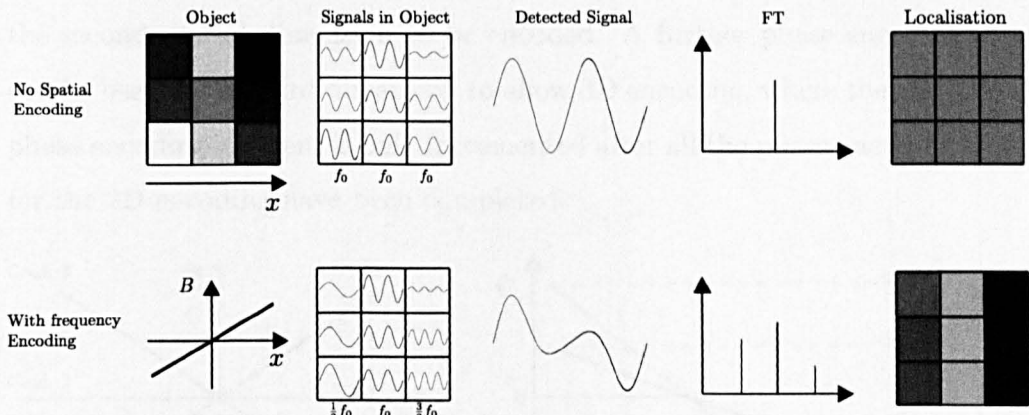


Figure 2.9: In the top row an object is imaged with no encoding gradients. The spins in the object all precess at the same frequency. The amplitude of the detected signal from any given macroscopic volume depends on the number of spins that are present. As the signal has the same frequency at all points in the object the Fourier transform of the signal contains only one component and therefore no spatial localisation is possible. When a frequency encoding gradient is applied (second row) the frequency varies with position and the Fourier transform of the total measured signal contains a number of components that can be used for 1D spatial localisation. However the second spatial dimension remains unencoded.

would not then be associated with a unique spatial location. Fortunately, phase encoding gradients can be used to get around this problem. These are applied before the signal is acquired in order to generate an additional net phase that depends on position, in a similar manner to frequency encoding. Since frequency is simply the rate of change of phase it is then possible to encode the signal in the second dimension by repeating the signal acquisition a number of times with different phase encoding gradient strengths used for each new acquisition. The rate of change of phase is then different at different points in the object depending on how far the point is away from the central turning point of the gradient (where the net phase accumulation due to the gradient will always be zero) (Figure 2.10). As rate of change of phase is simply equal to frequency the Fourier transform can be used to determine the rate of phase accumulation. Thus the one to one correspondence between rate of change of phase and position in the phase encoding direction allows

the second spatial dimension to be encoded. A further phase encoding step can be used in the third dimension to allow 3D encoding, where the additional phase encoding gradient is only incremented after all the phase encoding steps for the 2D encoding have been completed.

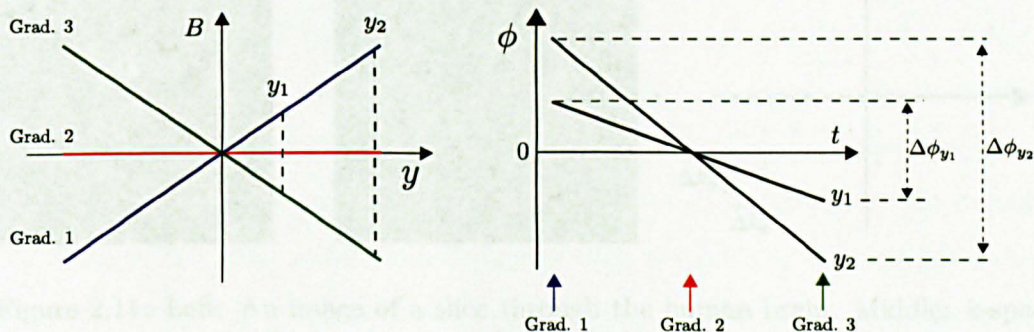


Figure 2.10: In this example an object is imaged three times with three different phase encoding gradients applied before data sampling. Gradient 1 causes a net phase offset that varies with position along the  $y$ -axis of the object, gradient 2 has strength 0 and causes no dephasing and gradient 3 produces a phase shift of opposite polarity to gradient 1 (Left image). The rate of change of phase over time (frequency) is then different at different points in the object. In this case the point  $y_2$  experiences a larger phase change over time due to the gradients than point  $y_1$  (Right image).

### Populating k-space

The signal that is acquired in this way can be constructed into a matrix with each signal acquisition, consisting of a signal with a range of frequencies due to the frequency encoding gradients, populating one line of the matrix. Each line will then have a different phase due to the phase encoding gradients. The matrix then effectively contains two dimensions of frequency information: one set of frequencies due to the frequency encoding gradients that are applied during signal acquisition and one set due to the presence of varying degrees of rates of change of phase in the data, due to the different phase encoding gradients that are applied before each signal acquisition. This matrix form of the spatially encoded NMR signal, is known as reciprocal space or more

commonly, k-space (see Figure 2.11). Different acquisition sequences can be used to populate k-space in a variety of ways. An example of how k-space is filled during a simple 2D gradient echo sequence is shown in Figure 2.12.

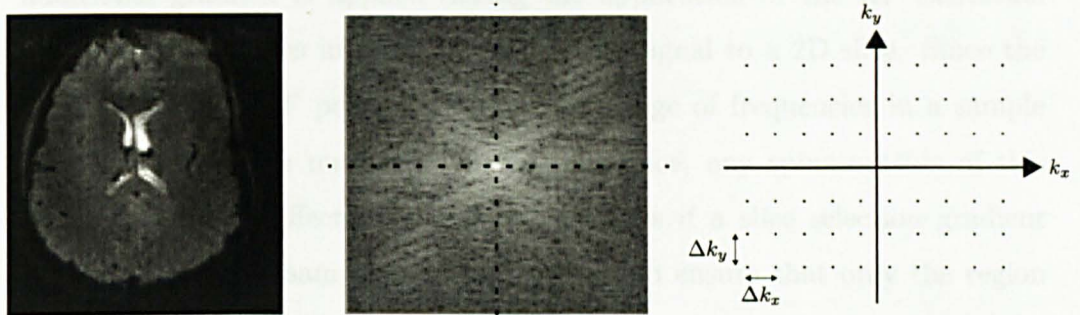


Figure 2.11: Left: An image of a slice through the human brain. Middle: k-space data for this image. Right: A representation of the discrete nature of the k-space data.

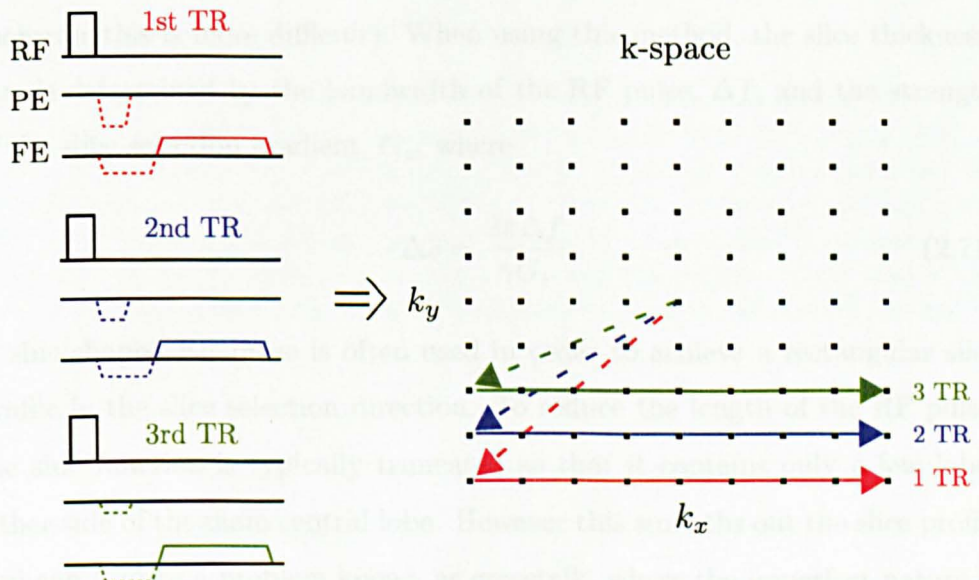


Figure 2.12: A representation of how k-space is filled during a 2D GE pulse sequence. During the first TR, the combination of the phase encoding gradient and frequency encoding preparation gradient, shift the point at which k-space is filled to the bottom left corner. The positive lobe of the frequency encoding gradient is then applied during sampling to acquire the first frequency encoded signal, populating the first line of k-space. During subsequent TRs the strength of the initial phase encoding gradient is altered so that different lines of k-space are encoded differently.

### 2.5.4 Slice Selection

Images are usually acquired using a slice selection technique, where an additional gradient is applied during the application of the RF excitation and refocusing pulses in order to localise the signal to a 2D slice. Since the bandwidth of an RF pulse determines the range of frequencies in a sample that will experience nuclear magnetic resonance, any spins outside of this range will not be effected by the pulse. Thus if a slice selection gradient is applied across a sample in such a way as to ensure that only the region of interest (i.e. the slice) contains spins with frequencies that match those present within the bandwidth of the RF pulse, the rest of the sample will be unaffected by the pulse (Figure 2.13). Acquiring more than one slice is then simply a case of repeating the acquisition using an RF pulse with a different carrier frequency, or by changing the isocentre of the slice selection gradient (however this is more difficult). When using this method, the slice thickness,  $\Delta z$ , is determined by the bandwidth of the RF pulse,  $\Delta f$ , and the strength of the slice selection gradient,  $G_z$ , where

$$\Delta z = \frac{2\pi\Delta f}{\gamma G_z}. \quad (2.71)$$

A sinc shaped RF pulse is often used in order to achieve a rectangular slice profile in the slice selection direction. To reduce the length of the RF pulse, the sinc function is typically truncated so that it contains only a few lobes either side of the main central lobe. However this smooths out the slice profile and can lead to a problem known as crosstalk, where the imperfect nature of the slice profile (i.e. its non-rectangular shape) means that the RF pulses also affect spins in neighbouring slices. When these adjacent slices are then selected for imaging, residual magnetisation perturbations exist due to the excitation of the previous slice. This problem can be alleviated by interleaving the slice selection process so that adjacent slices are not acquired immediately after

each other. For example this may involve acquiring odd numbered slices first, then even numbers. The slice selection gradient also causes dephasing across a slice, however this can be compensated for by applying a rephasing gradient lobe, directly after the slice selection gradient, that has opposite polarity and half the gradient area of the slice selection gradient.

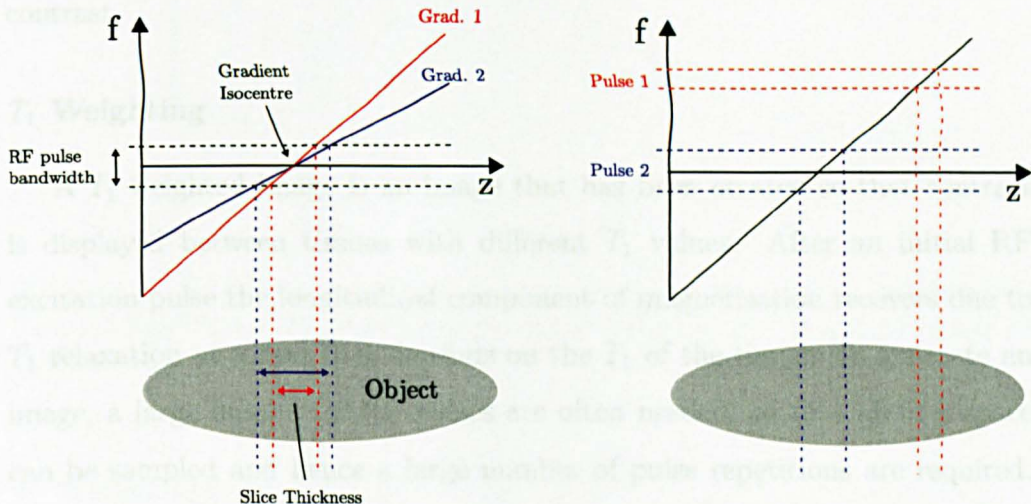


Figure 2.13: An example of how slice selection gradients can be applied during the application of an RF pulse to restrict the effects of the pulse to a predetermined slice. The strength of the gradient can be altered to change the slice thickness. In the left image the stronger gradient (Grad. 1) produces a thinner slice for a given RF pulse BW than the weaker gradient (Grad. 2). The central frequency of the bandwidth of the RF pulse can be changed to shift the position of the slice in the slice selection direction (right image). The pulse bandwidth can also be changed to alter the slice thickness.

### 2.5.5 Image Contrast

A significant benefit of MRI over more conventional medical imaging techniques such as X-ray computed tomography is the ability to use pulse sequences to generate images that are sensitive to a variety of different contrast mechanisms. This enables acquisitions to be tailored for use in obtaining information valuable for a range of medical conditions.

To some extent all MRI acquisitions are sensitive to the proton density of

the sample, however it is possible to change the contrast so that other contrast mechanism dominate. The three main types of image contrast weightings are known as: proton density weighting,  $T_1$  weighting and  $T_2$  weighting. There are however a number of other different contrast types, such as susceptibility weighting, diffusion weighting and Blood Oxygenation Level Dependent contrast.

### **$T_1$ Weighting**

A  $T_1$  weighted image is an image that has been created so that contrast is displayed between tissues with different  $T_1$  values. After an initial RF excitation pulse the longitudinal component of magnetisation recovers due to  $T_1$  relaxation at a rate that depends on the  $T_1$  of the tissue. To generate an image, a large number of RF pulses are often needed, so that all of k-space can be sampled and hence a large number of pulse repetitions are required. After a time TR between successive RF pulses, the amount of longitudinal magnetisation recovery that has occurred will be higher for tissues with a short  $T_1$  than for those with a long  $T_1$ . However, if the TR is long enough, the magnetisation in tissues that have both long and short  $T_1$  will have fully recovered before the next repetition. To maximise the  $T_1$  contrast produced by this process of saturation recovery, a short TR is required so that the amount of longitudinal magnetisation that is available to be converted to transverse magnetisation (signal) is highly dependent on the  $T_1$  of the tissue being imaged (Figure 2.14). Using a long TR suppresses  $T_1$  contrast. In  $T_1$  weighted images, tissues with a short  $T_1$  (e.g. fat) appear bright, because their longitudinal magnetisation will have recovered more, whereas tissues with a long  $T_1$  (e.g. cerebrospinal fluid) appear darker. To achieve optimum  $T_1$  weighting, not only do the effects of  $T_1$  contrast have to be maximised, but also the effects of  $T_2$  contrast have to be minimised, therefore a short TE is needed as well as a short TR.

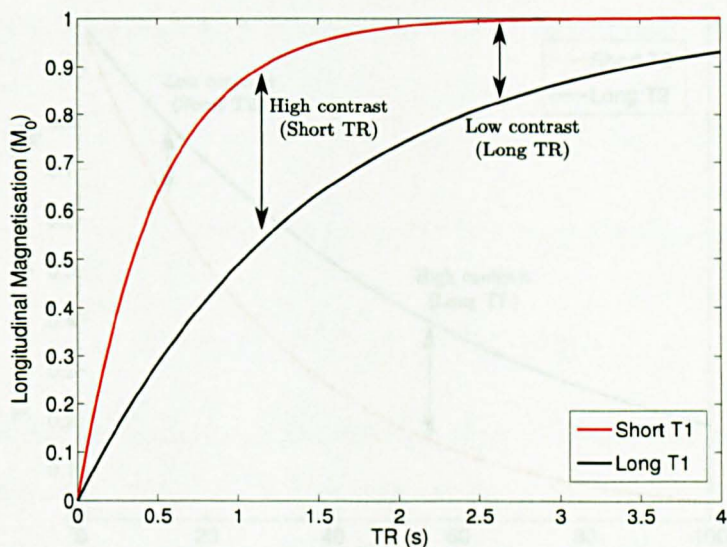


Figure 2.14:  $T_1$  relaxation curves, demonstrating how the contrast between two tissues with different  $T_1$  times depends on the TR. A short TR gives a higher  $T_1$  contrast.

## $T_2$ Weighting

The echo time of a sequence controls the amount of  $T_2$  decay that occurs before the echo is generated. Immediately after an excitation pulse, tissues with different  $T_2$  times but similar proton density, will have similarly sized net transverse magnetisations. After a time TE this magnetisation will have decreased by an amount dependent on  $T_2$ . Thus, using a long TE generates a large difference in signal strength between the tissue types and increases the  $T_2$  contrast, whereas using a short TE suppresses  $T_2$  contrast (Figure 2.15). In  $T_2$  weighted images, tissues with a short  $T_2$  (e.g. fat) appear dark and tissues with a long  $T_2$  (e.g. cerebrospinal fluid) appear bright. If the effects of magnetic field inhomogeneities are not reversed, such as in a GE acquisition, then this type of image will be  $T_2^*$  weighted. To achieve optimum  $T_2$  weighting the effects of  $T_2$  contrast have to be maximised and the effects of  $T_1$  contrast have to be minimised, therefore a long TR is needed, as well as a long TE.

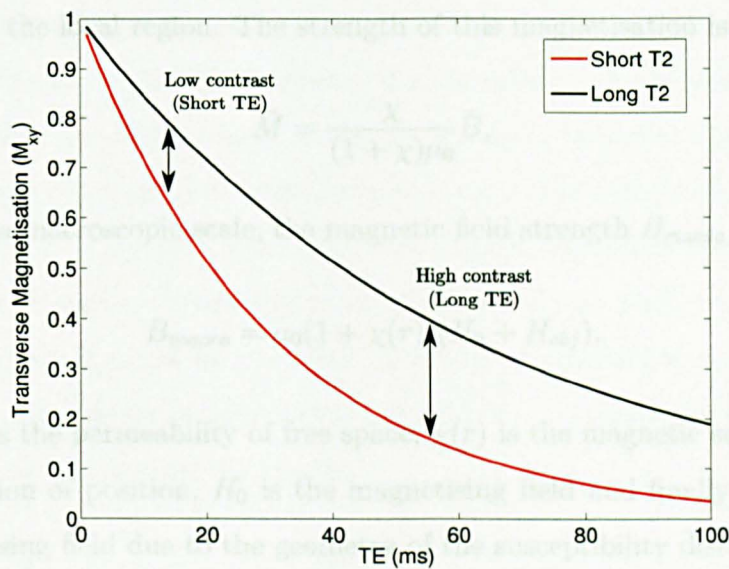


Figure 2.15:  $T_2$  relaxation curves, demonstrating how using a short TE gives low  $T_2$  contrast.

## Proton Density Weighting

A proton density weighted image is an image where the variations in signal intensity are mainly due to differences in the proton density within the tissues being scanned. The number of protons directly determines the number of spins available to produce signal and so proton density weighting is present within all images. To maximise the effect of proton density weighting,  $T_1$  and  $T_2$  contrast have to minimised by using a long TR and a short TE.

## Magnetic Susceptibility Effects

The degree to which a material is magnetised when in the presence of an external magnetic field can also have an effect on image contrast, and is described by a property known as its magnetic susceptibility  $\chi$ . Once magnetised a material will generate its own magnetic field that perturbs the external

$B_0$  field in the local region. The strength of this magnetisation is given by:

$$\bar{M} = \frac{\chi}{(1 + \chi)\mu_0} \bar{B}, \quad (2.72)$$

where, on a macroscopic scale, the magnetic field strength  $B_{macro}$  is given by:

$$B_{macro} = \mu_0(1 + \chi(r))(H_0 + H_{obj}), \quad (2.73)$$

where  $\mu_0$  is the permeability of free space,  $\chi(r)$  is the magnetic susceptibility as a function of position,  $H_0$  is the magnetising field and finally  $H_{obj}$  is the demagnetising field due to the geometry of the susceptibility distribution.

People are mostly made out of water which is diamagnetic and so  $\chi_{total}$  is negative, where  $\chi_{total} = \chi_{water} + \Delta\chi$ , because any paramagnetic changes in the body  $\Delta\chi$  will not usually change the overall properties of the tissue significantly enough to make it paramagnetic. Calculation of how the field varies at interface regions between tissues with different susceptibilities requires complex numerical calculations. However, a number of approximations can be made to simplify these calculations, such as modelling blood vessels as infinitely long cylinders. Changes in  $B$  due to susceptibility effects can cause artefacts such as signal dephasing and associated signal loss in MR images. In functional MRI, the changing susceptibility of blood with oxygen concentration is exploited to generate a contrast mechanism that provides insight into which parts of the brain are active during specific functional tasks (see Section 3).

### 2.5.6 Signal to Noise Ratio

The ability to distinguish between an NMR signal and random background noise depends on the ratio of the NMR signal strength to the level of noise in the signal. this is known as the signal to noise ratio (SNR). The noise in an

NMR experiment occurs mainly as a result of random thermal fluctuations in electrical current, within the subject and equipment, that are independent of the signal strength (Edelstein et al. 1986). However, in human subjects noise related to physiological functions, such as the beating heart and respiratory cycle, can be the dominant source of noise. This is especially problematic at higher field strengths (Triantafyllou et al. 2005). If the SNR in an image is too low, the NMR signal will be indistinguishable from the background noise.

There are a number of factors that influence the achievable SNR level, and a few of these will now be discussed.

### **SNR and $B_0$**

The strength of the static  $B_0$  field has a strong influence on SNR. As mentioned earlier, the population difference between spin states can be described by a Boltzmann distribution where:

$$\frac{N_{down}}{N_{up}} = e^{-\frac{\Delta E}{kT}} \quad (2.74)$$

and  $\Delta E = \gamma\hbar B_0$ . Thus with increasing  $B_0$  the population difference between the two states increases and more signal is detected. In fact, given that  $\Delta E \ll kT$  the following approximation can be obtained:

$$S \propto N_{up} - N_{down} \approx N_s \left( \frac{\gamma\hbar B_0}{2kT} \right), \quad (2.75)$$

where  $N_s$  is the number of spins and  $S$  is the amount of available signal. The amount of signal that is detected by a coil is also dependent on the field strength ( $B_0$ ). This is because the induced voltage is proportional to the rate of change of the magnetic fields that are produced due to the precessing nuclei, whose precessional frequency is described by the Larmor equation. Thus

$$V_{signal} \propto B_0 \quad (2.76)$$

However a number of effects counteract these theoretical gains such as the fact that it is harder to make coils that operate efficiently at high frequencies (associated with increasing field strength). As such, noise increases with field strength at a rate that lies somewhere between  $B_0^{1/4}$  and  $B_0$ , depending on whether the noise is dominated by the coil (non-conducting samples) or the subject (Human imaging at high field strength). Consequently, the relationship between field strength and SNR is typically proportional to  $B_0$  and not  $B_0^2$ .

### **SNR and Receiver Bandwidth**

Increasing the readout gradient bandwidth (BW) increases the range of frequencies in the signal and consequently reduces the SNR. When the BW is increased the total number of spins in a set frequency range is reduced due to the larger number of frequencies that are present and because there are only a set number of spins available to produce signal. However the noise level is uniform across frequency ranges and so adding more frequencies to the signal increases the noise power, resulting in a decrease in SNR. The overall signal originating from any given voxel remains the same. Therefore, increasing the receiver bandwidth decreases the SNR by increasing the noise within a voxel, not by decreasing the signal strength (Figure 2.16), as described by the following relationship:

$$\text{SNR} \propto \frac{1}{\sqrt{BW}} \quad (2.77)$$

### **SNR and Signal Averaging**

The number of signal averages (NSA) determines how much data is used to generate each line of k-space. When data is measured multiple times, random

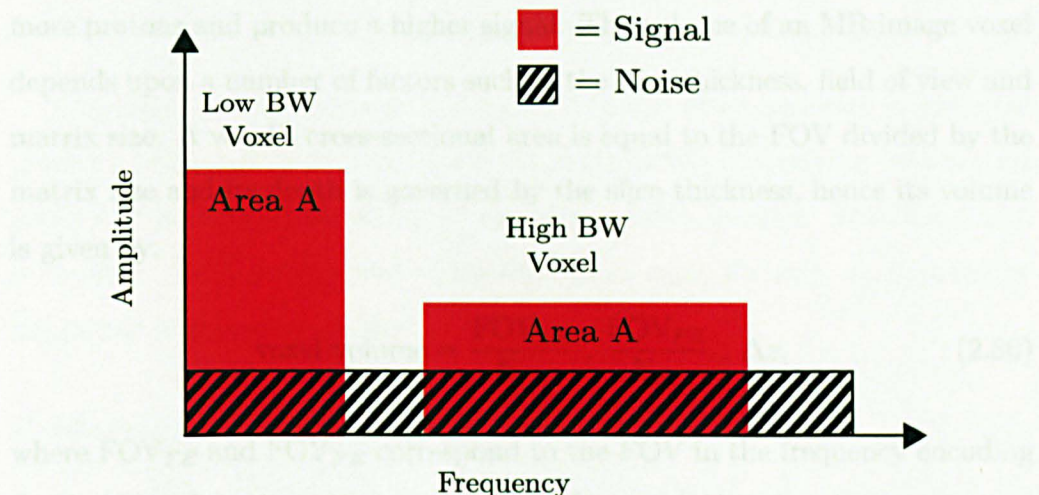


Figure 2.16: Imaging using a larger receiver bandwidth increases the noise level in any given voxel and decreases the SNR.

noise will change for each measurement whereas the signal will remain the same. Thus, signal averaging will tend to cause the noise to cancel whilst the true signal is enhanced, increasing the image SNR. Due to this behaviour, we get the following relations:

$$S \propto \text{NSA} \quad (2.78)$$

$$\text{Noise} \propto \sqrt{\text{NSA}} \quad (2.79)$$

Thus, doubling the NSA increases the SNR by  $\sqrt{2}$ , not 2. Doubling the NSA will also double the scan time and so this technique is not always the best method for increasing image SNR.

### SNR and Pixel Size

An MR image consists of a number of voxels representing the signals originating from specific volumes of tissue. The NMR signal strength in a region of tissue is dependent on the number of protons within the volume that have a component of magnetisation in the transverse plane. Larger volumes contain

more protons and produce a higher signal. The volume of an MR image voxel depends upon a number of factors such as the slice thickness, field of view and matrix size. A voxel's cross-sectional area is equal to the FOV divided by the matrix size and its depth is governed by the slice thickness, hence its volume is given by:

$$\text{voxel volume} = \frac{\text{FOV}_{FE}}{N_{FE}} \cdot \frac{\text{FOV}_{PE}}{N_{PE}} \cdot \Delta z, \quad (2.80)$$

where  $\text{FOV}_{FE}$  and  $\text{FOV}_{PE}$  correspond to the FOV in the frequency encoding / phase encoding directions respectively,  $N_{FE}$  and  $N_{PE}$  are the matrix sizes in the frequency / phase encoding directions and  $\Delta z$  is the slice thickness. Increasing  $N_{PE}$  reduces the noise in the image by  $\sqrt{N_{PE}}$ , through an effect similar to signal averaging. Thus the SNR is proportional to:

$$\text{SNR} \propto \text{volume} \cdot \sqrt{N_{PE}} \quad (2.81)$$

In contrast, when imaging using ionising radiation modalities such as Computed Tomography the SNR is proportional to the square root of the area and so reducing the pixel dimensions by a half only halves the SNR. Thus it is always advantageous to use the finest pixel size possible in order to allow fine detail to be visualised in areas with a sufficiently high SNR. In regions of low SNR, averaging of the pixel values recovers the original SNR. In MRI the situation is quite different because reducing the pixel size causes an irreversible loss of SNR in the image and averaging of pixel values will not increase the SNR to its original level. In MRI the pixel size has to be large enough to give an adequate SNR in the area of interest within an image to enable anatomical features to be accurately visualised, yet at the same time small enough to provide an adequate spatial resolution. Thus in MRI there is a key trade-off between image SNR and resolution.

### 2.5.7 Relaxation Constant Parameter Mapping

The relaxational constants  $T_1$ ,  $T_2$  and  $T_2^*$  are often sensitive to different physical properties of a sample and so can provide contrasting information about the underlying structure of the object being imaged. For this reason it is often useful to measure these relaxation rates directly, as opposed to weighting an image by them.

#### $T_1$ Mapping

For  $T_1$  mapping an inversion recovery sequence can be used in which a  $180^\circ$  RF pulse is first applied to invert the longitudinal magnetisation, then after a set time TI, during which the inverted magnetisation recovers due to  $T_1$  relaxation effects, a  $90^\circ$  RF pulse is applied. This converts the longitudinal magnetisation into transverse magnetisation, producing an FID. An additional  $180^\circ$  pulse can then be applied to generate a spin echo whose signal intensity depends on TI,  $T_1$ , TE and  $T_2$ . This signal can then be sampled using a number of different readout techniques (for example EPI, Figure 2.17). The signal detected during such as inversion recovery sequence is described by the following equation:

$$S(TI) = S_0 [1 - (1 - \cos(\alpha)) \cdot e^{-TI/T_1}] \quad (2.82)$$

where  $\alpha$  is the flip angle of the inversion pulse. By measuring the signal intensity multiple times, through sampling of either a gradient echo or spin echo, with a range of different TIs (keeping TE constant) it is possible to perform an exponential fit to the signal intensity at each voxel location as a function of TI and thus to measure  $T_1$  (Figure 2.18). When carrying out this kind of acquisition it is important to use a TR of at least  $5T_1$  in order to allow full recovery of longitudinal magnetisation before the pulse sequence is repeated. This type of fitting becomes more complicated when reconstructed

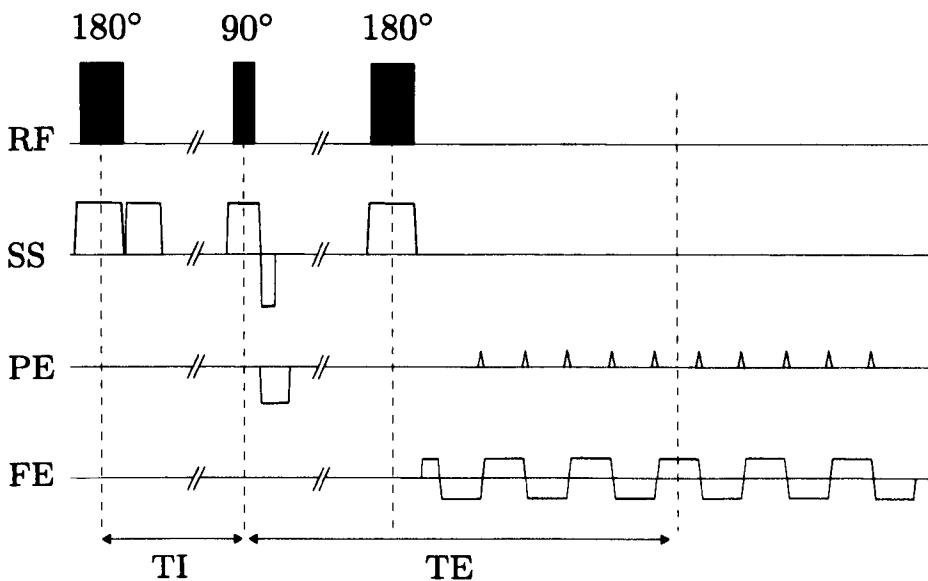


Figure 2.17: A SE EPI inversion recovery sequence. An initial  $180^\circ$  RF pulse is applied to invert the longitudinal magnetisation (with an optional spoiler to remove any unwanted transverse magnetisation resulting from the RF pulse). This is followed by a standard SE EPI readout module at time, TI.

modulus image data is used, because it isn't then possible to determine the sign of the measured signal, as a decay curve similar to the plot on the right in Figure 2.18 is actually detected. However, a fit to this can be found by using the absolute value of an exponential function, with the caveat that this can reduce the accuracy of the  $T_1$  estimates due to rectification of the noise around the zero-crossing point; tending to bias the  $T_1$  estimation upwards (Clare & Jezzard 2001).

### $T_2$ and $T_2^*$ Mapping

In a similar manner,  $T_2$  mapping can be performed by carrying out an imaging experiment on a sample using a SE sequence that is repeated with multiple different TE values whilst maintaining a fixed TR. A fit of the natural logarithm of the signal at each echo time on a voxel-by-voxel basis then allows  $T_2$  to be determined by calculating the gradient of the fit. This can be seen

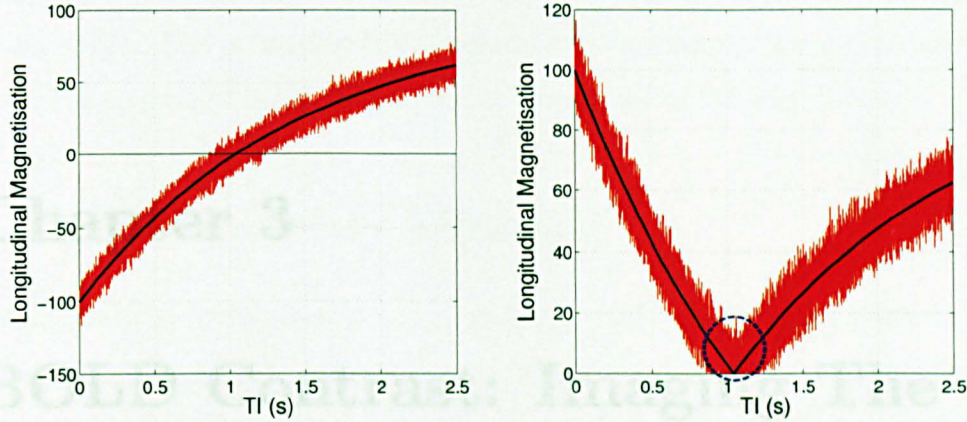


Figure 2.18: Left: A plot showing simulated results of how signal intensity varies as a function of inversion time ( $T_1$ ) in an inversion recovery sequence. Right: The detected signal recovery when using modulus image data. The blue circle highlights the region where noise rectification is problematic during fitting.

by considering the following signal equations:

$$S = M_0 \exp\left(-\frac{TE}{T_2}\right) \quad (2.83)$$

$$\ln(S) = \ln(M_0) - \frac{1}{T_2} \cdot TE \quad (2.84)$$

It should be noted that this technique does not take account of the additional signal loss brought about by the diffusion of protons through macroscopic field inhomogeneities ( $\Delta B_0$ ) and so, in fact, the measured signal is more accurately described by:

$$S = M_0 \exp\left(-\frac{TE}{T_2}\right) \exp\left(-\frac{2}{3} \cdot (\gamma \Delta B_0)^2 \cdot \left(\frac{TE}{2}\right)^3 \cdot D\right), \quad (2.85)$$

where  $D$  is the self diffusion coefficient. However, diffusion effects are generally fairly small.  $T_2^*$  mapping can be carried out in the same way but using a GE acquisition sequence.

# Chapter 3

## BOLD Contrast: Imaging The Brain

Neurological processes, whether conscious or not, are brought about due to the propagation of electrochemical signals in and between a multitude of nerve cells in the brain. The generation of these signals requires a continuous supply of energy from oxidative metabolic processes. In humans this requires a significant proportion of the body's energy resources, consuming  $\sim 20\%$  of the total oxygen and glucose supply. The raw materials necessary for these metabolic processes are supplied via the blood and hence any increase in neurological activity also heightens metabolic demand. In fact, it was first documented over a 100 years ago that a local increase in neurological activity causes a corresponding increase in regional cerebral blood flow (rCBF) (Mosso 1881) in order to supply fundamental elements such as oxygen (Fox & Raichle 1986). In MRI, the magnetic field strength in a local region, and hence signal strength, is sensitive to the presence of paramagnetic elements such as oxygen. Thus, this principle that brain activation level is correlated with blood flow and hence local oxygen concentration, which in turn affects the MR signal strength, forms the basis of an MR based functional imaging technique, commonly known as Blood Oxygenation Level Dependent (BOLD)

imaging, that can be used as a tool to probe neurological processes (Ogawa et al. 1992). The principles that underlie this functional imaging technique will be described in further detail in the remainder of this chapter.

### 3.1 Susceptibility Effects

In MRI the strength of the local magnetic field at any given point is influenced by the magnetic properties of the surrounding tissue. When placed in an external magnetic field magnetic materials become slightly magnetised, with the magnetisation aligned with the applied field, creating a small local field perturbation. The size of this effect can be explained by the product:  $\chi B_0$ , where  $\chi$  is the magnetic susceptibility of the material. The size of  $\chi$  depends on a number of factors including: the number of unpaired electron spins, the number of unpaired nuclear spins and the orbital motion of the electrons. However the contribution of the unpaired nuclear spins is negligible and the size of  $\chi$  is mainly determined by the number of unpaired electrons. For this reason deoxyhaemoglobin, with four unpaired electrons, is more paramagnetic than oxyhaemoglobin. Thus altering the amount of oxyhaemoglobin/deoxyhaemoglobin in a given area of the brain has an effect on the MR signal. The increase in local blood supply that is brought about due to elevated brain activation is much larger than that required to supply the cells in the region with an adequate level of oxygen. Thus, the net effect of increased neuronal activity, is a rise in the amount of oxyhaemoglobin in the local region. Indeed the over-supply of oxygen may be crucial in order to increase the rate at which oxygen is supplied to tissue via diffusion because it increases the oxygen concentration gradient between the capillaries and surrounding tissue, allowing diffusion of oxygen to occur at a higher rate (Jeppard et al. 2003). The localised control of blood flow may be influenced by a number of factors, such as the release of potassium ions, after nerve cell depolarisation

and also the release of the vasodilator nitric oxide (Iadecola 1993).

A local decrease in the concentration of deoxyhaemoglobin due to brain activation produces an increase in the local signal intensity relative to that found in the inactive state. When two materials with different magnetic susceptibilities are adjacent to each other a magnetic field gradient is created at the interface between them, and because of this the presence of deoxyhaemoglobin in blood will cause any protons within the surrounding tissue to experience a change in the local magnetic field strength. The nature of this effect depends on the size of the blood vessels, with larger blood vessels producing a longer-range effect. When the magnetic field gradients are large enough to cause the magnetic field to vary significantly across the dimensions of a voxel, signal dephasing dominates (Boxerman et al. 1995). That is the spins in the voxel experience a different magnetic field strength depending upon where they are. The signal emanating from the voxel is then composed of signals with a wide range of phase values, reducing the net signal intensity. The amount of signal attenuation that occurs is described by the term  $\Delta R_2^*$ , which is a measure of the relaxation rate of the signal due to the change in blood magnetic susceptibility on activation (Gati et al. 1997). Thus:

$$\Delta R_2^* = R_{2A}^* - R_{2B}^*,$$

where  $R_{2A}^*$  and  $R_{2B}^*$  are the relaxation rates of the activated and baseline states respectively. From this, it is fairly trivial to calculate that the change in signal intensity at a given echo time (TE) between the activated ( $S_A$ ) and baseline state ( $S_B$ ) is:

$$\Delta S = S_A - S_B = S_B (e^{-TE\Delta R_2^*} - 1) \quad (3.1)$$

Using the assumption that  $\text{TE} \cdot \Delta R_2^* \rightarrow 0$  allows the following approximation

$$e^{-\text{TE} \cdot \Delta R_2^*} \approx 1 - \text{TE} \cdot \Delta R_2^*$$

such that

$$\Delta R_2^* \approx -\frac{\Delta S/S_B}{\text{TE}} \quad (3.2)$$

Thus  $\Delta R_2^*$  can be determined by calculating the difference in signal intensity between the activated and baseline states and normalising by the base line signal intensity and the echo time. The magnitude of the change in magnetic field strength at the blood-tissue interface depends on the difference in susceptibilities between the blood and tissue and not on the size of the blood vessel.

## 3.2 Spatial Resolution

The spatial resolution of functional measurements based upon the BOLD response depends not only on the imaging resolution of the functional acquisition, but also, more fundamentally, on the spatially blurred nature of the BOLD contrast mechanism itself. In analogy to how a river might drain the water from distant hills, a significant proportion of the BOLD signal is generated due to the relatively long range susceptibility effects around large draining veins that are potentially distant from the true site of cortical activation (Lai et al. 1993, Turner 2002). This puts an inherent limit on the resolution that is achievable using GE imaging techniques and this may have been reached in high field experiments where data can now be acquired with resolutions as high as  $1\text{mm}^3$ . It may be possible to circumvent this fundamental resolution limit by using SE imaging sequences that are less sensitive to the susceptibility effects around large draining veins (described later in this

chapter), imaging at higher field strengths (due to the shortening of blood  $T_2$ ), or using novel functional paradigms. Indeed Menon & Goodyear (1999) describe an elegant solution that employs standard GE imaging techniques. They demonstrate that it is possible to remove the activation brought about due to large draining veins by stimulating different regions of the brain that are in close proximity and then subtracting the resultant activation maps. The pertinent idea being that functional regions that are very close together will be drained by the same large veins and that these veins will produce similar venous activation patterns upon activation. Subtraction of the activation maps from these spatially disparate functional regions will leave behind only the highly localised activation due to BOLD effects in the microvasculature that are highly specific to each functional site. Menon & Goodyear (1999) accomplish this by applying an alternating visual stimulus to each eye and conclude that the technique allows ocular dominance columns to be viewed at sub-millimetre resolution.

### 3.3 Field Strength

The size and nature of the BOLD response is also dependent on the strength of the external magnetic field. At lower field strengths the largest contributor to the net change in signal in a voxel, upon activation, is due to the change in signal contribution of the blood itself because of changes in blood oxygenation and volume. At 1.5T the intrinsic blood signal is greater than the intrinsic signal of the surrounding tissue, due to the longer  $T_2^*$  of blood (Wright & Hu 1991), thus an increase in local blood volume causes an increase in signal. However at 7T the  $T_2^*$  of blood is very short (see Table 3.1) (Thulborn et al. 1982) and so the intrinsic blood signal is low.

Field strength (T)	Blood water $T_2$ (ms)	Gray matter water $T_2$ (ms)
7	15	55
1.5	130	90

Table 3.1:  $T_2$  values at high and low field strengths

## 3.4 Water Diffusion

The random diffusion of water molecules through tissue alters the amount of BOLD contrast that can be detected as the diffusion decreases the amount of phase dispersion, and hence signal attenuation, that occurs due to the susceptibility effects around blood vessels. Diffusion is essentially a random process and so any spins undergoing diffusion experience an average of the field perturbations in a local region whose size is governed by the diffusion distance. This decreases the dephasing effects across a voxel and reduces the size of the GE BOLD response. The severity of this effect is dependent on the diffusion distance relative to the local field gradient and is greater when the field gradient is larger, i.e around smaller vessels.

The average displacement of a water molecule in one dimension can be described by the following:

$$\Delta x^2 = 2DT, \quad (3.3)$$

where D is the diffusion coefficient and T is the time over which diffusion occurs. The displacement in a 2D plane is then given by  $\sqrt{4DT}$ . If an echo time of 25ms is used in a GE sequence and D is given a value of  $1\mu\text{m}^2/\text{ms}$ , the diffusion distance will be  $\sim 10\mu\text{m}$ . This distance is approximately equal to the size of venules, larger than the size of capillaries and smaller than draining veins. The size of the diffusion distance relative to the effective range of the extra-vascular component of BOLD contrast (EV) can be seen for two different vessel sizes in Figure 3.1. Thus in a GE sequence the extra-

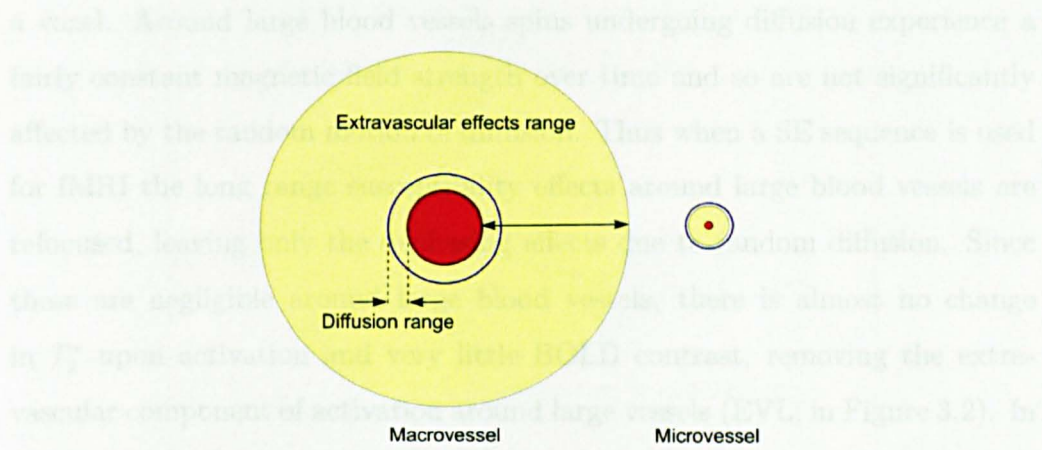


Figure 3.1: An example of the diffusion distance and the effective range of EV BOLD contrast for two vessels, one large ( $\sim 30\mu m$ , left) and one small ( $\sim 3\mu m$ , right), the relative scales are correct. The intra-vascular component (IV) is shown in red.

RF pulses leading to T<sub>2</sub>-BOLD contrast in the CA's compartment. This has vascular component of BOLD contrast is dominated by the effects around large draining veins due to the longer range of the field perturbations around these vessels and the contrast suppressing effects of molecular diffusion around capillaries. The size of the intra-vascular effect (IV) is mostly dependent on the  $B_0$ -field strength, with higher field strengths reducing the IV contribution.

## 3.5 SE Bold

It is also possible, although less common, to use a SE pulse sequence for fMRI. In a SE sequence the 180° RF pulse refocuses the signal dephasing due to static field inhomogeneities ( $T_2^*$  effects) and produces an image that is  $T_2$ -weighted. However the refocusing pulse does not refocus the random dephasing effects due to spin diffusion. Due to the random nature of diffusion, the net phase accumulated by a spin in the first half of the echo time is then different to that experienced in the second half of the echo time. Consequently the 180° RF pulse will not refocus all of the dephasing that has occurred within

a voxel. Around large blood vessels spins undergoing diffusion experience a fairly constant magnetic field strength over time and so are not significantly affected by the random motion of diffusion. Thus when a SE sequence is used for fMRI the long range susceptibility effects around large blood vessels are refocused, leaving only the dephasing effects due to random diffusion. Since these are negligible around large blood vessels, there is almost no change in  $T_2^*$  upon activation and very little BOLD contrast, removing the extra-vascular component of activation around large vessels (EVL, in Figure 3.2). In contrast, spins undergoing diffusion around small vessels (such as capillaries, EVS in Figure 3.2) experience a large range of field strengths over time, due to the large susceptibility induced magnetic field gradients around these vessels, these random signal dephasing diffusion effects are not refocused by the 180° RF pulse leading to  $T_2$  BOLD contrast in the EVS compartment. This has been confirmed in numerous studies (Duong et al. 2002, Yacoub et al. 2003, Harmer et al. 2011). Duong et al. (2002) showed that when using a high resolution slab selective EPI technique SE activation correlates very closely with maps showing changes in cerebral blood flow (CBF), with both showing activation occurring almost entirely in grey matter regions. Also, Lowe et al. (2000) found that  $\Delta R_2$  is more uniform across cortical and subcortical gray matter structures than  $\Delta R_2^*$ . They postulated that larger changes in  $\Delta R_2^*$  are detected across these structures due to the greater volume fraction of macrovessels in the cortical regions relative to subcortical regions, and that the uniformity of  $\Delta R_2$  across these regions suggests that  $\Delta R_2$  is less affected by the presence of macrovessels. In summary a SE sequence removes the majority of the EV effects of BOLD activation around large vessels, but leaves an effect due to diffusion around small vessels, enabling better localisation of the BOLD signal. Despite this, fMRI studies generally employ gradient echo (GE) rather than spin echo (SE) based imaging techniques because of the higher sensitivity provided by GE BOLD contrast (Michelich et al. 2006, Duong et al. 2002,

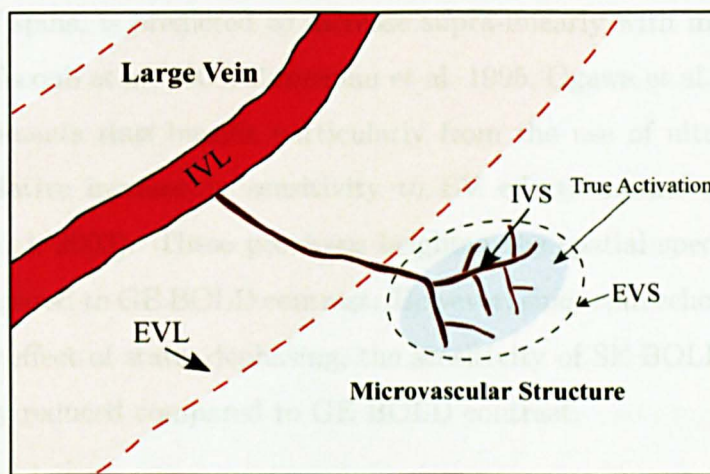


Figure 3.2: The BOLD signal compartments. GE EPI detects the contribution of all of these compartments, SE EPI suppresses the contribution from the EVL compartment leaving the IVL, IVS and EVS compartments. Diffusion gradients can be used to suppress the activation from the IVS, IVL and EVL compartments. Using a high magnetic field strength can also suppress the signal from the IVS and IVL compartments. Thus, at ultra high field SE BOLD is only sensitive to the EVS compartment.

Yacoub et al. 2003), despite its lower spatial specificity. However the increased signal-to-noise ratio (SNR) available at ultra-high field opens up the possibility of more routine use of SE techniques (Olman et al. 2010, Yacoub et al. 2008). BOLD contrast depends upon both intravascular (IV) and extravascular (EV) signal changes. As field strength is increased, the EV contribution dominates over IV effects due to the disproportionate shortening of the  $T_2$  of venous blood compared to that of tissue (Yacoub et al. 2003, Yacoub et al. 2001b): venous bloods  $T_2$  reducing from  $\sim 180$  ms at 1.5 T (Barth & Moser 1997) to  $\sim 40$  ms at 3 T and  $\sim 10$  ms at 7 T (Gardener et al. 2010). Thus at low field strength (e.g. 1.5 T) BOLD contrast is dominated by IV effects (Oja et al. 1999, Song et al. 1996), whilst at ultra-high field, BOLD signal is dominated by EV effects (at the echo times which are typically used in fMRI experiments). The EV BOLD effect due to static dephasing around large vessels is linearly dependent on magnetic field strength, whilst the EV effect around small vessels, due to

diffusion of spins, is predicted to increase supra-linearly with magnetic field strength (Yacoub et al. 2003, Boxerman et al. 1995, Ogawa et al. 1993). Spin echo experiments thus benefit particularly from the use of ultra-high field, and the relative increase in sensitivity to EV effects around small vessels (Yacoub et al. 2003). These processes heighten the spatial specificity of SE BOLD compared to GE BOLD contrast. However, since spin echo acquisitions refocus the effect of static dephasing, the sensitivity of SE BOLD contrast is significantly reduced compared to GE BOLD contrast.

## 3.6 BOLD contrast in fMRI

Having the ability to produce images with a contrast that is sensitive to the brain's activation level is very useful, as it allows for experiments to be carried out that assess neurological function. Activation levels can be assessed by repeatedly scanning a subject over time whilst they perform a specific neurological task at a number of different time points, separated by known intervals. If the temporal resolution of the dynamic acquisition is high enough and there is an adequate contrast to noise ratio (CNR), the time series will display a signal change, in the regions of the brain that are employed to process the task at hand, that correlates with the onsets of the stimuli. Regression analysis can then be used to assess whether a given region (voxel) shows activation. To allow this, the overall effect that the underlying activation has on the MR signal intensity has to be modelled. There are numerous techniques that have been developed for this, ranging from simple models that use a single gamma function (Buckner et al. 1996) to more complicated techniques that use a combination of gamma functions (Friston et al. 1998) or finite impulse response filters (FIR) (Goutte et al. 2000). These models are designed with one or more parameters that can be varied to allow an accurate fit to the data. Studies have shown that the shape and timing of the haemodynamic response

function (HRF) (Figure 3.3) can change across the brain due to differences in the vascular structure (Lee et al. 1995) and so it is beneficial to have a model that has some flexibility in these areas.

The characteristic shape of the HRF is shown in Figure 3.3, it has a number of notable features that are related to the underlying physiological processes. For example, immediately after the onset of a stimulus there is usually an initial dip in signal intensity (Yacoub et al. 2001a). It has been postulated that this occurs as a result of elevated levels of deoxyhaemoglobin in the blood, due to the heightened metabolic demand, in the period before the arrival of extra oxygen (delivered via an increase in CBF). Once the effects of vasodilators such as nitric oxide take hold, the increased blood volume provides an over-supply of oxygen to the local region and the signal intensity increases, this can be seen as the peak in the HRF in Figure 3.3 at around 5 seconds after the stimulus onset. The time between the stimulus onset and the return of the HRF to baseline levels can be as long as 20s. The HRF is almost invariably modelled as a linear time-invariant system, that is, the HRF invoked by a stimulus is considered to add linearly to the HRF of another stimulus in a manner that does not change with time. This is known as the general linear model or GLM. Using this assumption the predicted activation is calculated by convolving the HRF with a boxcar stimulus function, describing the on and off periods of the functional stimuli for the experiment, (Fig. 3.4) and then using regression analysis to determine what model parameters for the HRF best fit the measured time courses. This type of analysis can be carried out on a voxel-wise basis across the entire imaging data set to assess where activation occurs. To determine how well the measured data fits the predicted model, a statistical measure such as a z-score is usually displayed on a voxelwise basis. Due to the large number of voxels in a typical fMRI experiment it is important to apply a multiple comparisons correction factor (usually a Bonferroni correction factor (Rice 1989)). Otherwise a large number

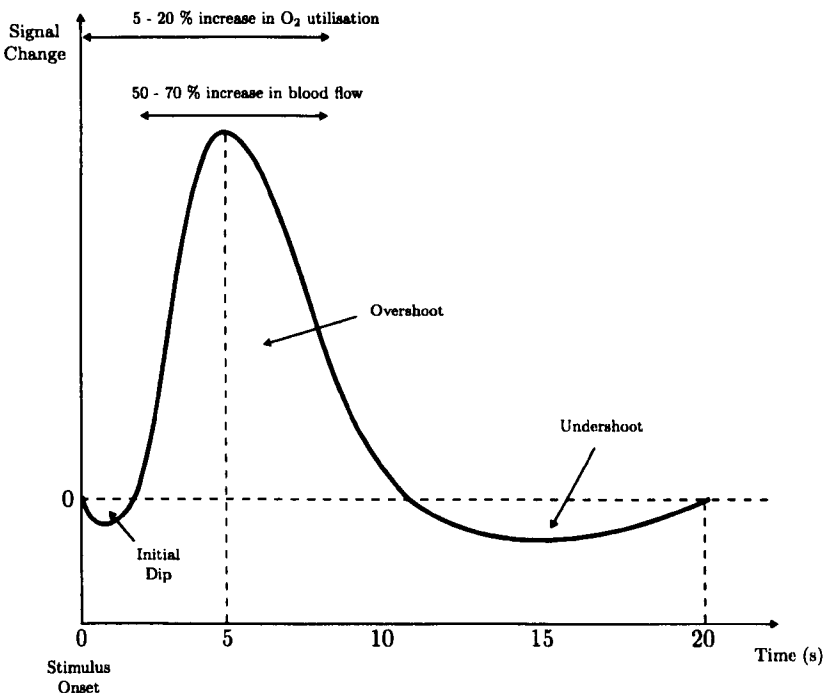


Figure 3.3: The Haemodynamic Response Function (HRF), showing typical timings.

of spatial locations would display statistically significant activation purely due to chance, confounding the results. Whilst this type of correction significantly reduces the number of false-positives it also increases the likelihood of false negatives, however this is considered less problematic in fMRI.

## Chapter 4

### Spatial location and strength of

BOLD activation in the visual system

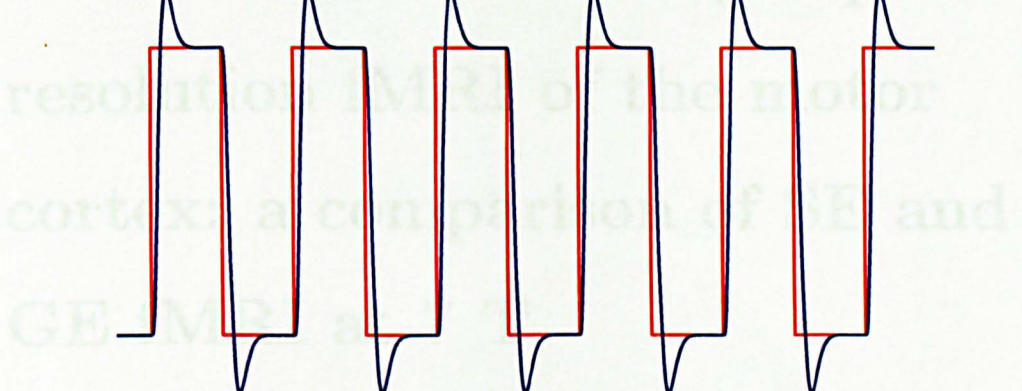


Figure 3.4: A block design experiment. The model for the haemodynamic response function is convolved with block design, representing the ON and OFF periods of the stimulus. The resulting model is then used during functional analysis as the predicted timecourse.

The brain is made up of a number of functional regions that are dedicated to the control and monitoring of specific cognitive processes such as hearing and vision. The major region is dedicated to the planning, control and execution of movements that are made by a cognitive task. The function and relative location were determined in the early 1900's via a series of invasive experiments in which electrodes were used to stimulate the brain directly. The major cortex can be divided into three main functional areas: the primary motor cortex (M1), the pre-motor cortex and the supplementary motor area (SMA). The primary motor cortex contains a point-to-point neural representation of the body. For example, under normal circumstances a point-to-point movement app-

# **Chapter 4**

## **Spatial location and strength of BOLD activation in high spatial resolution fMRI of the motor cortex: a comparison of SE and GE fMRI at 7 T**

### **4.1 The Motor Cortex**

The human brain is made up of a number of functional regions that are dedicated to the control and monitoring of specific cognitive processes, such as hearing and vision. The motor region is dedicated to the planning, control and execution of movements that are made on a voluntary basis. Its function and relative location were determined in the early 1900's via a series of invasive experiments in which electrodes were used to stimulate the brain directly. The motor cortex can be divided into three main functional sites, the primary motor cortex (M1), the pre-motor cortex and the supplementary motor area (SMA). The primary motor cortex contains a point to point neuronal repre-

sentation of every part of the body which can be moved on a voluntary basis. This can be represented schematically using a homuncular diagram (Figure 4.1).

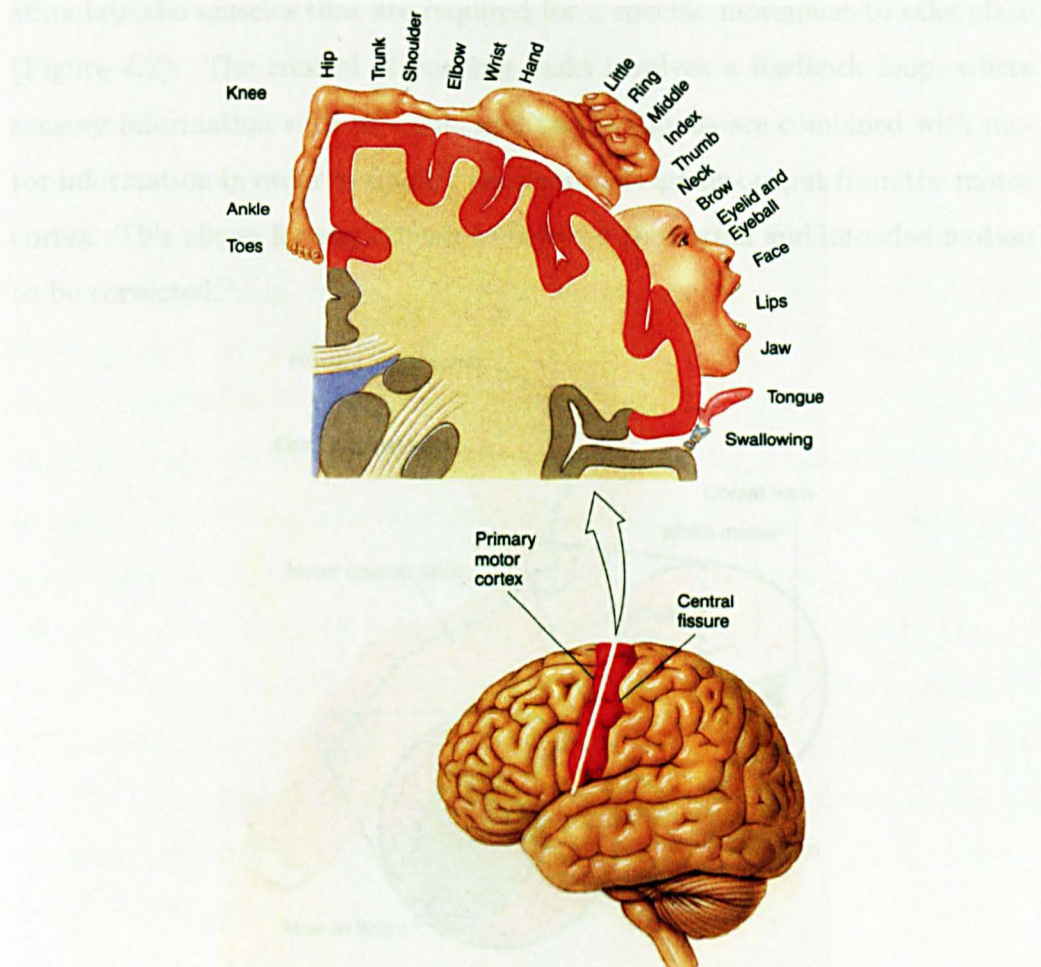


Figure 4.1: Motor Homunculus, demonstrating which regions of the brain are dedicated to controlling the movement of different parts of the body. (Figure modified from <https://courses.washington.edu/psy222/OverheadSlides/Sensorimotor%20System/Homunculus.jpg>)

These motor regions are responsible for controlling different aspects of movement. The primary and pre-motor cortex are used for the guidance of ongoing motion and control of the proximal and trunk muscles. Whereas the supplementary motor area is used for planning and co-ordination of more com-

plex movements (such as the co-ordination of bi-manual movements). Neuronal signals that are generated in the motor cortex descend down through the corticospinal tract, crossing over to the opposite side of the body, in order to stimulate the muscles that are required for a specific movement to take place (Figure 4.2). The control of ongoing tasks involves a feedback loop, where sensory information such as visual and tactile signals are combined with motor information in order to update the neuronal signals output from the motor cortex. This allows for any difference between the actual and intended motion to be corrected.

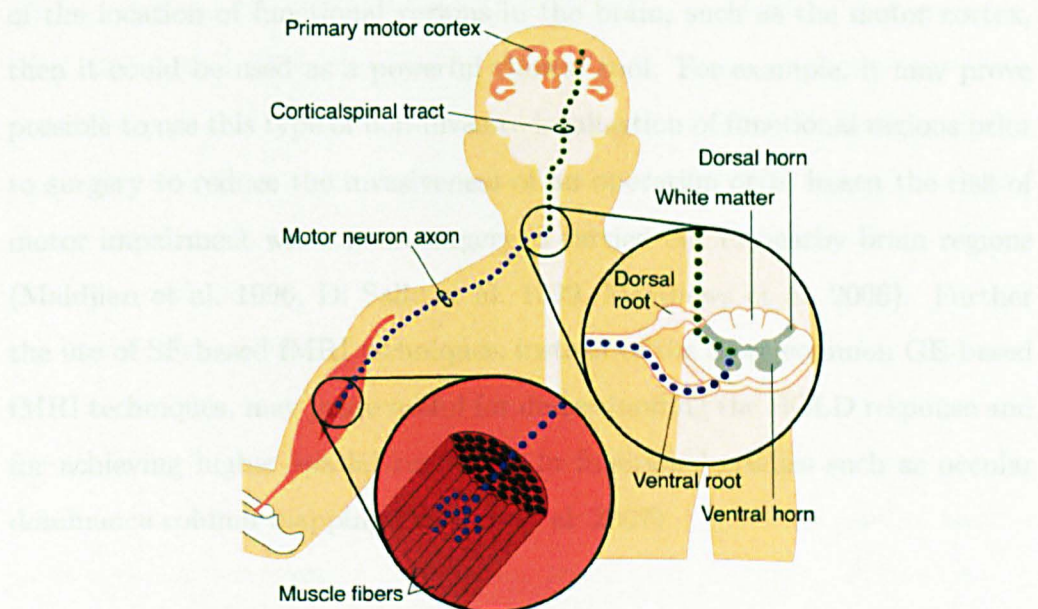


Figure 4.2: The neuronal pathway of the motor response. (Modified from <http://brainconnection.positscience.com/med/medart/1/motoranat-motorunit.jpg>)

The volume of the cortical region that is dedicated to a particular body area gives an indication as to the amount of control one has over it. This is represented in the homuncular diagram by the size of the corresponding body part that surrounds the surface of the brain (Figure 4.1). Thus the high dexterity that we have when it comes to complex hand and finger motion is in part due to the fact that a large area of the brain is dedicated to the control

of these body areas.

Since the development of MRI, functional task-based studies employing fMRI have allowed the location of the motor cortex to be determined accurately and non-invasively in in-vivo experiments. The localisation efficacy of fMRI was confirmed in an early study by Yousry et al. (1995) who compared the spatial location of fMRI activation in the motor cortex to the location of the motor cortex as determined by direct electrical stimulation during surgery and found good agreement between the two techniques. If further results can prove that fMRI can be used for the routine, robust and accurate detection of the location of functional regions in the brain, such as the motor cortex, then it could be used as a powerful clinical tool. For example, it may prove possible to use this type of non-invasive localisation of functional regions prior to surgery to reduce the invasiveness of an operation or to lessen the risk of motor impairment when neurosurgery is carried out in nearby brain regions (Maldjian et al. 1996, Di Salle et al. 1999, Matthews et al. 2006). Further the use of SE-based fMRI techniques, instead of the more common GE-based fMRI techniques, may prove useful for understanding the BOLD response and for achieving higher spatial resolution in functional studies such as ocular dominance column mapping (Yacoub et al. 2007).

## 4.2 Introduction

Although the vast majority of fMRI is carried out using GE BOLD contrast, current theory suggests that the SE BOLD response has higher spatial specificity to the underlying neuronal activity. Further, SE sequences are also less prone to the effects of magnetic field inhomogeneities, which can be particularly problematic at high field strength. Following on from this, if it is possible to both reliably and robustly detect the SE BOLD response its increased spatial specificity to the underlying neuronal activity would be particularly

beneficial in a number of developing clinical fields such as pre-surgical localisation of the motor cortex (Maldjian et al. 1996, Di Salle et al. 1999, Matthews et al. 2006). However the inherent insensitivity of the SE BOLD response to the long range extravascular effects around large blood vessels can be a double-edged sword, since this effect also reduces the overall sensitivity of the SE BOLD response to neuronal activity; making this response much harder to detect.

Due to the difficulties involved in its detection, there are only a limited number of studies that directly compare GE and SE BOLD contrast (Bandettini et al. 1994*a*, Lowe et al. 2000, Zhao et al. 2004, Yacoub et al. 2005, Zhao et al. 2006, Schaefer et al. 2008). In humans, these studies have generally been restricted to the visual cortex due to its strong haemodynamic response, with data acquired at a relatively coarse in-plane spatial resolution (Bandettini et al. 1994*a*, Lowe et al. 2000) or with a large slice thickness (Yacoub et al. 2005).

In the work described here, the increased BOLD contrast to noise ratio (CNR) at 7 T is exploited, along with the use of a multi channel receive coil, to offset the lower functional sensitivity of SE BOLD. We use the increased CNR to enable the GE and SE BOLD responses to a simple motor task to be accurately compared at high spatial resolution (1.5 mm isotropic) during a relatively short scan session ( $\sim 1$  hr). To gain insight into whether the underlying mechanisms that lead to GE and SE BOLD contrast have an effect that differs significantly when imaging at high spatial resolution, we use a region of interest (ROI)-based analysis to compare the spatial location of and signal change within activated regions, calculated via analysis of GE and SE data from the same subjects. Further, we calculate the position of areas of activation relative to the location of large draining veins (measured using high resolution venous mapping sequences). Using this information we test the accuracy of the theoretical assumption that suggests that the SE BOLD

response is more localised to the underlying microvasculature (representing the true location of neuronal activity) than to large draining veins. We also investigate the fractional SE BOLD signal change as a function of echo time and from this calculate the change in  $T_2$ - relaxation rate ( $\Delta R_2$ ) on activation.  $T_2$  data also enables the determination of the optimum echo time for SE fMRI studies of the motor cortex.

## 4.3 Methods

### 4.3.1 Data Acquisition

Five healthy subjects participated in this study (age 22-31 years; two males). Ethical approval was obtained from the University of Nottingham Medical School Ethics Committee and all subjects gave full written consent. Scanning was carried out on a 7 T Philips Achieva system, using a volume transmit head coil and a 16-channel receive coil (Nova Medical, Wilmington MA). To minimize motion, subject's heads were held in place using a customized MR-compatible vacuum pillow (B.U.W. Schmidt, Germany) and foam padding.

For the functional acquisitions, multi-slice, single-shot GE- and SE- echo planar imaging (EPI) sequences were used to acquire contiguous axial slices with a field of view (FOV) of  $192 \times 72\text{mm}^2$  (AP x RL), at 1.5 mm isotropic resolution. A reduced FOV was employed in the phase-encoding (RL) direction along with a SENSE acceleration factor of 2. This allowed the use of short SE echo times and readout durations (minimum TE = 30 ms, 24 ms readout duration). Image volumes were positioned so as to span the right primary motor cortex.

For the functional study, SE-EPI scans were acquired with echo times of 30, 35, 40, 45, 50 and 55 ms. A GE-EPI scan with a TE of 25 ms was also collected. Both GE and SE data were acquired with a TR of 2.4 s per volume,

with each volume comprising 16 slices. 78 volumes were collected for each dataset during the fMRI protocol.

The functional paradigm consisted of a visually-cued motor task, with a rest period of 16.8 s followed by 14.4 s of finger tapping using the left hand, repeated over 6 cycles. The paradigm commenced with a rest period to provide an initial baseline measurement.

$T_2^*$  maps were generated using 6 GE-EPI scans at different echo times (spanning 25-50 ms with 5 ms spacing). To increase the SNR, 20 volumes were acquired at each TE.  $T_1$ -weighted anatomical images with the same slice prescription, coverage, and resolution as the functional data were acquired using an MPRAGE sequence with linear phase encoding order (TE = 2.14 ms, TR = 14 ms, FA = 10°, TI = 960 ms, 2 averages). The entire scan session took approximately one hour.

High-resolution,  $T_2^*$ -weighted axial images were recorded for each subject in a separate scan session ( $0.25 \times 0.25 \times 1.5 \text{ mm}^3$  resolution over a  $192 \times 154 \text{ mm}^2$  field of view, TR = 320 ms, TE = 20 ms, 34 slices) to allow large veins to be identified. A  $T_1$ -weighted (MPRAGE) image at 1.5 mm isotropic resolution was also acquired, with the same slice prescription, to aid registration of the venous mask and the functional data.

### 4.3.2 Data Analysis

Data were realigned using AFNI (Cox 1996), with the GE data registered to the SE data, and analysed with a general linear model using FEAT in FSL (Smith et al. 2004). Noise pre-whitening was applied to the data along with high-pass temporal filtering. A high pass cut-off frequency corresponding to a period of 31.2 s (i.e. the length of a cycle) was used to compensate for signal drift. Data were not spatially smoothed in order to retain the high spatial resolution of the functional scans. Using FEAT, z-score activation maps were calculated for each echo time of the SE data and also for the GE data. For the

SE data, an additional z-score map was generated by carrying out functional analysis on the average of all six SE data sets for each subject.

### **$T_2$ Mapping**

$T_2$  maps were generated in functional space by using data from the initial rest period of each functional SE scan. This was accomplished by carrying out a weighted fit of the natural logarithm of the signal at each echo time on a voxel-by-voxel basis (Section 2.5.7). Multi echo time GE-EPI scans, acquired following the fMRI protocol, were analysed in a similar manner to generate  $T_2^*$  maps.

### **Reduced FOV Imaging**

To enable the rapid acquisition of high resolution images, the FOV in the phase encoding direction had to be reduced in size so that it encompassed only half of the head. When imaging in this way it is impossible to stop the effects of the encoding gradients in regions outside of the FOV and so signal aliasing artefacts can be problematic.

These artefacts can be present in both the frequency and phase encoding directions (if the FOV is smaller than the object in each of the corresponding directions). In the frequency encoding direction the higher frequency signals from outside of the FOV are indistinguishable from the signals originating inside it, as explained by Nyquist-Shannon sampling theory (Figure 4.3). As a result the encoding process causes these signals to contaminate the signal from within the FOV (by misinterpreting them as low frequency signals), causing fold-over artefacts (Figure 4.3). However, aliasing in the FE direction is generally not a problem as it can be easily remedied by applying a band pass filter to the NMR signal, which removes unwanted frequencies from outside the FOV whilst retaining those from within it.

Aliasing in the PE direction occurs for similar reasons, but due to phase

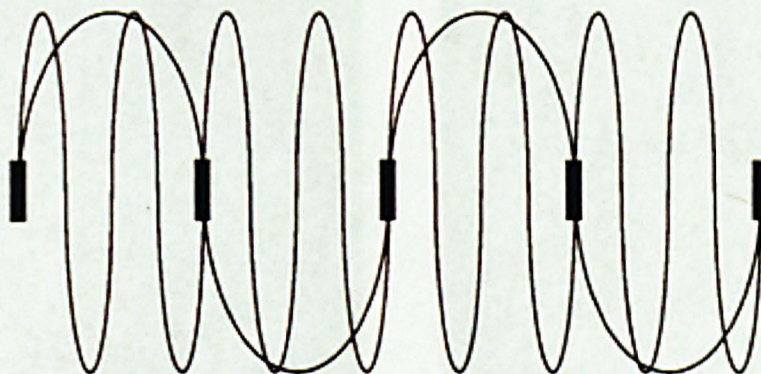


Figure 4.3: Aliasing. When using discrete sampling points two different frequencies can appear to have the same frequency.

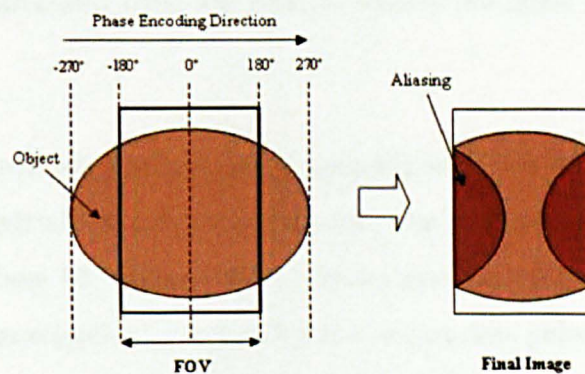


Figure 4.4: Aliasing artefact in the phase encoding direction.

instead of frequency effects (Figure 4.4). As the detected phase is always inherently wrapped between  $-\pi$  to  $+\pi$  it is not possible to filter phase using a band-pass filter and so aliasing occurs. To get around this problem saturation pulses can be used to remove the signal contribution from outside the FOV. An example of this outer volume suppression is shown in Figure 4.5. The left image displays a pronounced aliasing artefact in the PE direction where the front of the head has been wrapped around to the back of the image due to the reduced FOV. The image on the left demonstrates the effectiveness of a saturation pulse; with complete removal of the aliasing artefact.

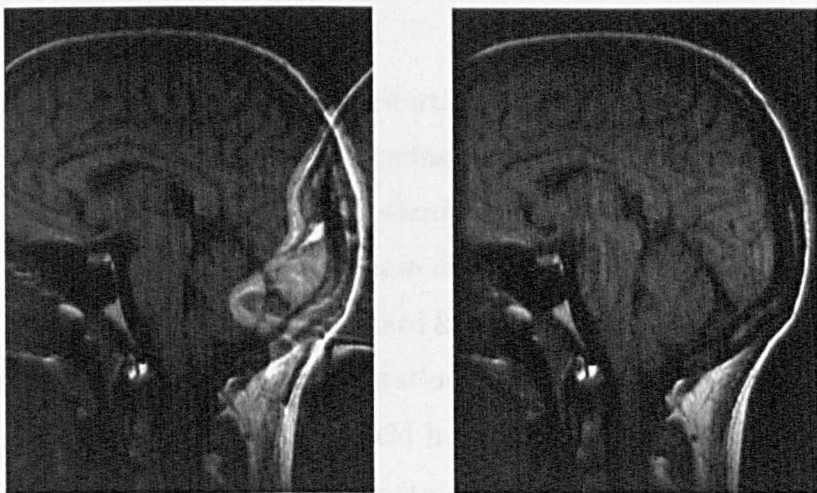


Figure 4.5: An example of the effects of aliasing artefacts using data from a separate scanning session. Severe wrap around aliasing can be seen in the left image. In the right image a saturation band was used to remove the signal from outside of the FOV.

In a standard saturation pulse, a spatially selective  $90^\circ$  RF pulse is used to flip the longitudinal magnetisation into the transverse plane (saturating the signal). These RF pulses have to be designed in such a way that the net transverse magnetisation, created by the saturation pulse, is kept as small as possible by intentional phase dispersion, so that no signal is detected. For additional signal attenuation, saturation pulses are usually followed by the application of spoiler gradients. In order to minimise any recovery of longitudinal magnetisation, imaging has to be carried out immediately after application of the saturation pulses.

When imaging is carried out at high field, such as in this study, this method of saturation tends to be ineffective due to the effect of  $B_1$  field in homogeneities (Pfeuffer et al. 2002). To get around this problem, a  $B_1$  field insensitive technique that uses amplitude- and frequency-modulated pulses with additional spoiler gradients (Luo et al. 2001), was employed.

## Shimming

To reduce the effects of image distortions, due to the presence of field inhomogeneities, an image-based shimming technique was employed (Poole & Bowtell 2008). At the start of each scanning session a  $B_0$  field-map was calculated by using the difference in phase of two gradient echo images acquired with echo times of 6 and 6.5 ms (Jezzard & Balaban 1995). The corresponding  $B_0$  information was used for computation of shim currents to second order, in such a way as to minimise any field inhomogeneities inside a cuboidal region ( $90 \times 50 \times 50 \text{ mm}^3$ , APxRLxFH) containing the pre-central gyrus (Poole & Bowtell 2008, Wilson et al. 2002). The shim values were fixed for all the remaining functional scans in the session.

## Fat Suppression

The Larmor frequency of a hydrogen nucleus depends to a small extent on the properties of the molecule that the hydrogen atom resides in. In biomedical MRI we detect signals from hydrogen contained within both fat and water. These molecules have very different physical properties. In fat, a large electron cloud reduces the strength of the external magnetic field within the molecule, reducing the Larmor frequency. This chemical shift is known as the fat-water shift and is equal to approximately 3.5 ppm. When imaging at 7 T this equates to a shift of 1043 Hz. This natural difference in precessional frequency means that any fat and water signals from a given volume will appear to originate from different locations after spatial encoding. The size of this spatial offset depends upon the bandwidth that is used for the acquisition, with lower bandwidths increasing the shift (Figure 4.6).

When using EPI at 7T, where typical bandwidths are 50 Hz/pixel in the phase encoding direction, the fat-water shift is  $\sim 20.9$  pixels! In comparison in the frequency encoding direction, where the bandwidth is usually around 3kHz, this shift is only around 1/3 of a pixel. Thus this effect is only really a

problem in the PE direction (Nagy & Weiskopf 2008).

When SE-EPI data are acquired at 7T, with a TE-value optimized for BOLD sensitivity, fat appears hyperintense. This is because the  $T_2$  of fat at 7 T ( $\sim 52$  ms (Ren et al. 2008)) is similar to the  $T_2$  of grey matter. In comparison, in a GE-EPI acquisition, optimised to have a TE that matches the  $T_2^*$  of grey matter ( $\sim 25$  ms), the fat signal is highly attenuated ( $T_2^*$  of fat  $\sim 10$  ms) and fat suppression is not strictly necessary. Fat suppression is therefore vital when imaging using SE-EPI at 7 T in order to remove image artefacts associated with fat shift effects.

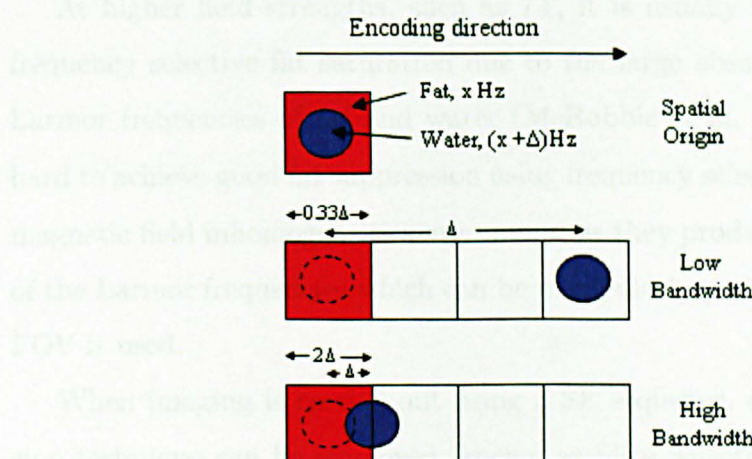


Figure 4.6: Fat-water chemical shift effects. When a small bandwidth is used for spatial encoding the resulting fat shift effect is large (middle). When the bandwidth is greater than the fat shift the effect is much less severe (bottom)

One effective technique that can be used for fat suppression is to apply an additional  $180^\circ$  RF pulse at the start of the scan to invert the longitudinal magnetisation in the volume. Image acquisition can then be timed to coincide with the point at which the longitudinal magnetisation of the fat has recovered to zero so that no fat signal is generated. This technique relies on the fact that fat has a considerably different  $T_1$  relaxation time to most other tissues. This type of sequence is known as STIR (Short inversion Time Inversion Recovery) (Bydder & Young 1985).

Another technique known as frequency-selective fat saturation can also be used for fat suppression. For this, an RF pulse is applied with a narrow range of frequencies, centred on the Larmor frequency of fat, so that only fat is excited. Spoiler gradients are then applied immediately after the RF pulse to dephase the signal before imaging is commenced, using the same principles described earlier for saturation pulses. This technique can be combined with STIR so that any signal that is not entirely nulled by the inversion pulse is spoiled. This type of suppression is generally known as SPIR (Spectral Inversion Recovery) (Kaldoudi et al. 1993).

At higher field strengths, such as 7T, it is usually more effective to use frequency selective fat saturation due to the large absolute difference in the Larmor frequencies of fat and water (McRobbie et al. 2003). However it is hard to achieve good fat suppression using frequency selective techniques when magnetic field inhomogeneities are present as they produce a spatial variation of the Larmor frequencies which can be particularly problematic when a large FOV is used.

When imaging is carried out using a SE sequence, a further fat suppression technique can be employed, known as Slice Selective Gradient Reversal (SSGR)(Gomori et al. 1988). In this method, the polarity of the slice-selection gradient and RF pulse frequency offset is reversed during application of the  $180^\circ$  RF refocusing pulse. Due to the fat-water shift the selective RF excitation pulse excites fat and water from slices that are displaced from one another in the slice direction. By inverting the polarity of the slice-selection gradient for the  $180^\circ$  RF pulse, the direction of displacement of the fat-slice relative to the water-slice is reversed. Provided that the fat-water shift is greater than the bandwidth of the selective RF pulses, the fat-slice that is excited by a nominal  $90^\circ$  RF pulse, applied in conjunction with a gradient of positive polarity, will have no overlap with the slice that experiences a selective  $180^\circ$  RF pulse applied with a gradient of negative polarity, and consequently no fat

signal is refocused at the time of the spin echo of the water signal (Figure 4.7).

The separation, D, (in mm) of the fat and water-slices is given by:

$$D = \delta B_0 / G \quad (4.1)$$

where  $\delta$  is the chemical shift of fat relative to water,  $B_0$  is the main magnetic field strength in Tesla, and G is the slice-selection gradient strength in T/m. In this study, the bandwidth of the excitation pulse (Hamming filtered sinc) was 628 Hz and for the refocusing pulse was 695 Hz. For excitation of a 1.5 mm-thick slice, this required the use of a 9.83 mT/m slice select gradient strength during application of the 90° RF-pulse, calculated from:

$$G_z = \frac{RF_{BW}}{\frac{\gamma}{2\pi} \Delta z} \quad (4.2)$$

where  $G_z$  is the gradient strength in the slice selection direction  $RF_{BW}$  is the RF bandwidth and  $\Delta z$  is the slice thickness. This resulted in a fat-water displacement, D, of 2.4 mm, and a reversed displacement of 2.15 mm for the selective 180° RF pulse. Since these values exceed the slice thickness, the fat signal in the SE image is strongly suppressed. A major benefit of the SSGR approach, compared to the methods described earlier, is that it does not require the use of additional RF pulses and so the SAR of a SE sequence employing SSGR is the same as a standard SE sequence. This is especially important at 7 T as the number of slices that can be acquired using SE sequences is often SAR limited when using short TRs.

A preliminary study was carried out in order to assess which fat suppression technique was most effective when using a SE EPI sequence with a large FOV at 7 T. For this, a volunteer was scanned using a SE EPI sequence with

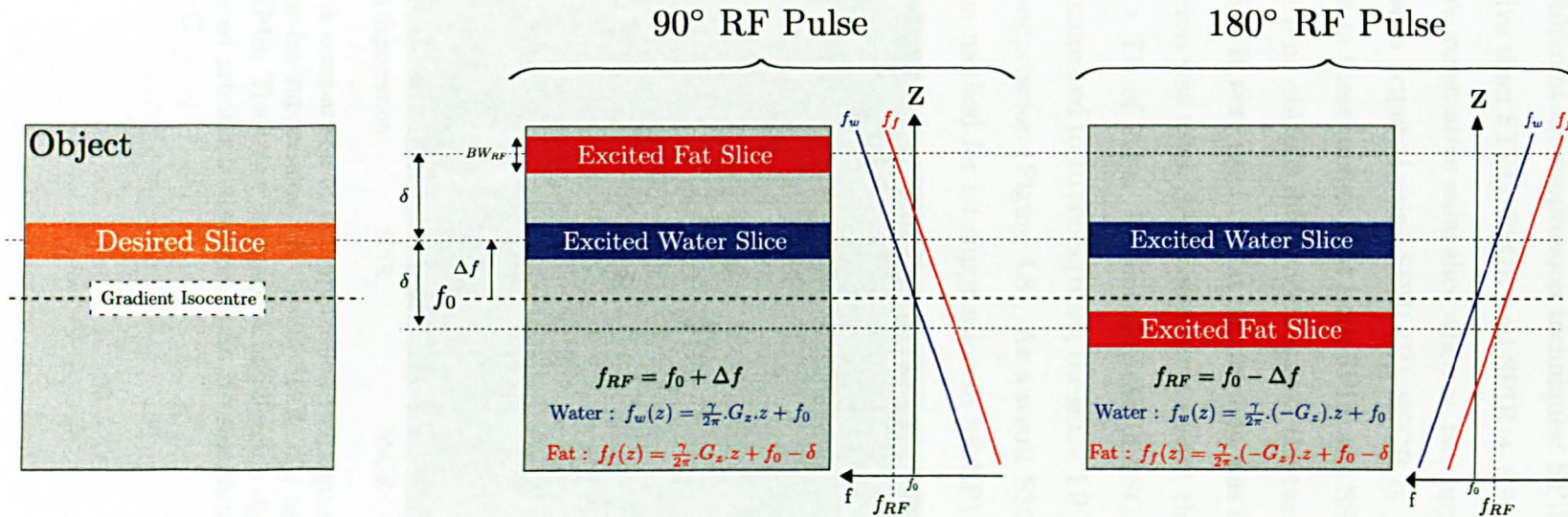


Figure 4.7: Slice Selection Gradient Reversal (SSGR). The polarity of the slice selection gradient is reversed upon application of the 180° RF pulse in a SE sequence so that fat does not experience both the 90° and 180° RF pulse. To allow slices to be chosen that lie away from the gradient isocentre the sign of the RF pulse frequency offset also has to be reversed. The technique only works if the bandwidth of the RF pulse ( $BW_{RF}$ ) is less than the fat-water shift ( $\delta$ ).

a range of different fat suppression techniques: SPIR (previously found to be more effective than STIR), SSGR and SPIR + SSGR. Figure 4.8A shows an image of a representative axial slice when no fat suppression was used; next to this are images acquired using SPIR (B), SSGR (C) and SSGR + SPIR (D). It is clear from these images that both SPIR and SSGR have removed the fat artefact (with no obvious difference between the two techniques). When both SPIR and SSGR were used the fat suppression was less effective. When SPIR fat suppression was used, SAR constraints meant that only 14 slices could be scanned in a TR of 2.4 s. In contrast, use of SSGR allowed the number of slices to be increased to 16 slices (using the same TR), whilst providing equally robust fat suppression (Figure 4.8). As a result SSGR was determined to be the optimum method for fat suppression in SE EPI functional imaging.

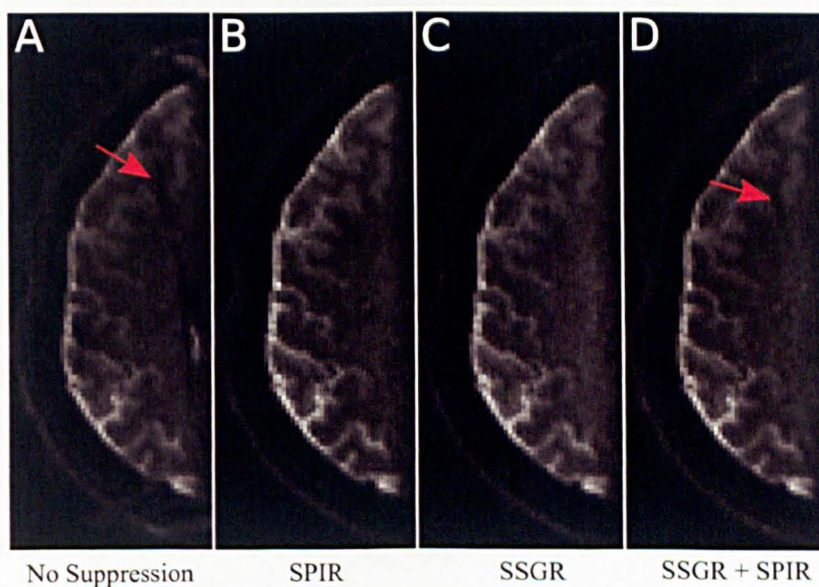


Figure 4.8: A comparison of fat suppression techniques. A : An axial scan of the head without fat suppression. B : using SPIR. C : using SSGR. D : using both SSGR and SPIR. The arrow in image A highlights a significant fat shift artefact, a less pronounced artefact is also seen in D. No significant fat-shift artefacts can be seen in B or C.

### Threshold-Free Cluster Enhancement

To reduce the effects of noise, z-score maps (generated using FEAT) were clustered using a recently developed technique known as Threshold-free cluster enhancement (TFCE) (Smith & Nichols 2009). TFCE maps provide a voxelwise measure of the amount of cluster-like spatial support for each voxel in a z-score map. The TFCE values in these maps represent the weighted sum of the height of the statistical map data (i.e. z-score) and the spatial extent of the cluster surrounding it.

For both the GE and average SE data the TFCE maps were thresholded at the 95th percentile of voxels with non-zero values to form binary masks representing voxels showing task-related activation. The masks were used to form regions of interest (ROI) for subsequent analysis.

Employing this technique meant that the ROI were not delimited by a z-score value chosen arbitrarily by the user but instead by an automatic process. For example, SE- and GE- statistical maps are often thresholded at differing z-scores to account for the large difference in CNR between these acquisition sequences (Michelich et al. 2006) and these threshold levels are often chosen arbitrarily. The TFCE technique provides a more objective method of ROI definition.

An additional 'average' SE ROI mask was defined using the TFCE map formed from the average of all the SE data for each subject (across TEs).

The average z-score and the  $T_2$  distribution of voxels in this 'average' ROI were measured. Similarly the average z-score and  $T_2^*$  distribution were determined for the GE ROI. The mean  $T_2$  and  $T_2^*$  values were calculated for both SE and GE ROI.

### Fractional Signal Change

The 'average' SE ROI was used to estimate the fractional signal change  $\Delta S/S$  and CNR at each echo time.  $\Delta S/S$  was calculated from the fractional

change in mean signal intensity across the ROI as a function of TE, using  $(S_{ON} - S_{OFF})/S$ .  $S_{ON}$  and  $S_{OFF}$  were calculated using the average of image volumes 5 to 8 (ON) and the average of image volumes 11 to 13 (OFF) from the average stimulus cycle (corresponding to an ON period between 12-19.2 s and an OFF period between 26.4-31.2 s in the stimulus cycle).  $S$  was calculated from the average of the baseline data acquired at the start of each scan. Data from all subjects were combined to calculate the average value of  $\Delta S/S$  at each of the echo times. Since  $\Delta S/S$  is expected to scale as  $|\Delta R_2 \cdot TE|$  (Gati et al. 1997),  $\Delta R_2$  was estimated from a weighted linear regression of  $\Delta S/S$  versus TE. This calculation was carried out using only the SE data in both the GE ROI and the 'average' SE ROI. The signal change normalised by the baseline signal at the shortest echo time was also calculated on a voxel-by-voxel basis for the 'average' SE ROI from  $(S_{ON} - S_{OFF})/S_{BASE}$ , where  $S_{ON}$  and  $S_{OFF}$  were determined as described above and  $S_{BASE}$  was the baseline signal for TE = 30 ms. The actual variation of the signal with TE from the ROI was also calculated by averaging over voxels.

The expected variation of  $(S_{ON} - S_{OFF})/S_{BASE}$  versus echo time was simulated for the 'average' SE ROI. This was accomplished by using the voxel-wise  $T_2$  values in the ROI to calculate the expected signal change, as described by the following:

$$\Delta S = S_0 \cdot e^{-TE/T_2} \cdot (e^{-TE \cdot \Delta R_2} - 1) \quad (4.3)$$

A  $\Delta R_2$  value of  $-0.85 \text{ s}^{-1}$  was used for these calculations (as estimated from the linear regression in Figure 4.13). The SE images from all subjects displayed a band like region of low signal intensity running along the bank of the pre-central gyrus in both the GE- and SE-EPI data, indicating a region in which the relaxation rate was elevated. In order to assess the signal behaviour

in this region, a mask spanning this dark-band was manually defined for each subject using the  $T_2$  maps.

### Venous Maps

To assess the tissue specificity of the activation measured from the GE- and SE-data, venous vessel masks were generated using the phase of high resolution,  $T_2^*$ -weighted images. The phase data were first unwrapped using PRELUDE in FSL and then high-pass filtered by subtracting a Gaussian smoothed version of the phase (using a kernel with a full-width at half maximum of 2 mm) so as to remove large length-scale phase variations. The phase data were then thresholded to produce high resolution venous masks. Venous masks were then dilated (using a 2D disk with a diameter of 1.5 mm) prior to down-sampling to 1.5 mm isotropic resolution to give information on both the vessel positions and the regions in their direct vicinity (dilation ensured that the position of the veins could be seen in the down-sampled image). The venous masks were aligned to the functional data in the following manner: first the whole head  $T_1$ -weighted MPRAGE images were realigned to the  $T_1$ -weighted MPRAGE images acquired during the functional session (which were spatially registered to the SE fMRI data); using the algorithm described by Nestares & Heeger (2000). The corresponding transform was then applied to the venous masks prior to binarisation (using a threshold value of 0.5). The fraction of active voxels that were common to the venous masks was assessed for the SE ROI at each echo time. The overlap with the vessel mask of voxels that were not common to the SE and GE ROI (which we call uncommon voxels) was also investigated.

### Temporal SNR

The temporal SNR (tSNR) of the SE- and GE-fMRI data was estimated using the SE- and GE- ROI respectively. tSNR was calculated from the mean

signal divided by the standard deviation over the initial baseline volumes for each echo time. This was calculated on a voxel by voxel basis and then averaged over voxels. BOLD contrast to noise ratio (CNR) was computed as  $CNR = tSNR * (\Delta S/S)$ .

The standard deviation across dynamics, during the baseline period, was used to provide an estimate of the relative magnitude of the thermal and physiological noise. This involved calculating the ratio of the average temporal standard deviation of voxels located in adjacent gray and white matter regions, and then making the assumption that thermal noise dominates in white matter whilst in gray matter a combination of both thermal and physiological noise is present.

## 4.4 Results

SSGR removed the vast majority of fat shift artefacts from the SE images. Significant activation was found for all subjects in the GE and SE data across all echo times.

Figure 4.9 illustrates the high accuracy that was achieved by image registration. Registration results are shown for the functional GE- and SE- EPI data sets and  $T_2^*$  weighted anatomical data (used to generate the vein maps). The red line overlaid on each image delineates the locus of the central sulcus identified from the SE EPI data

Figure 4.10 shows the GE (TE = 25 ms) and SE (TE = 45 ms) activation maps overlaid on the mean image (across volumes) of the corresponding EPI data for a representative subject. Corresponding  $T_2$  and  $T_2^*$  maps are also shown. The  $T_2$  map displays a dark band of low  $T_2$  values following the pre-central gyrus of the motor cortex.

Figure 4.11 shows an example of one of the high-pass filtered phase images that were used to create the venous masks. Examples of the high resolution

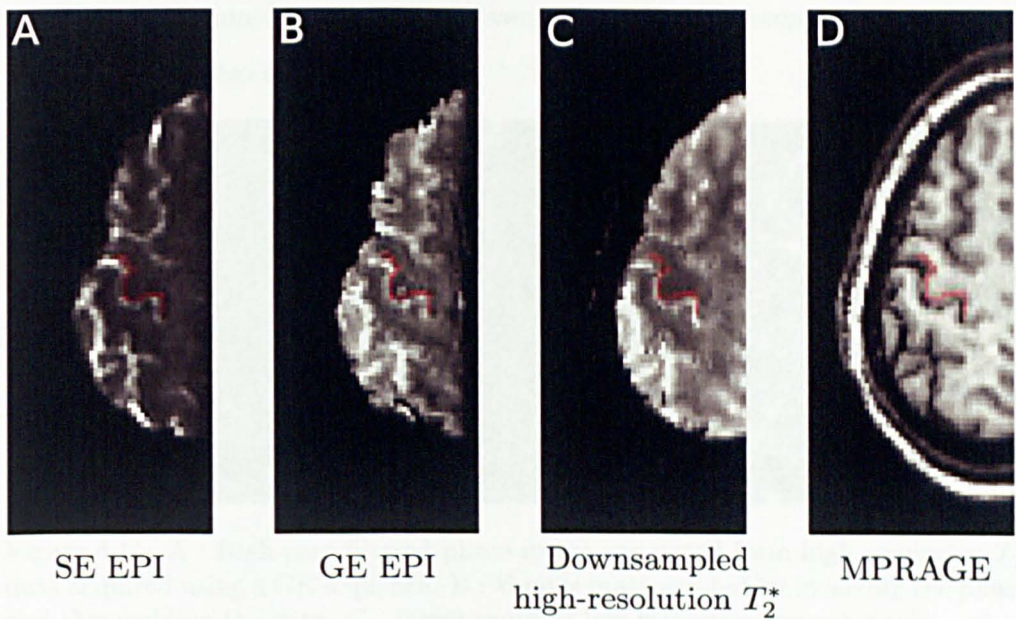


Figure 4.9: Alignment accuracy for a representative subject. A : mean SE-EPI fMRI data. B : mean GE-EPI fMRI data. C :  $T_2^*$ -weighted image used to form vein masks (downsampled to 1.5mm isotropic resolution). D : MPRAGE data. The red line highlights the central sulcus as identified on SE-EPI fMRI data.

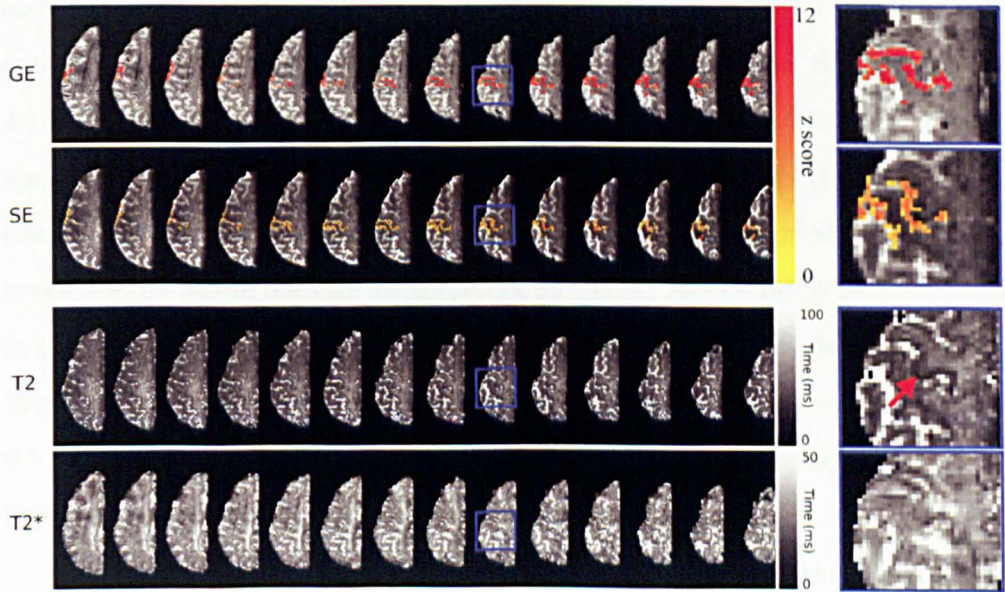


Figure 4.10: Activation maps from a representative subject overlaid on corresponding mean EPI images for GE ( $TE = 25$  ms) and SE ( $TE = 45$  ms) data. Corresponding  $T_2$  and  $T_2^*$  maps are also shown. A dark band of tissue with low  $T_2$  values ( $\sim 30$  ms) can be seen running along the bank of the pre-central gyrus of the motor cortex (arrow). The images on the right show the zoomed in blue box regions.

and low resolution (down-sampled) venous masks that were generated from these data are also shown.

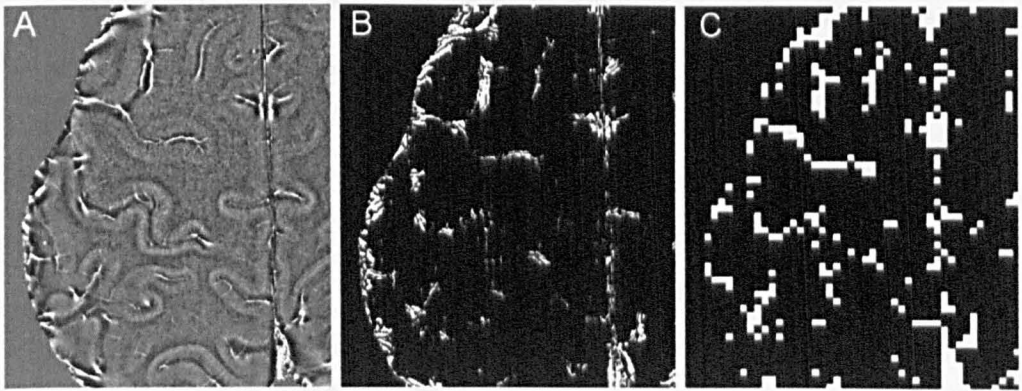


Figure 4.11: A : High-pass filtered phase image generated from high resolution  $T_2^*$  data acquired using a GE sequence. B : Venous mask created by inverting the phase and thresholding the data. C : Down-sampled low resolution venous mask.

Figure 4.12 A shows the temporal variation of the signal intensity in the GE-data averaged over the GE-ROI and in the SE-data ( $TE = 45$  ms) averaged over the 'average' SE ROI for a representative subject. The average signal across one stimulus cycle at each echo time is shown for the SE data (Figure 4.12 B). The ratio of the percentage signal changes of the SE ( $TE = 45$  ms) and GE data ( $TE = 25$  ms) was found to be  $0.48 \pm 0.05$  (i.e. GE BOLD percentage signal change was  $2.1 \pm 0.2$  times larger than for SE BOLD). The mean z-score in the relevant ROI (across subjects) was found to be 40 % higher in the GE data ( $8.5 \pm 0.4$ ) than in the 45 ms echo time SE data ( $6.1 \pm 0.5$ ). When only venous voxels were considered, the mean z-score was found to be  $9.5 \pm 0.2$  in the GE ROI and  $7.7 \pm 0.2$  in the SE ROI (22 % higher in the GE ROI).

The average temporal SNR (tSNR) in the GE ROI for the GE data was found to be  $46.9 \pm 3.6$  and the GE BOLD CNR was found to be  $3.5 \pm 0.2$ . Results for the SE data were echo time dependent, as shown in Figure 4.12 C, for a TE of 45 ms the tSNR was  $25.4 \pm 1.6$  and the CNR was  $1.0 \pm 0.1$ . At these echo times the ratio of GE CNR to SE CNR was therefore  $3.5 \pm 0.4$ .

The ratio of the noise amplitude in adjacent gray and white matter regions was found to be 1.16 for the SE data ( $TE=45\text{ms}$ ) and 1.17 for the GE data. Values close to unity indicate that thermal noise dominates as would be expected from the measured values of gray matter tSNR (see Figure 1 of Triantafyllou et al. (2005)).

For the SE data the average number of voxels in each ROI, generated using the TFCE technique, was found to be:  $783 \pm 36$ ,  $739 \pm 21$ ,  $708 \pm 24$ ,  $733 \pm 22$ ,  $723 \pm 19$ ,  $716 \pm 11$  for the echo times of 30, 35, 40, 45, 50 and 55ms respectively (with the standard error across subjects also shown). For the SEav ROI (generated from analysis of the average of the SE data across all echo times for each subject) this was  $741 \pm 17$  and for the GE data  $782 \pm 28$ .

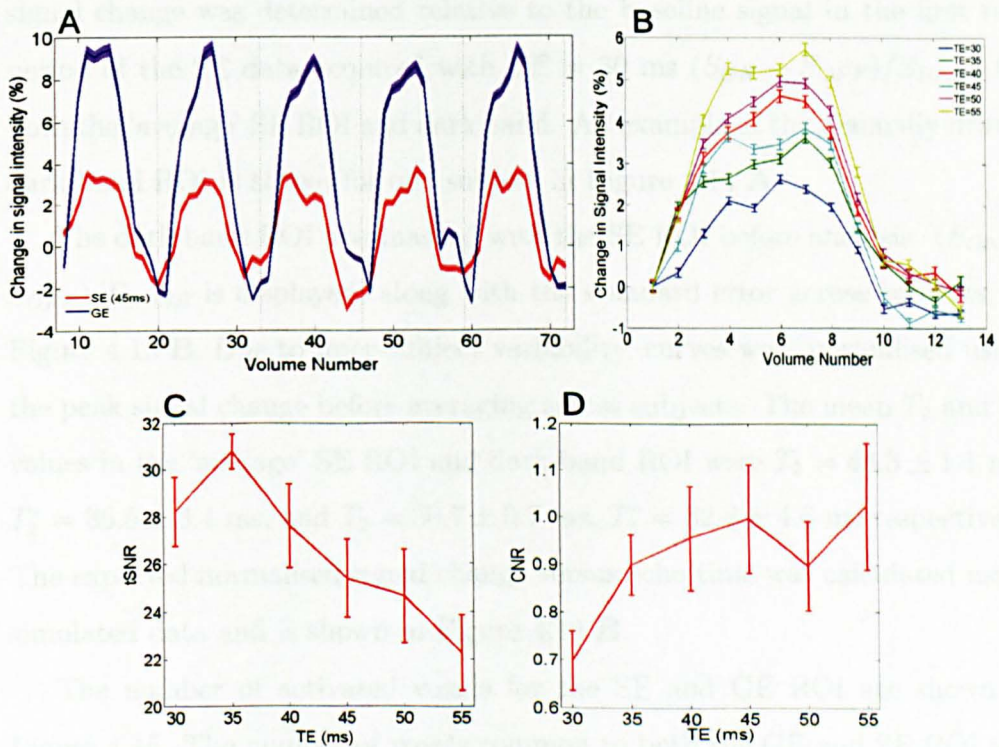


Figure 4.12: A : Example time-series showing BOLD percentage signal change for the GE data ( $TE = 25\text{ ms}$ ) averaged over the GE ROI and for SE data ( $TE = 45\text{ ms}$ ) averaged over the average SE ROI, for a representative subject. B : Average BOLD signal change across SE cycles at each echo time. C : tSNR and D : CNR as a function of echo time (TE) where the data shown in C and D are the average across subjects, with the error bars indicating the SEM.

The variation of the BOLD percentage signal change ( $\Delta S/S$ ) as a function of TE in the SE data can be seen in Figure 4.13 **A** for both the SE ROI (blue) and GE ROI (red). Using a weighted linear regression, the mean  $\Delta R_2$  was found to be  $-0.85 \pm 0.11 s^{-1}$  for the SE-ROI and  $-0.37 \pm 0.05 s^{-1}$  for the GE-ROI. In the region that is common to both ROI (com ROI)  $\Delta R_2$  was found to be  $-0.95 \pm 0.06 s^{-1}$ . In the region of the SE ROI that was uncommon to the GE ROI (SE uncommon ROI),  $\Delta R_2$  was  $-0.72 \pm 0.15 s^{-1}$ , in the part of the GE ROI that was uncommon to the SE ROI (GE uncommon ROI),  $\Delta R_2$  was  $0.17 \pm 0.11 s^{-1}$ , indicating that there are only small activation related signal changes in the SE data in this region (Figure 4.13 **B**).

To assess the echo time at which maximum SE contrast occurs, the BOLD signal change was determined relative to the baseline signal in the first rest period of the SE data acquired with  $TE = 30$  ms  $(S_{ON} - S_{OFF})/S_{BASE}$  for both the 'average' SE ROI and dark band. An example of the manually drawn dark band ROI is shown for one subject in Figure 4.14 **A**.

The dark band ROI was masked with the SE ROI before analysis.  $(S_{ON} - S_{OFF})/S_{BASE}$  is displayed, along with the standard error across subjects, in Figure 4.13 **B**. Due to inter-subject variability, curves were normalised using the peak signal change before averaging across subjects. The mean  $T_2$  and  $T_2^*$  values in the 'average' SE ROI and dark-band ROI were  $T_2 = 48.3 \pm 1.1$  ms,  $T_2^* = 36.5 \pm 3.4$  ms, and  $T_2 = 30.7 \pm 0.7$  ms,  $T_2^* = 32.8 \pm 4.6$  ms respectively. The expected normalised signal change versus echo time was calculated using simulated data and is shown in Figure 4.14 **B**.

The number of activated voxels for the SE and GE ROI are shown in Figure 4.15. The number of voxels common to both the GE and SE ROI was  $\sim 50\%$  of the total number in each ROI (Figure 4.15 **A**). It was found that 18 % ( $p = 0.046$ ) more voxels overlapped the venous mask for the GE ROI than the SE ROI when the whole ROI was considered, and 50 % ( $p = 0.040$ ) more when the non-overlapping region of the SE and GE ROIs was used as

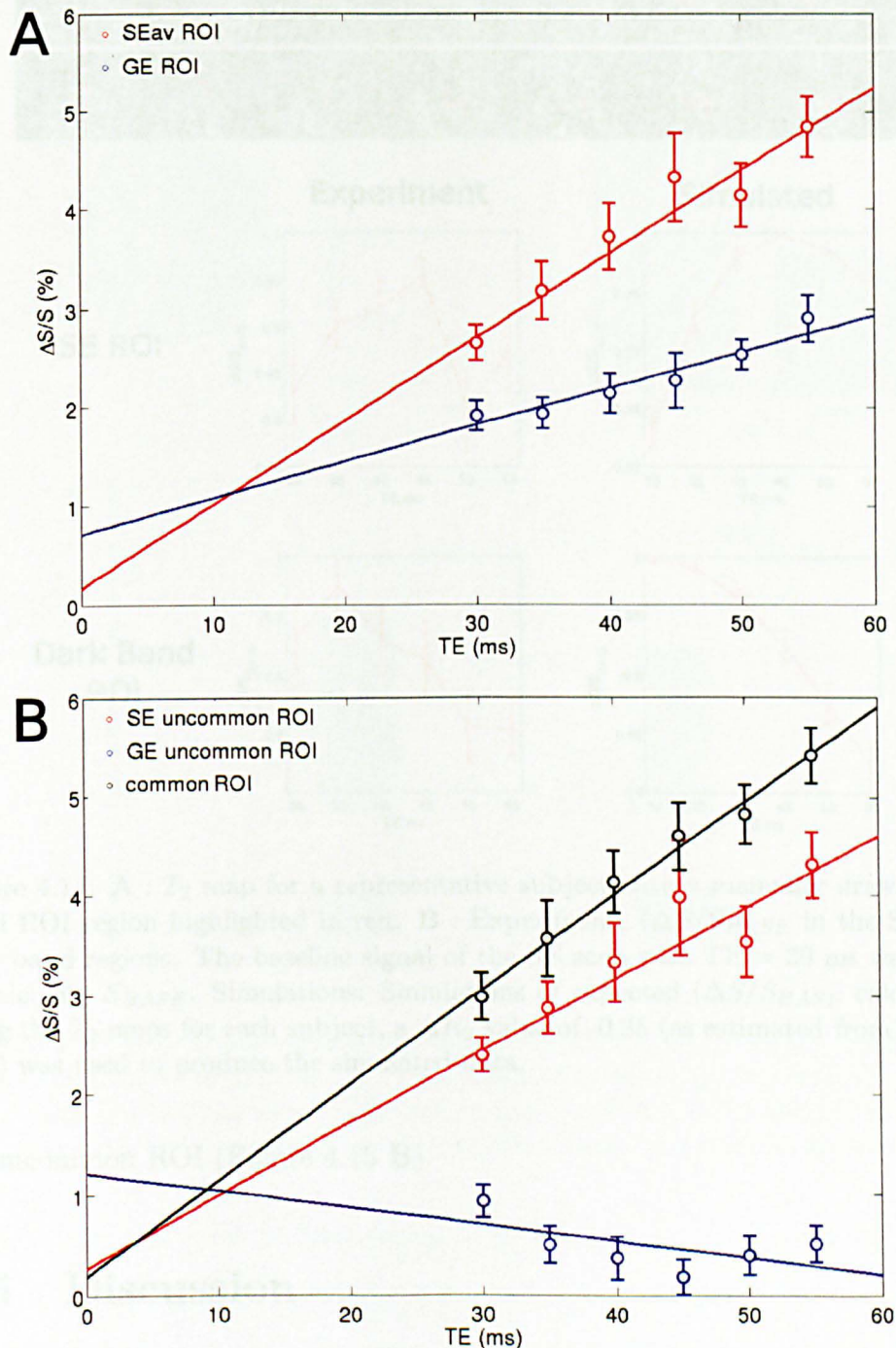


Figure 4.13: **A** :  $\Delta S/S$  in the SE 'average' ROI and GE ROI for SE data. Weighted least squares fits (weighted using  $1/(SEM^2)$ ) are shown along with errors on the gradient and y-intercept, with  $y = 0.085x [0.011] + 0.166 [0.491]$  ( $r=0.966$ ) and  $y = 0.037x [0.005] + 0.711 [0.234]$  ( $r=0.960$ ) for the SE and GE ROIs, respectively. **B** :  $\Delta S/S$  in the ROI common to both SE and GE ROI (com ROI), uncommon part of the SE and GE ROIs (SE uncommon ROI and GE uncommon ROI respectively) with  $y = 0.095x [0.006] + 0.188 [0.244]$  ( $r=0.993$ ),  $y = 0.072x [0.015] + 0.273 [0.630]$  ( $r=0.928$ ) and  $y = -0.017x [0.011] + 1.207 [0.484]$  ( $r=0.601$ ) for the common, SE uncommon and GE uncommon ROIs respectively.

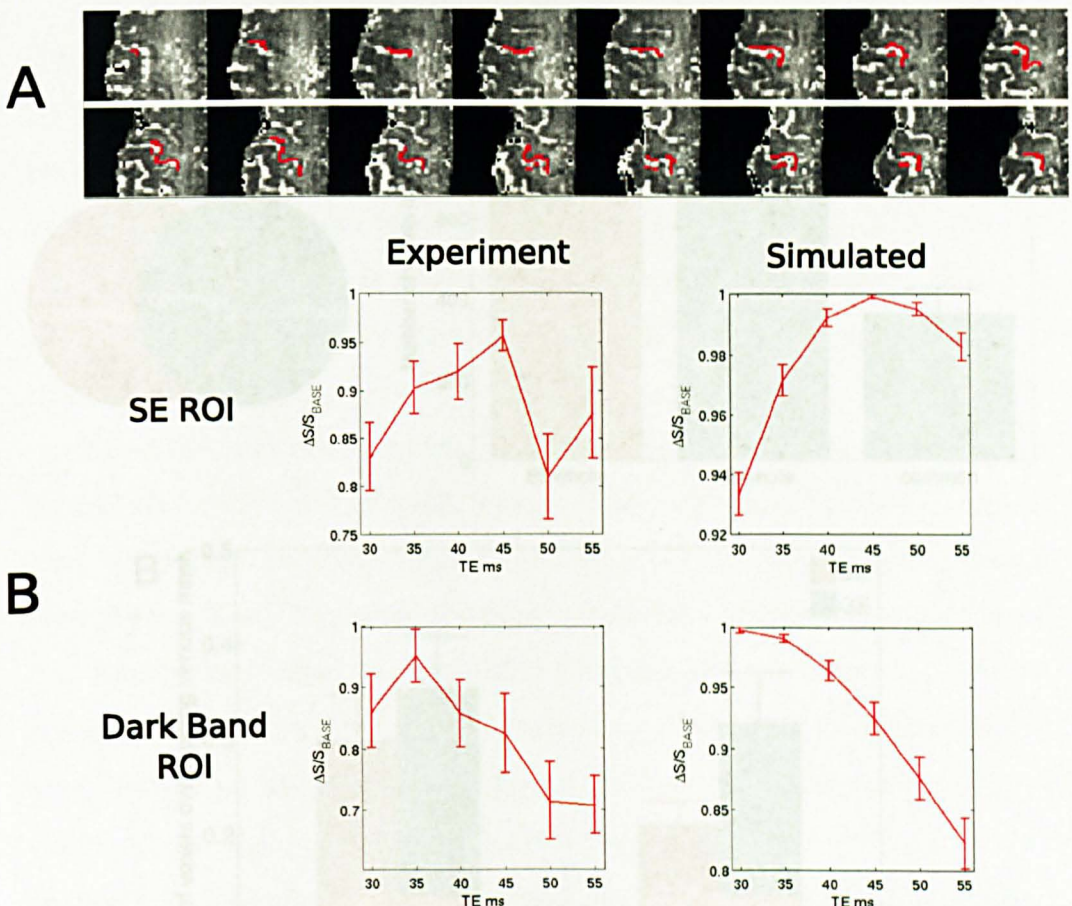


Figure 4.14: **A** :  $T_2$  map for a representative subject with a manually drawn dark band ROI region highlighted in red. **B** : Experiment: ( $\Delta S/S_{BASE}$  in the SE and dark band regions. The baseline signal of the SE scan with  $TE = 30$  ms was used to calculate  $S_{BASE}$ . Simulations: Simulations of expected ( $\Delta S/S_{BASE}$  calculated using the  $T_2$  maps for each subject, a  $\Delta R_2$  value of -0.85 (as estimated from Figure 4.13) was used to produce the simulated data.

an uncommon ROI (Figure 4.15 B).

## 4.5 Discussion

Using the TFCE method, activation was found to be highly localised to the cortical strip in the pre-central gyrus in both the SE and GE data for all subjects (Figure 4.10). The average number of voxels in the GE and SE ROI were found to be very similar, as would be expected when using the TFCE

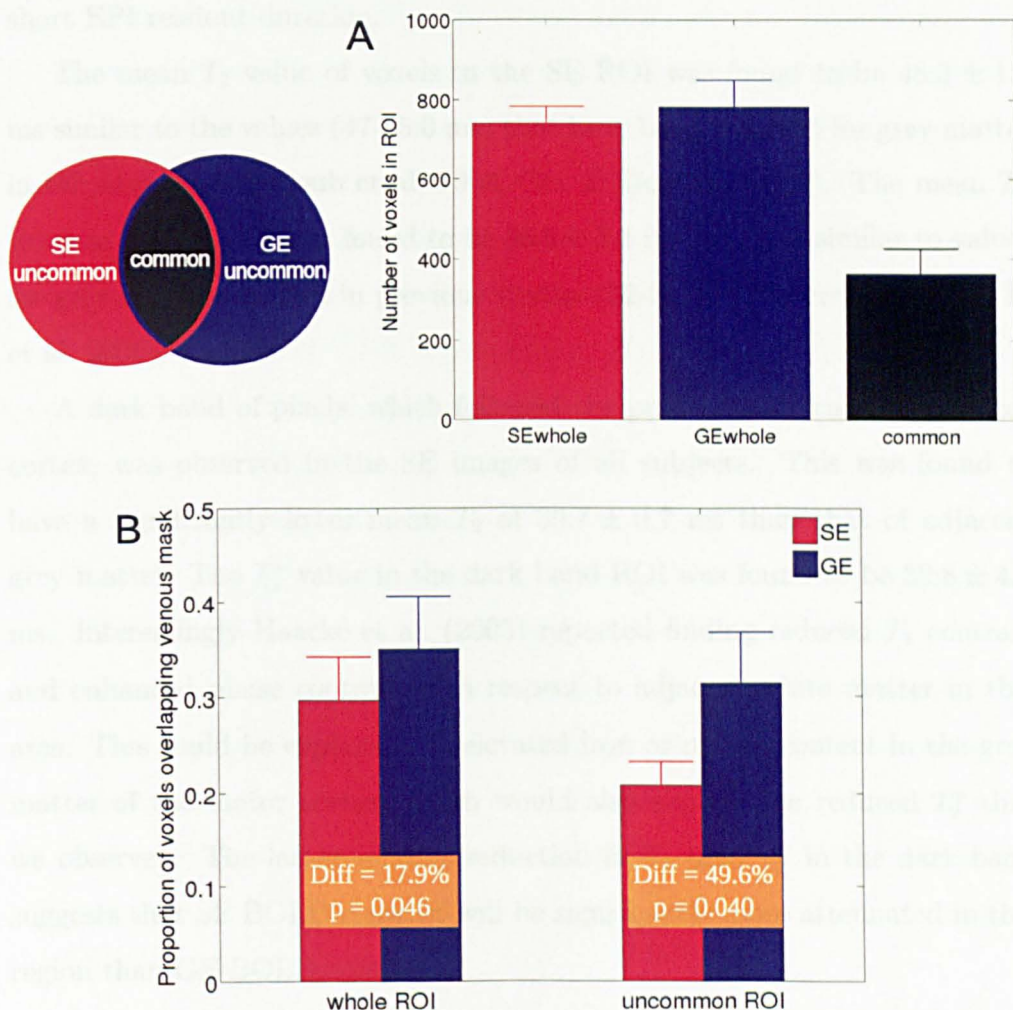


Figure 4.15: **A** : Average number of voxels in the SE and GE ROIs and number of voxels common to both ROIs. **B** : Proportion of voxels in the whole (average SE and GE ROIs) and uncommon ROIs (SE uncommon ROI and GE uncommon ROI) which overlap with the venous mask. Two tailed t-test statistics are also shown.

method (Figure 4.15 **A**). Interestingly the number of active voxels common to both GE and SE ROIs was less than half the total number in each, giving a strong indication that the areas of activation identified from the BOLD response are indeed different for the GE and SE acquisitions. The purity of the SE signal was ensured by employing crusher gradients around the 180 ° RF pulse, to kill off any none-SE signal pathways, and through the use of a

short EPI readout duration.

The mean  $T_2$  value of voxels in the SE ROI was found to be  $48.3 \pm 1.1$  ms similar to the values (47-55.0 ms) that have been reported for grey matter in the literature (Yacoub et al. 2003, Cox & Gowland 2010). The mean  $T_2^*$  value in the SE ROI was found to be  $36.5 \pm 3.4$  ms, which is similar to values for grey matter reported in previous studies (32-36 ms) (Peters et al. 2007, Li et al. 2006).

A dark band of pixels, which followed the pre-central gyrus of the motor cortex, was observed in the SE images of all subjects. This was found to have a significantly lower mean  $T_2$  of  $30.7 \pm 0.7$  ms than that of adjacent grey matter. The  $T_2^*$  value in the dark band ROI was found to be  $32.8 \pm 4.6$  ms. Interestingly Haacke et al. (2005) reported finding reduced  $T_1$  contrast and enhanced phase contrast with respect to adjacent white matter in this area. This could be explained by elevated iron or myelin content in the grey matter of the motor cortex, which would also explain the reduced  $T_2^*$  that we observed. The larger relative reduction in  $T_2$  than  $T_2^*$  in the dark band suggests that SE BOLD contrast will be significantly more attenuated in this region than GE BOLD contrast.

For the optimum SE echo time of 45 ms the percentage signal change in the SE ROI region (using the average cycle) was measured to be  $4.3 \pm 0.5$  %, whilst the GE data (TE = 25ms) percentage signal change was  $8.9 \pm 0.7$  %, resulting in a SE to GE ratio of  $0.48 \pm 0.05$  which is in good agreement with the value of 0.46 reported by Yacoub et al. (2005) in the visual cortex at 7 T (using similar echo times). The smaller fractional signal change in the SE data was largely the cause of the factor of 3.5 reduction in the BOLD CNR which we measured when comparing the GE and the SE data. Some of the reduction does however result from the lower tSNR in the SE data. This may result from greater steady state signal saturation and larger magnetisation transfer effects occurring in the SE data as a result of the repeated application of

180° RF pulses. The plot of CNR versus TE for the SE data (Figure 4.12 C) was relatively flat over the range of echo times investigated as a result of the competing effects of the reduction in tSNR and the increase in percentage signal change with increasing TE.

The measured percentage signal change was found to vary linearly with echo time (Figure 4.13), in agreement with numerous previous studies (Yacoub et al. 2003, Duong et al. 2003, Schaefer et al. 2008).  $\Delta R_2$  for the SE-ROI was calculated to be  $-0.85 \pm 0.11\text{s}^{-1}$  and  $-0.37 \pm 0.05\text{s}^{-1}$  for the GE-ROI. These values are higher than those reported at 7 T in a large ROI in the visual area by Duong et al. (2003), who found  $\Delta R_2$  to be  $-0.21\text{s}^{-1}$  and, in the case of the SE ROI, also higher than the value of  $-0.51 \pm 0.14\text{s}^{-1}$  reported by Schaefer et al. (2008) in the motor cortex at 7 T. The reduction in  $\Delta R_2$  in the GE-ROI is expected as the GE ROI will contain voxels that are activated due to non- $T_2$ -related BOLD effects. For the GE ROI a significant non-zero intercept was found, while the intercept was not significantly different from zero for the SE ROI. The non-zero intercept for the GE-ROI data most likely reflects the effects of in-flowing blood and line broadening (Yacoub et al. 2005, Schaefer et al. 2008, Uludag et al. 2009).

Since the TFCE method was used in this study, the GE and SE BOLD ROI contain a similar number of voxels. The GE BOLD ROI would therefore be expected to have an increased sensitivity to large draining veins and thus to show significant  $T_2^*$  changes due to large vessel BOLD and in-flow effects. In the uncommon region of the SE ROI,  $\Delta R_2$  was found to be  $-0.72 \pm 0.15\text{s}^{-1}$ , slightly lower than in the whole SE ROI. In the uncommon part of the GE ROI,  $\Delta R_2$  was found to be  $+0.17 \pm 0.15\text{s}^{-1}$ : this result can be better understood by observing the data in Figure 4.13, from which it can be seen that the percentage SE signal change in the uncommon portion of the GE ROI is less than 1 % across nearly all echo times. This indicates that there is no significant SE BOLD contrast in this region and so no TE dependent trend.

This also implies that the area of the GE ROI that is uncommon to the SE ROI is activated due to underlying effects to which SE images are not sensitive. These are most likely due to extravascular effects around large vessels. In the ROI defined to be common to both the GE and SE activation,  $\Delta R_2$  was found to be  $-0.95 \pm 0.06 s^{-1}$ .

Figure 4.14 shows the measured percentage signal change, relative to the baseline signal of the SE data set acquired with  $TE = 30$  ms, as a function of echo time. For the SE ROI (mean  $T_2 = 48.3 \pm 1.1$  ms) these results show that the largest change occurs for an echo time of approximately 45 ms. This is in agreement with the simulations, though a dip at an echo time of 50 ms in the real data is not seen in the simulated data. In the dark band ROI (mean  $T_2 = 30.7 \pm 0.7$  ms) the peak signal change occurred at a TE of  $\sim 35$  ms, close to the tissue  $T_2$  and in fairly good agreement with the simulated data which showed the largest signal change at 30 ms (the shortest TE considered in the simulation).

The regions which showed significant activation in the GE data contained more voxels overlying venous blood vessels than the activated regions identified from the SE measurements (Figure 4.14 **B**). This difference was most pronounced when the uncommon ROIs were compared (50 %,  $p=0.040$ ) as opposed to the average SE and GE ROIs (termed whole ROIs in Figure 4.15) (18 %,  $p=0.046$ ). The results indicate that the GE and SE ROIs contain a common region that contains voxels overlying venous sites, but in regions where the SE and GE BOLD activation does not overlap, the proportions of voxels that occur at venous sites is much less in the SE case; indicating that GE BOLD is more sensitive to the effects due to larger blood vessels slightly offset from the site of SE based BOLD activation. The common region between SE and GE activation is most likely due to contributions from extravascular signal from small vessels and residual intravascular effects (Yacoub et al. 2003). Despite the postulated increase in functional spatial specificity of the SE BOLD

response, large changes in  $R_2$  may still occur at a few sites where very large vessels are present due to the diffusion of water through field gradients around individual red blood cells (Bandettini et al. 1994*b*).

It is important to acknowledge that the optimal SE percentage signal change was on average a factor of  $2.08 \pm 0.22$  times lower than that produced by GE BOLD based sequences, and the CNR a factor of  $3.5 \pm 0.4$  times less. It is likely that the advantage of SE BOLD fMRI will therefore be the increased specificity apparent at ultra-high spatial resolution, but this must be compared with the selectivity achievable with GE BOLD using selective adaptation (Grill-Spector & Malach 2001) or multivariate pattern analysis (MVPA) (Kamitani & Tong 2006, Cox & Savoy 2003) to resolve fine functional features.

## 4.6 Conclusion

Analysis based on the TFCE method allowed comparison of the spatial location and percentage signal change in active brain regions in GE and SE data, collected at ultra high field (7 T) and high spatial resolution (1.5 mm isotropic), during the execution of a simple motor task.

An echo time of 45 ms was found to be optimal at 7 T for fMRI experiments on the motor cortex using SE-EPI (producing a large signal change relative to the shortest echo time), similar to the average  $T_2$  of the voxels in the SE-ROI.

We identified a dark band in SE images of the motor cortex corresponding to a region in which  $T_2$  and  $T_2^*$  were significantly reduced, possibly due to increased iron and/or myelin content (Haacke et al. 2005).

Interestingly the number of active voxels common to both GE and SE ROIs was found to be less than half the total number in each, indicating that the areas of activation identified from the BOLD response were different for the GE and SE acquisitions. Further, regions which showed significant

activation in the GE data were found to contain significantly more voxels overlying venous blood vessels than the activated regions identified in the SE data.

These results support evidence in the literature that SE based BOLD contrast is predominantly sensitive to different underlying mechanisms than GE BOLD contrast. The data suggests that the origin of the SE BOLD response is most likely due to extravascular effects around small blood vessels, whereas the GE BOLD response is sensitive to the extravascular effects around both small and large vessels (with the large vessel effects dominating). This indicates that the SE BOLD response is indeed more spatially specific to the underlying neuronal activation. The work presented in this chapter has now been published (Harmer et al. 2011).

# Chapter 5

## Off-Resonance Field Effects: EPI Artefact Correction

### 5.1 Theory

Most modern MRI scanners can generate static magnetic fields with a uniformity of better than 1 ppm over a central volume with a diameter of around 40 cm. This high uniformity is essential in MR imaging because the precessional frequency of spins in a sample ( $\omega_0$ ) is governed by the strength of the local magnetic field; as described by the Larmor equation. To induce magnetic resonance in these spins an RF pulse is applied that has a frequency that matches the resonant frequency. Any significant variation in  $\omega_0$  across the sample will reduce the effectiveness of the RF pulse. During an MRI acquisition a number of magnetic field gradients are applied in order to spatially localise the signal so that images can be produced (Section 2.5). The gradients impart a change in magnetic field strength that varies linearly across the sample, in such a way that the field strength has a linear relation to position in the object. Inhomogeneities in the main magnetic field ( $\Delta B_0$ ) also cause the field strength to vary as a function of spatial location, disrupting the proportionality between magnetic field strength and position. If unaccounted

for, these adversely effect the encoding process and lead to errors in image reconstruction that manifest as geometric distortions in the reconstructed image. Variations in the sign and magnitude of the field inhomogeneity across the imaging volume cause the signal from different parts of the sample to be shifted by varying amounts and so will also change its apparent spin density.

Magnetic field inhomogeneities can be produced in a number of ways. A common cause of first order global  $B_0$  offsets ( $\Delta B_0$ ) is the inaccurate calibration of gradient shim coils. However, in most modern scanners these effects can be corrected for by carrying out shim coil calibrations at the start of a scanning session. A more problematic effect arises due to the presence of the sample itself. When an object is placed in a magnetic field the material that makes up the sample will increase or decrease the local magnetic field strength by an amount that depends upon its magnetic permeability ( $\mu$ ). Paramagnetic materials cause the magnetic field lines to bunch together slightly inside the material, increasing the local magnetic field strength, whereas diamagnetic materials cause the field lines to spread apart reducing it. This relation is given by :

$$\bar{B} = \mu \bar{H} \quad (5.1)$$

where  $\bar{B}$  is the physical magnetic field and  $\bar{H}$  is the vector field (equal to  $\frac{B}{\mu_0}$  when no material is present). This property of materials is often described in terms of the magnetic susceptibility  $\chi$ , where  $\mu = (1 + \chi)\mu_0$ . This relation leads to the following:

$$\bar{B} = (1 + \chi)\mu_0 \bar{H} \quad (5.2)$$

where  $\chi$ , for diamagnetic, paramagnetic and ferromagnetic materials is defined by  $\chi < 0$ ,  $\chi > 0$  and  $\chi \gg 0$  respectively. In humans  $\chi < 0$  because tissue is generally weakly diamagnetic (Haacke et al. 1999). Variations in the local

magnetic field due to these susceptibility effects can be a significant problem in MRI.

### 5.1.1 Off-Resonance Effects in Conventional imaging Sequences

During sampling under a readout gradient of strength,  $G_x$ , the phase of the measured signal from position,  $x$ , in a sample, at time  $t$  relative to the start of sampling, is given by:

$$\phi(x, t) = \gamma G_x x t + \gamma \Delta B_0(x) t \quad (5.3)$$

$$\phi(x, t) = \gamma G_x x t \left( 1 + \frac{\Delta B_0(x)}{G_x x} \right) \quad (5.4)$$

$$\phi(x, t) = k_x x' \quad (5.5)$$

where

$$k_x = \gamma G_x t \quad (5.6)$$

$$x' = x + \frac{\Delta B_0(x)}{G_x} \quad (5.7)$$

Thus, spins located at position,  $x$ , will be encoded at position,  $x'$ , in the reconstructed image. Furthermore because  $\Delta B_0$  is a function of  $x$ , the difference between  $x$  and  $x'$  will change with  $x$  and lead to location dependent image distortions. In a perfectly uniform magnetic field the FOV ( $L$ ) is given by :

$$L = \frac{1}{\Delta k} \quad (5.8)$$

$$= \frac{1}{\gamma G \Delta t} \quad (5.9)$$

where  $G_x$  is the imaging gradient and  $\Delta t$  the sampling interval. In the presence of field inhomogeneities this changes to  $L'$ , given by:

$$L' = \frac{1}{\gamma(G + G_{\Delta B_0}) \Delta t} = \left( \frac{G}{G + G_{\Delta B_0}} \right) L \quad (5.10)$$

Thus, when  $G_{\Delta B_0} > 0$  the FOV,  $L'$ , reduces, effectively increasing the size of the object. Whereas when  $G_{\Delta B_0} < 0$  the FOV increases; reducing the size of the object. This stretching/compression will vary across the image, depending on the size of the local magnetic field inhomogeneity.

If we consider the effects of a magnetic field inhomogeneity that changes in the phase encoding direction (PE) we get :

$$x' = x + \frac{\Delta B_0(y)}{G_x}, \quad (5.11)$$

where spins originating from  $x$  are again encoded at position  $x'$  in the reconstructed image. However, in this case  $\Delta B_0(y)$  does not change with  $x$  but produces a net phase offset that varies with  $y$ . This effectively shifts the position of spins along  $x$  as a function of their position in  $y$ , changing the shape of the ROI that defines the voxel, from a square/rectangle to a parallelogram. This does not alter the relationship between position in  $y$  and rate of change of phase and so does not cause distortions in the PE direction. This can be better seen by considering the phase difference between two lines of k-space:

$$\phi_1 = \gamma G_x t x \left( 1 + \frac{\Delta B_0(y)}{G_x x} \right) + \gamma G_{y,1} y \tau_{PE} \quad (5.12)$$

$$\phi_2 = \gamma G_x t x \left( 1 + \frac{\Delta B_0(y)}{G_x x} \right) + \gamma G_{y,2} y \tau_{PE} \quad (5.13)$$

$$\Delta\phi = \gamma \Delta G_y y \tau_{PE} \quad (5.14)$$

where  $\Delta G_y$  is the strength of the phase encoding gradient step and  $\tau_{PE}$  is its duration. This phase difference does not depend on  $\Delta B_0$ . Thus with

conventionally acquired non-EPI acquisition techniques image distortion is only problematic in the FE direction.

### 5.1.2 Off-Resonant Field Effects in EPI

In a single shot GE EPI sequence every line of k-space is acquired during a single TR period. This enables very rapid multi-slice acquisitions to be carried out (Figure 5.1) and allows MRI to be used for functional imaging with a relatively high temporal resolution. However, as a result of the way that the data are acquired, EPI is very susceptible to distortion artefacts brought about by magnetic field inhomogeneities. This can be problematic when registering EPI images to those created using conventional acquisition sequences such as MPRAGE, which are less susceptible to field inhomogeneity related distortions.

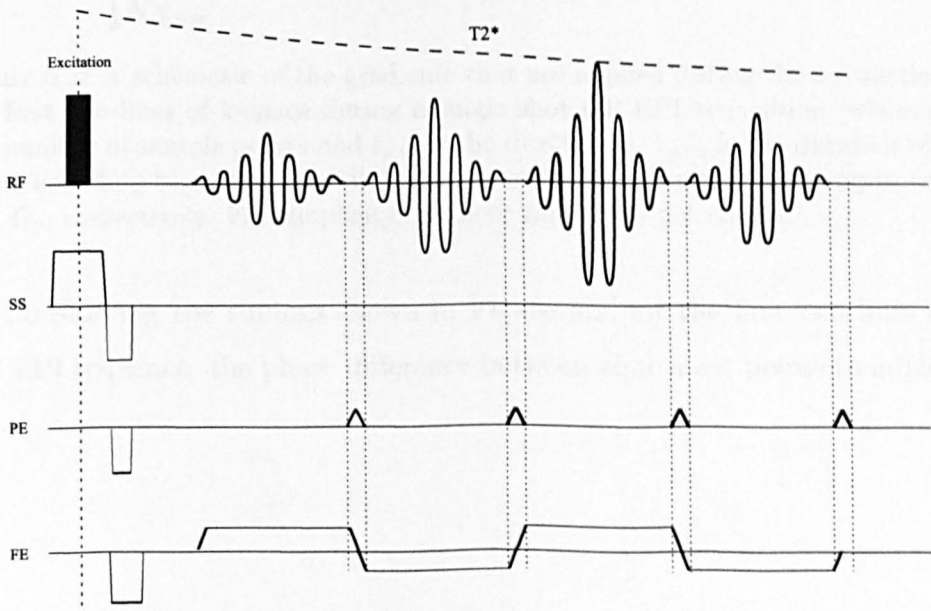


Figure 5.1: A blipped GE EPI acquisition sequence. The time to acquire one slice can be <100 ms.

In single shot EPI, any phase evolution that occurs, due to the presence of  $B_0$  inhomogeneities, continues across different lines of k-space (Figure 5.3)

(in a standard non-EPI acquisition the phase is generally reset between the acquisition of successive k-space lines). This continuous evolution of phase generates a significant phase difference between adjacent lines of k-space, resulting in severe  $\Delta B_0$  related image artefacts.

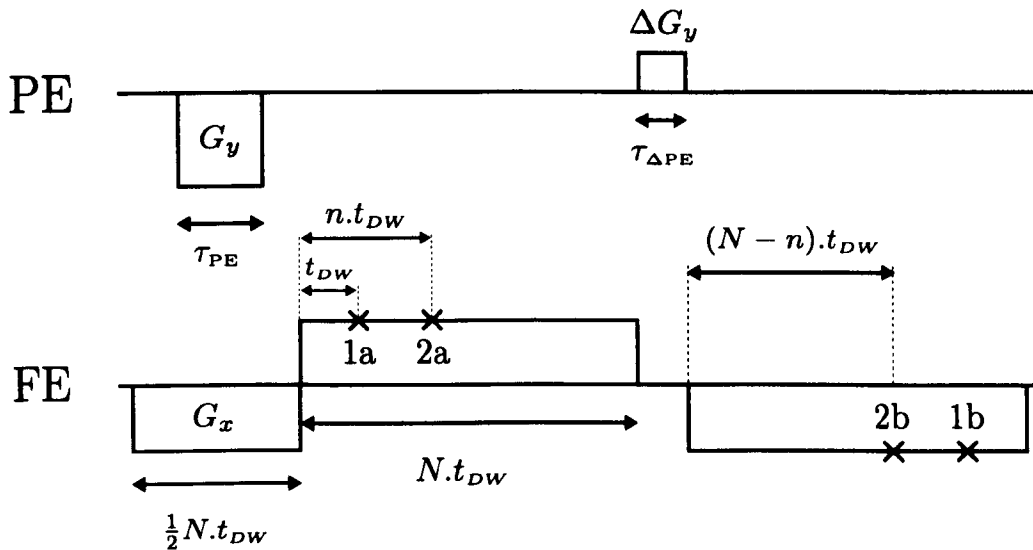


Figure 5.2: A schematic of the gradients that are applied during the acquisition of the first two lines of k-space during a single shot GE EPI acquisition, where  $N$  is the number of sample points and  $t_{DW}$  is the dwell time.  $\tau_{\Delta PE}$  is the duration of the phase encoding blip. The read and phase encoding gradients have strengths of  $G_x$  and  $G_y$ , respectively. For simplicity, gradient ramps are not shown.

Considering the timings shown in Figure 5.2, for the first two lines of a GE EPI sequence, the phase difference between equivalent points in adjacent

lines of k-space is given by :

$$\begin{aligned}\phi_{2a} = \gamma & \left[ G_x x \left( n t_{DW} - \frac{N t_{DW}}{2} \right) \right. \\ & - G_y y \tau_{PE} \\ & \left. + \Delta B_0 \left( \frac{N t_{DW}}{2} + n t_{DW} \right) \right] \quad (5.15)\end{aligned}$$

$$\begin{aligned}\phi_{2b} = \gamma & \left[ G_x x \left( N t_{DW} - \frac{N t_{DW}}{2} - (N-n) t_{DW} \right) \right. \\ & - G_y y \tau_{PE} + \Delta G_y y \tau_{\Delta PE} \\ & \left. + \Delta B_0 \left( \frac{N t_{DW}}{2} + \tau_{\Delta PE} + N t_{DW} + (N-n) t_{DW} \right) \right] \quad (5.16)\end{aligned}$$

$$\Delta\phi = \gamma \left[ \Delta G_y y \tau_{\Delta PE} + \Delta B_0 \left( \tau_{\Delta PE} + 2(N-n) t_{DW} \right) \right] \quad (5.17)$$

Due to the way that k-space is sampled during an EPI acquisition, every other line of k-space has to be reversed before reconstruction (Figure 5.3): i.e. the first point that is sampled during acquisition of the first line of k-space is equivalent to the last point that is sampled during acquisition of the second line of k-space. This can be seen in Figure 5.2 and has been taken account of in the derivation of Equation 5.17.

The phase difference between the points where  $k_x$  is equal to zero in successively sampled lines of k-space, is then:

$$\Delta\phi = \gamma \left[ \Delta G_y y \tau_{\Delta PE} + \Delta B_0 \left( \tau_{\Delta PE} + N_x t_{DW} \right) \right], \quad (5.18)$$

which can be written as:

$$\Delta\phi = \gamma \Delta G_y y' \tau_{\Delta PE}, \quad (5.19)$$

where

$$y' = y + \frac{\Delta B_0}{\Delta G_y} \left( \frac{\tau_{\Delta PE} + N_x t_{DW}}{\tau_{\Delta PE}} \right). \quad (5.20)$$

If the FOV and matrix size in the y direction are given by  $L_y$  and  $N_y$  respectively, then the voxel size,  $\Delta y$ , is given by:

$$\Delta y = \frac{L_y}{N_y}, \quad (5.21)$$

and knowing that:

$$L_y = \frac{1}{\Delta k_y}, \quad (5.22)$$

we get:

$$\Delta y = \frac{1}{N_y \Delta k_y}, \quad (5.23)$$

Then assuming linear gradients are used, we get the following:

$$\Delta k_y = \Delta G_y \tau_{\Delta PE} \quad (5.24)$$

$$\Delta y = \frac{1}{N_y \Delta G_y \tau_{\Delta PE}}, \quad (5.25)$$

Substituting this definition into Equation 5.20 provides:

$$y' = y + \Delta B_0 N_y (\tau_{\Delta PE} + N_x t_{DW}) \Delta y \quad (5.26)$$

Since the gradient bandwidth per pixel is given by:

$$BW_{PE,pix} = \frac{1}{N_y \Delta t_{PE}} \quad (5.27)$$

$$= \frac{1}{N_y (\tau_{\Delta PE} + N_x t_{DW})}, \quad (5.28)$$

the magnitude of the  $\Delta B_0$  induced distortions in the PE direction can be determined:

$$y' = y + \frac{\Delta B_0}{\text{BW}_{\text{PE,pix}}} \Delta y \quad (5.29)$$

Using a similar derivation, the distortions in the FE direction can be described by:

$$x' = x + \frac{\Delta B_0}{\text{BW}_{\text{FE,pix}}} \Delta x \quad (5.30)$$

Since the bandwidth in the PE direction is much less than in the FE direction, the distortions in an EPI acquisition are much more severe in the PE direction.

In single shot EPI, image artefacts in the FE direction occur in the same way as described for conventional imaging sequences (as described by Equation 5.30). The absolute size of the distortions in both the FE and PE direction for a typical GE EPI sequence, used for functional imaging at 7 T, will now be calculated, using some of the sequence parameters in Table 5.1. Using

matrix size	64 x 64
$\tau_{\Delta PE}$	390 $\mu s$
FE bandwidth	3000 Hz/pix
PE bandwidth	40 Hz/pix
$\Delta B_0$	100 Hz
dwell time ( $t_{DW}$ )	5.2 $\mu s$

Table 5.1: Typical scan parameters for a single shot EPI sequence at 7T

Equation 5.30 the distortion in the FE direction will be :

$$x' = x \left[ 1 + \frac{100}{3000} \right] \Delta x \quad (5.31)$$

$$x' = x + 0.033 \Delta x \quad (5.32)$$

Similarly, using Equation 5.29, the distortions in the PE direction will be:

$$y' = y \left[ 1 + \frac{100}{40} \right] \Delta y \quad (5.33)$$

$$y' = y + 2.5 \Delta y \quad (5.34)$$

These shifts equate to a displacement of 0.033 pixels in the FE direction and 2.5 pixels in the PE direction; highlighting the importance of distortion correction in the PE direction.

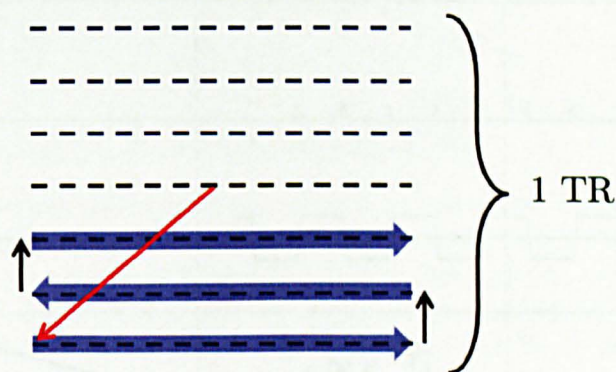


Figure 5.3: Continuous phase evolution in EPI. Each subsequent line of k-space is sampled in the opposite direction

SE EPI sequences are also susceptible to  $\Delta B_0$ -induced image distortions, but are less affected by signal dropout than GE EPI due to the refocusing effect of the 180° RF pulse. A schematic representation of a SE EPI acquisition can be seen in Figure 5.4.

A number of different techniques can be employed to correct for off-resonance effects. Generally the first step will involve reducing the large length scale variations in  $B_0$  by shimming the magnet more effectively. The scope of this technique for correcting for the effects of more rapidly changing field offsets is fundamentally limited by hardware constraints. In a typical case, accurate shimming can only be implemented within a small ROI inside the FOV and can only correct for first, second or third order spatial variations of the field (at best). Higher order variations, such as those due to the susceptibility

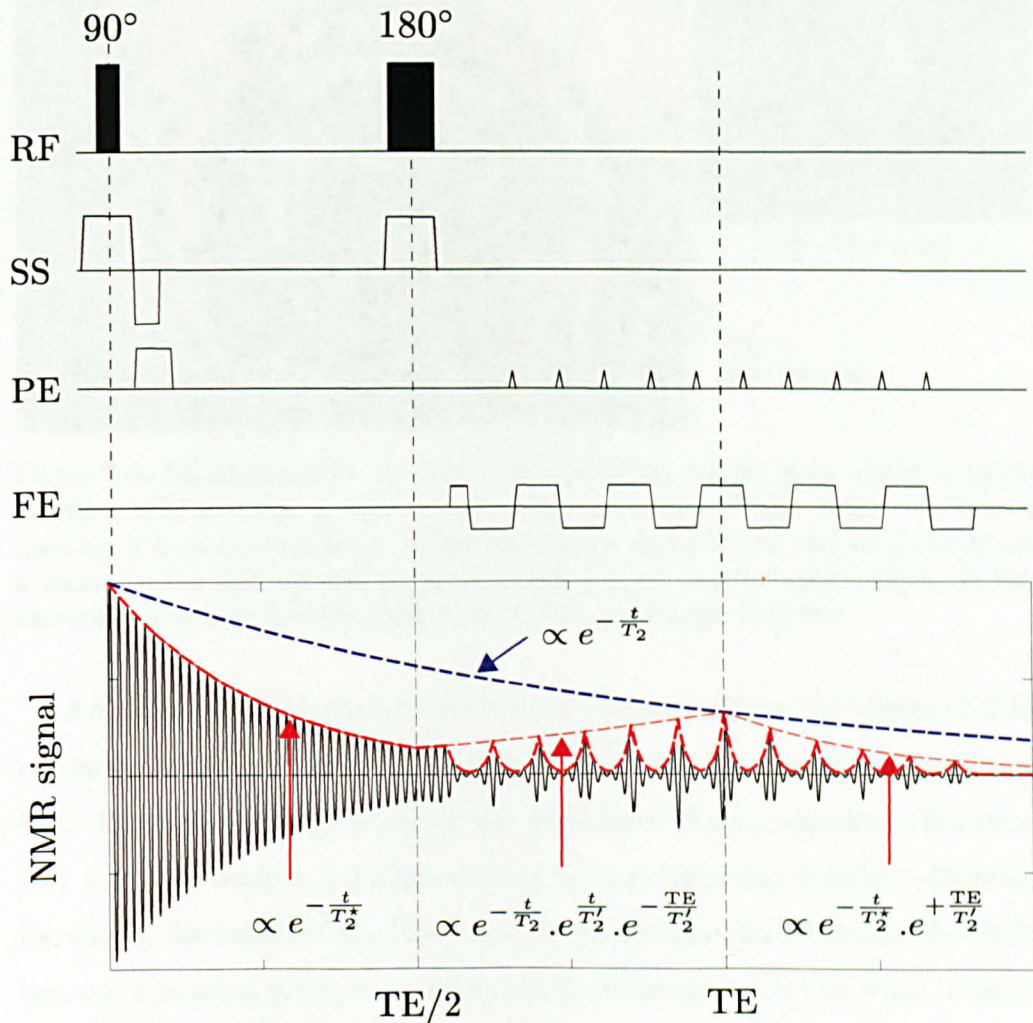


Figure 5.4: A SE EPI sequence with blipped phase encoding gradients. A Matlab simulation of the resulting NMR signal envelope is also shown. During time  $t=0$  to  $t=TE/2$  the signal decays due to both  $T_2$  and  $T'_2$  effects (i.e.  $T_2^*$ ). From time  $TE/2$  to  $TE$  the  $T'_2$  effects are reversed, whilst  $T_2$  decay continues. At time  $TE$  the dephasing effects of  $T'_2$  are completely reversed. For  $t > TE$  the signal decreases exponentially due to  $T_2^*$  effects. The dephasing and rephasing effects of the readout gradients are also shown

differences between different tissue types can't be completely corrected using typical shim coils (Figure 5.5)

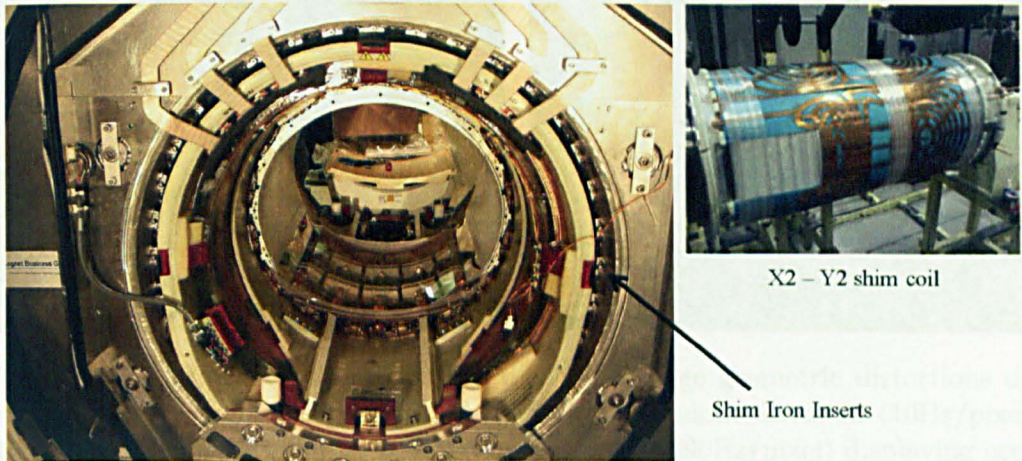


Figure 5.5: Shimming methods. Left : shim iron inserts are often added to newly installed MRI scanners to reduce  $\Delta B_0$  inhomogeneities. Right: Shim coils can be used on a scan by scan basis to further reduce these effects and to some extent account for the field altering properties of the object that is being imaged. In this example a non-standard shoulder slotted shim coil design is shown.

Another effective technique that can be used to reduce the effects of  $\Delta B_0$  inhomogeneities is to increase the bandwidth of the imaging gradients (Figure 5.6). If we consider the phase of the MR signal during sampling (Equation 5.7) then it is easy to see that as  $G \Rightarrow \infty$  the distortion vanishes. However increasing the bandwidth of the encoding gradients also decreases the SNR, because the noise power is uniform across frequencies, and so when a larger bandwidth is employed the overall amount of noise is increased. In Figure 5.6 the reduced distortion but increased noise, produced by increasing the bandwidth in the read direction, is clearly evident. This increase in noise limits the scope of this technique.

A number of methods have been developed by various groups that allow distortion artefacts to be corrected using post-processing steps. A selection of these will be described in the following section.

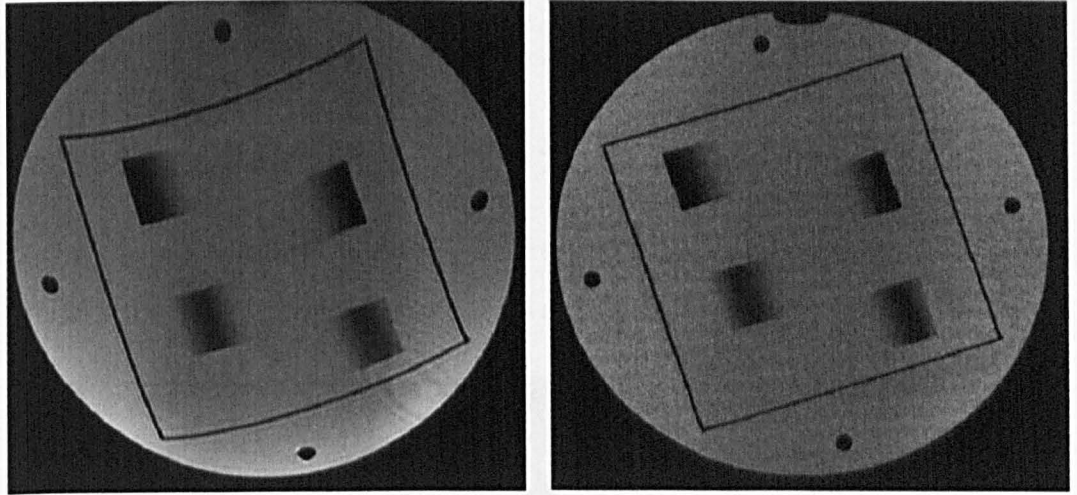


Figure 5.6: Left: Image of a phantom displaying large geometric distortions due to employing a deliberately low bandwidth in the readout direction (10Hz/pixel). Right: High bandwidth image of the same phantom (390Hz/pixel) displaying accurate geometry but with reduced SNR. The images were acquired using a standard non-EPI GE sequence. Consequently, in this example, the distortions are in the FE direction (top-bottom in the image)

### 5.1.3 Phase Information

The amount of phase evolution that occurs during a GE acquisition depends, amongst other things, upon the integral of the field strength over time (minus the reference field strength). This depends on a number of factors, such as the gradient history and  $\Delta B_0$  (see Equation 2.58). Consequently, it is possible to measure  $\Delta B_0$  by acquiring two images, using the same imaging gradients, but different echo times, and then subtracting the phase of one image from the other (Jezzard & Balaban 1995). From Equation 2.58, it can be seen that if the imaging gradients are kept the same, but the echo time is changed the subtraction of two phase images will give:

$$\Delta\phi = \gamma\Delta B_0\Delta TE. \quad (5.35)$$

Making it possible to determine  $\Delta B_0$ :

$$\Delta B_0 = \frac{\Delta\phi}{\gamma\Delta TE} \quad (5.36)$$

An example slice from a single shot GE EPI acquisition, along with a  $\Delta B_0$  map measured using this technique, is shown in Figure 5.7.

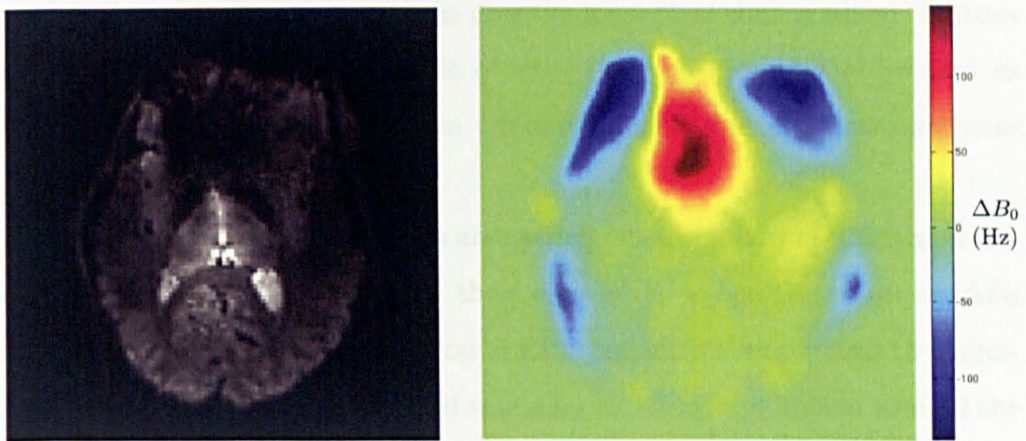


Figure 5.7: Left: A slice from a single shot GE EPI acquisition. Right: The corresponding  $\Delta B_0$  map; calculated by subtracting the phase from two images with different echo times ( $\Delta TE = 3$  ms). The data were acquired with a 2mm isotropic resolution, a matrix size of  $112 \times 112$  and a SENSE acceleration factor of 2 in the PE direction. The PE direction is Left-Right in these images.

This dual echo time technique can only be used for GE acquisitions because the refocusing effect of the  $180^\circ$  RF pulse in a SE acquisition removes the  $\Delta B_0$  information from the phase data.

#### 5.1.4 Image Artefact Correction Strategies

Once we have a  $\Delta B_0$  map it can be used to generate a pixel shift map by comparing the size of the frequency offset per pixel to the bandwidth per pixel of the encoding gradients. This can be used to transform a distorted image into undistorted space on a voxel-by-voxel basis. Correcting for distortion alone is not the best method of achieving an accurate representation of the

true image due to signal dilution/concentration effects. This occurs when the signal emanating from a voxel is spread, due to the encoding process, across a region that is either larger or smaller than the size of the region that it actually originated from, because of spatially varying field inhomogeneities. Jezzard & Balaban (1995) developed a technique to correct for this by calculating the gradient of the pixel shift map and then multiplying the intensity of each pixel in the image by a factor of one plus the local pixel shift gradient. Hutton et al. (2002) suggest that this type of intensity correction should be used as standard, but note that in certain circumstances it can also increase noise levels.

Most  $\Delta B_0$  mapping techniques are carried out using non-EPI GE anatomical acquisition sequences, due to their high SNR. When the resulting  $\Delta B_0$  maps are used for artefact correction of EPI sequences this can lead to a number of problems, for example signal smearing artefacts can appear around the edge regions of the images after the correction has been carried out. This occurs because in this situation,  $\Delta B_0$  maps are measured in undistorted space whereas the EPI data are encoded in distorted space. Thus, the value of the measured  $\Delta B_0$ , at a given voxel location in the  $\Delta B_0$  map, does not represent the true  $\Delta B_0$  value for the corresponding pixel location in the EPI map. If this effect is not accounted for it will reduce the accuracy of the correction technique and, more problematically, mean that the edge regions of the EPI data may lie outside of the regions of measured  $\Delta B_0$  values. The random phase readings that are recorded from outside of the object, due to the lack of signal, will produce meaningless  $\Delta B_0$  values and can lead to signal smearing artefacts at the edge of the image. Similar artefacts can also occur if there is subject motion between the acquisitions of the field map and the EPI data. One method of reducing this effect is to first self distort the  $\Delta B_0$  map before employing it for distortion correction of the EPI data. To overcome some of these problems, Jezzard & Balaban (1995) describe a technique where

they mask the  $\Delta B_0$  map, by thresholding the modulus image data, and then fit a polynomial inside the mask region. They extrapolate the polynomial fit to cover the regions outside of the mask, to remove edge discontinuities whilst forcing the fit to decay slowly to zero when outside of the mask. Their methodology helps allow these maps to be used for distortion correction when small movements are present.

An alternative approach to eliminating this problem is to use an EPI sequence to measure  $\Delta B_0$ , ensuring that the same encoding gradient bandwidths are used as are employed in the acquisition that needs distortion correction, so that the resulting  $\Delta B_0$  maps are in the same distorted space. Due to the speed at which EPI acquisitions can be acquired it is possible to scan multiple volumes and average them together to increase SNR in the same acquisition time that a conventional non-EPI generated field map can be acquired; alleviating the problem of reduced SNR when using an EPI acquisition.

### **Simulated Phase Evolution Rewinding (SPHERE)**

Kadah & Hu (1997) developed a technique that allows both distortion correction and intensity correction to be carried out in one step. When an object  $f(v)$  is imaged in the presence of  $B_0$ -field inhomogeneities, using an EPI sequence, the Fourier encoding process can be described by:

$$D(k) = \int f(\mathbf{v}) e^{i2\pi\gamma\Delta B_0 t(k)} e^{-i2\pi\mathbf{k}\cdot\mathbf{v}} dv, \quad (5.37)$$

where  $t(k)$  is the sampling time. The extra encoding term causes the reconstructed image to be distorted from its true shape by an amount dependent upon the size of the local  $\Delta B_0$ . Kadah & Hu (1997) proposed a method called simulated phase evolution rewinding that corrects for this by effectively reversing the effect of this additional exponential encoding term, using the following

transformation:

$$\hat{D}(k) = \int \hat{f}(\mathbf{v}) e^{-i2\pi\gamma\Delta B_0 t(k)} e^{-i2\pi\mathbf{k}\cdot\mathbf{v}} dv, \quad (5.38)$$

where  $\hat{f}$  is an approximation of the undistorted image (i.e. the distorted image). Fourier transformation of  $\hat{D}(k)$  yields a distortion corrected image. The  $\Delta B_0$  map that is needed for this technique to work can be calculated using a technique such as the dual echo time technique described earlier. The major benefit of this method is that the intensity values in the corrected image are inherently corrected for signal dilution/concentration effects without having to make error-prone calculations of the gradient of the pixel shift map.

### 5.1.5 Dynamic Correction

All of the distortion correction techniques that have been described so far rely on the assumption that the  $\Delta B_0$  field is stationary. However this is not always the case. If a subject moves in the scanner the  $\Delta B_0$  field, which depends on the orientation and location of the subject, will change. Most correction techniques rely on the assumption that the  $\Delta B_0$  field is temporally static and try to overcome the problems associated with such movement by fitting a polynomial to the measured field map that decays towards zero in the regions outside of the imaged object. This has two main consequences. Firstly it reduces the effect of high spatial frequency changes, effectively smoothing the field map. Secondly, it reduces the severity of signal smearing/dropout that can occur at air-tissue interfaces when there has been motion after the  $\Delta B_0$  map was recorded. This is because the technique effectively smears the  $\Delta B_0$  map so that the regions outside of the body have defined  $\Delta B_0$  values, and as a consequence movement of the patient is less problematic. However the technique is not ideal because, assuming there is a high enough SNR, the higher spatial frequency terms in the  $\Delta B_0$  map may represent a true

local change in the magnetic field that could have arisen due to the local proximity of two tissue types with large magnetic susceptibility differences, such as at air-tissue or tissue-bone interfaces. This is especially problematic when imaging at high magnetic field strength (Chen & Wyrwicz 1999) and in functional studies; where a large number of dynamics are recorded whilst a subject is performing some task, such as a motor task, which can induce head motion. Further, this technique also assumes that the  $\Delta B_0$  field is fixed in scanner space, when in fact a significant component of the  $\Delta B_0$  field is created due to the presence of the object in the scanner and as such will move with it.

As a consequence of these effects, it is desirable to have a  $\Delta B_0$  mapping technique that can be carried out on a regular basis throughout a scanning session without adding significant amounts of time to the length of the session. A number of techniques have been described in the literature that can be used for dynamic distortion correction (Chen & Wyrwicz 1999, Zeng et al. 2004), however they also significantly increase the overall acquisition time, which can be problematic in fMRI studies. One approach is to alter the echo time of each volume in the sequence so that the phase from two consecutive volumes can be subtracted to generate dynamic field maps. However in order to create useful field maps using the phase information from just two EPI images the  $\Delta TE$  would have to be at least 3 ms (shown in the next section) which would also produce a significant change in the contrast of the two images, severely limiting the practicality of its use in most fMRI studies, since this contrast change would likely confound most functional analysis techniques.

Lamberton et al. (2007) describe a technique to overcome this problem that makes dynamic distortion correction possible during functional experiments, without increasing the overall acquisition time. By careful consideration of the origins of phase contrast information, de Moortele et al. (2005) describe

how the phase in an MR image can essentially be represented by:

$$\phi = \phi_{coil} + \phi_{B_1} + \phi_{\Delta B_0} + \phi_{residual} \quad (5.39)$$

where  $\phi_{coil}$  is a phase term brought about due to the RF receiver coil,  $\phi_{B_1}$  is the phase due to the properties of the RF transmission pulse,  $\phi_{\Delta B_0}$  is the phase associated with magnetic field inhomogeneities and  $\phi_{residual}$  takes into account any remaining residual phase. Lamberton et al. (2007) simplify this representation by assuming that the voxel-by-voxel phase in an image ( $\phi$ ), can be modelled as having two components, an essentially static, non  $\Delta B_0$  dependent term, ( $\phi_0$ ), and a potentially time varying, dynamic  $\Delta B_0$  dependent term ( $\phi_1$ ):

$$\phi = \phi_0 + \phi_1 \quad (5.40)$$

where,

$$\phi_1 = \gamma \Delta B_0 t \quad (5.41)$$

Thus, to calculate the time varying field offset  $\Delta B_0(t)$  from a measurement of  $\phi$ , the  $\phi_0$  term has to be accounted for.  $\phi_0$  is brought about due to a number of factors such as the RF field, bandpass filters and inaccurate k-space centering (Lamberton et al. 2007, de Moortele et al. 2005), as well as static field inhomogeneity effects. Non-centred k-space can occur due to pulse timing errors, eddy currents and imperfect encoding gradients. All these  $\phi_0$  factors are independent of the imaged object and can introduce phase variations across all three dimensions.

It is possible to measure  $\phi_0$  by calculating  $\Delta B_0$  using a dual echo time

technique:

$$\phi_0 = \phi - \gamma \Delta B_0 TE \quad (5.42)$$

Once calculated, this can be subtracted from the phase images produced during a dynamic EPI acquisition sequence (see Figure 5.8) so that distortion maps can be generated on a dynamic basis:

$$\Delta\omega(t) = \frac{\phi(t) - \phi_0}{TE} \quad (5.43)$$

One disadvantage of this technique is that the phase images require complicated and time consuming spatial and temporal unwrapping, temporal unwrapping is needed to ensure there are no large phase jumps between dynamics.

Lamberton et al. (2007) use a small smoothing kernel on the  $\phi_0$  map, to increase the stability of the technique in the presence of motion, and then carry out 3rd order polynomial fitting. This is likely a sound approximation because due to its nature  $\phi_0$  should be a smoothly varying function.

In more recent work, Hahn et al. (2009) describe a modification to the method devised by Lamberton et al. (2007) that removes the necessity for phase unwrapping. In their technique they calculate the difference between the resonance offset between each dynamic and the average resonance offset of all the dynamics: If two complex images  $I_1$  and  $I_2$ , are acquired at echo times of  $TE_1$  and  $TE_2$  respectively, then the phase of each image can be calculated by taking the complex argument:

$$\arg(I_1) = \phi_1 = \phi_0 + \Delta\omega \cdot TE_1 \quad (5.44)$$

$$\arg(I_2) = \phi_2 = \phi_0 + \Delta\omega \cdot TE_2, \quad (5.45)$$

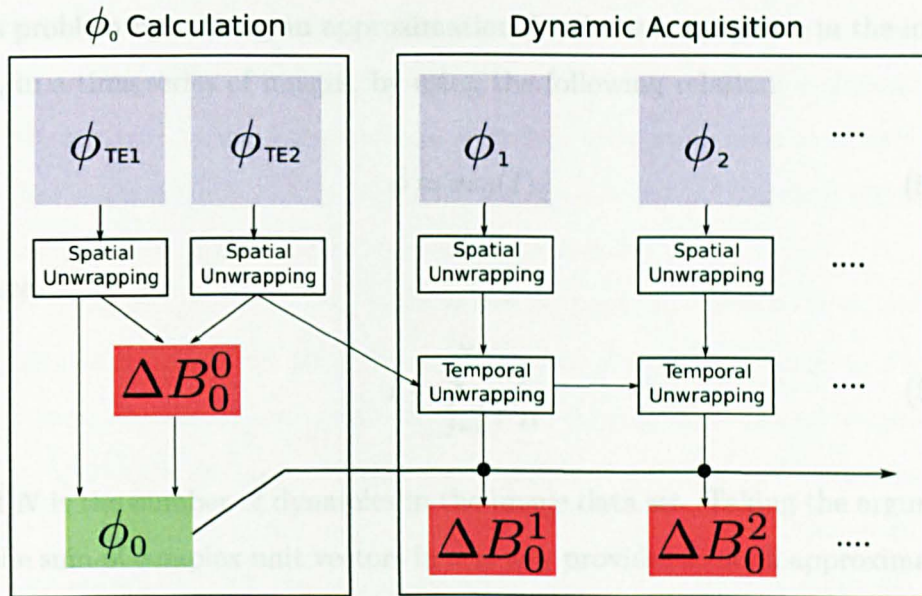


Figure 5.8: Dynamic field mapping technique, modified from Lamberton et al. (2007).  $\Delta B_0^0$  is the static field inhomogeneity, and  $\phi_0$  is the static phase component.  $\Delta B_0^n$  is the dynamic component of the field inhomogeneity at time point  $n$ , and  $\phi_n$  is the corresponding dynamic component of the phase.

such that

$$\arg(I_2) - \arg(I_1) = \Delta\omega \cdot \Delta TE, \quad (5.46)$$

where  $\Delta TE = TE_2 - TE_1$ . Equation 5.46 can then be recast as:

$$\Delta\omega = \frac{\arg(I_2 I_1^*)}{\Delta TE}, \quad (5.47)$$

where the \* represents the complex conjugation. If the  $\phi_0$  component is represented as a hypothetical complex image,  $I_0$ , acquired with an echo time of 0, then we get the solution described by Lamberton et al. (2007):

$$\Delta\omega(t) = \frac{\arg(I_1(t) \cdot I_0^*)}{TE} \quad (5.48)$$

However as mentioned earlier, this technique requires complicated spatial and temporal unwrapping. Hahn et al. (2009) describe a technique to overcome

this problem by making an approximation for the average phase in the image ( $\bar{\phi}$ ), in a time series of images, by using the following relation:

$$\bar{\phi} \approx \arg(\bar{I}), \quad (5.49)$$

where

$$\bar{I} = \sum_{j=1}^N \frac{I_j}{|I_j|}, \quad (5.50)$$

and  $N$  is the number of dynamics in the image data set. Taking the argument of the sum of complex unit vectors in this way provides a rough approximation to the mean phase, provided that the maximum phase difference between dynamics isn't too large. An approximation of the average frequency offset due to magnetic field inhomogeneities can then be calculated, by subtracting  $\phi_0$ , as follows:

$$\overline{\Delta\omega} = \frac{\arg(\bar{I} \cdot I_0^*)}{TE} \quad (5.51)$$

If we define:

$$\delta\omega(t) = \Delta\omega(t) - \overline{\Delta\omega} \quad (5.52)$$

where  $\delta\omega(t)$  is the difference between the resonance offset during the  $t^{th}$  acquisition and the average resonance offset, this leads to :

$$\delta\omega(t) = \frac{\arg\left(I(t) \cdot \sum_{j=1}^N \frac{I_j^*}{|I_j|}\right)}{TE} \quad (5.53)$$

This result no longer depends on  $I_0$  and because the average phase is subtracted from the phase for each dynamic, phase unwrapping is not required, provided the difference between the phase for any given volume and the av-

erage phase is less than  $2\pi$ , which is generally true apart from in the most extreme cases. This method does not correct for static field inhomogeneity effects, but can be combined with a standard dual echo time reference scan to allow both static and dynamic effects to be corrected. An implementation of this approach is described in Sections 5.3 and 5.5.

Hahn et al. go on to test what effect dynamic distortion correction has on functional activation analysis in the presence of temporal  $\Delta B_0$  variations. They measure this for both real and simulated data using standard Magnitude-Only (MO) and the more recently developed technique of complex constant-phase (CP) activation analysis. They conclude that dynamic distortion correction improves both the accuracy and power of activation analysis when using a CP model and also, but to a lesser extent, when using a MO model. They suggest that temporally varying field inhomogeneities can remove large amounts of activation when carrying out CP analysis with only a static distortion correction regime and that the activation can be recovered when their dynamic distortion correction technique is employed. They also recommend carrying out dynamic distortion correction prior to motion correction to increase the accuracy of the motion correction.

## 5.2 Introduction

In the remainder of this chapter three studies are described. We start the first study by experimentally determining the optimum  $\Delta TE$  for an EPI based dual echo time  $\Delta B_0$  mapping acquisition at 7 T, in order to generate robust  $\Delta B_0$  maps with minimal phase wrapping. We then test the effectiveness of a number of  $\Delta B_0$  map filtering techniques, in order to reduce the impact of noise and to extrapolate  $\Delta B_0$  values to regions with insufficient SNR available for direct measurement. Following on from this, we implement a SPHERE based distortion correction technique and test its effectiveness, on phantom and human head data, in regions of both moderate and severe  $\Delta B_0$  inhomogeneity. We then implement a technique based on the work described by Lamberton et al. (2007) and Hahn et al. (2009), in order to carry out  $\Delta B_0$  mapping on a dynamic basis, and demonstrate how such a technique can be used to carry out dynamic  $\Delta B_0$  mapping and to monitor field variations, during a functional hyperoxia experiment. Looking at field changes that occur, due to increased oxygen levels in the sinuses, during periods of hyperoxia.

Building on the work from the first study, the second study in this chapter describes the development stages and subsequent testing of a unique solution that enables dynamic distortion correction of SE EPI data, by modifying a SE-EPI sequence to acquire a GE-EPI image prior to the 180° RF pulse. In this work we demonstrate how the phase of the GE data, from such a dual GE/SE EPI acquisition, can be used for dynamic field monitoring, allowing simultaneous distortion correction of both the GE and SE EPI data.

In the final study, the SPHERE technique is modified so that the phase evolution rewinding process is carried out on upsampled k-space data (as recommended by Techavipoo et al. (2007)), in order to remove the aliasing artefacts that are generated in regions of large  $\Delta B_0$  offsets, such as around the sinuses. Using this, we demonstrate how a dual GE/SE EPI sequence can be used in auditory and motor fMRI experiments to allow both GE- and

SE-BOLD based activation analysis to be carried out, with dynamic field monitoring and correction.

## 5.3 Application: Dynamic $\Delta B_0$ measurement during Hyperoxia

### 5.3.1 Introduction

When a sample composed of materials with different magnetic susceptibilities is placed in an external magnetic field, a field perturbation is created at the boundaries between regions of different susceptibilities. In in-vivo imaging experiments this effect is strongest at air-tissue interfaces, due to the paramagnetic and diamagnetic nature of oxygen and tissue respectively. Recently, a number of groups have carried out functional studies in which the partial pressure of inhaled oxygen was elevated (causing hyperoxia) in order to increase venous oxygen saturation (Rostrup et al. 1995) thus modulating the amplitude of the BOLD response. The results of these experiments have been used to estimate venous cerebral blood volume (Bulte et al. 2007, Blockley et al. 2012) and for BOLD calibration (Chiarelli et al. 2007). However, an increase in the amount of inspired oxygen causes a corresponding increase in the size of the field perturbation,  $\Delta B_0$ , in regions close to the oral cavity and sinuses. This can lead to unwanted variations in signal strength during periods of hyperoxia. It is therefore important to quantify the size of the field inhomogeneities due to variation in oxygen content of the inspired air. In this study we carry out  $\Delta B_0$  mapping on a dynamic basis to assess the nature of the  $B_0$  variations that occur during a hyperoxia functional paradigm.

### 5.3.2 Method

Five healthy subjects participated in this study (age 22-28 years; three males). Ethical approval was obtained from the University of Nottingham Medical School Ethics Committee and all subjects gave full written consent. Scanning was carried out on a 7 T Philips Achieva system, using a volume

transmit head coil and a 16-channel receive coil (Nova Medical, Wilmington MA).

End-tidal O<sub>2</sub> and CO<sub>2</sub> partial pressures were controlled and monitored using a gas delivery breathing circuit (Respiract<sup>TM</sup>, Thornhill Research Inc., Toronto, Canada).

The partial pressure of O<sub>2</sub> was modulated between the subject's baseline level of  $\sim 110$  mmHg and 500mmHg (hyperoxia). The paradigm consisted of 3 minutes of breathing normal air followed by 3 minutes of breathing air with enhanced oxygen concentration, and a final 3 minutes at normal oxygen levels. The paradigm was repeated twice.

Isocapnia was maintained throughout the experiment, at the subjects baseline level ( $\sim 40$  mmHg). A single shot EPI acquisition, covering the region from the level of the sinuses up to the top of the head (TR = 2.4s, TE = 25ms, SENSE factor = 3, voxel bandwidth in the PE direction = 41.5 Hz, 30 axial slices, 400 dynamics, 2mm isotropic resolution, matrix size 96 x 96), was performed throughout the respiratory challenge. A dual echo time EPI acquisition was also carried out (using TEs of 25 and 28ms with 10 repeats of each TE), for mapping of the static  $\Delta B_0$  field prior to the acquisition of data during the functional paradigm.

Initial tests were carried out during a separate session to calculate the optimum  $\Delta TE$  for the dual echo time EPI acquisition, using  $\Delta TE$  values ranging from 1 to 5ms. Data were acquired from a phantom and the human head. 10 repeated measurements were made at each  $\Delta TE$ , and the standard deviation of the results was then used to assess what the optimum  $\Delta TE$  was, i.e. the shortest  $\Delta TE$  that produced consistent results shot to shot. Short TEs are essential to minimise the problems associated with unwrapping  $2\pi$  phase wraps. The phantom data were acquired at 2mm isotropic resolution with 10 slices and a matrix size of 64 x 64. The human head data were acquired at 2mm isotropic resolution using a matrix size of 96x40, with the

largest dimension in the readout direction. 20 slices were acquired. The human head data results were also compared to the standard Philips, non-EPI,  $\Delta B_0$  mapping sequence ( $\Delta TE$  of 0.5 ms) at similar resolution (2.5mm x 3mm) and slice coverage (20 slices).

To reduce the effects of noise a 7th order three dimensional polynomial fit was applied to the  $\Delta B_0$  maps that were used in the hyperoxia experiment.

Dynamic phase information, collected during the hyperoxic challenge, were combined with static field measurements to construct dynamically varying absolute  $\Delta B_0$  field maps; using the technique described in Section 5.1.5 (Lamberton et al. 2007, Hahn et al. 2009). The magnitude of the voxel shifts due to hyperoxia were estimated by comparing the frequency of the hyperoxia-induced field shifts to the voxel bandwidth in the phase encoding direction.

### 5.3.3 Results

$\Delta B_0$  profiles generated using a dual echo time EPI acquisition, are shown across a phantom in Figure 5.9. In the left image,  $\Delta B_0$  profiles are shown for 5 different  $\Delta TE$ s (using  $\Delta TE$  values ranging from 1 to 5ms). The standard deviation of the field maps which were generated using  $\Delta TE$  s of 1 and 3ms are shown on the graph on the right.

$\Delta B_0$  profiles across a human head are shown in Figure 5.10.  $\Delta B_0$  values generated using both a dual echo time EPI sequence ( $\Delta TE = 3\text{ms}$ ) and a standard Philips non-EPI dual echo time technique ( $\Delta TE = 0.5\text{ms}$ ), are shown. There is little difference between the NEX = 1 and NEX = 20 EPI data, however local differences can be seen between the non-EPI and EPI data.

The effectiveness of the sphere based distortion correction algorithm (see Section 5.1) was tested by carrying out static distortion correction on phantom data. The results for this are shown in Figure 5.11. The results for distortion correction under more severe conditions are shown in Figure 5.12 (Based on

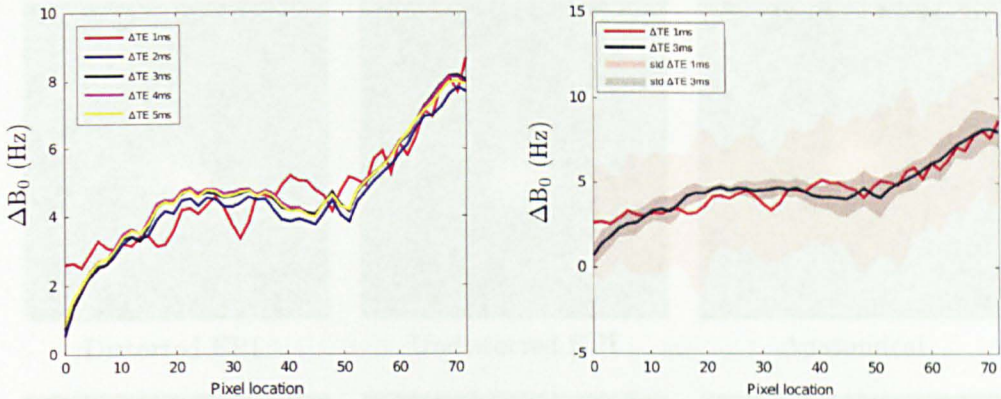


Figure 5.9:  $\Delta B_0$  profiles across a phantom. Results were produced using the average of 10 field maps, using data from a dual echo time acquisition. Left : Profiles from field maps acquired using  $\Delta TE$ s ranging from 1 to 5 ms. Right: Standard deviation of the data acquired using  $\Delta TE$ s of 1 and 3 ms.

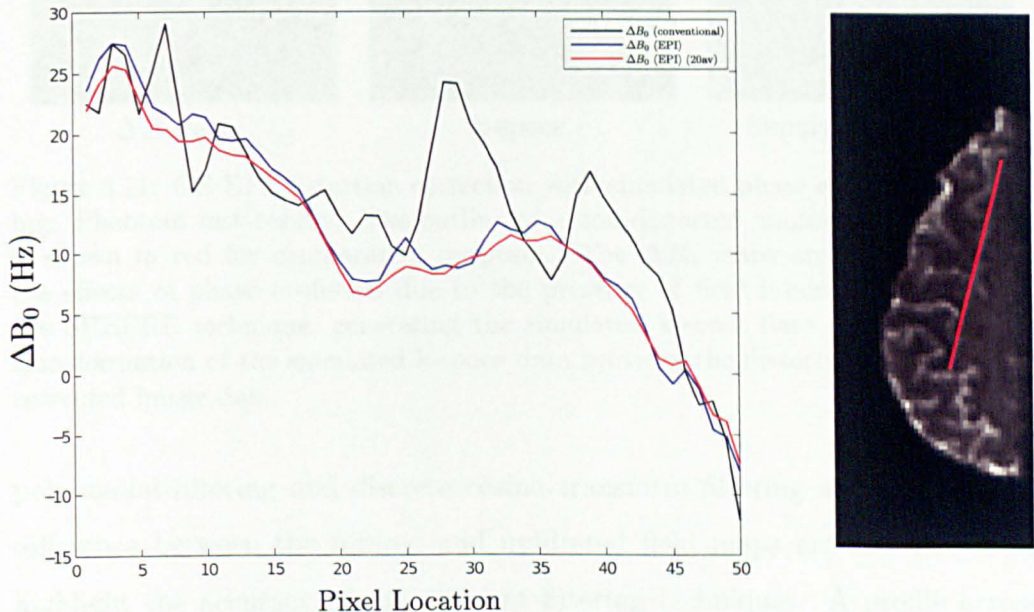


Figure 5.10:  $\Delta B_0$  profile across a human head. Results for both EPI and non-EPI dual echo time acquisitions are shown. The EPI data is shown with both no averaging (blue) and with averaging over 20 dynamics (red). The location of the profile in the head is shown by the red line in the anatomical image on the right.

data acquired using the same phantom shown in Figure 5.11).

The effects of using different filtering/fitting methods on static  $\Delta B_0$  maps, taken from human head data, using a slice taken at the level of the sinuses, are demonstrated in Figure 5.13. Results produced using median filtering,

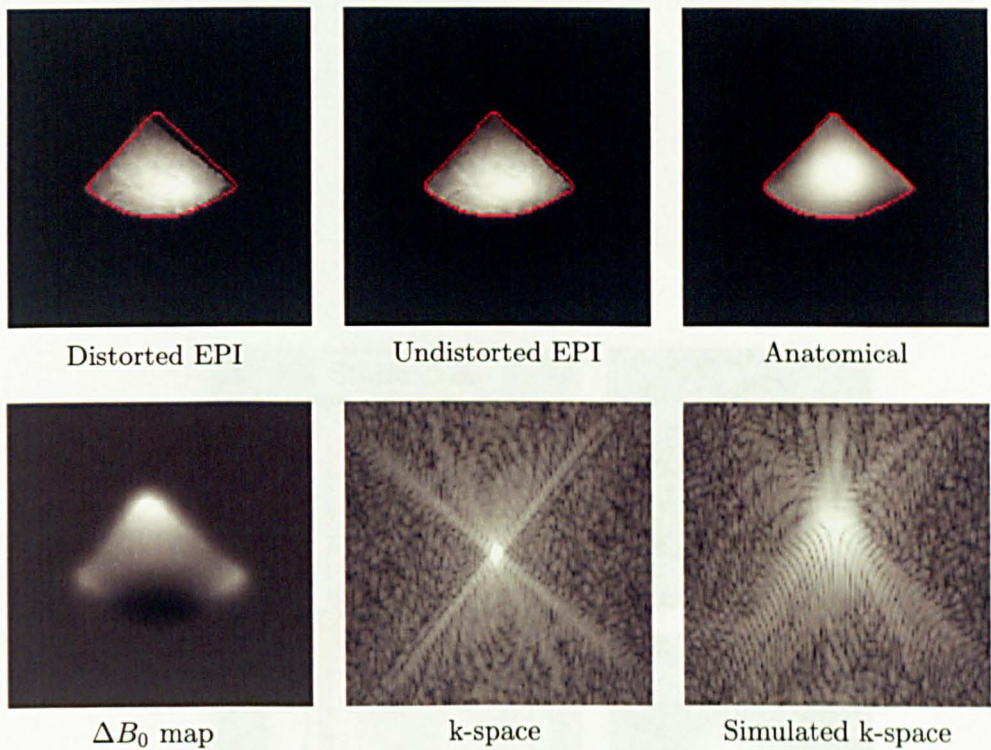


Figure 5.11: GE EPI distortion correction with simulated phase evolution rewinding: Phantom test results. The outline of a non-distorted anatomical acquisition is shown in red for comparative purposes. The  $\Delta B_0$  maps are used to rewind the effects of phase evolution due to the presence of field inhomogeneities using the SPHERE technique, generating the simulated k-space data. Inverse Fourier transformation of the simulated k-space data provides the distortion and intensity corrected image data.

polynomial filtering and discrete cosine transform filtering are shown. The difference between the filtered and unfiltered field maps are also shown to highlight the accuracy of the different filtering techniques. A profile across the sinus region is shown for each of these fits in Figure 5.14.

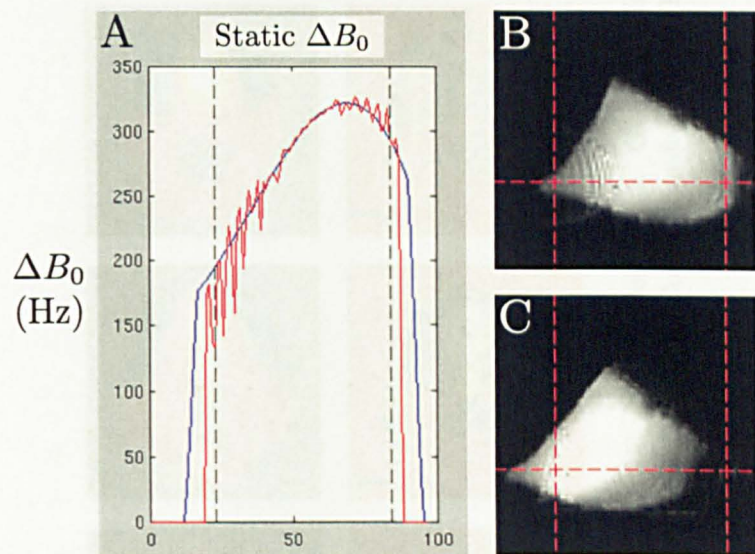


Figure 5.12: Distortion correction of phantom data. The original distorted image can be seen in **B**. The SPHERE corrected image can be seen in **C**. Signal drop out can't be corrected using this approach. A plot of the measured field inhomogeneity is also shown in **A**, the profile corresponds to the red dashed line going from left to right in the distorted modulus image in **B**. The vertical red dashed lines in **B** (and dashed black lines in **A**) represent the extremities of the  $\Delta B_0$  mask. Areas outside this region (away from the centre of the phantom) were not used during the polynomial fit, however the polynomial fits were extrapolated out away from the edges of the phantom to reduce adverse edge effects. The polynomial fits were calculated to 4th order in 2D.

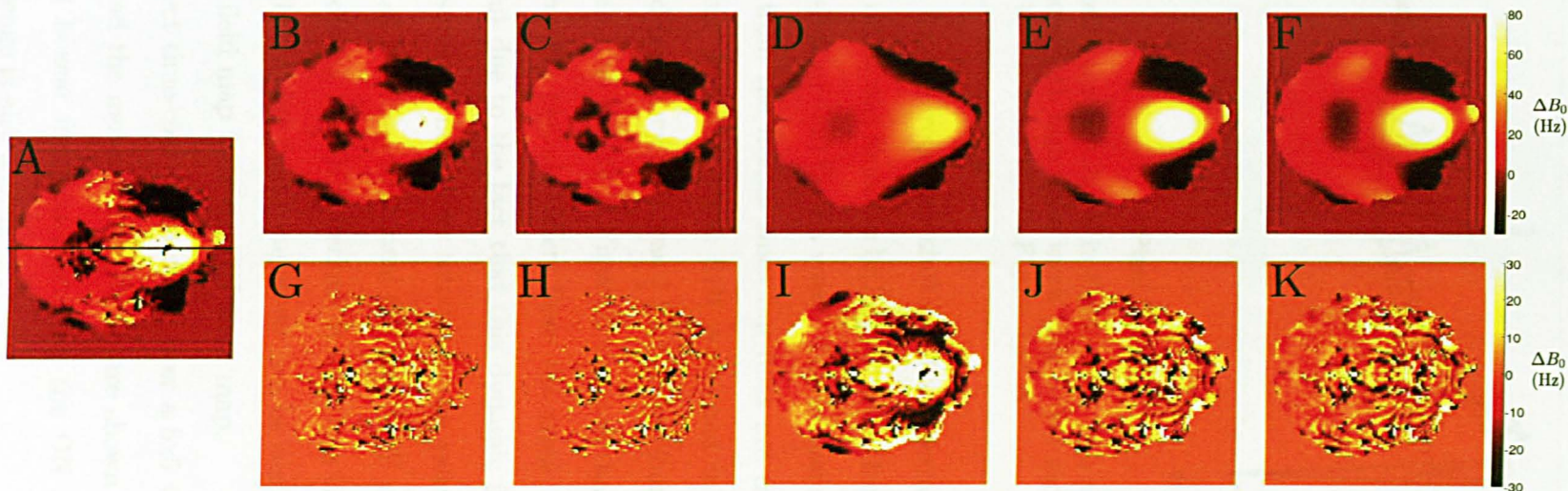


Figure 5.13: Static  $\Delta B_0$  field maps. **A**: unfiltered field map. **B - F** : filtered field maps. **G - K** : difference between filtered and unfiltered field maps. The following filters were used: **B**: 3x3 Median filter. **C**: Cosine transform filter. **D**: 4th order polynomial fit. **E**: 7th order polynomial fit. **F**: 10th order polynomial fit.

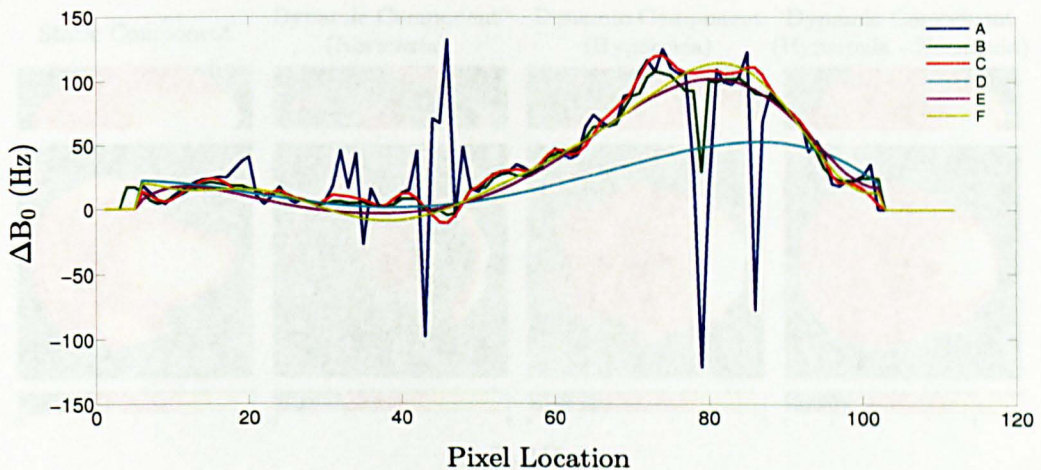


Figure 5.14: Profiles through **A** - **F** in Figure 5.13. It is clear that median filtering struggles in regions with high noise levels (due to low signal). The location of the profile is shown by the black line in Figure 5.13 **A**

The results for the frequency shift due to hyperoxia are shown in Figure 5.15. The field offset was found to be largest in the frontal sinus, up to 20 Hz, representing a shift of  $\sim 50\%$  of a voxel. The frequency offset decreases with distance away from the frontal sinus but does not drop to zero and affects the whole brain. In a  $5 \times 5$  voxel ROI positioned in the motor cortex, the hyperoxia-based frequency shift was  $3.1 \pm 0.2$  Hz (mean  $\pm$  std over subjects),  $\sim 7\%$  of a voxel. The results in Figure 5.15 show that the average field map during the normoxia periods differs from the static field component. This is brought about due to the fact that this dynamic field mapping technique effectively measures the field offset relative to the mean field offset across time (i.e. the mean of both the functional ON and OFF periods), hence the field map averaged during the OFF periods is less than the mean. However, the true dynamically varying field component can be easily found by subtracting the OFF state field map from the ON state map.

Single subject time-courses, averaged over a  $5 \times 5$  voxel ROI in the frontal sinus (black) and the motor cortex (blue) are shown in Figure 5.16. An arbitrarily scaled boxcar function describing the ON and OFF states of the hyperoxic challenge is also shown.

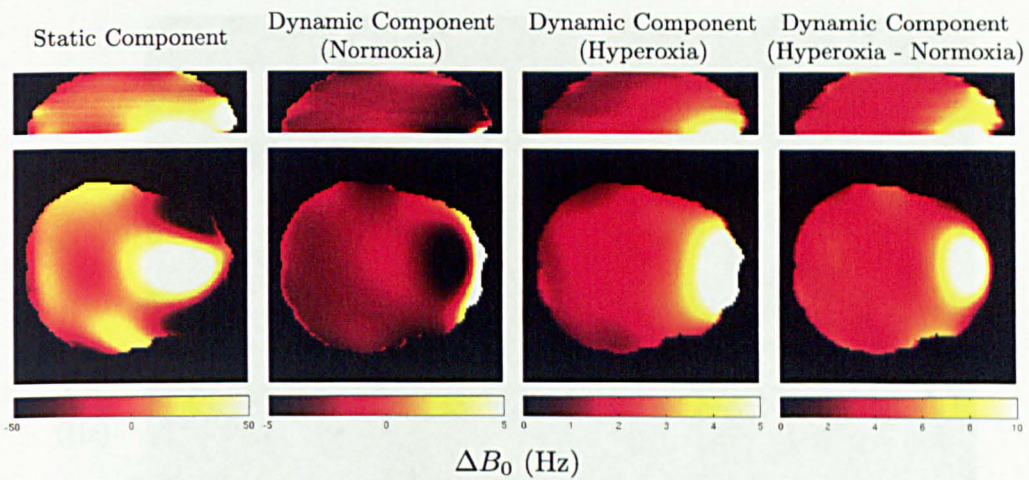


Figure 5.15:  $\Delta B_0$  field maps during normoxia and hyperoxia for an example subject. The AP direction is right to left in each image. Top row: Sagittal view. Bottom row: Axial view.

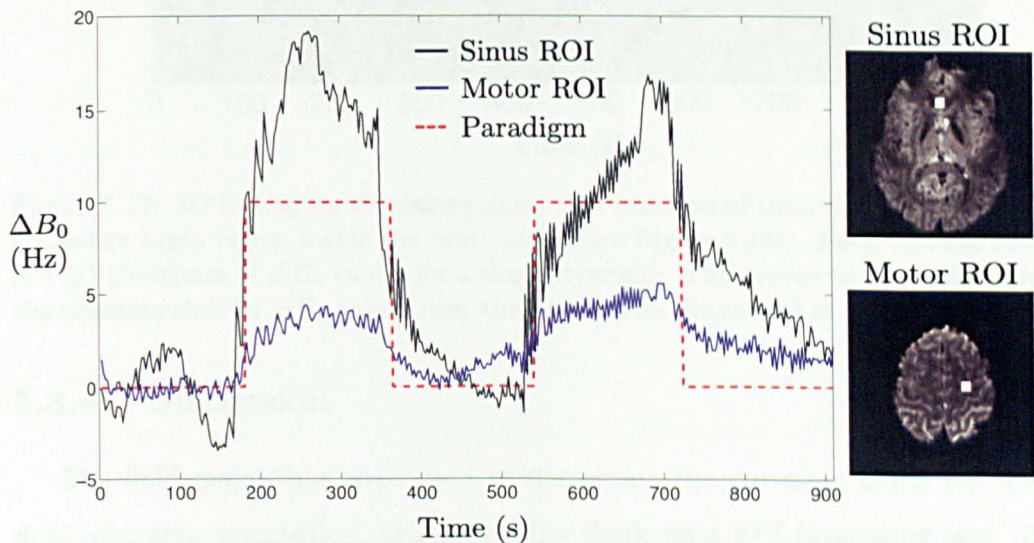


Figure 5.16: Dynamic  $\Delta B_0$  measurements in 5x5 voxel ROIs in a region close to the frontal sinuses (black) and motor cortex (blue). The functional paradigm for the hyperoxic challenge is also shown (red).

A histogram of  $\Delta B_0$  values across time is shown in Figure 5.17 for an example subject. Values were taken using data from the entire masked head region. For clarity the scaling on the y-axis has been set to clip some of the extreme  $\Delta B_0$  values.

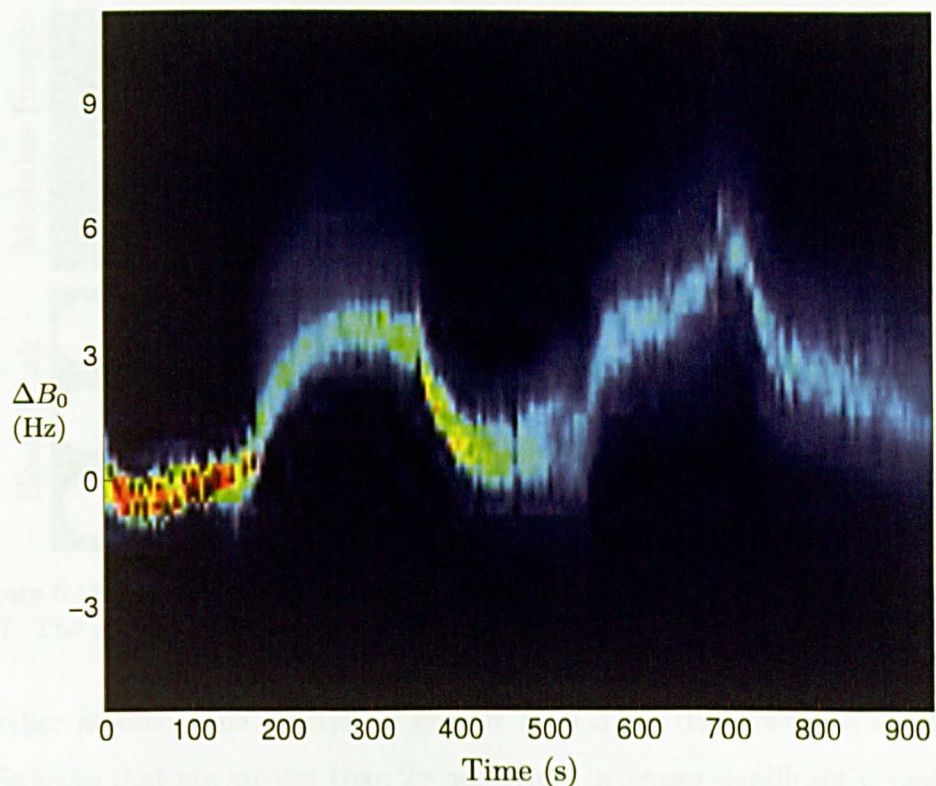


Figure 5.17: 3D histogram displaying  $\Delta B_0$  as a function of time (calculated using the entire brain region inside the brain mask (see Figure 5.18)). Each vertical line is a 2D histogram of  $\Delta B_0$  values for a single dynamic. This serves to highlight both the absolute shift in  $\Delta B_0$  values over time as well as the spread of values.

### 5.3.4 Discussion

The field maps that were used to determine the optimum  $\Delta TE$  for the dual echo time acquisition, acquired using single shot EPI (averaging over 10 dynamics), are very similar for all  $\Delta TE$ s (1 - 5 ms) (Figure 5.9). Without averaging, the field maps acquired using shorter  $\Delta TE$ s ( $< 3\text{ms}$ ) were less consistent than those based on the longer  $\Delta TE$  values ( $\geq 3\text{ms}$ ), with results varying significantly; this is shown by the large standard deviation. The data demonstrate that in order to acquire accurate field maps using single shot GE EPI at 7T, when using only a few dynamic averages (to minimise the acquisition time), it is preferential to use a  $\Delta TE$  of around 3ms. Above this value there was little improvement in the standard deviation of the results.

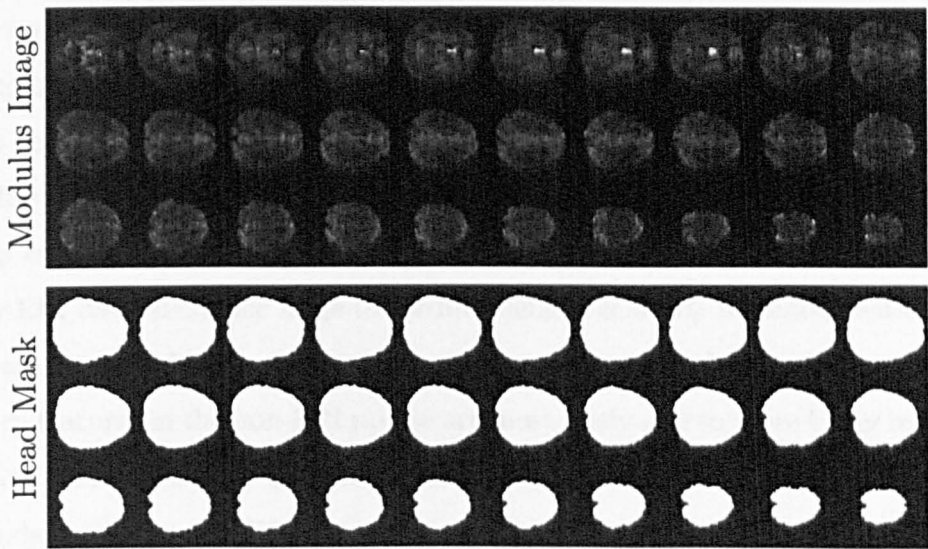


Figure 5.18: The mask region that was used for the 3D histogram data in Figure 5.17. (The modulus data are also shown.)

Further at echo time differences greater than 3 ms the likelihood of phase differences that are greater than  $2\pi$  occurring, increases significantly, making it necessary to apply phase unwrapping. In comparison, in a study at 2 T Hutton et al. (2002) found a  $\Delta TE$  of 10 - 15 ms to be optimal when using GE EPI to produce  $\Delta B_0$  maps, as a result of the smaller field inhomogeneities that are present at 2 T relative to 7 T. Indeed, simply scaling their recommended  $\Delta TE$  values by the ratio of the corresponding field strengths would equate to a  $\Delta TE$  range of 2.9 - 4.3 ms at 7 T.

To determine the difference between EPI and non-EPI based  $\Delta B_0$  maps, when using human head data, a conventional non-EPI based dual echo time GE acquisition was also carried out. The EPI field maps were created using a  $\Delta TE$  of 3 ms whereas the non-EPI data were acquired using the standard philips image acquisition technique using a  $\Delta TE$  of 0.5 ms. Figure 5.10 shows profiles across the  $\Delta B_0$  maps for both acquisition methods. The EPI based field maps show very little benefit from carrying out dynamic averaging, as predicted by using a  $\Delta TE$  of 3ms. They also show very good agreement with the data generated using the conventional non-EPI sequence. However there

are a few points where significant differences can be seen (see pixel location 30 in Figure 5.10). To some degree these differences are expected due to the fact that the EPI based acquisitions are acquired in distorted space, however such extreme differences are not expected. The results show that the  $\Delta B_0$  map created using the EPI data varies across space more smoothly than the non-EPI data and since large to medium length scale  $B_0$  inhomogeneities are generally smoothly varying functions, due to the way they are created, the sharp features in the non-EPI profile are most likely due to there being regions of low SNR. This may in part be due to the low  $\Delta TE$  that was used in the standard Philips non-EPI sequence.

The accuracy of the distortion correction technique was assessed by scanning a phantom using both a GE EPI acquisition and a conventional non-EPI based anatomical imaging sequence and comparing the resulting images before and after distortion correction (Figure 5.11). The outline of the undistorted anatomical acquisition (red) clearly highlights the severity of the distortion in the GE EPI acquisition. However redistributing k-space to rewind the effects of phase evolution, brought about due to the  $\Delta B_0$  field, provides very effective distortion correction of the EPI data. The distortion correction technique was also found to perform well in the presence of severe  $\Delta B_0$  variations, where, despite the magnitude of the distortions, accurate geometric distortion correction was still achieved (Figure 5.12). This technique cannot however correct for regions of signal dropout, such as in the bottom right corner of the phantom. Further improvements to EP acquisitions in conditions such as this, where there are large magnetic field inhomogeneities, could be accomplished by employing SE EPI, because the refocusing pulse should reduce the severity of any signal drop out. However, a side effect of using a SE acquisition with a refocusing pulse is that the  $\Delta B_0$  information in the phase data is also refocused and so cannot be used to measure  $\Delta B_0$ . A solution to this problem is developed in the next section.

To reduce the contaminating effects of noise it is important to filter the field maps. In this study we found that the optimum filtering method depended upon the severity of  $\Delta B_0$ , more specifically, on its spatial rate of change. The degree of smoothing that is required also depends upon the SNR of the data, and consequently upon  $\Delta TE$ ,  $B_0$  field strength and a number of image acquisition parameters such as voxel size. Hutton et al. (2002) assessed the standard deviation of  $\Delta B_0$  in a homogeneous region of the field map and found that the standard deviation decreased as the kernel size of a Gaussian smoothing filter was increased, but that the effect was much less pronounced when the field maps were generated using longer  $\Delta TE$  s due to the increase in SNR that occurs when longer  $\Delta TE$  s are used.

The phantom data shown in Figures 5.11 and 5.12 indicate that low order polynomial fits can effectively correct for significant distortions when they are brought about due to large, but slowly varying  $B_0$  field offsets. However when rapid spatial variations in  $\Delta B_0$  are present, such as around the sinuses, low order polynomials are ineffective (Figure 5.13). For filtering in these regions a median filtering technique can be used, however this does not work in regions of signal dropout where instead higher order polynomials should be employed. We have demonstrated that even in extreme cases, such as the region around the sinuses during a hyperoxic study (with field offsets of up to 100Hz), a 7th order polynomial fit can be used to accurately model the  $\Delta B_0$  variation (Figure 5.13). With the benefit that the fit to the field map at any point is backed up by data from across the entire brain, leading to robust estimations of the  $\Delta B_0$  field even in regions of low signal. Using even higher order polynomials provides little additional benefit and significantly increases the overall computation time and memory requirements. To improve speed and accuracy, the polynomial fitting was only applied to data within a mask region, calculated by thresholding the modulus image data, with the results then extrapolated out to cover the regions of missing signal intensity.

We also demonstrate the use of a discrete cosine transformation technique (Hutton et al. 2002) based on a robust method recently developed by Garcia (2010). This automatically determines the amount of smoothing to apply by using a generalised cross validation technique. The method provided robust multi-dimensional smoothing and allowed the high spatial frequency variations to be accurately fitted much more rapidly than with high order polynomial techniques. The discrete cosine transform technique provided very similar accuracy to the median filtering method but with the added benefit that it can provide a reasonable fit in regions with missing data, such as at pixel location 80 in Figure 5.14, where median filtering fails.

The results in this study have demonstrated the feasibility of carrying out dynamic  $\Delta B_0$  mapping during a functional MRI acquisition, a hyperoxic challenge, using just one additional reference scan. In a cross field study at 3 T and 7 T, Pilkinton et al. (2011) also mapped the change in  $\Delta B_0$  due to hyperoxia, however they were limited to collecting  $\Delta B_0$  maps during a separate functional run and with a significantly lower temporal resolution (5  $\Delta B_0$  maps for each of the functional ON and OFF periods) than the technique that has been described here (75  $\Delta B_0$  maps for each ON and OFF period). They also found the largest  $\Delta B_0$  effects in the frontal sinus.

The results demonstrate that the additional field shift due to the presence of increased oxygen in the sinuses during the hyperoxia periods extends over the whole head. The field offsets, due to hyperoxia alone, were found to be largest around the frontal sinus (up to 20 Hz), representing shifts of around 50% of a voxel. Thus over a functional run the composition of spins within a voxel, that make up the signal from the voxel as a whole, will vary significantly. Near high contrast boundaries, the shifting of the boundary in and out of the voxel could significantly alter the overall signal intensity in the voxel. This task-correlated signal change may confound the results of studies looking at how the BOLD related signal changes during hyperoxia. However, our results

also show that the frequency offset decreases quite significantly with distance away from the sinuses. In a 5x5 voxel ROI positioned in the motor cortex, the frequency shift due to hyperoxia was found to be  $3.1 \pm 0.2$  Hz (mean  $\pm$  std over subjects), representing a shift of  $\sim 7\%$  of a voxel. In the visual cortex the shift was found to be  $\sim 5\%$  of a voxel. This magnitude of shift will be less problematic, but may still confound the results of BOLD studies. Further work needs to be carried out to assess what effect such dynamic voxel composition changes will have on the data. This will likely depend upon the local anatomical structure surrounding a voxel. It may prove useful to model this using a digital phantom of the human head to determine where the effect will be most significant. It may be possible to use dynamic distortion correction, using the techniques described here, to correct for any such signal changes.

### 5.3.5 Conclusion

We have demonstrated the ability to calculate dynamic  $\Delta B_0$  maps using a dual GE EPI sequence at 7 T using just one initial reference scan. We found that an optimum  $\Delta TE$  of  $\sim 3$ ms should be used for the initial dual echo time EPI acquisition in order to maximise SNR whilst minimising the scan duration and severity of phase wrapping. We demonstrate that for accurate filtering of the resulting field maps high order (7th order or above) polynomials are required. However we also show that it is possible to use a discrete cosine transform filtering technique to cope with even higher spatial frequency variations in  $\Delta B_0$ . We demonstrate that dynamic  $\Delta B_0$  mapping can be used to monitor field variations during functional hyperoxia experiments without having to change the acquisition sequence. The results demonstrate that the additional field shift due to the presence of increased oxygen in the sinuses during the hyperoxic periods extends over the whole head. The field offsets, due to hyperoxia alone, were found to be largest in the frontal sinus, around

50% of a voxel, whilst shifts in the motor and visual cortices were found to be approximately 7% and 5% of a voxel respectively. We recommend that the techniques described here should be employed during all hyperoxia studies to monitor the induced temporal variations in  $\Delta B_0$ .

## 5.4 Development of a Dual GE / SE EPI sequence

### 5.4.1 Introduction

In a SE EPI sequence the refocusing effect of the  $180^\circ$  RF pulse removes any  $\Delta B_0$  information contained within the phase. It is therefore impossible to employ dynamic distortion correction using the methods described by Lamberton et al. (2007) and Hahn et al. (2009) for SE EPI.

Here we develop a unique solution to circumvent this problem. We describe how dynamic distortion correction can be applied to SE EPI data by modifying a SE-EPI sequence to acquire a GE image prior to the  $180^\circ$  RF pulse and by then using the phase of the GE EPI data to monitor changes in the magnetic field inhomogeneity. Since both the GE and SE images are acquired simultaneously with identical readout gradients they show the same distortions which can both be corrected. By exploiting parallel imaging we demonstrate that it is possible to incorporate the additional GE EPI sampling without increasing the echo time of the SE data to an unusable level. This type of acquisition should be of particular value in fMRI studies where the added information, due to having both GE and SE data, can be used to probe the functional nature of the BOLD response in more depth. In this section the development and testing of the modified dual GE/SE EPI acquisition that is required for this technique is described. It is then outlined how this acquisition scheme can be used for dynamic distortion correction of both GE and SE EPI data.

### 5.4.2 Method

A standard single shot SE EPI sequence consists of a  $90^\circ$  RF pulse followed by a  $180^\circ$  refocusing pulse. After the refocusing pulse a blipped EPI sampling

module is employed to encode the data in k-space. The initial FID signal, from the 90° RF pulse, is not sampled and decays away.

In the proposed modification to this sequence an additional EPI readout module is added between the 90° and 180° RF pulses to sample the FID signal so that both GE and SE EPI acquisitions can be acquired (Figure 5.19). The resulting phase information from the GE data is then used to monitor field variations to allow off-resonance artefact correction of both the GE and SE EPI data. All modifications were made to the standard Philips SE EPI acquisition using the Philips GOAL-C programming language.

The main problem that had to be addressed throughout the development of this sequence was ensuring that the sampling process of the FID did not affect the generation and sampling of the spin echo.

To ensure that the GE phase data can be used to accurately correct the  $\Delta B_0$  image artefacts of both GE and SE data, the two images have to be acquired in the same distorted space. This was accomplished by ensuring that the bandwidth (BW) of the encoding gradients were the same for both acquisitions.

It should be noted that adding additional echo-planar imaging gradients places a constraint on the minimum echo time that can be achieved for the SE EPI because hardware restrictions limit the speed at which k-space can be fully sampled. This can be problematic because if the echo time of the SE is made too long the SNR of the resulting image will be too low for it to be of use. This is a particular issue when imaging at ultra high field strength due to the reduction of  $T_2$  with increasing field, however this effect is somewhat offset by the increase in CNR at high field strength. Taking advantage of recent developments in parallel imaging and coil technology, by employing a 32 channel receive coil, allows a work-around to this problem. Having information from multiple coils allows parallel imaging to be used at high acceleration factors, whilst maintaining a robust image quality. Using

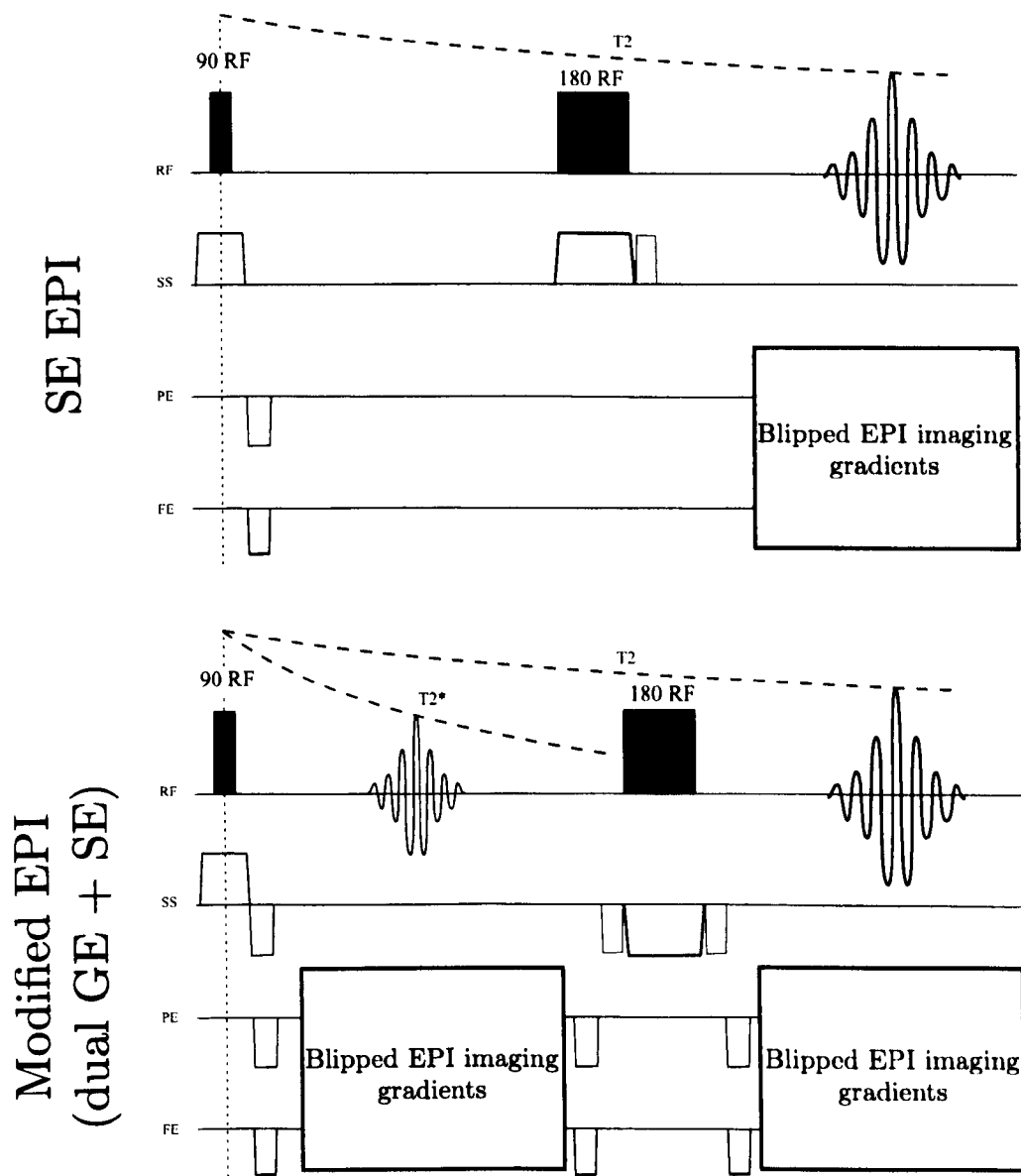


Figure 5.19: Top: Standard SE EPI sequence with blipped gradient EPI sampling. Bottom : Modified Dual echo GE / SE EPI sequence, incorporating two blipped gradient EPI sampling modules and slice selective gradient reversal. The gradients for the acquisition of the GE EPI are fully balanced.

parallel imaging in this way means that less lines of k-space have to be acquired in order to sample k-space fully, thus significantly reducing the length of the EP sampling module.

We also add inherent fat suppression to the SE acquisition by reversing

the polarity of the slice selection gradient for the 180° RF pulse, relative to that of the 90° pulse (see Section 4.3.2).

Due to the spatial variation of the applied RF field, which is exacerbated at high field, it is difficult to produce a uniform flip angle (FA) over the whole sample when applying an RF pulse. Usually any deviations away from the desired FA manifest themselves as a slight decrease in the signal strength, when imaging using a GE sequence, and so this is not normally a significant problem. However, in SE sequences any deviation of the refocusing pulse away from 180° can cause additional signal pathways to exist (Bernstein et al. 1994). These can take the form of either stimulated echoes or FIDs which can contaminate the signal from the spin echo during sampling. If these are not accounted for, the acquired data will no longer be a pure spin echo; changing the contrast of the image. Here we remove these extra pathways by applying crusher gradients either side of the 180° RF pulse. The gradient pulse applied after the 180° RF pulse dephases the FID signal, whilst the gradient pulse prior to the 180° RF pulse stops the true spin echo signal from being destroyed by the FID crusher, by reversing its effects so that the net dephasing effect on the spin echo signal pathway is zero. In the standard SE EPI sequence the first crusher is combined with the slice selection rephasing gradient. However in the modified dual GE/SE EPI sequence this is not possible as each slice has to be rephased before the GE EPI is sampled and so an extra crusher gradient had to be added in the slice selection gradient direction prior to the 180° pulse. It is generally considered that a minimum phase dispersion equivalent to  $4\pi$  is needed across the slice for adequate signal reduction to be achieved (Bernstein et al. 1994). The required crusher gradient area is given by the following expression:

$$A_R = \frac{\Delta\phi}{\gamma\Delta z}, \quad (5.54)$$

where  $\Delta z$  is the slice thickness and  $\Delta\phi$  the required phase variation. The maximum performance of the imaging gradients on the 7T Philips system (at the time of testing this sequence) was a slew rate of 166 mT/m/ms and a gradient amplitude of 33mT/m. Assuming a slice thickness of 2.5 mm gives a value of  $A_R$  of 18.8 mT.ms/m. Assuming a trapezoidal gradient waveform, the ramp and plateau times that are required to produce this are:

$$\tau_{ramp} = \frac{G}{\text{slew rate}} \quad (5.55)$$

$$\tau_{plateau} = \frac{A_R}{G} - \tau_{ramp} \quad (5.56)$$

which gives a minimum ramp time of  $\tau_{ramp} = 0.20ms$  and a minimum plateau time of  $\tau_{plateau} = 0.37ms$ . This leads to a minimum crusher gradient duration of  $0.77ms$ . Due to the importance of these calculations a number of scans were carried out using a range of gradient amplitudes to check that the calculations were correct. For this, imaging was carried out with the  $180^\circ$  RF pulse turned off so that only the signals that were generated via unwanted pathways were encoded and assessed.

## Results

A schematic of the final dual GE/SE EPI sequence is shown in Figure 5.20; all the major elements that make up the sequence have been labelled.

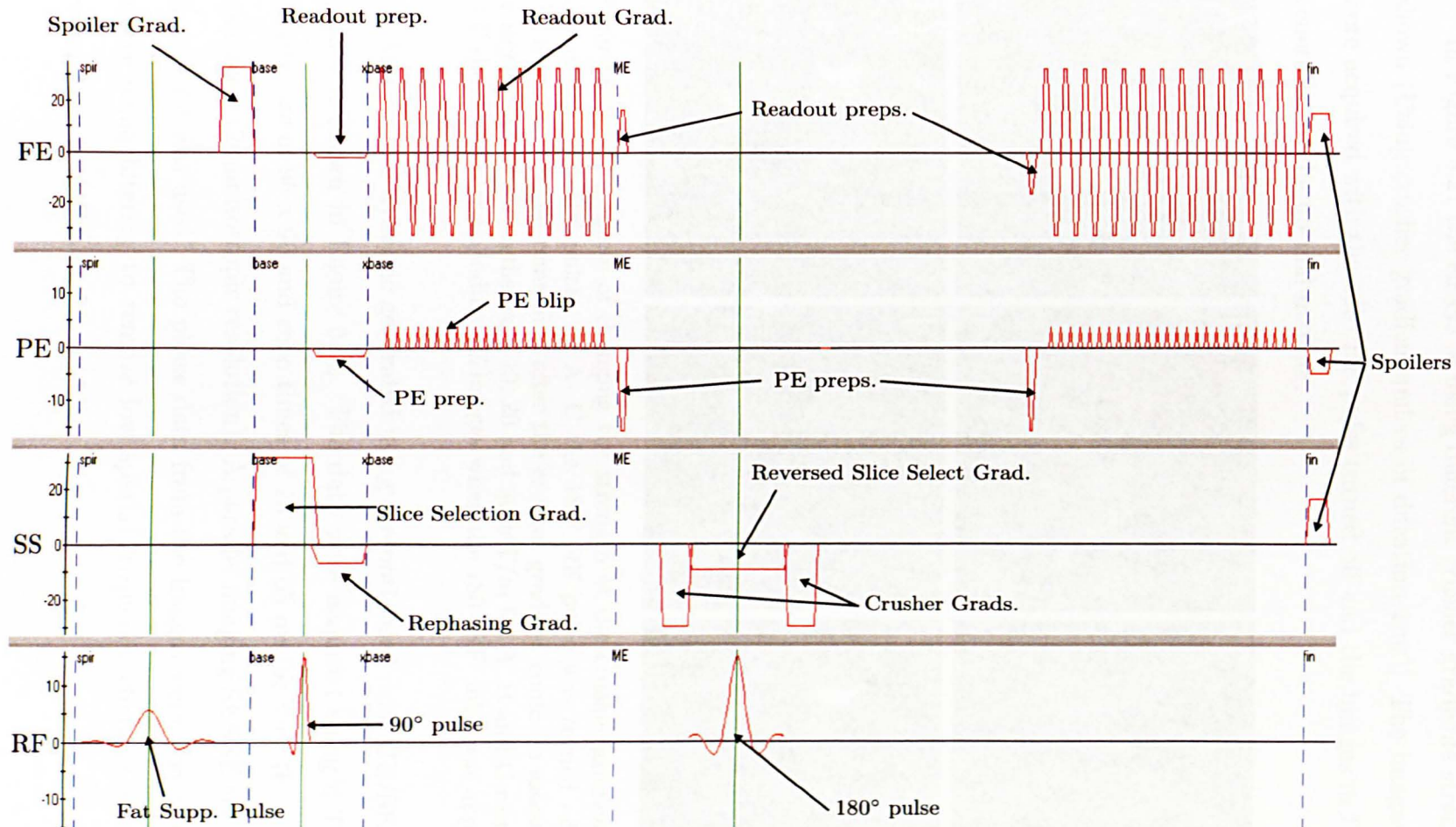


Figure 5.20: Final Dual GE/SE EPI sequence. This example used echo times of 10ms and 50ms for the GE and SE acquisitions respectively (2mm isotropic resolution, SENSE = 4).

In Figure 5.21 the effects of using different crusher gradients strengths are shown (Using crusher gradient pulses of duration 1ms). The images in A-C were acquired with the 180° RF pulse turned off and the images in D-F were generated in the normal manner.

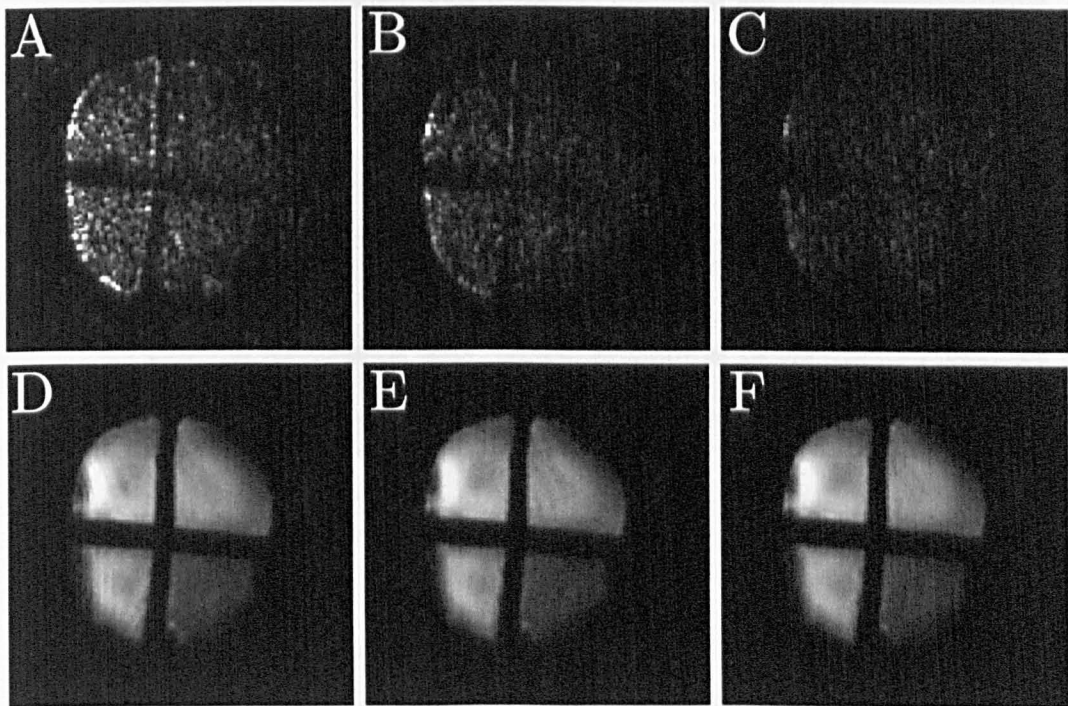


Figure 5.21: The effects of changing the strength of the crusher gradients either side of the 180° RF pulse. In A- C the 180° RF pulse was turned off so that the amount of signal remaining after the crusher gradient could be assessed. The crusher gradient strengths were 10, 20 and 30 mT/m for A, B and C respectively. D-F shows the corresponding SE images when the 180° RF pulse was applied.

An example dynamic generated using the optimised dual GE/SE EPI sequence is shown in Figure 5.22. The data were acquired using a TR of 3s, matrix size of 96 x 96 and echo times of 18 and 65 ms for the GE and SE respectively (2mm isotropic resolution). A parallel imaging SENSE acceleration factor of 4 was used. The phase data from the images were first unwrapped before being filtering to remove low spatial frequency changes; in order to reveal local phase changes.

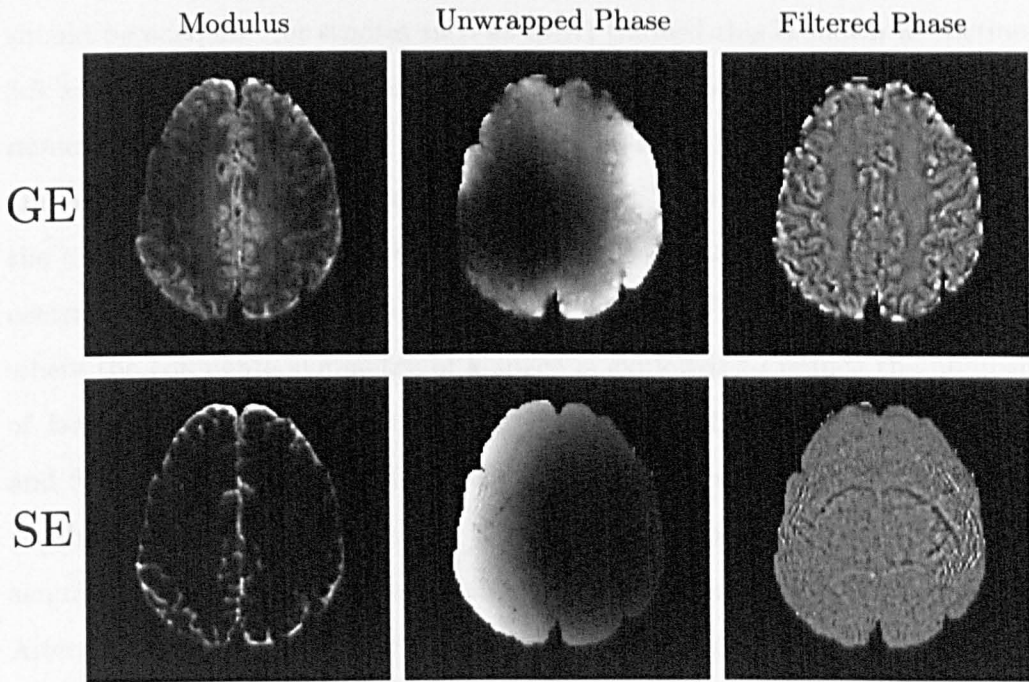


Figure 5.22: Example images generated using the dual GE/SE EPI sequence. Both modulus and phase data are displayed.

## Discussion

Images acquired using the dual GE/SE EPI sequence are shown in Figure 5.22. Both the GE and SE EPI data have high SNR. The added  $\Delta B_0$  information can be clearly seen in the GE phase, both global (in the unwrapped phase) and local variations (in the filtered phase) being evident. The refocusing pulse in the SE sequence completely removes these effects. Parallel imaging artefacts can be seen in the SE phase data due to the high SENSE factor that was used, however these are not as strongly evident in the modulus data.

The echo time of the SE acquisition was largely limited by the echo time of the GE readout and the matrix size of the acquisition. However in the example shown in Figure 5.22, where the GE echo time was set to 18ms, which is slightly reduced from the optimal value of 25ms, it was still possible to acquire the SE image with an echo time of 65ms. Both these echo times

should be adequate for studies such as fMRI (indeed this is shown in Section 5.5 and Chapter 6). Further, the GE echo time could have been set to a minimum of 15 ms, reducing the minimum possible SE echo time to 62 ms. One possible solution to reduce the TE of the SE further (without changing the image resolution) would be to re-order the k-space sampling so that the central line of k-space is acquired first using a half-Fourier type acquisition, where the conjugate symmetry of k-space is exploited to reduce the number of k-space lines that have to be acquired. Depending on the matrix size and SENSE acceleration factor that are used this could reduce the TE by anything from around 5-10 ms (A line of k-space typically takes  $\sim 0.5$ ms to acquire assuming  $\sim 128$  points are sampled and typical bandwidths are used). Alternatively a reduced size FOV could be used along with suppression slabs to remove unwanted signal from outside the FOV.

Figure 5.21 shows the effect of changing the strength of the crusher gradients on either side of the  $180^\circ$  RF pulse. In A, where the gradient amplitude was set too low, the signal from the unwanted pathways are clearly visible. The effects of this appear as artefacts in image D. It is clear that the signal contamination diminishes with increasing gradient amplitude, up to a point where it is almost completely removed in image C. The signal contamination could also be reduced by increasing the length that the crusher gradients are applied for, however this would then increase the minimum TE that could be achieved for the SE.

One problem with the current implementation of this sequence is its susceptibility to Nyquist ghosting artefacts, due to mis-alignment of k-space lines. The standard SE EPI sequence acquires extra data without any phase encoding, between the application of the  $90^\circ$  and  $180^\circ$  RF pulse. These data are then used to correct for Nyquist ghosting by measuring the phase differences between the non-phase encoded echoes. Based on the assumption that because there are no phase encoding steps, there should be no phase difference

between the inverse fourier transform of each echo. Any differences that exist are then likely to be constant or linear phase errors that will cause Nyquist ghosting artefacts (Bernstein et al. 1994). These phase errors can be used to correct for ghosting. As a result, Nyquist ghosting was observed on some of the data that were collected during this work. However, this effect can be remedied by applying post-processing based correction techniques (Buonocore & Zhu 2001).

This type of dual echo sequence could be particularly beneficial in fMRI studies because the extra GE image can be used in conjunction with the SE data for analysis of activation; allowing information on both the GE and SE BOLD contrast mechanisms to be assessed. Further because both images are acquired with a very small temporal separation, the temporal characteristics of these BOLD response mechanisms can be directly compared. Problems associated with registration of the GE and SE images, that can occur due to the difference in contrast of the two images types, is also no longer an issue with this dual acquisition. Dynamic motion correction could be carried out on either the GE or the SE dynamic data sets, with the calculated motion correction parameters then applied to the other data set, making the assumption that motion between the GE and SE data that occurs in the period between the acquisition of the two central lines of k-space for the GE and SE EPI data is minimal (i.e. most motion that occurs over a time of  $\sim 40$  ms is negligible).

## 5.5 Application : Dynamic Off-Resonance Correction of Simultaneously Acquired GE and SE EPI data measured using a dual GE/SE EPI sequence

### 5.5.1 Introduction

The development and testing of a dual GE/SE EPI sequence was described in the previous section. This section now shows how this sequence can be used to overcome the problems associated with carrying out distortion correction on SE EPI data, i.e. the inability to measure  $\Delta B_0$  when using SE EPI due to the inherent lack of  $\Delta B_0$  information in the phase of the SE data. We extend the Lamberton and Hahn (Lamberton et al. 2007, Hahn et al. 2009) techniques to allow absolute and dynamic correction of simultaneously acquired GE and SE EPI data using the modified dual echo sequence. In addition the SPHERE technique is modified to carry out phase evolution rewinding on upsampled k-space data (as recommended by Techavipoo et al. (2007)) in order to remove the aliasing artefacts that are otherwise generated.

To assess the effectiveness of this method, the spatial correspondence of distortion-corrected 7T EP-images are compared with conventional anatomical scans. Further, an auditory fMRI experiment is performed to test whether the technique can be used to carry out artefact correction in a real world scenario, involving the auditory cortex, which is an area prone to significant distortions (due to the presence of air-tissue interfaces in the sinuses). For completeness a motor task based fMRI experiment was also carried out.

### 5.5.2 Method

All scanning was carried out on healthy volunteers using a 7T Philips Achieva whole body scanner with a 16 channel receive coil. Auditory fMRI was performed using sparse imaging, in which a 20-slice GE/SE EPI axial volume was acquired in the first 2s of a 10s TR period. Sound stimuli, comprised broadband noise modulated at 10 Hz ( $\sim 80$  dB) presented for 20 s, commencing  $\sim 5$  s prior to the readout, followed by a 20 s baseline period. This was repeated for 10 cycles. We used the dual GE/SE EPI acquisition with a GE EPI echo time (TE) of 20 ms, and an asymmetric SE EPI TE of 58 ms (i.e. the central line of k-space was acquired at a time point slightly offset from that of the spin echo echo time). Data were acquired at 2 mm isotropic resolution using a bandwidth of 35.6 Hz/pixel in the PE direction, and a SENSE factor of 2. Static  $\Delta B_0$  maps were generated using the dual echo time technique with data acquired using a GE-EPI acquisition (10 volumes, 5 at each echo time) and an echo time difference of 2 ms. These data were acquired using the same scan parameters as the functional acquisition to ensure the distortions were equal.

The SE data for the auditory experiment was carried out asymmetrically because the study was performed during the development of the dual GE/SE EPI sequence, at a point when symmetry for the SE had yet to be hard coded into the sequence. However the exact same principles, of using the  $\Delta B_0$  data from the first GE to correct for distortions for both data sets, still applies.

Subsequently, a motor-task based fMRI study involving bilateral finger movement was carried out, using a GE TE of 14 ms and a symmetric SE TE of 62 ms. Data were acquired at 2 mm isotropic resolution using a bandwidth of 54.1 Hz/pixel in the PE direction. A SENSE acceleration factor of 4 was employed, using a 32 channel receive coil and a TR of 7.5s, in which 20-slice volumes were acquired. The motor fMRI study was carried out using a fully developed version of the GE/SE EPI sequence with SE data acquired

symmetrically.

All fMRI analysis was carried out using FEAT (FSL, Oxford, UK) with motion-corrected data. No spatial smoothing was applied.

$\Delta B_0$  field maps were filtered by removing high spatial frequency terms from a discrete cosine transformation (Garcia 2010), so as to reduce noise and edge effects.

The processing pipeline for the dynamic distortion correction of simultaneously acquired GE and SE EPI data is shown in Figure 5.23 (steps involving the masking of data are not displayed). Phase information contained within the GE EPI data of each functional acquisition is used to calculate how  $\Delta B_0$  varies over time relative to the mean  $\Delta B_0$  (Hahn et al. 2009). These dynamic  $\Delta B_0$  maps are combined with the static  $\Delta B_0$  map to create dynamically varying  $\Delta B_0$  maps that also include the contribution of static field inhomogeneities. The dynamic  $\Delta B_0$  maps are then used to rewind the effects of phase evolution, due to the presence of field inhomogeneities, for both the GE and SE EPI data. This is accomplished by generating artificial (or simulated) k-space data using the original k-space data from the GE and SE EPI scans and the measured  $\Delta B_0$  results. Inverse Fourier transformation of the simulated k-space data provides the distortion and intensity corrected image data.

The phase evolution rewinding process used by the SPHERE technique effectively phase encodes the image with an extra phase term that cancels out the additional phase that was imparted due to the presence of field inhomogeneities. This allows an undistorted image to be constructed by taking the inverse Fourier transform of the rephase encoded image. However problems with this technique can occur when  $\Delta B_0$  is too large because the additional simulated phase encoding can cause significant ripple like artefacts in the reconstructed image due to re-gridding effects (Chiou et al. 2003). Techavipoo et al. (2007) developed a technique to correct for this by upsampling k-space prior to phase evolution rewinding. They found that an upsample factor of 4

in the PE direction was optimum (See Figure 3 in Techavipoo et al. (2007)). Since we expect the regions surrounding the sinuses to be affected by relatively large magnetic field inhomogeneities we also employ this technique; using their recommended upsampling factor of 4.

To aid the visual assessment of the effectiveness of the artefact correction technique, outlines of major anatomical contrast boundaries were drawn on a selection of slices from the motor fMRI data, using images acquired with anatomical acquisitions as guidance.

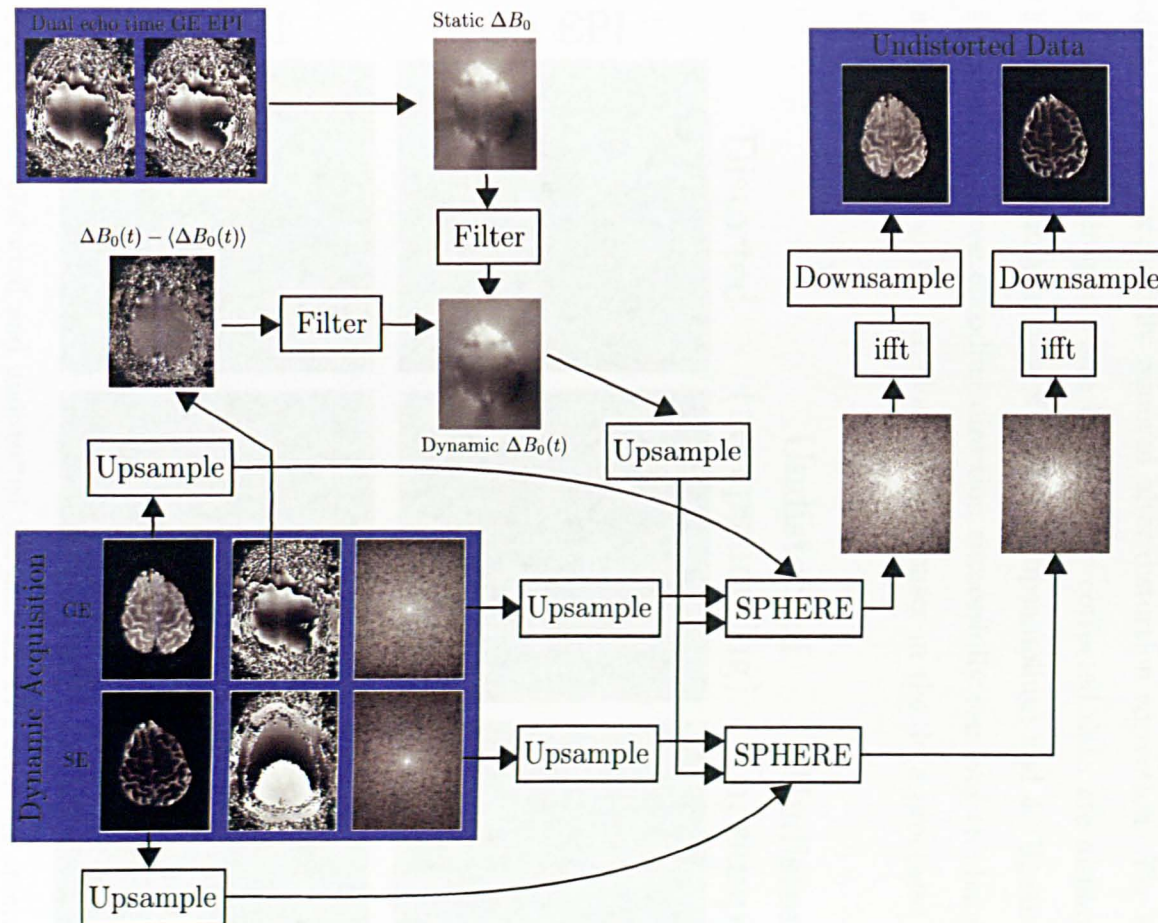


Figure 5.23: Processing pipeline for dynamic distortion correction of simultaneously acquired GE and SE EPI data.

### 5.5.3 Results

In Figure 5.24, both distorted and undistorted GE and SE EPI data are shown for one axial slice in the head. Significant distortions due to off-resonance field effects are present in both the uncorrected GE and SE EPI data and are successfully removed after distortion correction. The effects of k-space upsampling can also be seen; the corrected data are displayed with k-space upsampling factors of 1 (i.e. no upsampling) and 4. Upsampling k-space in the phase encoding direction successfully removes the banding like artefacts that can be seen close to the sinuses in the data processed without upsampling.

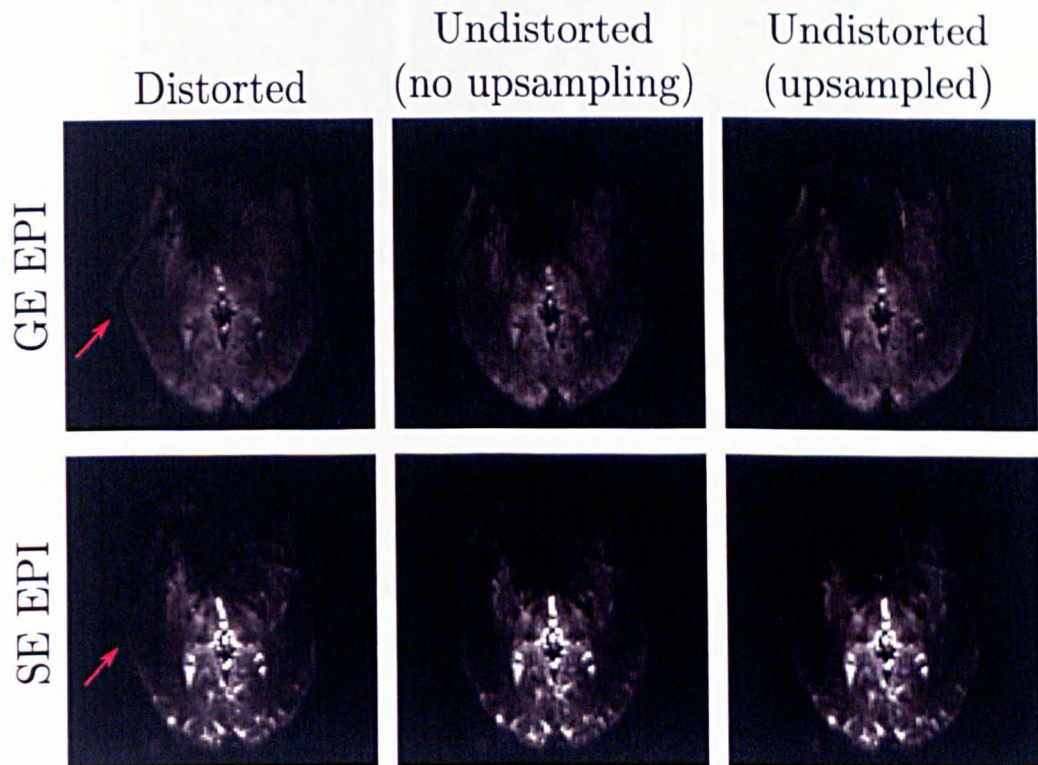


Figure 5.24: Distorted and undistorted GE and SE EPI data are shown using a slice at the same level as the sinuses. Distortion corrected images are displayed both without k-space upsampling and with an upsampling factor of 4. Significant distortion can be seen on the left of the brain (red arrows) in the undistorted data.

Results from the auditory fMRI experiment can be seen in Figure 5.25.

Distorted and undistorted data are shown for both the GE and asymmetric SE data. An anatomical acquisition is also displayed and overlaid with fMRI data from the asymmetric SE acquisition.

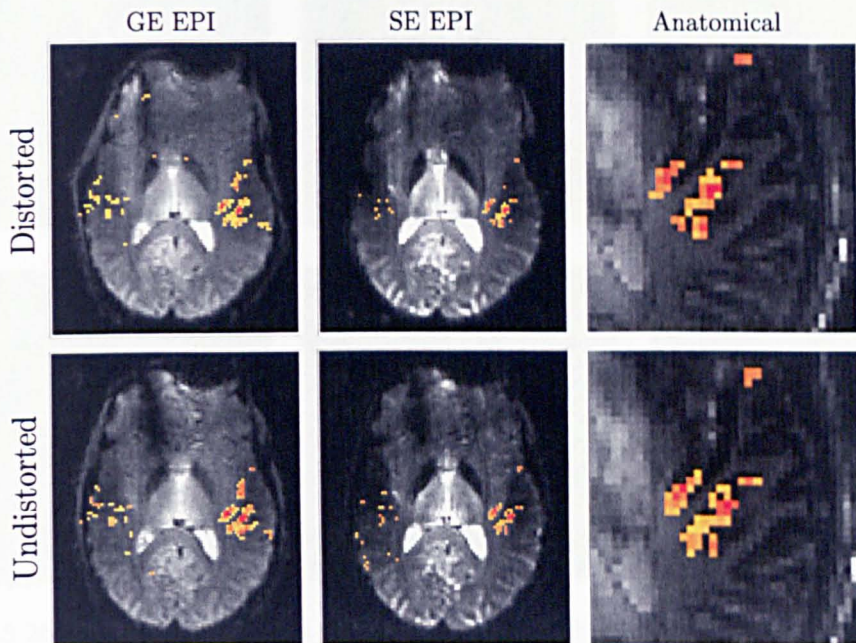


Figure 5.25: Auditory fMRI. Both distorted and undistorted GE and SE EPI data are displayed with overlayed fMRI activation. The SE fMRI data is also shown overlayed onto an anatomical scan.

The effectiveness of the distortion correction of the SE EPI data is demonstrated in Figure 5.26 for two axial slices. A selection of high contrast boundaries, drawn using data from the anatomical scan, are displayed (in red) to allow visual assessment of the accuracy of the distortion correction.

fMRI results from the motor task experiment are shown in Figure 5.27. A number of slices are displayed for both the GE and SE EPI data. Results are shown before and after distortion correction. fMRI activation results (after clustering using TFCE) are overlaid on the EPI data.

#### 5.5.4 Discussion

We have demonstrated that absolute and dynamic distortion correction can be successfully applied to both GE and SE EPI data using a dual GE/SE

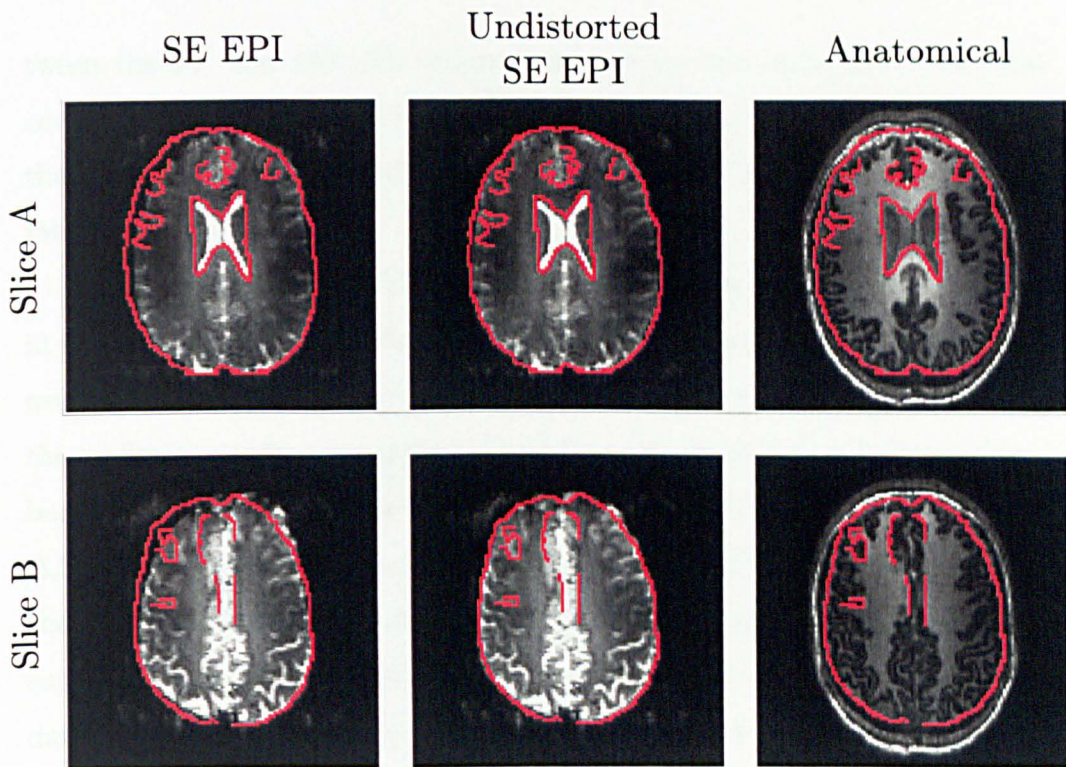


Figure 5.26: SE EPI distortion correction. Both original and undistorted SE EPI data are shown alongside an anatomical scan for two different slices. An anatomical outline, taken from the anatomical scan, is shown in red.

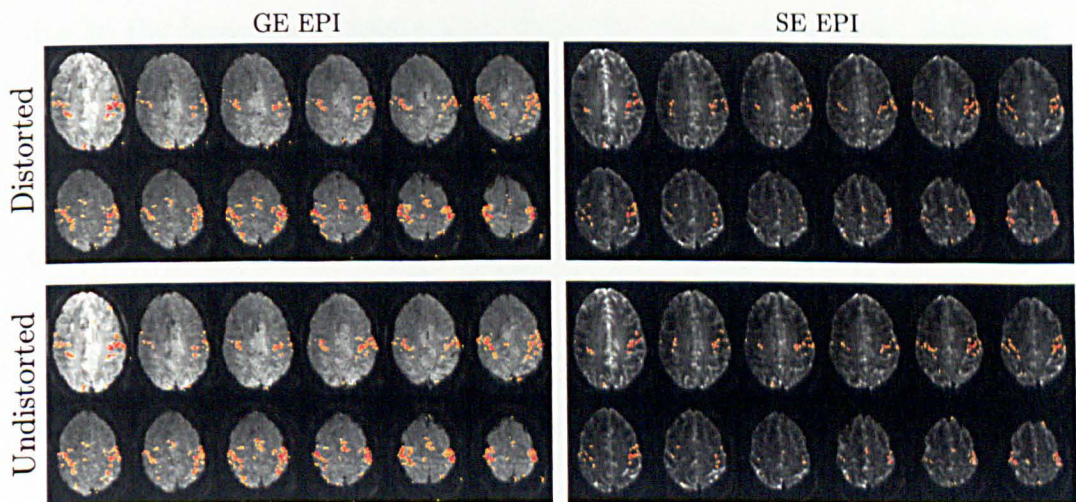


Figure 5.27: Motor fMRI: Distorted and undistorted GE and SE EPI data are displayed with fMRI activation overlayed on top.

EPI acquisition and just one initial reference scan.

We found that the addition of extra echo-planar encoding gradients be-

tween the 90° and 180° RF pulses increased the minimum echo time that could be achieved for the SE data (dependent on the matrix size). However the accessible echo times fell in a good range for fMRI, as highlighted by our fMRI experiments.

In Figure 5.24, both GE and SE EPI data are shown for one axial slice in the head. Significant distortions due to off-resonance field effects were present in both data sets (see left side of brain). After distortion correction these effects are almost completely removed. Without k-space upsampling a banding like artefact can be seen close to the sinuses where there is a large  $\Delta B_0$  inhomogeneity. However upsampling k-space to 4 times its original size in the phase encoding direction, before carrying out phase evolution rewinding, successfully removed this effect. It is important to note that upsampling the data in this manner significantly increases the post-processing time of the technique (by over an order of magnitude!).

Results from the auditory fMRI experiment are shown in Figure 5.25. The most significant effects of distortion correction can be seen around the sinuses due to the large static field variations in this region. The mean  $\Delta B_0$  field inhomogeneity in the functional ROI in Herschel's gyrus was found to be  $\sim 23$  Hz, leading to a sub-pixel shift in this region. However fMRI analysis after dynamic distortion correction appears to show better alignment with the gray matter. This will have to be verified in a larger study with a larger cohort.

The effectiveness of the technique for correcting for the large static  $\Delta B_0$  induced distortions can be seen more clearly in Figure 5.26. These images clearly demonstrate that anatomical outlines of the brain match the corresponding anatomical features in EP-images more accurately after distortion correction is carried out.

For the motor task, significant fMRI activation can be seen in both the GE and SE EPI data in both the distorted and undistorted data. The more

diffuse nature of the GE BOLD response can be clearly seen. Despite these promising results it remains for future work to determine whether dynamic distortion correction of simultaneously acquired GE and SE EPI data improves the functional power of activation analysis. This may largely depend upon the functional task that is being carried out and where in the head the functional area is relative to the anatomical regions where large susceptibility changes are expected; such as near the sinuses. It may also depend upon the type of fMRI activation analysis that is carried out. Indeed, in a study looking at dynamic distortion correction of GE EPI data, Hahn et al. (2009) found dynamic correction to be beneficial, in terms of increased statistical power in fMRI studies where complex data is used for activation analysis instead of the more commonly used modulus data. They also found that dynamic distortion correction improved subsequent motion correction.

## 5.6 Conclusion

A technique that allows image artefacts, produced due to off-resonance field effects, to be corrected on a dynamic basis for both GE and SE EPI data when scanning using a dual GE/SE EPI sequence has been described. The use of the sequence and method for dynamic distortion correction has been demonstrated for both auditory and motor fMRI data. Using the techniques developed here, we have provided a method that allows accurate dynamic distortion correction to be applied to both GE and SE EPI data using just one initial reference scan. These corrections provide improved alignment to anatomical data, which may be particularly advantageous for techniques such as cortical flattening of activation maps.

# **Chapter 6**

## **Dual GE/SE EPI : Resting State Functional Magnetic Resonance Imaging**

### **6.1 Background**

The human brain consumes approximately 20% of the body's energy yet makes up only 2% of its mass (Raichle et al. 2001). This vastly disproportionate energy consumption per unit mass, relative to the rest of the body, can be attributed to the large metabolic demands of the brain that are required to support ongoing intrinsic spontaneous neuronal activity (Fox & Raichle 2007). It has been postulated that this resting state baseline activity is associated with a number of processes that have to be controlled continuously, such as the control and monitoring of internal processes in the body. Larger more abstract baseline level mechanisms, such as alertness to the surrounding world, may also require the co-ordination of a large number of functional regions in the brain.

Until recently, most fMRI studies have concentrated on assessing how the brain's function, whilst a specific goal-related task is being performed (e.g.

finger movement) differs from its function when the brain is at rest (Friston 1996, Logothetis et al. 2001, Yacoub et al. 2005, Harmer et al. 2011).

More recently there has been interest in the underlying changes in brain activity whilst at rest. In the field of fMRI there have been some question as to whether this functional activation is indeed due to the presence of underlying neuronal processes, as it may instead be brought about as a result of other non-neuronal BOLD related metabolic responses, like variation in cardiac output (Mitra et al. 1997, Lowe et al. 1998, Cordes et al. 2000). Such problems can arise because the low sampling frequency, typically used in fMRI, may cause aliasing of cardiac and respiratory effects into the low frequency ranges associated with the BOLD response (De Luca et al. 2006). Cordes et al. (2001) suggested that it is only these low temporal frequencies that contribute significantly to regionally specific BOLD correlations. However, work carried out using fMRI at high sampling frequencies has shown that low frequency fluctuations, associated with the BOLD response, are still present even when this type of aliasing is not problematic, somewhat negating this fear (Biswal et al. 1995, Lowe et al. 1998). This is further supported by a number of studies that show a correlation between low frequency BOLD signal fluctuations and variations in electrical activity detected using EEG (Goldman et al. 2002, Laufs et al. 2003).

In an early paper by Biswal et al. (1995), fMRI was used to detect the BOLD response to these spontaneous neuronal processes. This involved using correlation analysis to compare the similarity of voxel-wise time-courses. These authors found that low frequency fluctuations,  $< 0.1\text{Hz}$ , in the resting state of the brain, in somatosensory regions, had high temporal correlations at a number of spatial locations known to be associated with motor function. They suggested that the high correlation between these regions was an indication of the existence of a resting state network.

A confounding factor in the detection of these resting state networks (RSN)

is the difficulty in knowing whether or not the brain is at rest or is involved in a conscious task-related thought process, for example making plans or imagining playing a sport. To circumvent this problem Raichle et al. (2001) defined a baseline state, using quantitative Positron Emission Tomography (PET), by studying the relationship between oxygen delivery and utilisation; specifically the oxygen extraction fraction (OEF). They demonstrated the uniformity of the OEF during a resting state acquisition, and postulate that the mean OEF represents the metabolic equilibrium state, when the brain is in its resting state. They suggest that any regions showing a significant deviation from the mean OEF represent areas undergoing task-related brain activation. They also detect a reduction in the baseline activity during task-based studies in midline areas of the brain (specifically the posterior cingulate, precuneus and medial prefrontal cortex). Noting that damage to these regions is known to lead to difficulties in perceiving the visual field as a whole, this finding provides evidence that resting state networks in these areas are related to processes that keep us alert to the surrounding world. Using this definition, Raichle et al. (2001) describe a default mode network of brain function that involves areas such as the posterior cingulate, precuneus and medial prefrontal cortex.

In a review article, Gusnard & Raichle (2001) concluded that resting state networks, found in the posterior cingulate cortex and precuneus, are associated with the brain's continuous monitoring of the world around us, for example for the detection of nearby predators. They also go as far as to suggest that resting state networks may provide organisms with a stable sense of perspective relative to the external world, i.e a 'self'.

More recently, fMRI has widely been used to detect this default mode network (DMN), somewhat negating the earlier concerns regarding the confounding affects of unwanted task related activation (Greicius et al. 2003, Buckner et al. 2008, Bluhm et al. 2009, Hale et al. 2010).

### 6.1.1 Resting State Network Detection

Most of the early fMRI studies to detect resting state networks utilised correlation-based analysis techniques (Lowe et al. 1998, Cordes et al. 2000, Fox et al. 2006). These methods require the selection of an initial seed location within a resting state network, which is usually taken as either a single voxel or, to reduce the effects of noise, the average time-course from an ROI of voxels. Once the seed location is selected, a Pearson correlation coefficient is then calculated between the time-series of the seed region, and that from each of the individual voxels, on a voxel-wise basis; providing a measure of the covariance of the time-series (normalised by the product of their standard deviations). The resulting correlation coefficient maps are then thresholded using the required p-value (typically around 0.05) and, following the application of Bonferroni multiple comparisons correction factor (to account for the large number of voxels within an MR imaging volume), used to generate an image that shows which regions of the brain are significantly correlated with the seed region.

A significant problem with such a-priori seed selection is that it relies on the assumption that the seed voxel time-course is a good approximation to the time-course of the network (Beckmann et al. 2005, Kiviniemi et al. 2003, Van De Ven et al. 2004, De Luca et al. 2006). This may not necessarily be the case due to the arbitrary nature of seed selection and because the seed time-course can be comprised of a superposition of signals from different sources such as spatially varying artefacts, which may not be present at all locations in the network.

To circumvent this problem, a number of groups use independent component analysis to separate a signal into a number of additive linear subcomponents that are maximally statistically independent of each other (Comon 1994). This can be accomplished by minimisation of the mutual information contained within the signals. Beckmann & Smith (2004) extend the ICA tech-

nique to include a gaussian noise term in the model to avoid problems associated with over-fitting of the data and to allow Z-score maps to be generated (probabilistic independent component analysis or PICA). Their modification allows the overall problem to be solved using a technique similar to the GLM, with the major difference being that the mixing matrix, analogous to the design matrix in GLM, is determined using the data itself. As these techniques are data-driven, i.e. are not looking for a specific time-course shape, they also allow the detection of signal correlations that occur due to unwanted signal artefacts. Beckmann et al. (2005) showed that even when imaging at a relatively long TR of 3 s (where respiratory and cardiac effects can be temporally aliased into the low frequency regions in which the resting state networks lie), ICA can effectively separate cardiac and respiratory effects from those effects that are of interest. For example, Cole et al. (2010) concluded that spatial overlap between the DMN and respiratory artefact regions, detected using ICA, are generally fairly small. In comparison seed-based correlation analysis (SCA) techniques can be severely affected by signal artefacts, often to the extent where meaningful correlation analysis is impossible.

Non-BOLD related signal fluctuations can be a major confound in the analysis of resting state data. In a 7 T study, Bianciardi et al. (2009) look at how much variance in the resting state signal can be explained by non-neuronal sources. Their results showed that low frequency drift (< 0.01 Hz), attributable to scanner instability, accounted for ~35% of the total variance within the grey matter (equating to a 3.2% signal change). For this reason, it is vitally important to remove these effects before analysing the data.

## 6.2 Introduction

Spontaneous, low frequency fluctuations in connected resting state networks have been identified in  $T_2^*$ -weighted GE BOLD data (Biswal et al. 1995,

Lowe et al. 1998, Cordes et al. 2000, Fox et al. 2006). One such network is the default mode network (DMN) which comprises the medial prefrontal cortex, posterior cingulate, precuneus and parietal cortex (Raichle et al. 2001).

At 7 T, the increase in the sensitivity of SE BOLD contrast, compared to lower field strengths, means it can be used for functional imaging. Applying SE BOLD to study resting state data potentially allows RSNs to be detected with a higher spatial specificity to the underlying microvasculature. SE-EPI has the added benefit that it is insensitive to signal-dropout due to through-slice dephasing. Studies have indicated that there may be a disruption to the DMN in a range of neurological and psychiatric disorders such as Alzheimers, autism and depression (Jin et al. 2011, Buckner et al. 2008, Bluhm et al. 2009). Thus knowledge of the DMN may be of practical use in these fields of research. Any added spatial specificity that may be brought about through the use of the SE BOLD response will also be beneficial.

This study therefore aims to use a modified dual GE/SE EPI sequence at 7 T to identify functional connectivity maps in both SE- and GE-BOLD data. Correlated fluctuations in  $T_2^*$ - and  $T_2$ -weighted images across multiple echo times in the DMN and other areas are assessed.

A novel technique for measuring the ratio of the changes in relaxation rate on activation in gradient and spin echo data ( $\delta R_2^*/\delta R_2$ ), based on resting state signal fluctuations in the DMN, is also described. This is the first time that the spin echo  $\Delta R_2$  has been measured in resting state data.

## 6.3 Methods

### 6.3.1 Data acquisition

Data were collected on a 7 T Philips Achieva System using a volume transmit and 32-channel receive coil. A dual GE/SE EPI sequence was implemented by modifying a SE EPI sequence (as described in Section 5.4) to

acquire a GE image prior to the 180° RF pulse so as to allow the almost simultaneous acquisition of GE and SE images (temporal separation ~50ms, dependent on echo time). The sequence was used to collect 150 volumes of GE and SE EPI resting state fMRI data on 5 subjects. Each volume comprised 16 axial slices spanning a region from the ventricles to close to the top of the brain. Images were acquired at 3 mm isotropic resolution using a bandwidth of 56.6 Hz/pixel and a TR of 3 s (SENSE acceleration factor 2). The functional data acquisition was repeated four times allowing the collection of GE/SE images with echo time pairs of 17/60, 22/70, 27/80 and 32/90 ms. Inversion recovery (IR) images (10 inversion times ranging from 100 to 2000 ms) were also collected to allow tissue segmentation.

To circumvent problems associated with a-priori seed selection, a sophisticated multivariate probabilistic independent component analysis technique (PICA) was employed in this study; implemented using MELODIC (FSL, Oxford, UK) (Beckmann & Smith 2004). Each data set was analysed using a range of different total ICA component numbers, from 30 to 120 components. The resulting component maps were then visually studied for the presence of resting state networks. The optimum number of ICA components was visually determined on a scan by scan and subject by subject basis by identifying which number of components detected the most resting state networks with the least network splitting.

### 6.3.2 Filtering

For ICA analysis low frequency drifts were removed using a Gaussian weighted local straight line fit to the data (Marchini & Ripley 2000), implemented as part of the MELODIC software package. To improve image SNR, the functional data was smoothed to 5mm isotropic resolution using a Gaussian kernel before the ICA analysis.

For the voxel-wise results, such as the correlation analysis, low frequency

drifts were removed by detrending the data. This involved fitting a 2nd order polynomial to each voxel's time series and then subtracting this fit from the data. This allowed any drift in signal to be removed on a voxel-wise basis.

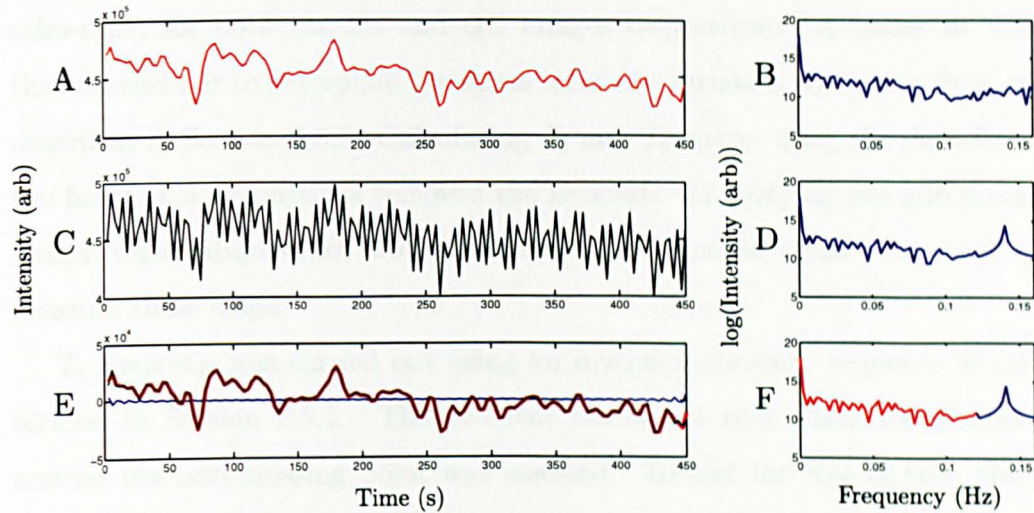


Figure 6.1: Low pass filtering. **A** : An example voxel time series **B**: The corresponding spectrum. **C** : The signal after contamination with a 0.14Hz cosine signal. **D** : Corresponding frequency space; the additional noise can be clearly seen. **E** : The filtered contaminated signal (black line) after removing any frequencies above 0.12Hz in frequency space and applying an inverse Fourier transformation. The original signal is also shown (red line) alongside the difference between the original and filtered signal (blue line). **F** The masked region of frequency space (red line).

To reduce the effects of high frequency noise, low pass filter was applied before the voxel-wise correlation and fractional signal change analysis (Figure 6.1). This was accomplished by setting frequencies above a cut-off frequency (0.12Hz) to zero. The cut-off frequency was chosen in order to preserve the BOLD related response (expected to occur at frequencies less than 0.12Hz (Biswal et al. 1995)) whilst removing higher frequency noise. The first and last points in each time series were then removed to reduce the ringing effects that can occur when using this type of filter.

### 6.3.3 $T_2/ T_2^*/ T_1$ maps

$T_2$  and  $T_2^*$  maps were created by calculating the mean signal across all volumes during the functional acquisitions in a voxel-wise fashion for each echo-time, for both the SE and GE images respectively. A linear fit was then carried out to determine the signal intensity variation with echo time, as described in Section 2.5.7. Calculating  $T_2$  and  $T_2^*$  maps using the data from the functional acquisitions removed the necessity for carrying out additional spatial registration which would be required if separate scans were used to measure these maps.

$T_1$  mapping was carried out using an inversion recovery sequence as described in Section 2.5.7. The problem associated with noise rectification around the zero crossing point was assessed. To test the size of this effect a fit was performed to a noisy simulated recovery curve using both the true polarity (real) and modulus data, using a simulated  $T_1 = 1.5\text{s}$  and  $M_0 = 100$  (Figure 6.2). The fitting procedure was repeated 1000 times. The  $T_1$  and  $M_0$  values, calculated from the fits, are shown in Table 6.1. A slight increase can be seen in the  $T_1$  values that were calculated using the modulus data, however this effect was considered too slight to significantly effect the results in this study.

Fit method	$T_1$ (s)	$M_0$ (arb)
True data	1.502 (0.003)	99.965 (0.186)
Mod data	1.518 (0.004)	99.898 (0.189)

Table 6.1:  $T_1$  and  $M_0$  results taken from exponential fits to simulated inversion recovery data, using both the true polarity data and modulus only (positive polarity) data. The average results are shown from 1000 repeat runs.

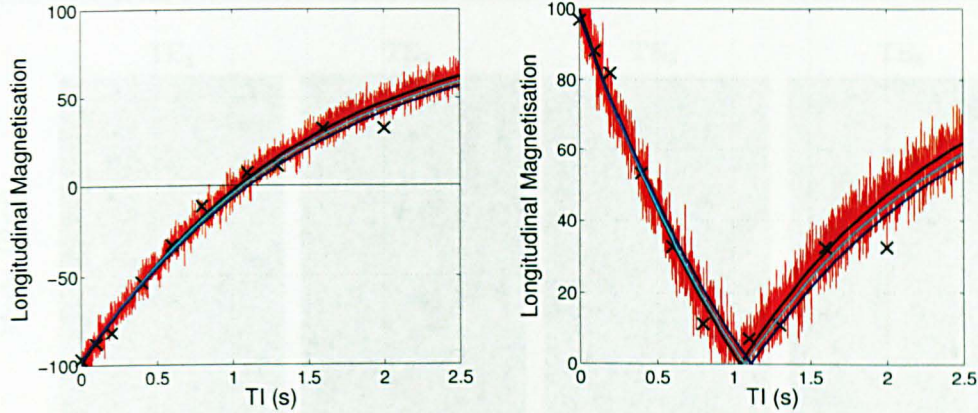


Figure 6.2: An example of the problems that can arise when fitting to modulus data using simulated data with added Gaussian noise (SNR 20). The black crosses represent the points at which the signal was sampled. The solid black line displays the true theoretical signal recovery curve ( $T_1 = 1.5\text{s}$ ,  $M_0 = 100$ ). The dark blue line shows the best fit that was obtained using the modulus data ( $T_1 = 1.60\text{s}$ ,  $M_0 = 97.9$ ) and light blue line using the true data ( $T_1 = 1.54\text{s}$ ,  $M_0 = 98.1$ ) (from the left plot).

### 6.3.4 Masks

In order to assess the nature of the resting state SE/GE signal variations, a number of different ROIs were scrutinised. An ROI was created for the DMN by visually identifying the ICA components that corresponded to the DMN (with reference to the literature) for each functional run. These were then used to create masks for both the GE and SE BOLD data with different masks created for each of the functional runs (i.e. for each echo time pair). Masks were then first eroded and then dilated, using a disk kernel with a diameter of 3 pixels, to remove small noisy cluster regions. A common mask across echo times was then generated for each subject, for both the SE and GE data, by combining the separate masks and choosing voxels that were common to at least 3 of the 4 echo times (Figure 6.3). A further mask that was common to both the combined GE and SE DMN masks (COM) was created via multiplication of the two binary masks. Gray matter masks were also produced for each subject by thresholding the calculated  $T_1$  maps, with

the threshold level determined via visual assessment of the resulting masks.

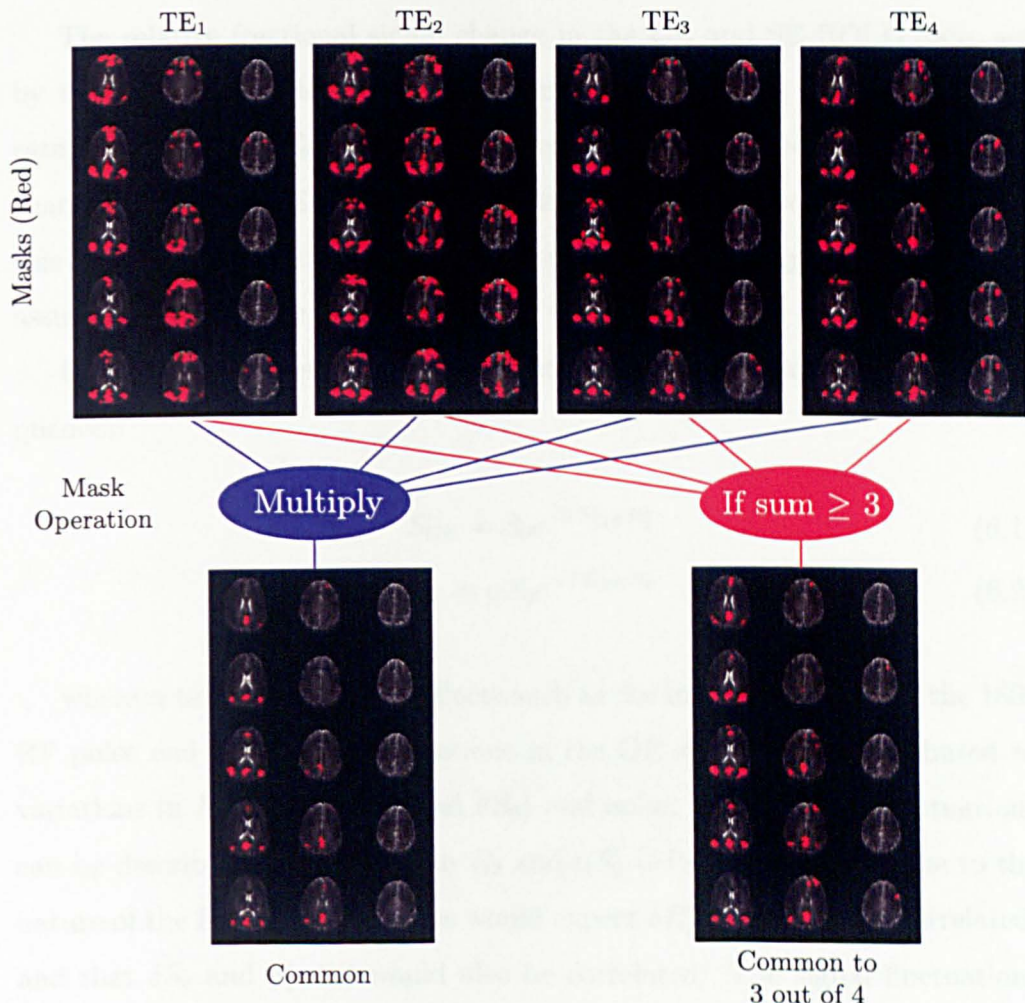


Figure 6.3: Processing pipeline for the DMN ICA based mask creation. GE ICA DMN masks that were created by carrying out ICA on the functional acquisitions acquired at each of the four different echo times, are shown for a representative subject (Top row). The mask common to all four masks is also shown (bottom left), along with a mask representing voxels common to at least 3 out of the 4 masks (bottom right).

## GE/SE Correlation Analysis

To assess how the signal fluctuations in the GE data related to those in the SE data, a correlation analysis was performed between each dual GE/SE image pair on a voxel-wise basis.

### 6.3.5 Resting state GE/SE signal fluctuations

The relative fractional signal change in the GE and SE BOLD data, set by the ratio of the change in relaxation rate  $\delta R_2^*$  or  $\delta R_2$  to the relaxation rate  $R_2$  or  $R_2^*$ , was also calculated by considering how the fractional signal change varied with TE for both the SE and GE data. The steps taken to allow this calculation in the absence of a task-driven functional paradigm, and the assumptions made are described below:

First we must consider the signal detected using GE and SE imaging sequences:

$$S_{GE} = S_0 e^{-TE_{GE}R_2^*} \quad (6.1)$$

$$S_{SE} = \alpha S_0 e^{-TE_{SE}R_2} \quad (6.2)$$

where  $\alpha$  takes into account effects such as the imperfect nature of the 180° RF pulse and diffusion. Fluctuations in the GE signal can be attributed to variations in  $R_2^*$  and  $S_0$  ( $\delta R_2^*$  and  $\delta S_0$ ) and noise. Similarly, SE fluctuations can be described by variations in  $R_2$  and  $\alpha S_0$  ( $\delta R_2$  and  $\delta(\alpha S_0)$ ). Due to the nature of the BOLD response one would expect  $\delta R_2^*$  and  $\delta R_2$  to be correlated, and that  $\delta S_0$  and  $\delta(\alpha S_0)$  would also be correlated. The signal fluctuations can then be described by:

$$S_{GE} = (S_0 + \delta S_0) e^{-TE_{GE}(R_2^* + \delta R_2^*)} + n \quad (6.3)$$

$$S_{SE} = (S_0 + \delta(\alpha S_0)) e^{-TE_{SE}(R_2 + \delta R_2)} + N \quad (6.4)$$

where  $n$  and  $N$  represent the thermal noise in the GE and SE signals respectively. For conciseness, in the following derivation only the case for the GE signal is detailed, since the method described can be applied in both cases, the final result for the SE case is quoted. If we approximate the GE signal by

considering only terms to first order in  $\delta R_2^*$  and  $\delta S_0$  this gives:

$$S_{GE} = (S_0 + \delta S_0)(1 - TE.\delta R_2^*)e^{-TE.R_2^*} + n \quad (6.5)$$

which can be expanded to:

$$S_{GE} = S_0 e^{-TE.R_2^*} + \delta S_0 e^{-TE.R_2^*} - S_0 \cdot TE \cdot \delta R_2^* e^{-TE.R_2^*} + n \quad (6.6)$$

By setting  $S_0 e^{-TE.R_2^*} = \langle S_{GE} \rangle$  and calculating the fractional signal change:

$$\delta R_{GE} = \frac{S_{GE}}{\langle S_{GE} \rangle} - 1 \quad (6.7)$$

We get the following relation:

$$\delta R_{GE} = \frac{\delta S_0}{S_0} - TE \cdot \delta R_2^* + \frac{n}{\langle S_{GE} \rangle} \quad (6.8)$$

Calculating the variance of the fractional signal fluctuations then gives :

$$\begin{aligned} Var(\delta R_{GE}) &= Var\left(\frac{\delta S_0}{S_0}\right) + Var(-TE \cdot \delta R_2^*) + Var\left(\frac{n}{\langle S_{GE} \rangle}\right) \\ &\quad + 2.Cov\left(\frac{\delta S_0}{S_0}, -TE \cdot \delta R_2^*\right) + 2.Cov\left(\frac{\delta S_0}{S_0}, \frac{n}{\langle S_{GE} \rangle}\right) \\ &\quad + 2.Cov\left(-TE \cdot \delta R_2^*, \frac{n}{\langle S_{GE} \rangle}\right) \end{aligned} \quad (6.9)$$

Assuming that fluctuations in  $\frac{\delta S_0}{S_0}$  and  $R_2^*$  do not correlate with thermal noise,  $n$ , and that the mean values of  $\delta R_2^*$ ,  $\frac{\delta S_0}{S_0}$  and  $n$  are equal to 0, this gives the following result:

$$\begin{aligned} \langle \delta R_{GE} \rangle &= \left\langle \left( \frac{\delta S_0}{S_0} \right)^2 \right\rangle + TE^2 \langle (\delta R_2^*)^2 \rangle + \frac{\langle n^2 \rangle}{\langle S_{GE} \rangle^2} \\ &\quad - 2.TE \left\langle \frac{\delta S_0}{S_0} \cdot \delta R_2^* \right\rangle \end{aligned} \quad (6.10)$$

If we assume the correlations between  $\delta S_0$  and  $\delta R_2^*$  are small then this results in:

$$\langle(\delta R_{GE})^2\rangle - \frac{\langle n^2 \rangle}{\langle S_{GE} \rangle^2} = \left\langle \left( \frac{\delta S_0}{S_0} \right)^2 \right\rangle + TE^2 \langle(\delta R_2^*)^2\rangle \quad (6.11)$$

Similarly for the SE case, with the added assumption that  $\frac{\delta(\alpha S_0)}{\alpha S_0} = \frac{\delta(S_0)}{S_0}$ , this gives:

$$\langle(\delta R_{SE})^2\rangle - \frac{\langle N^2 \rangle}{\langle S_{SE} \rangle^2} = \left\langle \left( \frac{\delta S_0}{S_0} \right)^2 \right\rangle + TE^2 \langle(\delta R_2)^2\rangle \quad (6.12)$$

Thus it is possible to plot the mean of the squared fractional signal change (minus the thermal noise term) as a function of the square of the echo time. As BOLD signal fluctuations tend to occur on time scales of approximately 5-8s, assuming a relatively short TR is used along with low pass filtering, the influence of the thermal noise term should be minimal (Triantafyllou et al. 2010) and can thus be ignored:

$$\langle(\delta R_{GE})^2\rangle \simeq \left\langle \left( \frac{\delta S_0}{S_0} \right)^2 \right\rangle + TE^2 \langle(\delta R_2^*)^2\rangle \quad (6.13)$$

$$\langle(\delta R_{SE})^2\rangle \simeq \left\langle \left( \frac{\delta S_0}{S_0} \right)^2 \right\rangle + TE^2 \langle(\delta R_2)^2\rangle \quad (6.14)$$

$|\delta R_2^*|$  and  $|\delta R_2|$  can therefore be determined by calculating the gradients of linear fits of the mean of the squared fractional signal change as a function of the square of the echo time, via regression analysis.

## 6.4 Results

Dual GE/SE EPI acquisitions were used for successfull identification of the DMN in both the SE and GE BOLD resting state data in all subjects. Example DMN ICA maps for all 5 subjects are shown in Figure 6.4 (one GE and SE echo time pair is shown for each subject), with the thresholded ICA results shown overlaid onto the temporal mean of the corresponding functional scan. The spatial characteristics of the DMN, with nodes in the medial frontal cortex, posterior cingulate, precuneus and parietal cortex, as described in the literature (Raichle et al. 2001, Smith et al. 2009, Buckner et al. 2008), can be clearly seen.

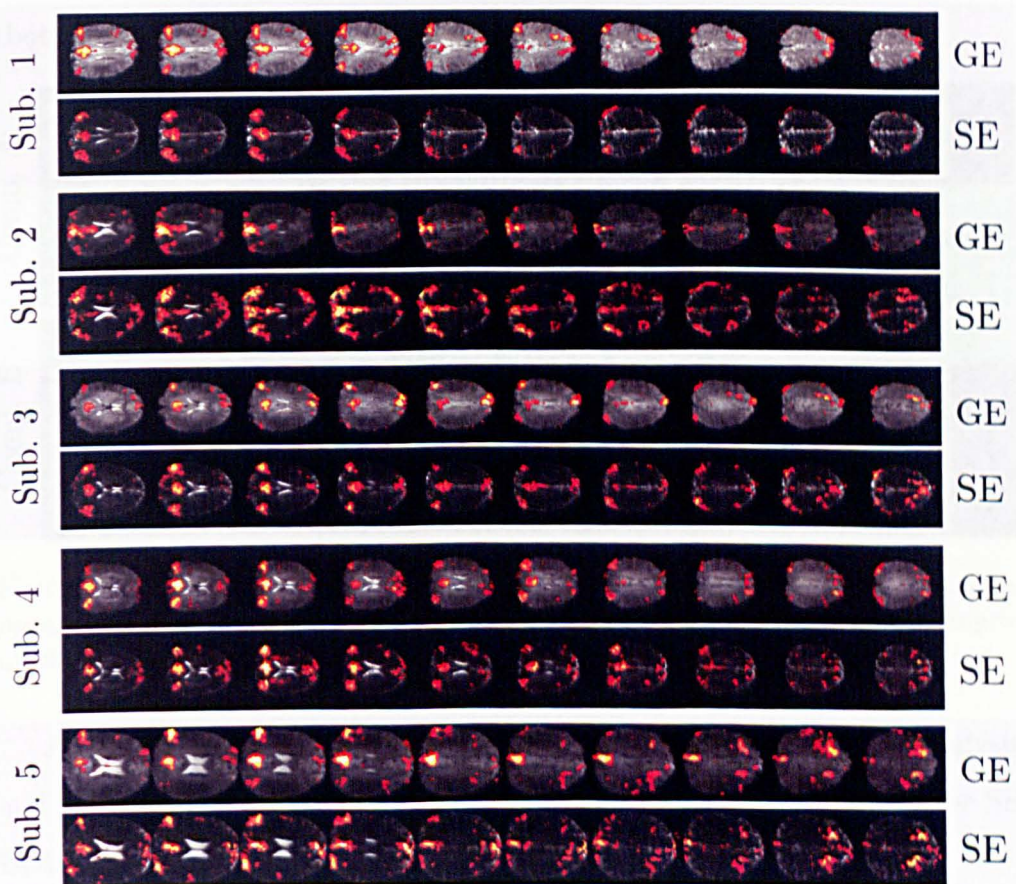


Figure 6.4: Example DMN components from ICA analysis are shown for all subjects overlaid onto the mean of the corresponding functional scans. Robust networks can be seen in both the GE and SE BOLD data.

The only effective method of calculating the optimum number of ICA components, in order to detect functional networks in the presence of signal artefacts whilst minimising network splitting, was to analyse each data set multiple times. For each run a different number of components was used, with the optimum number of components manually identified after processing. Consequently the number of components used ranged from between 40 and 120 depending on the data set. An example of some of the spatially correlated artefacts that were picked out using ICA are shown in Figure 6.5, while an example of the problem of network splitting can be seen in Figure 6.6, where ICA has split the DMN across two components. This can be better visualised when the ICA components are binarised and then overlaid onto one image (bottom image in Figure 6.6).

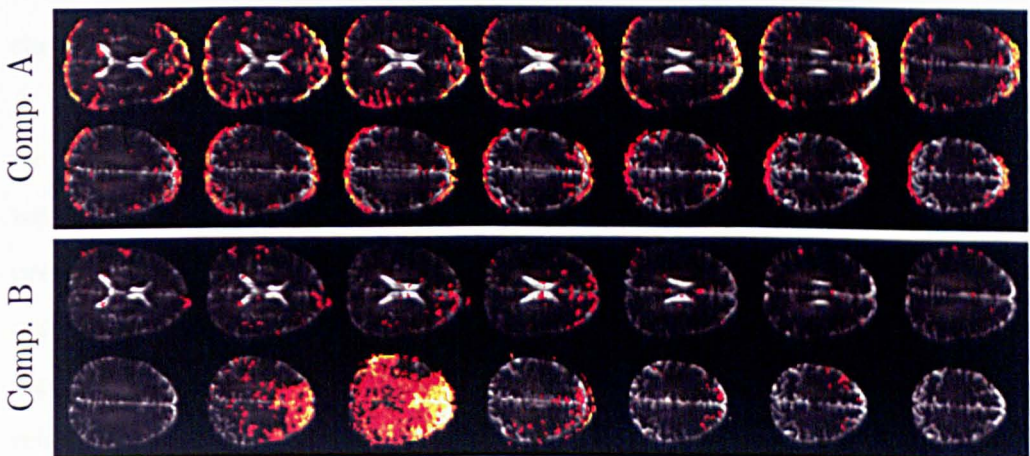


Figure 6.5: Two ICA components displaying image artefacts. The artefact in component A is most likely due to head motion during the functional acquisition (despite motion correction).

A number of other functional networks were detected during data analysis and are shown in Figure 6.7 for GE BOLD networks and Figure 6.8 for SE BOLD networks.

The variation of the GE and SE BOLD responses with TE can be seen in Figure 6.9. Analysis was carried out using the average signal in the respective GE and SE ICA masks. Two methods,  $\frac{\sigma(S)}{S}$  and  $\frac{\Delta S}{S}$ , were used to characterise

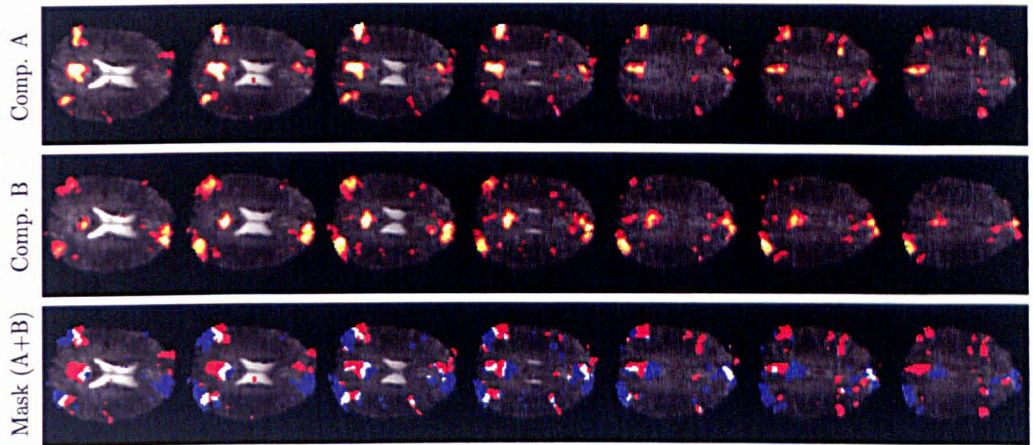


Figure 6.6: Two ICA components, calculated using a single functional data set, both displaying parts of the DMN. This network splitting can arise when trying to separate the data into too many statistically independent components using ICA. In the bottom image a mask of the two networks is shown, with component A in red, component B in blue and the overlapping regions in white.

the fluctuating BOLD signal.

For the first method we use the standard deviation of the signal over time to characterise the signal fluctuations (Figure 6.9). For the second method we use the difference between the maximum and minimum signal intensities present in the filtered time series,  $\Delta S$ , as an indicator of the magnitude of signal fluctuations. In both cases the signal variation was scaled by the average signal intensity. Both methods produced results that show an increase in relative signal variation with echo time.

The average  $T_2$ ,  $T_2^*$  and  $T_1$  values in each of the ICA DMN mask regions are given in Table 6.2.

ICA Mask	$T_1$	$T_2$	$T_2^*$
GE	1676 (17)	43.9 (1.2)	27.5 (1.5)
SE	1691 (14)	42.7 (1.0)	26.9 (1.3)
COM	1733 (28)	43.1 (1.4)	27.6 (1.8)

Table 6.2:  $T_2$ ,  $T_2^*$  and  $T_1$  values in each of the ICA mask regions. Times are in ms along with the standard error.

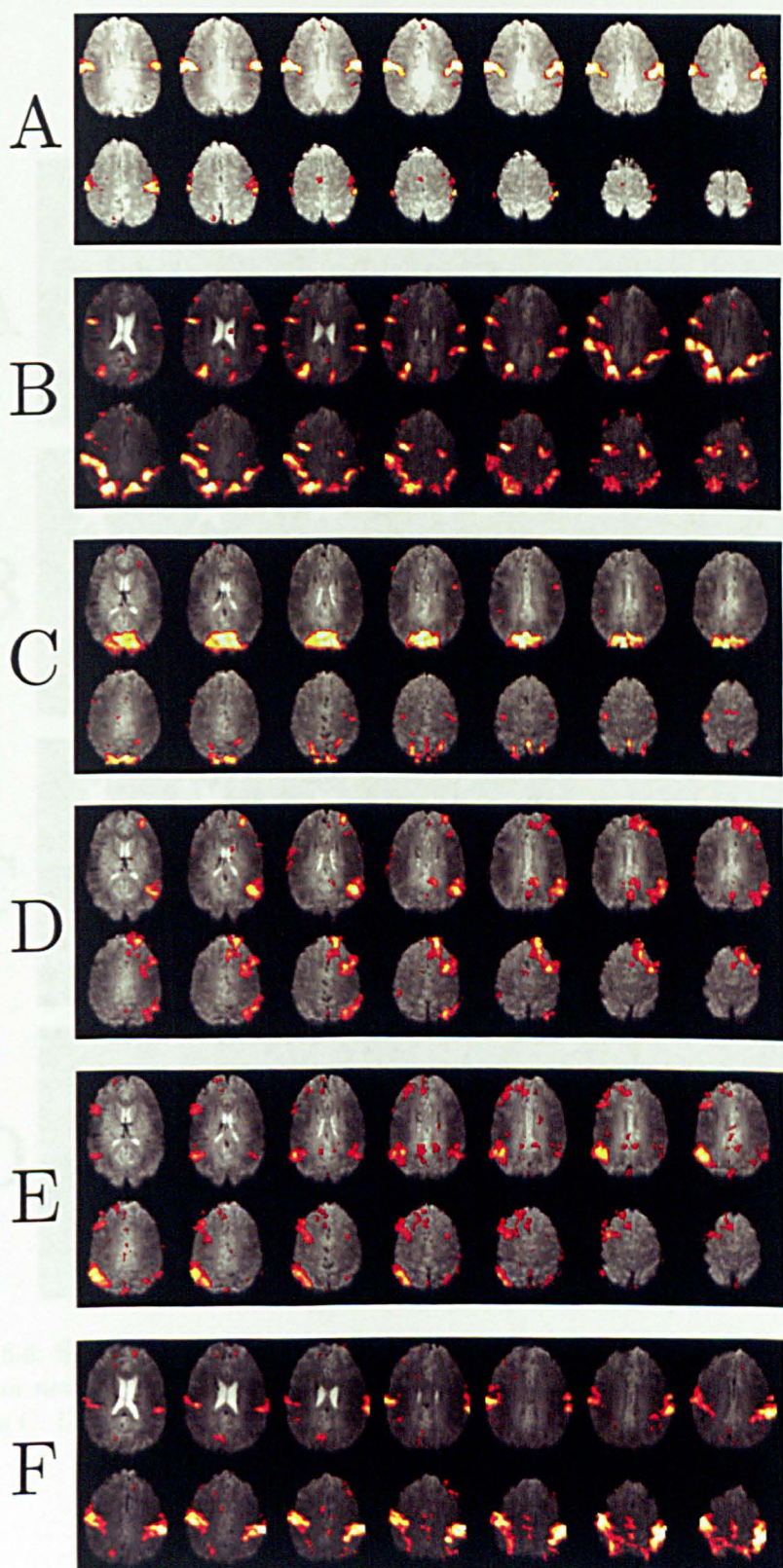


Figure 6.7: GE BOLD based resting state functional networks, detected using ICA.  
A: Motor network B: Network in the occipitotemporal (BA 37) and precentral (BA 4) areas C: Visual network D: Dorsal Attention Network (DAN) E: Dorsal Attention Network (Mirror of D) F: Somatosensory network

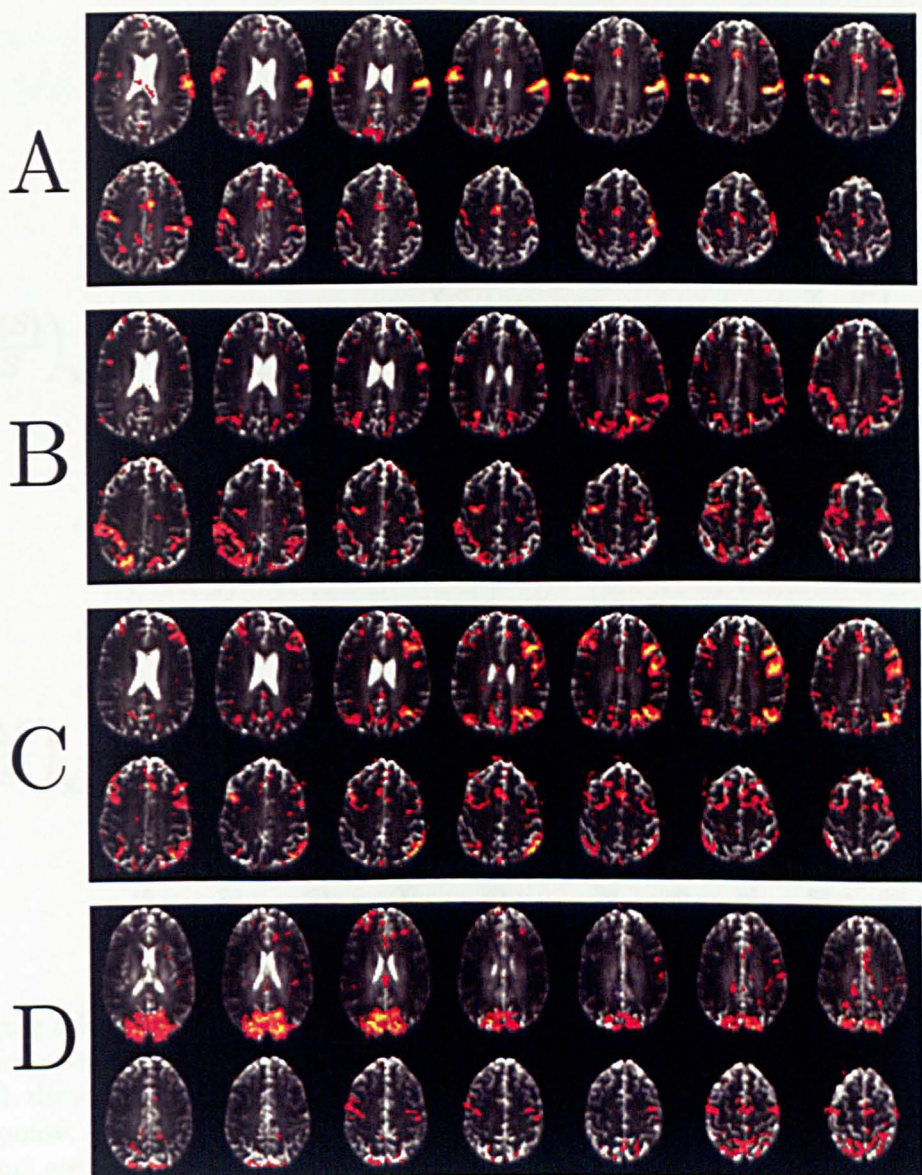


Figure 6.8: SE BOLD based resting state functional networks, detected using ICA.  
A: Motor network B: Network in the occipitotemporal (BA 37) and precentral (BA 4) areas C: Dorsal Attention Network D: Visual network

The following section between each functional ROI mask contains GE and SE data obtained by thresholding the subjects' images to show the following. The GE and SE ICA masks were used to examine whether any significant changes in the BOLD signal occur across the GE and SE data sets.

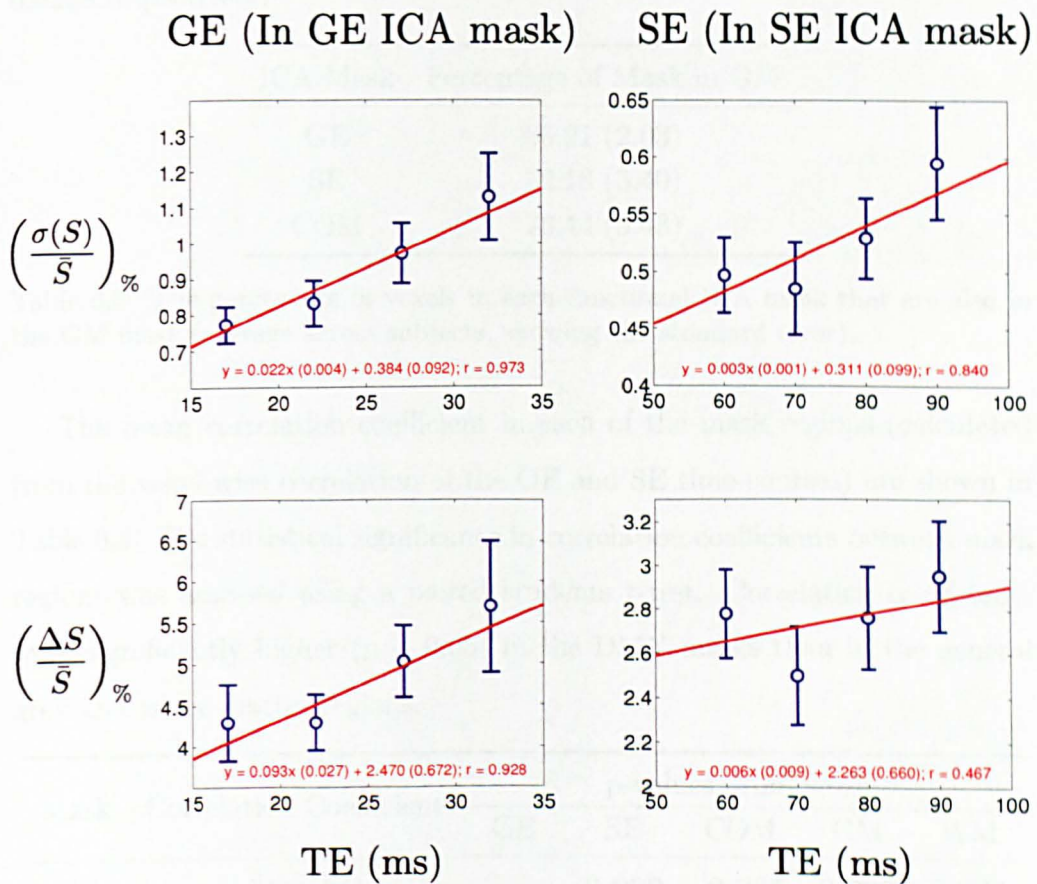


Figure 6.9: Changes in the BOLD signal vs TE for GE and SE data, using the average signal from each ROI. The average result across subjects is shown, along with the standard error. Two different measures are used to characterise the BOLD response,  $\frac{\sigma(S)}{\bar{S}}$  (top) and  $\frac{\Delta S}{\bar{S}}$  (bottom). Fits to the data (weighted by the standard error) are also shown.

The percentage overlap between each functional ICA mask and the GM mask (determined by thresholding each subjects T1 map) is shown in Table 6.3. The SE and COM ICA masks were found to contain a significantly higher number of voxels in GM than the GE ICA masks (with p-values of 0.0361 and 0.0228 respectively).

ICA Mask	Percentage of Mask in GM
GE	66.21 (2.03)
SE	72.18 (3.40)
COM	73.44 (3.43)

Table 6.3: The percentage of voxels in each functional ICA mask that are also in the GM mask (average across subjects, showing the standard error).

The mean correlation coefficient in each of the mask regions (calculated from the voxel-wise correlation of the GE and SE time-courses) are shown in Table 6.4. The statistical significance in correlation coefficients between mask regions was assessed using a paired students t-test. Correlation coefficients were significantly higher ( $p < 0.05$ ) in the DMN masks than in the general grey and white matter regions.

Mask	Correlation Coefficient	p-values, from t-test				
		GE	SE	COM	GM	WM
GE	0.64 (0.01)	-	<b>0.022</b>	<b>0.005</b>	<b>0.026</b>	<b>0.024</b>
SE	0.68 (0.01)	<b>0.022</b>	-	<b>0.035</b>	<b>0.005</b>	<b>0.011</b>
COM	0.69 (0.01)	<b>0.005</b>	<b>0.035</b>	-	<b>0.004</b>	<b>0.010</b>
GM	0.59 (0.01)	<b>0.026</b>	<b>0.005</b>	<b>0.004</b>	-	<b>0.024</b>
WM	0.47 (0.05)	<b>0.024</b>	<b>0.011</b>	<b>0.010</b>	<b>0.024</b>	-

Table 6.4: Correlation coefficients in the GE, SE and common DMN masks, as well as the general GM and WM regions. The standard error across subjects is shown in brackets. Differences between the mask regions were assessed using a paired students t-test (p-values are shown). All results demonstrate significance at  $p < 0.05$

An example correlation map is shown in Figure 6.10 alongside histograms

of the correlation coefficients in each of the separate mask regions. The histogram from the grey matter region peaks at a correlation coefficient of around 0.6. Conversely the white matter has a peak at around 0.2.

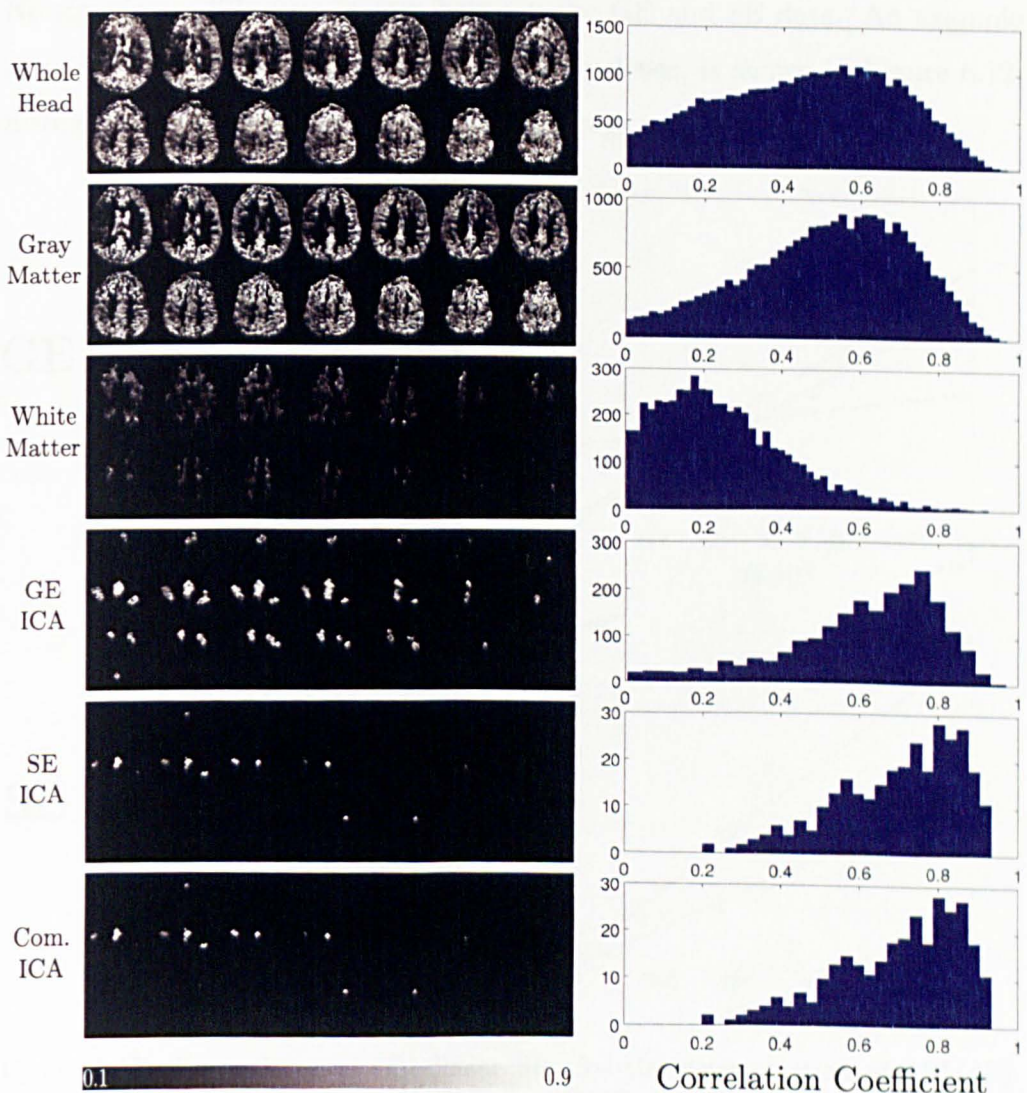


Figure 6.10: GE/SE correlation map for an example subject. Histograms displaying the correlation coefficient values in the different mask regions are also shown. (TE pair = 17/60 ms)

The results for the ratio of  $\delta R_2^*$  to  $\delta R_2$  are shown in Table 6.5. Regression analysis was carried out on a voxel wise basis and then averaged in each of the different mask regions and across subjects. Some examples of individual voxel-

wise linear fits are shown in Figure 6.11. From the average results across all subjects,  $\delta R_2^*/\delta R_2$  values were significantly higher in the GM than the WM. All DMN ICA masks were also found to be significantly higher than the WM. No significant difference is seen between the GE and SE data. An example ratio map, showing  $\delta R_2^*/\delta R_2$  on a voxel-wise basis, is shown in Figure 6.12, histograms are shown for each of the mask regions.

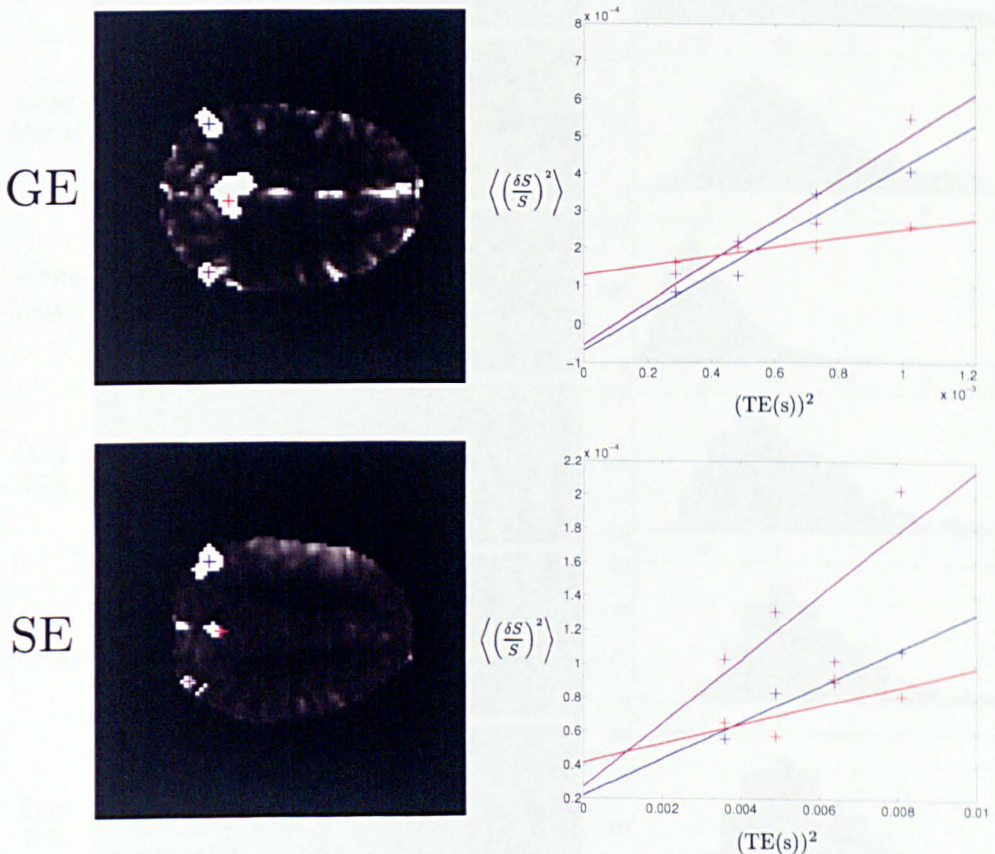


Figure 6.11: Example voxel-wise linear fits, for the determination of  $\delta R_2^*/\delta R_2$ . Results are shown for an example subject in DMN mask locations. Both GE and SE data are displayed.

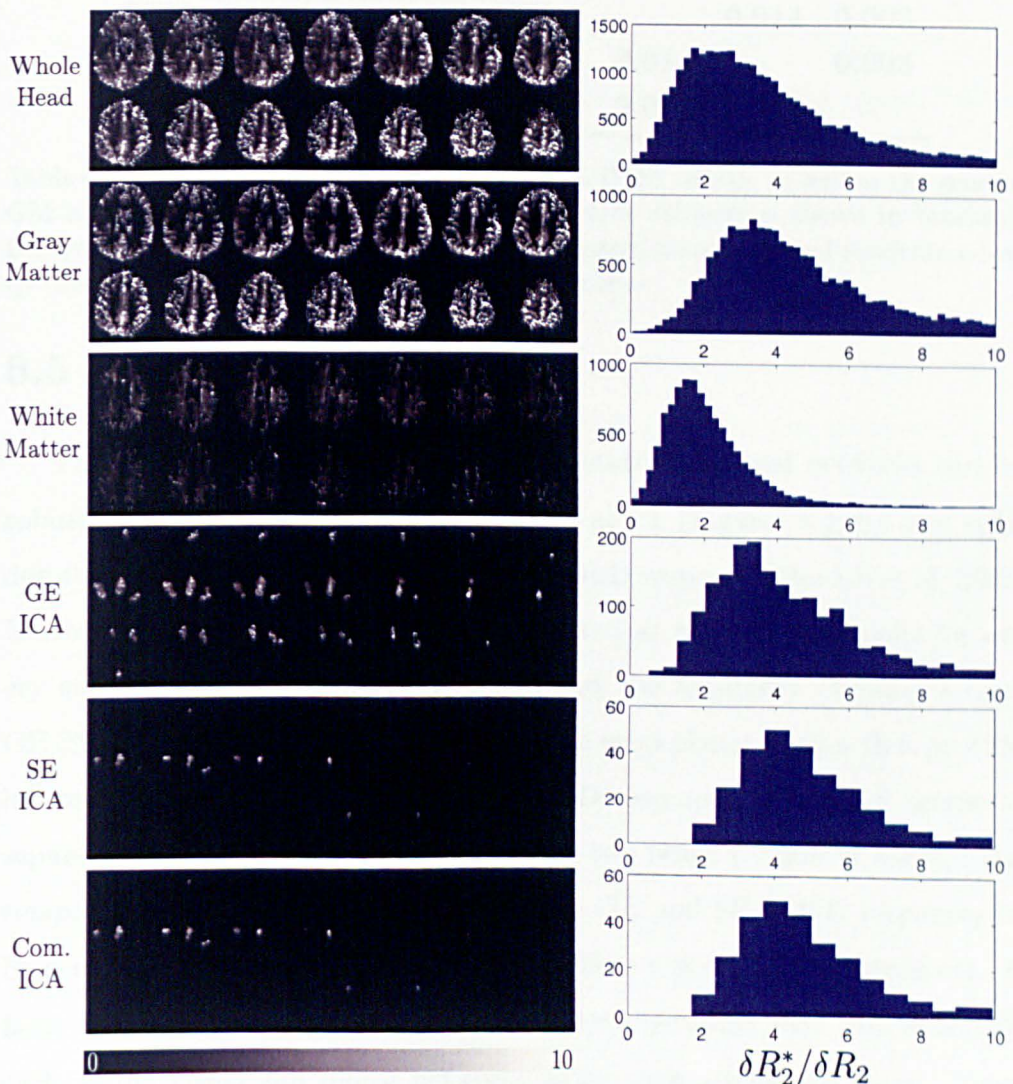


Figure 6.12:  $\delta R_2^*/\delta R_2$  map for an example subject. Histograms for the different mask regions are also shown.

Mask	$\delta R_2^*/\delta R_2$	p-values, from t-test				
		GE	SE	COM	GM	WM
GE	2.92 (0.18)	-	0.326	0.109	0.051	<b>0.000</b>
SE	3.12 (0.18)	0.326	-	0.704	<b>0.035</b>	<b>0.000</b>
COM	3.16 (0.13)	0.109	0.704	-	<b>0.014</b>	<b>0.000</b>
GM	2.47 (0.28)	0.051	<b>0.035</b>	<b>0.014</b>	-	<b>0.003</b>
WM	1.29 (0.12)	<b>0.000</b>	<b>0.000</b>	<b>0.000</b>	<b>0.003</b>	-

Table 6.5:  $\delta R_2^*/\delta R_2$  in the GE, SE and common DMN masks, as well as the general GM and WM regions. The standard error across subjects is shown in brackets. Differences between the mask regions were assessed using a paired students t-test (p-values are shown).  $p < 0.05$  indicates significance

## 6.5 Discussion

These results demonstrate that resting state functional networks can be robustly detected using SE-BOLD contrast at 7T (Figures 6.4, 6.7 and 6.8), despite the reduced sensitivity of the SE BOLD response (Yacoub et al. 2005, Harmer et al. 2011). The DMN was detected at all echo time pairs for every subject. Further we have demonstrated the feasibility of using a dual GE/SE EPI sequence in order to acquire two echo-planar images that provide information on both the GE and SE BOLD response. The small temporal separation between the acquisition of these two scans ( $\sim 50ms$ ) allowed the temporal characteristics of the resting state GE and SE BOLD responses to be accurately compared, in a manner not before reported in the literature. A large number of other, non-DMN, resting state networks were also detected, such as the visual and motor networks along with artefactual maps. Some examples are shown in Figures 6.7 and 6.8. We found that all the resting state default mode networks were highly localised to the grey matter regions, despite the spatial smoothing carried out as part of the ICA analysis.

Using the dual GE/SE data the resting state GE and SE BOLD signal fluctuations were scrutinised to assess how they changed with echo time. Due

to the resting state nature of these experiments an approximation to the temporal nature of the BOLD percentage signal change had to be made, due to the lack of task related ON and OFF states that one would typically use to determine this. Two different methods of characterising this change were used 1) the difference between the maximum and minimum signal intensities,  $\Delta S$ , present in the filtered time series data, scaled by the average signal, and 2) the standard deviation of the signal variation over time scaled by the average signal (Figure 6.9). Both indicate that the fractional GE BOLD signal (in the GE ICA mask) increases with TE in agreement with a number of studies in the literature (Yacoub et al. 2003, Duong et al. 2003, Schaefer et al. 2008). Whilst only method 2 showed a significant increase with TE for the SE BOLD data. This may be due to the increased sensitivity of method 1 to image artefacts. For example, if a brief spike in signal intensity occurs, due to the presence of a temporally succinct artefact that has not been removed by filtering,  $\Delta S/S$  will not provide a good approximation to the BOLD related signal change, whereas method 2 is less susceptible to this effect.

During the analysis of these data the number of ICA components that were used, in order to accurately detect the default mode network, varied across subjects due to the presence of signal artefacts. Significant changes in signal intensity, due to image artefacts, were detected as individual or multiple components during ICA analysis and had the effect of reducing the number of free components that were available to identify the networks of interest. Examples of some of these artefacts are shown in Figure 6.5. The artefact in component A is most likely due to inter-scan subject motion because the effect is seen most significantly at the boundaries between regions that have a high contrast difference, such as at the edge of the brain and around the ventricles. The large change in signal intensity at these boundaries is brought about due to voxels effectively moving along a high contrast gradient between the two regions. The ability of ICA to detect such artefacts make it a useful

tool for assessing the quality of functional data sets, in this case highlighting the imperfect nature of motion correction. In component B, ICA detects a further artefact where a significant fraction of the brain shows correlated signal variations in one slice. It is not clear what produced this artefact.

When a large number of components were employed during ICA, in an attempt to account for the effects of image artefacts, the networks of interest, such as the DMN, were often split across multiple components, as shown in Figure 6.6. To account for this effect, any split components that were found were combined together before data processing into a single mask region that was deemed to represent the whole DMN. This problem, of having no prior knowledge of the optimum number of ICA components to use, and the solution, which involved carrying out ICA on each data set multiple times using a different number of component for each run, highlights a time consuming problem associated with use of the ICA technique. In some promising recent work, Wang (2011) have attempted to address this problem using a constrained ICA model, where the number of components does not have to be pre-determined. They accomplish this by placing constraints on the source separation process, based on prior information. They suggest the method may be of particular benefit for analysis of resting state data because it is possible that constraint templates could be built using the large number of resting state networks that have already been detected in the literature. However, by its very nature, this type of constrained ICA (CICA) will be less data-driven than standard ICA methods.

To give an indication as to the spatial location of the DMN mask regions relative to the underlying grey matter, the spatial overlap between the SE and GE BOLD ICA masks and the grey matter mask were measured. The results demonstrated that the SE and common ICA masks have a tendency to be more grey matter specific than the GE ICA masks (p-values of 0.0361 and 0.0228 respectively), possibly due to the lower spatial specificity of the

GE BOLD response.

Signal correlations between the GE and SE BOLD data were found to be significantly higher in the GE, SE and common DMN ICA maps than in the grey matter as a whole. Signal correlations were significantly lower in the white matter than in the grey matter or DMN ICA masks. This is logical because if the majority of signal fluctuations (after filtering) are indeed due to the action of the BOLD response, brought about due to underlying neuronal processes, then the correlation should be higher in the grey matter where these responses take place. This can be seen to good effect in the example data set shown in Figure 6.10, where the correlation map appears to have effectively segmented the grey matter from the white matter. It should be noted that this delineation was not as clear for all subjects due to the adverse effects of some image artefacts causing a small, but noticeable base level correlation across the imaging volume. The higher correlation in the resting state network regions relative to the rest of the grey matter is also understandable because these resting state neuronal processes should occur over time-scales much longer than the temporal separation between the GE and SE BOLD data ( $> 50ms$ ) and thus be temporally synced. Provided that the same networks are present in both the GE and SE images, there should be a higher correlation in these regions than in the rest of the grey matter taken as a whole. The assumption that the SE BOLD response has a higher spatial specificity to underlying neuronal activity than the GE BOLD response, may explain the increased correlation between the two contrast mechanisms in the SE DMN in comparison to the GE DMN. If the SE BOLD response more accurately represents the true location of the underlying neuronal activity, then the more diffuse GE BOLD response should correlate more highly with the SE response in the SE mask regions than in the more diffuse GE mask regions. Whereas the entire SE mask region should correlate well with the GE mask region, leading to a higher average correlation value. This effect is indeed seen in the

data, with the correlation coefficient found to be significantly higher in the SE mask region than in the GE mask.

No significant differences for the ratio of  $\delta R_2^*/\delta R_2$  were found between the GE ( $2.92 \pm 0.18$ ), SE ( $3.12 \pm 0.18$ ) and common ( $3.16 \pm 0.13$ ) DMN ICA masks. However all of these values were found to be significantly higher than the value measured in white matter ( $1.29 \pm 0.12$ ) with both the SE and common regions also significantly higher than the grey matter region as a whole ( $2.47 \pm 0.28$ ). The results in resting state network regions agree well with the value of 2.6 measured by Yacoub et al. (2005) in the motor cortex at 7 T using a task based functional acquisition. This suggests that the technique that was described and implemented in this study in order to measure this ratio using non-task related functional resting state data, is indeed producing the results described in the theory (Section 6.3.5).

The ratio of  $\delta R_2^*/\delta R_2$  has been measured at a range of field strengths, using task related functional paradigms, by a number of different groups. In an early study at 1.5T Bandettini et al. (1994a) measured this value to be  $3.52 \pm 0.56$ , in further studies at 1.5T Lowe et al. (2000) and (Stroman et al. 2001) measured this as  $3.3 \pm 0.9$  and  $3.7$  respectively. At 3T Stroman et al. (2001) measured this as 3.8. There has been a lot of interest in the literature as to whether this ratio decreases with increasing field strength. For convenience, and to aid assessment of this, these values along with the average value taken from the GE and SE DMN ICA masks from this study are shown in Figure 6.13. The data indicates that there may well be a decrease in the ratio with increasing field strength however this reduction is relatively small. Yacoub et al. (2005) propose that the ratio as a whole may not show a strong decrease with increasing field strength due to the presence of both intra- and extra-vascular BOLD effects. They go on to suggest that only the extra-vascular component should decrease significantly with increasing field strengths.

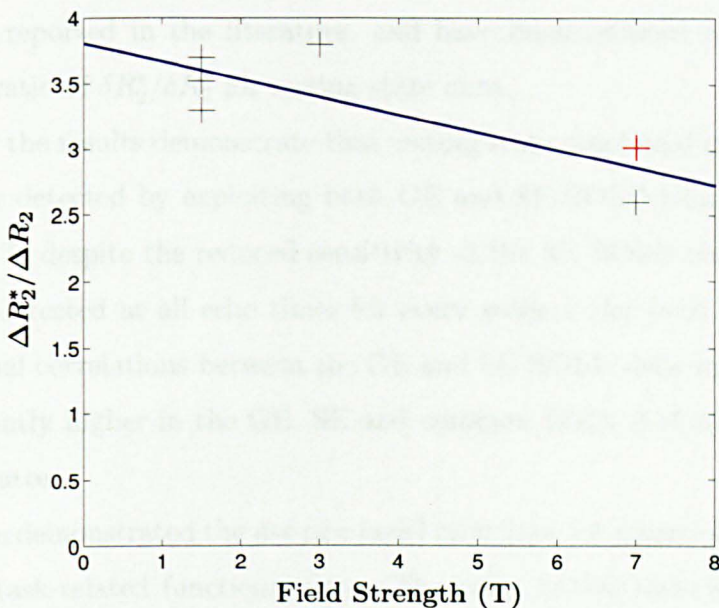


Figure 6.13:  $\delta R_2^*/\delta R_2$  using data taken from multiple studies in the literature (Bandettini et al. 1994a, Lowe et al. 2000, Stroman et al. 2001, Yacoub et al. 2005), including the average value taken from the SE and GE ICA mask in this study (red cross). The blue line shows a linear fit to the data  $y = -0.13x + 3.8$  ( $R^2 = 0.65$ )

The extra information gained by measuring both GE and SE BOLD data, with a low temporal separation, during a functional acquisition, along with the methods demonstrated for assessing the nature of the BOLD response, should prove useful in a wide range of functional studies.

## 6.6 Conclusion

We have demonstrated the feasibility of using a dual GE/SE EPI sequence in order to acquire two echo-planar images that provide information on both the GE and SE BOLD response, that are time synchronised; by exploiting the high SNR available at 7 T and when imaging with a 32 channel receive coil. We have demonstrated that the correspondingly small temporal separation between the GE and SE data ( $\sim 50ms$ ) allows the temporal characteristics of the resting state GE and SE BOLD responses to be compared, in a manner

not before reported in the literature, and have demonstrated a method to assess the ratio of  $\delta R_2^*/\delta R_2$  for resting state data.

Further the results demonstrate that resting state functional networks can be robustly detected by exploiting both GE and SE-BOLD contrast mechanisms at 7 T, despite the reduced sensitivity of the SE BOLD response. The DMN was detected at all echo times for every subject (for both GE and SE data). Signal correlations between the GE and SE BOLD data were found to be significantly higher in the GE, SE and common DMN ICA maps than in the grey matter.

We have demonstrated the use of a novel technique for measuring  $\delta R_2^*/\delta R_2$  using non task-related functional data. The value of this ratio in the DMN regions agrees well with published results from other groups that have used functional task related paradigms to estimate  $\delta R_2^*/\delta R_2$ .

# Chapter 7

## Conclusion

The work presented in this thesis is directed towards the development and implementation of a number of ideas and methods that allow echo-planar imaging to be carried out for fMRI at ultra high field strength (7 T), despite the significant problems associated with implementing fMRI at high field. Techniques have been presented that enable off-resonance effects, that plague this type of acquisition, to be measured on a dynamic basis (and subsequently corrected for), for both GE and SE EPI data.

In the first study (**Chapter 4**) a method is presented that takes advantage of the increase in BOLD CNR at ultra high field strength, to enable fMRI to be carried out using both gradient echo and spin echo EPIs at high spatial resolution during a motor task. These findings show that the relative location of activated voxels for the GE and SE BOLD responses, differs significantly. Further, using sensitive venous mapping techniques, the results also demonstrate that regions showing statistically significant activation in GE EPI data contain significantly more voxels overlying venous blood vessels sites than activated regions identified in SE EPI data. These results lend strong weight to theories in the literature that suggest that SE BOLD contrast is actually sensitive to different underlying physiological mechanisms than GE BOLD contrast. It suggests that the SE BOLD response arises due to the extravascular magnetic

susceptibility effects around small blood vessels, and that in contrast the GE BOLD response is sensitive to the extravascular effects around both small and large blood vessels, with the large vessel effects dominating. This points to the fact that the SE BOLD response is indeed more spatially specific to the underlying neuronal activation and thus, in situations where enough SNR is available (such as at high field strengths), may be a more powerful tool for probing neurological processes than standard GE based techniques. This work has now been published (Harmer et al. 2011).

The second study described in this thesis (**Chapter 5**) probes the effect that magnetic field inhomogeneities have on EPI acquisitions. First, a technique is introduced that can be employed to measure  $\Delta B_0$  on a dynamic basis during a functional hyperoxia experiment. This is used to assess the size of susceptibility effects that occur, due to increased levels of oxygen concentration, during hyperoxia. The findings show that the effects are global in nature, extending over the whole head, and that the field offsets, due to hyperoxia alone, are largest in the frontal sinus, but still present in both the motor and visual cortices. Consequently, the author recommends that this simple to implement technique should be used during all hyperoxia studies so that the induced temporal variations in  $\Delta B_0$  can be monitored and if necessary corrected for (for example to aid image registration). This may also prove helpful when analysing data at a group level, where initial registration to a template is required. In the second section of this chapter a unique solution is described that enables dynamic off resonance correction of SE EPI data that circumvents the problem associated with using a SE sequence to measure  $\Delta B_0$ . This technique is developed further to show that it can be used to collect GE and SE EPI data simultaneously whilst allowing dynamic distortion correction of both the GE and SE data sets. This principle is demonstrated in a preliminary study where dynamic distortion correction is carried out on GE and SE EPI data collected during auditory and motor fMRI studies. Hence,

this chapter describes a unique method that allows highly accurate dynamic distortion correction to be carried out on simultaneously acquired GE and SE EPI data using just one initial reference scan. Correcting for off-resonance effects in this manner allows improved alignment to anatomical data, which may be particularly advantageous for techniques such as the cortical flattening of activation patterns.

In **Chapter 6**, the final study in this thesis, a dual GE/SE EPI sequence is used to probe the resting state BOLD response and identify functional connectivity maps in SE- and GE-BOLD data. The work demonstrates how the correspondingly small temporal separation between the GE and SE data ( $\sim 50ms$ ) that this sequence provides, allows the temporal characteristics of the resting state GE and SE BOLD responses to be compared, in a manner not previously reported in the literature. This is used to assess correlated fluctuations in  $T_2^*$ - and  $T_2$ -weighted images across multiple echo times in the default mode network and other areas. Signal correlations between the GE and SE BOLD data are found to be significantly higher in the default mode network regions than in the gray matter as a whole. Further, a novel technique for measuring  $\delta R_2^*/\delta R_2$  using non task-related resting state data is also described. The results for this in the DMN regions agree well with published results from other groups that use normal functional task related paradigms with a definite functional ON and OFF period.

# Bibliography

- Bandettini, P. a., Wong, E. C., Jesmanowicz, a., Hinks, R. S. & Hyde, J. S. (1994a), 'Spin-echo and gradient-echo EPI of human brain activation using BOLD contrast: a comparative study at 1.5 T.', *NMR in biomedicine* **7**(1-2), 12–20.
- Bandettini, P. A., Wong, E. C., Jesmanowicz, A., Hinks, R. S. & Hyde, J. S. (1994b), 'Spin-echo and gradient-echo EPI of human brain activation using BOLD contrast: a comparative study at 1.5 T.', *NMR in biomedicine* **7**(1-2), 12–20.
- Barth, M. & Moser, E. (1997), 'Proton NMR relaxation times of human blood samples at 1.5 T and implications for functional MRI.', *Cellular and molecular biology NoisyleGrand France* **43**(5), 783–791.
- Beckmann, C. F., DeLuca, M., Devlin, J. T. & Smith, S. M. (2005), 'Investigations into resting-state connectivity using independent component analysis'. *Philosophical Transactions of the Royal Society of London - Series B: Biological Sciences* **360**(1457), 1001–1013.
- Beckmann, C. F. & Smith, S. M. (2004), 'Probabilistic independent component analysis for functional magnetic resonance imaging.', *IEEE transactions on medical imaging* **23**(2), 137–52.
- Bernstein, M. A., Grgic, M., Brosnan, T. J. & Pelc, N. J. (1994), 'Reconstructions of phase contrast, phased array multicoil data.', *Magnetic Resonance in Medicine* **32**(3), 330–334.
- Bianciardi, M., Fukunaga, M., Van Gelderen, P., Horovitz, S. G., De Zwart, J. A., Shmueli, K. & Duyn, J. H. (2009), 'Sources of functional magnetic resonance imaging signal fluctuations in the human brain at rest: a 7 T study.', *Magnetic Resonance Imaging* **27**(8), 1019–1029.
- Biswal, B., Yetkin, F. Z., Haughton, V. M. & Hyde, J. S. (1995), 'Functional connectivity in the motor cortex of resting human brain using echo-planar MRI.', *Magnetic Resonance in Medicine* **34**(4), 537–41.

- Bloch, F. (1946), 'Nuclear Induction (Bloch 1946)', *Physical Review* **70**(7 and 8).
- Blockley, N. P., Driver, I. D., Fisher, J. a., Francis, S. T. & Gowland, P. a. (2012), 'Measuring venous blood volume changes during activation using hyperoxia.', *NeuroImage* **59**(4), 3266–74.
- Bluhm, R., Williamson, P., Lanius, R., Théberge, J., Densmore, M., Bartha, R., Neufeld, R. & Osuch, E. (2009), 'Resting state default-mode network connectivity in early depression using a seed region-of-interest analysis: decreased connectivity with caudate nucleus.', *Psychiatry and clinical neurosciences* **63**(6), 754–61.
- Boxerman, J. L., Bandettini, P. a., Kwong, K. K., Baker, J. R., Davis, T. L., Rosen, B. R. & Weisskoff, R. M. (1995), 'The intravascular contribution to fMRI signal change: Monte Carlo modeling and diffusion-weighted studies in vivo.', *Magnetic Resonance in Medicine* **34**(1), 4–10.
- Buckner, R. L., Andrews-Hanna, J. R. & Schacter, D. L. (2008), 'The brain's default network: anatomy, function, and relevance to disease.', *Annals of the New York Academy of Sciences* **1124**, 1–38.
- Buckner, R. L., Bandettini, P. A., O'Craven, K. M., Savoy, R. L., Petersen, S. E., Raichle, M. E. & Rosen, B. R. (1996), 'Detection of cortical activation during averaged single trials of a cognitive task using functional magnetic resonance imaging.', *Proceedings of the National Academy of Sciences of the United States of America* **93**(25), 14878–14883.
- Bulte, D., Chiarelli, P., Wise, R. & Jezzard, P. (2007), 'Measurement of Cerebral Blood Volume in Humans Using Hyperoxic MRI Contrast', *Journal of Magnetic Resonance Imaging* **1**, 894–899.
- Buonocore, M. H. & Zhu, D. C. (2001), 'Image-based ghost correction for interleaved EPI'. *Magnetic resonance in medicine : official journal of the Society of Magnetic Resonance in Medicine / Society of Magnetic Resonance in Medicine* **45**(1), 96–108.
- Bydder, G. M. & Young, I. R. (1985), 'MR imaging: clinical use of the inversion recovery sequence', *J Comput Assist Tomogr* **9**(4), 659–675.
- Chen, N.-K. & Wyrwicz, A. M. (1999), 'Correction for EPI distortions using multi-echo gradient-echo imaging.', *Magn Reson Med* **41**(6), 1206–1213.
- Chiarelli, P. A., Bulte, D. P., Wise, R., Gallichan, D. & Jezzard, P. (2007), 'A calibration method for quantitative BOLD fMRI based on hyperoxia', *37*, 808–820.

- Chiou, J.-Y., Ahn, C. B., Muftuler, L. T. & Nalcioglu, O. (2003), 'A simple simultaneous geometric and intensity correction method for echo-planar imaging by EPI-based phase modulation.', *IEEE transactions on medical imaging* **22**(2), 200–5.
- Clare, S. & Jezzard, P. (2001), 'Rapid T(1) mapping using multislice echo planar imaging.', *Magnetic Resonance in Medicine* **45**(4), 630–4.
- Cole, D. M., Smith, S. M. & Beckmann, C. F. (2010), 'Advances and pitfalls in the analysis and interpretation of resting-state fMRI data.', *Frontiers in systems neuroscience* **4**(April), 8.
- Comon, P. (1994), 'Independent Component Analysis - a new concept?', *Signal Processing* **36** 287314 .
- Cordes, D., Haughton, V. M., Arfanakis, K., Carew, J. D., Turski, P. A., Moritz, C. H., Quigley, M. A. & Meyerand, M. E. (2001), 'Frequencies contributing to functional connectivity in the cerebral cortex in "resting-state" data', *AJNR Am J Neuroradiol* **22**(7), 1326–1333.
- Cordes, D., Haughton, V. M., Arfanakis, K., Wendt, G. J., Turski, P. A., Moritz, C. H., Quigley, M. A. & Meyerand, M. E. (2000), 'Mapping functionally related regions of brain with functional connectivity MR imaging.', *AJR American Journal Of Neuroradiology* **21**(9), 1636–1644.
- Cox, D. D. & Savoy, R. L. (2003), 'Functional magnetic resonance imaging (fMRI) "brain reading": detecting and classifying distributed patterns of fMRI activity in human visual cortex.', *NeuroImage* **19**(2 Pt 1), 261–270.
- Cox, E. F. & Gowland, P. A. (2010), 'Simultaneous quantification of T2 and T'2 using a combined gradient echo-spin echo sequence at ultrahigh field.', *Magnetic Resonance in Medicine* **64**(5), 1440–1445.
- Cox, R. W. (1996), 'AFNI: software for analysis and visualization of functional magnetic resonance neuroimages.', *Computers and biomedical research an international journal* **29**(3), 162–173.
- De Luca, M., Beckmann, C. F., De Stefano, N., Matthews, P. M. & Smith, S. M. (2006), 'fMRI resting state networks define distinct modes of long-distance interactions in the human brain.', *NeuroImage* **29**(4), 1359–1367.
- de Moortele, P.-F. V., Akgun, C., Adriany, G., Moeller, S., Ritter, J., Collins, C. M., Smith, M. B., Vaughan, J. T. & Uurbil, K. (2005), 'B(1) destructive interferences and spatial phase patterns at 7 T with a head transceiver array coil.', *Magn Reson Med* **54**(6), 1503–1518.

- Di Salle, F., Formisano, E., Linden, D. E., Goebel, R., Bonavita, S., Pepino, A., Smaltino, F. & Tedeschi, G. (1999), 'Exploring brain function with magnetic resonance imaging.', *European Journal of Radiology* **30**(2), 84-94.
- Duong, T. Q., Yacoub, E., Adriany, G., Hu, X., Ugurbil, K. & Kim, S.-G. (2003), 'Microvascular BOLD contribution at 4 and 7 T in the human brain: gradient-echo and spin-echo fMRI with suppression of blood effects.', *Magnetic Resonance in Medicine* **49**(6), 1019-27.
- Duong, T. Q., Yacoub, E., Adriany, G., Hu, X., Ugurbil, K., Vaughan, J. T., Merkle, H. & Kim, S.-G. (2002), 'High-resolution, spin-echo BOLD, and CBF fMRI at 4 and 7 T.', *Magnetic Resonance in Medicine* **48**(4), 589-93.
- Fox, M. D. & Raichle, M. E. (2007), 'Spontaneous fluctuations in brain activity observed with functional magnetic resonance imaging.', *Nature Reviews Neuroscience* **8**(9), 700-711.
- Fox, M. D., Snyder, A. Z., Zacks, J. M. & Raichle, M. E. (2006), Coherent spontaneous activity accounts for trial-to-trial variability in human evoked brain responses., Technical Report 1, Department of Radiology, Washington University in St. Louis, St. Louis, Missouri 63110, USA. foxm@npg.wustl.edu.
- Fox, P. T. & Raichle, M. E. (1986), 'Focal physiological uncoupling of cerebral blood flow and oxidative metabolism during somatosensory stimulation in human subjects.', *Proceedings of the National Academy of Sciences of the United States of America* **83**(4), 1140-1144.
- Friston, K. J. (1996), Statistical parametric mapping and other analyses of functional imaging data, in A. W. Toga & J. C. Mazziotta, eds, 'Brain Mapping The Methods', Academic Press, pp. 363-386.
- Friston, K. J., Josephs, O., Rees, G. & Turner, R. (1998), 'Nonlinear event-related responses in fMRI'. *Magnetic Resonance in Medicine* **39**(1), 41-52.
- Garcia, D. (2010), 'Robust smoothing of gridded data in one and higher dimensions with missing values'. *Computational Statistics & Data Analysis* **54**(4), 1167-1178.
- Gardener, A. G., Francis, S. T., Prior, M., Peters, A. & Gowland, P. A. (2010), 'Dependence of blood R2 relaxivity on CPMG echo-spacing at 2.35 and 7 T.', *Magnetic Resonance in Medicine* **64**(4), 967-974.

- Gati, J. S., Menon, R. S., Ugurbil, K. & Rutt, B. K. (1997), 'Experimental determination of the BOLD field strength dependence in vessels and tissue.', *Magnetic Resonance in Medicine* **38**(2), 296–302.
- Goldman, R. I., Stern, J. M., Engel Jr., J. & Cohen, M. S. (2002), 'Simultaneous EEG and fMRI of the alpha rhythm', *NeuroReport* **13**(18), 2487–2492.
- Gomori, J. M., Holland, G. A., Grossman, R. I., Gefter, W. B. & Lenkinski, R. E. (1988), 'Fat suppression by section-select gradient reversal on spin-echo MR imaging. Work in progress.', *Radiology* **168**(2), 493–495.
- Goutte, C., Nielsen, F. A. & Hansen, L. K. (2000), 'Modeling the haemodynamic response in fMRI using smooth FIR filters.', *IEEE Trans Med Imaging* **19**(12), 1188–1201.
- Greicius, M. D., Krasnow, B., Reiss, A. L. & Menon, V. (2003), 'Functional connectivity in the resting brain: a network analysis of the default mode hypothesis.', *Proceedings of the National Academy of Sciences of the United States of America* **100**(1), 253–258.
- Grill-Spector, K. & Malach, R. (2004), 'fMR-adaptation: a tool for studying the functional properties of human cortical neurons.', *Acta Psychologica* **107**(1-3), 293–321.
- Gusnard, D. A. & Raichle, M. E. (2001), 'Searching for a baseline: functional imaging and the resting human brain.', *Nature Reviews Neuroscience* **2**(10), 685–694.
- Haacke, E. M., Brown, R. W., Thompson, M. R. & Venkatesan, R. (1999), *Magnetic Resonance Imaging: Physical Principles and Sequence Design*, Vol. 1st, Wiley-Liss.
- Haacke, E. M., Cheng, N. Y. C., House, M. J., Liu, Q., Neelavalli, J., Ogg, R. J., Khan, A., Ayaz, M., Kirsch, W. & Obenauer, A. (2005), 'Imaging iron stores in the brain using magnetic resonance imaging.', *Magn Reson Imaging* **23**(1), 1–25.
- Hahn, A. D., Nencka, A. S. & Rowe, D. B. (2009), 'Improving robustness and reliability of phase-sensitive fMRI analysis using temporal off-resonance alignment of single-echo timeseries (TOAST).', *NeuroImage* **44**(3), 742–52.
- Hahn, E. L. (1950). 'Spin Echoes', *Physical Review* **80**(4), 580–594.
- Hale, J. R., Brookes, M. J., Hall, E. L., Zumer, J. M., Stevenson, C. M., Francis, S. T. & Morris, P. G. (2010), 'Comparison of functional connectivity

- in default mode and sensorimotor networks at 3 and 7T.', *Magma New York NY* **23**(5-6), 339–349.
- Harmer, J., Sanchez-Panchuelo, R. M., Bowtell, R. & Francis, S. T. (2011), 'Spatial location and strength of BOLD activation in high-spatial-resolution fMRI of the motor cortex: a comparison of spin echo and gradient echo fMRI at 7T.', *NMR in biomedicine* (January).
- Hutton, C., Bork, A., Josephs, O., Deichmann, R., Ashburner, J. & Turner, R. (2002), 'Image distortion correction in fMRI: A quantitative evaluation.', *NeuroImage* **16**(1), 217–40.
- Iadecola, C. (1993), 'Regulation of the cerebral microcirculation during neural activity: is nitric oxide the missing link?', *Trends in neurosciences* **16**(6), 206–14.
- Jezzard, P. & Balaban, R. S. (1995), 'Correction for geometric distortion in echo planar images from B0 field variations.', *Magnetic Resonance in Medicine* **34**(1), 65–73.
- Jezzard, P., Matthews, P. M. & Smith, S. M. (2003), *Functional MRI : An Introduction to Methods*, Vol. 17, Oxford University Press.
- Jin, M., Pelak, V. S. & Cordes, D. (2011), 'Aberrant default mode network in subjects with amnestic mild cognitive impairment using resting-state functional MRI.', *Magnetic resonance imaging* **30**(1), 48–61.
- Kadah, Y. M. & Hu, X. (1997), 'Simulated phase evolution rewinding (SPHERE): a technique for reducing B0 inhomogeneity effects in MR images.', *Magn Reson Med* **38**(4), 615–627.
- Kaldoudi, E., Williams, S. C., Barker, G. J. & Tofts, P. S. (1993), 'A chemical shift selective inversion recovery sequence for fat-suppressed MRI: theory and experimental validation.', *Magn Reson Imaging* **11**(3), 341–355.
- Kamitani, Y. & Tong, F. (2006), 'Decoding seen and attended motion directions from activity in the human visual cortex.', *Current Biology* **16**(11), 1096–1102.
- Kiviniemi, V., Kantola, J.-H., Jauhainen, J., Hyvärinen, A. & Tervonen, O. (2003), 'Independent component analysis of nondeterministic fMRI signal sources.', *NeuroImage* **19**(2 Pt 1), 253–260.
- Lai, S., Hopkins, A. L., Haacke, E. M., Li, D., Wasserman, B. A., Buckley, P., Friedman, L., Meltzer, H., Hedera, P. & Firedland, R. (1993), Identification of Vascular Structures as a Major Source of Signal Contrast in High Resolution 2D and 3 D Functional Activation Imaging of the Motor Cortex at 1, in 'T Preliminary Results', Vol. 30, pp. 387–392.

- Lamberton, F., Delcroix, N., Grenier, D., Mazoyer, B. & Joliot, M. (2007), 'A new EPI-based dynamic field mapping method: application to retrospective geometrical distortion corrections.', *Journal of magnetic resonance imaging : JMRI* **26**(3), 747-55.
- Laufs, H., Kleinschmidt, A., Beyerle, A., Eger, E., Salek-Haddadi, A., Preibisch, C. & Krakow, K. (2003), 'EEG-correlated fMRI of human alpha activity', *NeuroImage* **19**(4), 1463-1476.
- Lee, A. T., Glover, G. H. & Meyer, C. H. (1995), 'Discrimination of large venous vessels in time-course spiral blood-oxygen-level-dependent magnetic-resonance functional neuroimaging.', *Magn Reson Med* **33**(6), 745-754.
- Li, T.-Q., van Gelderen, P., Merkle, H., Talagala, L., Koretsky, A. P. & Duyn, J. (2006), 'Extensive heterogeneity in white matter intensity in high-resolution T2\*-weighted MRI of the human brain at 7.0 T.', *Neuroimage* **32**(3), 1032-1040.
- Logothetis, N. K., Pauls, J., Augath, M., Trinath, T. & Oeltermann, A. (2001), 'Neurophysiological investigation of the basis of the fMRI signal', *Nature* **412**(6843), 150-157.
- Lowe, M. J., Lurito, J. T., Mathews, V. P., Phillips, M. D. & Hutchins, G. D. (2000), 'Quantitative comparison of functional contrast from BOLD-weighted spin-echo and gradient-echo echoplanar imaging at 1.5 Tesla and H<sub>2</sub> 15O PET in the whole brain.', *Journal of cerebral blood flow and metabolism : official journal of the International Society of Cerebral Blood Flow and Metabolism* **20**(9), 1331-40.
- Lowe, M. J., Mock, B. J. & Sorenson, J. A. (1998), Functional connectivity in single and multislice echoplanar imaging using resting-state fluctuations., Technical Report 2, Department of Medical Physics, University of Wisconsin, Madison, USA.
- Luo, Y., De Graaf, R. A., DelaBarre, L., Tannús, A. & Garwood, M. (2001), 'BISTRO: an outer-volume suppression method that tolerates RF field inhomogeneity.', *Magnetic Resonance in Medicine* **45**(6), 1095-1102.
- Maldjian, J., Atlas, S. W. & Howard Et Al, R. S. (1996), 'Functional magnetic resonance imaging of regional brain activity in patients with intracerebral arteriovenous malformations before surgical or endovascular therapy', *Journal Of Neurosurgery* **84**, 477-483.
- Mansfield, P. (1977), 'Multi-planar image formation using NMR spin echoes', *Journal of Physics C Solid State Physics* **10**(3), L55-L58.

- Marchini, J. L. & Ripley, B. D. (2000), 'A new statistical approach to detecting significant activation in functional MRI.', *NeuroImage* **12**(4), 366–80.
- Matthews, P. M., Honey, G. D. & Bullmore, E. T. (2006), 'Applications of fMRI in translational medicine and clinical practice.', *Nature Reviews Neuroscience* **7**(9), 732–744.
- McRobbie, D. W., Moore, E. A., Graves, M. J. & Prince, M. R. (2003), *MRI from Picture to Proton*, Cambridge University Press.
- Menon, R. S. & Goodyear, B. G. (1999), 'Submillimeter functional localization in human striate cortex using BOLD contrast at 4 Tesla: implications for the vascular point-spread function.', *Magnetic Resonance in Medicine* **41**(2), 230–5.
- Michelich, C. R., Song, A. W. & Macfall, J. R. (2006), 'Dependence of gradient-echo and spin-echo BOLD fMRI at 4 T on diffusion weighting.', *NMR in biomedicine* **19**(5), 566–72.
- Mitra, P. P., Ogawa, S., Hu, X. & Uurbil, K. (1997), 'The nature of spatiotemporal changes in cerebral hemodynamics as manifested in functional magnetic resonance imaging.', *Magnetic Resonance in Medicine* **37**(4), 511–518.
- Mosso, A. (1881), *Über den Kreislauf des Blutes im menschlichen Gehirn : Untersuchungen*, von Veit.
- Nagy, Z. & Weiskopf, N. (2008), 'Efficient fat suppression by slice-selection gradient reversal in twice-refocused diffusion encoding.', *Magn Reson Med* **60**(5), 1256–1260.
- Nestares, O. & Heeger, D. J. (2000), 'Robust multiresolution alignment of MRI brain volumes.', *Magnetic Resonance in Medicine* **43**(5), 705–15.
- Ogawa, S., Menon, R. S., Tank, D. W., Kim, S. G., Merkle, H., Ellermann, J. M. & Ugurbil, K. (1993), 'Functional brain mapping by blood oxygenation level-dependent contrast magnetic resonance imaging. A comparison of signal characteristics with a biophysical model.', *Biophys J* **64**(3), 803–812.
- Ogawa, S., Tank, D. W., Menon, R., Ellermann, J. M., Kim, S. G., Merkle, H. & Ugurbil, K. (1992), 'Intrinsic signal changes accompanying sensory stimulation: functional brain mapping with magnetic resonance imaging.', *Proceedings of the National Academy of Sciences of the United States of America* **89**(13), 5951–5.

- Oja, J. M., Gillen, J., Kauppinen, R. A., Kraut, M. & Van Zijl, P. C. (1999), 'Venous blood effects in spin-echo fMRI of human brain.', *Magnetic Resonance in Medicine* **42**(4), 617–626.
- Olman, C. a., Van de Moortele, P.-F., Schumacher, J. F., Guy, J. R., Urbil, K. & Yacoub, E. (2010), 'Retinotopic mapping with spin echo BOLD at 7T.', *Magnetic resonance imaging* **28**(9), 1258–69.
- Peters, A. M., Brookes, M. J., Hoogenraad, F. G., Gowland, P. A., Francis, S. T., Morris, P. G. & Bowtell, R. (2007), 'T2\* measurements in human brain at 1.5, 3 and 7 T.', *Magnetic Resonance Imaging* **25**(6), 748–753.
- Pfeuffer, J., Van De Moortele, P.-F., Yacoub, E., Shmuel, A., Adriany, G., Andersen, P., Merkle, H., Garwood, M., Ugurbil, K. & Hu, X. (2002), Zoomed functional imaging in the human brain at 7 Tesla with simultaneous high spatial and high temporal resolution., Technical Report 1, Center for Magnetic Resonance Research, University of Minnesota Medical School, 2021 6th Street S.E., Minneapolis, Minnesota 55455, USA. josef.pfeuffer@tuebingen.mpg.de.
- Pilkington, D. T., Gaddam, S. R. & Reddy, R. (2011), 'Characterization of paramagnetic effects of molecular oxygen on blood oxygenation level-dependent-modulated hyperoxic contrast studies of the human brain.', *Magnetic resonance in medicine : official journal of the Society of Magnetic Resonance in Medicine / Society of Magnetic Resonance in Medicine* **66**(3), 794–801.
- Poole, M. & Bowtell, R. (2008), 'Volume parcellation for improved dynamic shimming.', *MAGMA* **21**(1-2), 31–40.
- Raichle, M. E., MacLeod, A. M., Snyder, A. Z., Powers, W. J., Gusnard, D. A. & Shulman, G. L. (2001), 'A default mode of brain function', *Proceedings of the National Academy of Sciences of the United States of America* **98**(2), 676–682.
- Ren, J., Dimitrov, I., Sherry, A. D. & Malloy, C. R. (2008), 'Composition of adipose tissue and marrow fat in humans by <sup>1</sup>H NMR at 7 Tesla', *Journal Of Lipid Research* **49**(9), 2055–2062.
- Rice, W. R. (1989), 'Analyzing tables of statistical tests', *Evolution* **43**(1), 223–225.
- Rostrup, E., Toft, P. B. & Gardet, K. (1995), 'Human Brain Induced by Hypo- and Hyperoxia', *Imaging* **8**(June 1994), 41–47.
- Schaefer, A., van der Zwaag, W., Francis, S. T., Head, K. E., Gowland, P. & Bowtell, R. (2008), 'High resolution SE-fMRI in humans at 3 and 7 T using a motor task.', *Magma (New York, N.Y.)* **21**(1-2), 113–20.

- Smith, S., Jenkinson, M., Woolrich, M. W., Beckmann, C. F., Behrens, T. E. J., Johansen-Berg, H., Bannister, P. R., Luca, M. D., Drobnjak, I., Flitney, D. E., Niazy, R. K., Saunders, J., Vickers, J., Zhang, Y., Stefano, N. D., Brady, J. M. & Matthews, P. M. (2004), 'Advances in functional and structural MR image analysis and implementation as FSL.', *Neuroimage* **23 Suppl 1**, S208—S219.
- Smith, S. M., Fox, P. T., Miller, K. L., Glahn, D. C., Fox, P. M., Mackay, C. E., Filippini, N., Watkins, K. E., Toro, R., Laird, A. R. & Beckmann, C. F. (2009), 'Correspondence of the brain's functional architecture during activation and rest.', *Proceedings of the National Academy of Sciences of the United States of America* **106**(31), 13040–5.
- Smith, S. & Nichols, T. E. (2009), 'Threshold-free cluster enhancement: addressing problems of smoothing, threshold dependence and localisation in cluster inference.', *Neuroimage* **44**(1), 83–98.
- Song, A. W., Wong, E. C., Tan, S. G. & Hyde, J. S. (1996), 'Diffusion weighted fMRI at 1.5 T.', *Magnetic Resonance in Medicine* **35**(2), 155–158.
- Stroman, P. W., Krause, V., Frankenstein, U. N., Maliszka, K. L. & Tomanek, B. (2001), 'Spin-echo versus gradient-echo fMRI with short echo times.', *Magnetic resonance imaging* **19**(6), 827–31.
- Techavipoo, U., Lai, S., Dimitrov, I., Lackey, J., Shi, J. & Guan, X. (2007), 'A ROBUST APPROACH FOR CORRECTION OF SUSCEPTIBILITY ARTIFACTS IN EPI Department of Radiology , 2 Department of Neurosurgery , Thomas Jefferson University , Philips Medical Systems , 4 Computer Science Department , Stony Brook University', pp. 125–128.
- Thulborn, K. R., Waterton, J. C., Matthews, P. M. & Radda, G. K. (1982), 'Oxygenation dependence of the transverse relaxation time of water protons in whole blood at high field.', *Biochim Biophys Acta* **714**(2), 265–270.
- Triantafyllou, C., Hoge, R. D., Krueger, G., Wiggins, C. J., Potthast, A., Wiggins, G. C. & Wald, L. L. (2005), Comparison of physiological noise at 1.5 T, 3 T and 7 T and optimization of fMRI acquisition parameters., Technical Report 1, MGH/MIT/HMS A.A. Martinos Center for Biomedical Imaging, Massachusetts General Hospital, Department of Radiology, Charlestown, 02129, USA. christin@nmr.mgh.harvard.edu.
- Triantafyllou, C., Polimeni, J. R. & Wald, L. L. (2010), 'Physiological noise and signal-to-noise ratio in fMRI with multi-channel array coils.', *NeuroImage* .

- Turner, R. (2002), 'How Much Cortex Can a Vein Drain? Downstream Dilution of Activation-Related Cerebral Blood Oxygenation Changes', *NeuroImage* **16**(4), 1062–1067.
- Uludag, K., Müller-Bierl, B. & Uurbil, K. (2009), 'An integrative model for neuronal activity-induced signal changes for gradient and spin echo functional imaging.', *NeuroImage* **48**(1), 150–65.
- Van De Ven, V. G., Formisano, E., Prvulovic, D., Roeder, C. H. & Linden, D. E. J. (2004), 'Functional connectivity as revealed by spatial independent component analysis of fMRI measurements during rest.', *Human Brain Mapping* **22**(3), 165–178.
- Wang, Z. (2011), 'Fixed-point algorithms for constrained ICA and their applications in fMRI data analysis.', *Magnetic resonance imaging* **29**(9), 1288–303.
- Wilson, J. L., Jenkinson, M., De Araujo, I., Krriegelbach, M. L., Rolls, E. T. & Jezzard, P. (2002), Fast, fully automated global and local magnetic field optimization for fMRI of the human brain., Technical Report 2, Centre for Functional Magnetic Resonance Imaging of the Brain, University of Oxford, John Radcliffe Hospital, Oxford, OX3 9DU, United Kingdom.
- Wright, G. A. & Hu, B. S. (1991), 'Estimating oxygen saturation of blood in vivo with MR imaging at 1.5 T', *Journal of Magnetic Resonance Imaging* **1**(3), 275–283.
- Yacoub, E., Duong, T. Q., Van De Moortele, P.-F., Lindquist, M., Adriany, G., Kim, S.-G., Uurbil, K. & Hu, X. (2003), 'Spin-echo fMRI in humans using high spatial resolutions and high magnetic fields.', *Magnetic Resonance in Medicine* **49**(4), 655–64.
- Yacoub, E., Harel, N. & Ugurbil, K. (2008), 'High-field fMRI unveils orientation columns in humans.', *Proceedings of the National Academy of Sciences of the United States of America* **105**(30), 10607–12.
- Yacoub, E., Shmuel, A., Logothetis, N. & Uurbil, K. (2007), 'Robust detection of ocular dominance columns in humans using Hahn Spin Echo BOLD functional MRI at 7 Tesla.', *Neuroimage* **37**(4), 1161–1177.
- Yacoub, E., Shmuel, A., Pfeuffer, J., Moortele, P.-f. V. D. & Adriany, G. (2001a), 'Investigation of the initial dip in fMRI at 7 Tesla', *NMR in Biomedicine* pp. 408–412.
- Yacoub, E., Shmuel, A., Pfeuffer, J., Moortele, P. F. V. D., Adriany, G., Andersen, P., Vaughan, J. T., Merkle, H., Ugurbil, K. & Hu, X. (2001b), 'Imaging brain function in humans at 7 Tesla.', *Magn Reson Med* **45**(4), 588–594.

- Yacoub, E., Van De Moortele, P.-F., Shmuel, A. & Uurbil, K. (2005), 'Signal and noise characteristics of Hahn SE and GE BOLD fMRI at 7 T in humans.', *NeuroImage* **24**(3), 738–50.
- Youssry, T. A., Schmid, U. D., Jassoy, A. G., Schmidt, D., Eisner, W. E., Reulen, H. J., Reiser, M. F. & Lissner, J. (1995), 'Topography of the cortical motor hand area: Prospective study with functional MR imaging and direct motor mapping at surgery', *Radiology* **195**(1), 23–29.
- Zeng, H., Gatenby, J. C., Zhao, Y. & Gore, J. C. (2004), 'New approach for correcting distortions in echo planar imaging.', *Magn Reson Med* **52**(6), 1373–1378.
- Zhao, F., Wang, P., Hendrich, K., Ugurbil, K. & Kim, S.-G. (2006), 'Cortical layer-dependent BOLD and CBV responses measured by spin-echo and gradient-echo fMRI: insights into hemodynamic regulation.', *NeuroImage* **30**(4), 1149–1160.
- Zhao, F., Wang, P. & Kim, S.-g. (2004), 'Cortical Depth-related Functional R2 and R2 \* Changes at 9 . 4 T'. *Biophysical Journal* **11**, 2004–2004.